

**KINETIC MODELLING AND A NOVEL
PACKED BED PHOTOCATALYTIC REACTOR**

by

Mehrab Mehrvar

A thesis
presented to the University of Waterloo
in fulfillment of the
thesis requirement for the degree of
Doctor of Philosophy
in
Chemical Engineering

Waterloo, Ontario, Canada, 1998

©Mehrab Mehrvar, 1998



**National Library
of Canada**

**Acquisitions and
Bibliographic Services**

**395 Wellington Street
Ottawa ON K1A 0N4
Canada**

**Bibliothèque nationale
du Canada**

**Acquisitions et
services bibliographiques**

**395, rue Wellington
Ottawa ON K1A 0N4
Canada**

Your file Votre référence

Our file Notre référence

The author has granted a non-exclusive licence allowing the National Library of Canada to reproduce, loan, distribute or sell copies of this thesis in microform, paper or electronic formats.

The author retains ownership of the copyright in this thesis. Neither the thesis nor substantial extracts from it may be printed or otherwise reproduced without the author's permission.

L'auteur a accordé une licence non exclusive permettant à la Bibliothèque nationale du Canada de reproduire, prêter, distribuer ou vendre des copies de cette thèse sous la forme de microfiche/film, de reproduction sur papier ou sur format électronique.

L'auteur conserve la propriété du droit d'auteur qui protège cette thèse. Ni la thèse ni des extraits substantiels de celle-ci ne doivent être imprimés ou autrement reproduits sans son autorisation.

0-612-30630-5

The University of Waterloo requires the signatures of all persons using or photocopying this thesis. Please sign below, and give address and date.

Abstract

A superior parameter estimation approach, based on the Box-Draper method of non-linear estimation using all the experimental data, is described and compared to the method of initial rates. It is shown that this approach results in better and more objective parameter estimates in the Langmuir-Hinshelwood kinetic models typically applicable to photocatalytic reactions.

The photocatalytic degradation of tetrahydrofuran, 1,4-dioxane, and their mixture is achieved in near-UV illuminated aqueous titanium dioxide slurries.

Two different commercial photocatalysts, Degussa P25 and HombiKat UV 100, are used to degrade 1,4-dioxane photocatalytically in an annular slurry photoreactor. The optimum photocatalyst loading for Degussa P25 is found to be 1.5 g L^{-1} while for Hombikat UV 100, it is between $3.0\text{--}4.0 \text{ g L}^{-1}$. The photoactivity of Degussa P25 is higher than Hombikat at lower concentrations whereas it is lower at higher concentrations. The photoactivity of UV 100 titanium dioxide is found to be twice that of Degussa P25 at optimum concentrations. Degussa P25 titanium dioxide with the optimum concentration of 1.5 g L^{-1} is used in the kinetic studies of tetrahydrofuran, 1,4-dioxane, and their mixture.

Using both gas chromatography/mass spectrometry (GC/MS) and ion chromatography (IC) methods, possible intermediates for the photocatalytic degradation of tetrahydrofuran and 1,4-dioxane are identified. 2(3H)-Furanone, dihydro- (γ -butyrolactone), succinic acid, acetic acid, formic acid, β -hydroxybutyric acid, and glycolic acid are identified as tetrahydrofuran intermediates during its photocatalytic reaction. Similarly, 1,2-ethanediol, difor-

mate, acetic acid, formic acid, 3-hydroxybutyric acid, and glycolic acid are identified as intermediates of the photocatalytic degradation of 1,4-dioxane.

Based on the proposed intermediates, reaction mechanism pathways and kinetic models for the photocatalytic degradation of tetrahydrofuran, 1,4-dioxane, and their mixture are developed. It is shown that the photocatalytic degradation of tetrahydrofuran and the binary system follows a modified Langmuir-Hinshelwood rate form whereas 1,4-dioxane follows a simple Langmuir-Hinshelwood model.

Finally, a novel tellerette packed bed photoreactor (TPBP) is introduced. Stainless steel is used to make the tellerette packings. The experiments reveal that mass transfer limitations in this packed bed photoreactor are insignificant, such that the reaction appears to be kinetically controlled. Also, it is shown that the ratio of the surface area of the photocatalyst to the photoreactor volume is adequate and sufficient UV light penetrates throughout the system.

Acknowledgments

I would like to express my deepest gratitude to my supervisors, Prof. Murray Moo-Young and Prof. William A. Anderson, for their valuable guidance and support throughout the creation of this thesis. My regards are due to Prof. Jenő Scharer, Prof. Robert Hudgins, and Prof. Susan Andrews, the Advisory Committee members of my Ph.D. thesis, for their valuable input throughout this study. My sincere thanks is also extended to Prof. James R. Bolton (the University of Western Ontario, London, Ontario, Canada), the external member of my Ph.D. thesis committee.

I wish to acknowledge Prof. Park M. Reilly for his valuable contributions in the statistical portion of this thesis. I would also like to acknowledge Dr. Susan Andrews and Dr. Sigrid Peldszus for their help in the GC/MS analyses. The author is thankful to Ralph Dickhout and Mark Sobon for their analytical assistance, Ernie Strutzenberger for his help in electrical assemblies, and Rick Hecktus for his efforts in making the tellerette packings. I thank the Engineering Machine Shop for manufacturing the photoreactor set-up. I would also like to thank all my friends and colleagues and all the staff and faculty members in the Chemical Engineering Department for providing a supportive working environment and helping me keep everything in perspective.

I would have found this achievement much more difficult without the support of my family. I owe a special debt to my wife, Laleh Haghparast, my son, Cina, and my daughter, Sheila. Thank you for your patience and understanding during my graduate studies.

To:
my beloved wife, Laleh,
my son, Cina,
my daughter, Sheila,
and my parents.

Contents

Abstract	iv
Acknowledgments	vi
List of Tables	xiv
List of Figures	xvi
Nomenclature	xxv
1 INTRODUCTION	1
2 LITERATURE REVIEW	7
2.1 Photocatalysis and its Fundamental Concepts	7
2.2 Mechanism of Photocatalysis	10
2.3 Kinetic Studies of Heterogeneous Photocatalytic Degradation of Water Pollutants	14
2.3.1 General Background	15

2.3.2	Conventional Langmuir-Hinshelwood (LH) isotherm	17
2.3.3	Langmuir-Hinshelwood (LH) isotherm for a Multicomponent System in Photocatalysis	18
2.3.4	Langmuir-Hinshelwood (LH) Model in Photocatalysis	19
2.3.5	Photocatalysis and Effective Parameters	20
2.4	Effects of Carbonate and Bicarbonate Ions on Photocatalysis .	21
2.5	Tetrahydrofuran and 1,4-Dioxane: Their Environmental Fate and Physical Properties	22
2.6	Photoreactor Design in Photocatalysis	25
2.6.1	Photoreactors and Their Configurations	25
2.6.2	Photoreactor Modelling	26
2.7	Photocatalysis Applications	30
2.8	Concluding Remarks	32
3	MATERIALS AND METHODS	34
3.1	Materials	34
3.2	Slurry Photoreactor Setup	37
3.3	Photoreactor Operation	42
3.4	Packed Bed Photoreactor Set-Up	44
3.4.1	Packings	44
3.4.2	Immobilization Technique	45
3.4.3	Packed Bed Experimental Setup	48

3.5	Analytical Techniques	49
3.5.1	Gas Chromatography (GC)	49
3.5.2	Solid Phase MicroExtraction (SPME)	52
3.5.3	Gas Chromatography/Mass Spectrometry (GC/MS)	55
3.5.4	Ion Chromatography Analysis (IC)	57
3.5.5	Total Organic Carbon (TOC) and Total Inorganic Carbon (TIC) Analyses	58
3.5.6	UV Absorbance and Transmittance Analyses	59
3.6	Safety Precautions	59
4	NON-LINEAR PARAMETER ESTIMATION FOR A DY- NAMIC MODEL	61
4.1	Introduction	62
4.2	Problem Definition	67
4.3	Statistical Analysis	69
4.4	An Example	76
4.5	Concluding Remarks	81
5	PHOTOCATALYTIC DEGRADATION OF TETRAHYDRO- FURAN, 1,4-DIOXANE, AND THEIR MIXTURE	89
5.1	Introduction	89
5.2	Illumination Time	90
5.3	Mass Transfer Effects in the Slurry Photoreactor	91

5.4	Dark Reactions and Photolysis	93
5.4.1	Dark Reaction	93
5.4.2	Photolysis	95
5.5	Photocatalyst Optimization	98
5.5.1	P25 Titanium Dioxide	98
5.5.2	Hombikat UV 100 Titanium Dioxide	99
5.5.3	Comparison Between Degussa P25 and Hombikat UV 100 Titanium Dioxides	101
5.6	Experimental Procedures for the Kinetic Studies	106
5.7	Reaction Mechanisms for the Photocatalytic Degradation of THF and DIOX	113
5.7.1	Photocatalytic Reaction Mechanisms for THF	113
5.7.1.1	GC/MS Results for THF Degradation	113
5.7.1.2	Ion Chromatography Results for THF Degrada- tion	114
5.7.1.3	THF Reaction Mechanisms	120
5.7.1.4	THF Rate Equations	130
5.7.2	Photocatalytic Reaction Mechanisms for DIOX	135
5.7.2.1	GC/MS Results for DIOX Degradation	136
5.7.2.2	Ion Chromatography Results for DIOX Degrada- tion	136
5.7.2.3	DIOX Reaction Mechanisms	139
5.7.2.4	DIOX Rate Equations	145

5.8	Biodegradability of Intermediates	148
5.9	Photocatalytic Degradation of Tetrahydrofuran	149
5.10	Photocatalytic Degradation of 1,4-Dioxane	154
5.11	Photocatalytic Degradation of γ -Butyrolactone (GBL)	166
5.12	Photocatalytic Degradation of a Binary System (Mixture of THF and DIOX)	167
5.13	Effects of Carbonate and Bicarbonate Ions on Photocatalysis .	175
5.14	Concluding Remarks	186
6	A NOVEL PACKED BED PHOTOREACTOR	195
6.1	Introduction	195
6.2	Packed Bed Photoreactor Operation	196
6.3	Results and Discussion	197
6.3.1	Light Distribution	197
6.3.2	Degradation of 1,4-Dioxane	199
6.3.3	Radiation Modelling and Mass Transfer in the Packed Bed Photoreactor	203
6.3.4	Energy Efficiency of the Packed Bed Photoreactor	215
6.4	Anodization of Pure Titanium to Titanium Dioxide	218
6.5	Concluding Remarks	218
7	CONCLUSIONS AND RECOMMENDATIONS	220

7.1	Conclusions	220
7.2	Recommendations for Future Work	224
	Bibliography	227
	APPENDICES	263
A	Method of Statistical Analysis of Dynamic Model	264
A.1	Dynamic Model	265
A.2	Sensitivity Equations	265
B	Preparing Solutions for both Calibrations and Runs	270
C	Error Analysis	273
C.1	Quality Control Analysis	273
C.2	Analysis of Variance Using the Method of Hierarchical Design Experiments	276
D	Diffusion Coefficient of 1,4-Dioxane in Water	281
E	Cost Estimation for a Photocatalysis Process	283

List of Tables

2.1	Physical properties of tetrahydrofuran and 1,4-dioxane [133].	24
2.2	Summary of different supports on which titanium dioxide was immobilized.	27
2.3	Examples of different immobilized photoreactor configurations studied previously.	28
3.1	Physical properties and supplemental information for two different photocatalysts, titanium dioxide, used in this work. This information was provided by the suppliers.	36
5.1	Absorption spectra characteristics of tetrahydrofuran, 1,4-dioxane, and γ -butyrolactone.	96
5.2	Possible intermediates for the photocatalytic degradation of tetrahydrofuran.	115
5.3	Possible intermediates for the photocatalytic degradation of 1,4-dioxane.	137
5.4	THF kinetic parameters in dynamic model Equations (5.44).	150

5.5	THF kinetic parameters considering no intermediates in the LH model Equations (5.68).	152
5.6	THF kinetic parameters in LH model Equations (5.69) considering GBL as its intermediate.	153
5.7	DIOX kinetic parameters in dynamic model Equations (5.66).	161
5.8	DIOX kinetic parameters for the LH model in Equation (5.68) without any intermediates.	166
5.9	Binary kinetic parameters in dynamic model (Equations (5.70)).	174
5.10	Kinetic parameters in binary model Equations (5.71): no intermediates were included in the model.	175
5.11	Binary kinetic parameters in LH model Equations (5.72) considering one intermediate for THF.	176
6.1	Examples of the values of the EE/O for different photoreactors studied previously.	217
C.1	Sample data in the hierarchical design experiments shown in Figure C.2.	279
C.2	Analysis of variance (ANOVA) using hierarchical design experiments for the photocatalyst optimization experiments.	280

List of Figures

2.1	Schematic diagram of an illuminated semiconductor photocatalyst particle along with the oxidation and reduction reactions. adopted from Turchi [213].	11
2.2	Chemical structures of tetrahydrofuran and 1,4-dioxane.	23
3.1	Schematic diagram of the slurry photoreactor set-up.	39
3.2	The configuration of tellerette packings made by the stainless steel wire.	46
3.3	Schematic diagram of the packed bed photoreactor set-up.	50
3.4	A typical calibration curve for 1,4-dioxane, $C_{DIOX} = (107.19 \pm 2.32) \times A_r$ [mg L^{-1}] where $A_r = A_{DIOX}/A_{I.S.}$; $R^2 = 0.9923$	53
4.1	The initial rate data plot for perchloroethylene (PCE) (raw data adopted from Turchi [213]).	64
4.2	General algorithm for studying the kinetic modeling.	66
4.3	The algorithm of the nonlinear parameter estimation of a dynamic model in kinetic studies.	75

4.4	The algorithm of the contours for the joint confidence of the parameters in the dynamic model.	77
4.5	The residuals in the linear (initial rate) model.	83
4.6	The residuals in the non-linear parameter estimation for PCE data (experimental data were adopted from Turchi [213]). . . .	84
4.7	The Concentration-Time plot for the Photocatalytic Degradation of PCE (experimental data were adopted from Turchi [213]).	85
4.8	Joint confidence interval for the PCE kinetic parameters in the non-linear model.	86
4.9	Joint 95% confidence interval for the PCE kinetic parameters in the linear (initial rate) model.	87
4.10	Joint 95% confidence interval for the PCE kinetic lumped parameters in the linear (initial rate) model.	88
5.1	Dark reaction for 1,4-dioxane in the slurry photoreactor, no photocatalyst and no UV light.	94
5.2	Photolytic degradation of 1,4-dioxane (lights on, no photocatalyst). $C_{0,DIOX} = 30.4 \text{ mg L}^{-1}$	97
5.3	Photocatalytic degradation of 1,4-dioxane in the slurry photoreactor with different Degussa P25 TiO_2 photocatalyst loadings. $C_{0,DIOX} = 27.8 \text{ mg L}^{-1}$. The system was aerated before runs.	100
5.4	Photocatalytic degradation of 1,4-dioxane in the slurry photoreactor with different UV-100 TiO_2 photocatalyst loading, $C_{0,DIOX} = 27.8 \text{ mg L}^{-1}$. The system was aerated before runs. .	102

5.5	Comparison between first order rate constants for UV-100 and Degussa P25 TiO ₂ catalysts in the slurry photoreactor for different TiO ₂ loadings. C _{0,DIOX} =27.8 mg L ⁻¹ . Error bars indicate the 95% confidence intervals.	107
5.6	Comparison between initial rates for UV-100 and Degussa P25 TiO ₂ catalysts in the slurry photoreactor for different TiO ₂ loadings. C _{0,DIOX} =27.8 mg L ⁻¹	108
5.7	Light extinction and transmittance at 350 nm for different TiO ₂ slurry solutions in a 1 cm cell.	109
5.8	Comparison between UV-100 and Degussa P25 TiO ₂ photocatalysts in the slurry photoreactor at low TiO ₂ loading. [TiO ₂]=0.5 g L ⁻¹ and C _{0,DIOX} =27.8 mg L ⁻¹	110
5.9	Comparison between UV-100 and Degussa P25 TiO ₂ photocatalysts in the slurry photoreactor at high TiO ₂ loading. [TiO ₂]=4.0 g L ⁻¹ and C _{0,DIOX} =27.8 mg L ⁻¹	111
5.10	Comparison between UV-100 and Degussa P25 TiO ₂ photocatalysts for the photocatalytic degradation of 1,4-dioxane in the slurry photoreactor at the optimum TiO ₂ loadings. C _{0,DIOX} =27.8 mg L ⁻¹	112
5.11	Molecular structures of tetrahydrofuran and its possible intermediates in the photocatalysis of tetrahydrofuran.	116

5.12	Typical Ion Chromatogram of standard solution containing organic acids at $50 \mu\text{g L}^{-1}$ concentration in tap water; superscripts indicate coelution: 1. with lactate and glycerate. 2. with propionate. 3. with oxalacetate.	118
5.13	Typical Ion Chromatogram of sample taken from photocatalytic reaction of tetrahydrofuran.	119
5.14	Proposed reaction mechanism for the photocatalytic degradation of tetrahydrofuran.	121
5.15	Details of the tetrahydrofuran oxidation by hydroxyl radical attack.	125
5.16	Molecular structures of 1,4-dioxane and its possible intermediates in photocatalytic DIOX degradation.	138
5.17	Typical Ion Chromatogram of 1,4-dioxane sample in the photocatalysis reaction.	140
5.18	Proposed reaction mechanism for the photocatalytic degradation of 1,4-dioxane.	141
5.19	Dissolved oxygen profile for the photocatalytic degradation of THF in the slurry photoreactor.	155
5.20	Photocatalytic degradation of THF along with its intermediate, γ -butyrolactone (GBL), in the slurry photoreactor; $C_{0,THF}=329 \mu\text{M}$	156
5.21	Comparison of the different models for the photocatalytic degradation of THF along with its intermediate, γ -butyrolactone (GBL), in the slurry photoreactor; $C_{0,THF}=257 \mu\text{M}$	157

5.22	Comparison of the different models for the photocatalytic degradation of THF along with its intermediate, γ -butyrolactone (GBL), in the slurry photoreactor: $C_{0,THF}=329 \mu\text{M}$	158
5.23	Comparison of the different models for the photocatalytic degradation of THF along with its intermediate, γ -butyrolactone (GBL), in the slurry photoreactor: $C_{0,THF}=1.25 \text{ mM}$	159
5.24	Photocatalytic degradation of DIOX along with its intermediate, 1,2-ethanediol.diformate (EDD), in the slurry photoreactor: $C_{0,DIOX}=394 \mu\text{M}$	162
5.25	Comparison of the different models for the photocatalytic degradation of DIOX along with its intermediate, 1,2-ethanediol, diformate (EDD), in the slurry photoreactor: $C_{0,DIOX}=134 \mu\text{M}$	163
5.26	Comparison of the different models for the photocatalytic degradation of DIOX along with its intermediate, 1,2-ethanediol, diformate (EDD), in the slurry photoreactor: $C_{0,DIOX}=394 \mu\text{M}$	164
5.27	Comparison of the different models for the photocatalytic degradation of DIOX along with its intermediate, 1,2-ethanediol, diformate (EDD), in the slurry photoreactor: $C_{0,DIOX}=787 \mu\text{M}$	165
5.28	First order kinetic test for the photocatalytic degradation of γ -butyrolactone in the slurry photoreactor; $k'_{GBL}=0.0194 \text{ min}^{-1}$ and $R^2=0.973$	168
5.29	Dissolved oxygen (DO) profile for the photocatalytic degradation of γ -butyrolactone in the slurry photoreactor.	169

5.30	First order kinetics for the photocatalytic degradation of γ -butyrolactone in the slurry photoreactor; $k = 0.0194 \text{ min}^{-1}$.	170
5.31	TIC/TOC profile for the photocatalytic degradation of γ -butyrolactone in the slurry photoreactor.	171
5.32	Photocatalytic degradation of the mixture of THF and DIOX along with THF intermediate, γ -butyrolactone (GBL), in the slurry photoreactor: $C_{0,THF}=87.9 \mu\text{M}$ and $C_{0,DIOX}=98.4 \mu\text{M}$; Models are based on the modified LH forms.	177
5.33	Comparison of the different models for the photocatalytic degradation of the mixture of THF and DIOX along with THF intermediate, γ -butyrolactone (GBL), in the slurry photoreactor: $C_{0,THF}=87.9 \mu\text{M}$ and $C_{0,DIOX}=98.4 \mu\text{M}$.	178
5.34	Comparison between single and binary systems for the photocatalytic degradation of THF in the slurry photoreactor: $C_{0,THF}=204 \mu\text{M}$ in single system and $C_{0,THF}=144 \mu\text{M}$ in binary system.	179
5.35	Comparison between single and binary systems for the photocatalytic degradation of DIOX in the slurry photoreactor: $C_{0,DIOX}=134 \mu\text{M}$ in single system and $C_{0,DIOX}=78.5 \mu\text{M}$ in binary system.	180
5.36	Binary model using kinetic parameters from single runs; $C_{0,THF}=87.9 \mu\text{M}$ and $C_{0,DIOX}=98.4 \mu\text{M}$.	181

5.37	pH profile for the photocatalytic degradation of the binary system (THF and DIOX) in the presence of NaHCO ₃ in the slurry photoreactor.	188
5.38	Effect of sodium bicarbonate on the photocatalytic degradation of the binary system (THF and DIOX) in the slurry photoreactor. for the run with sodium bicarbonate: [NaHCO ₃]=76.4 mg L ⁻¹	189
5.39	Effect of sodium bicarbonate on the photocatalytic degradation of the binary system (THF and DIOX) in the slurry photoreactor. for the run with sodium bicarbonate: [NaHCO ₃]=214 mg L ⁻¹	190
5.40	TOC profile for the photocatalytic degradation of the binary system (THF and 1,4-DIOX) in the presence of sodium bicarbonate.	191
5.41	TIC profile for the photocatalytic degradation of the binary system (THF and 1,4-DIOX) in the presence of sodium bicarbonate.	192
5.42	A typical carbon balance profile for the photocatalytic degradation of the binary system (THF and 1,4-DIOX) in the presence of sodium bicarbonate. [NaHCO ₃]=76.4 mg L ⁻¹	193
5.43	Effects of Photocatalysis on NaHCO ₃ in the absence of organics; [NaHCO ₃]=214 mg L ⁻¹	194

6.1	Light distribution in the packed bed photoreactor from one side. The light intensities were measured with a 320–380 nm electromagnetic wavelength sensor. The photoreactor was filled with water.	198
6.2	Test for first order kinetics of 1,4-dioxane in the packed bed photoreactor: $Q=2.08 \text{ L min}^{-1}$ (0.55 gpm).	204
6.3	Photocatalytic degradation of 1,4-dioxane in the packed bed photoreactor (solid and dotted lines are first order kinetic models). $Q=2.08 \text{ L min}^{-1}$ (0.55 gpm); $\tau=3.75 \text{ min}$	205
6.4	First order rate constant versus Reynolds number for the photocatalytic degradation of 1,4-dioxane in the packed bed photoreactor.	206
6.5	Mass transfer effect by correlations of the Sherwood number versus Reynolds number (Equations (6.3) and (6.4)) for a single cylinder with a perpendicular flow [68, 209].	207
6.6	Cylindrical photoreactor geometry.	211
6.7	Irradiance distribution in the packed bed photoreactor with uniform, parallel, and radial radiation from outside using the Beer-Lambert law. The inner radius of the photoreactor is 0.0525 m.	212
6.8	Local apparent rate constant profile for the degradation of 1,4-dioxane in the packed bed photoreactor for different attenuation coefficients. The radiation model is based on the Beer-Lambert law radiation model.	213

6.9	Local Damköhler number profile in the packed bed photoreactor for different attenuation coefficients. The radiation model is based on the Beer-Lambert law.	214
C.1	A sample of quality control chart for controlling GC analysis. Samples were analyzed to find the initial concentration of 1,4-dioxane in the slurry photoreactor. Definitions: σ = standard deviation, sample avg = sample average, UCL = Upper Control Limit ($+3\sigma$), LCL = Lower Control Limit (-3σ), UWL = Upper Warning Limit ($+2\sigma$), LWL = Lower Warning Limit (-2σ), Avg = Average.	275
C.2	The $2 \times 8 \times 2$ hierarchical design experiments for the initial concentrations of 1,4-dioxane in the photoreactor for photocatalyst optimization trials. S_i 's are the initial concentrations of 1,4-dioxane in the slurry photoreactor for the i^{th} run and R_i is the i^{th} run.	278

Nomenclature

ROMAN LETTERS

- A* Electron acceptor such as oxygen. see equation (2.9)
- a* Specific surface area of the packings. [$\text{m}^2 \text{m}^{-3}$]
- a* Specific surface area of the particles in solution. [$\text{m}^2 \text{m}^{-3}$]
- \underline{A}_i An approximation to the Hessian matrix. see equation (4.15)
- a_c* Titanium dioxide particle area normal to illumination. [m^2]
- A_{DIOX}* GC peak area for 1,4-dioxane
- A_{I.S.}* GC peak area for internal standard
- A_i* GC peak area for the component *i*
- A_{r,EDD}* GC peak area ratio for EDD. see equation (5.65)
- A_{r,i}* GC peak area ratio
- A_{r,i}* The GC peak area ratio for component *i*
- a_s* Particle surface area. [m^2]
- c* the velocity of light, $2.998 \times 10^{-8} \text{ m s}^{-1}$
- C₀* Initial concentration or bulk solution concentration of organic species, [M] or [mol m^{-3}]
- C_i* Concentration of component *i*, [M], see equation (2.18), page 19

D	Diffusion coefficient, [$\text{m}^2 \text{s}^{-1}$]
D	Electron donor, see equation (2.9)
D_{AB}°	Diffusivity of A in very dilute solution in solvent B. [$\text{m}^2 \text{s}^{-1}$]
\bar{d}_p	Average particle diameter. [m]
d_{wire}	Diameter of wires (packings). [m]
Da	Damköhler number. [dimensionless]
DF	Density Function
e^-	Semiconductor conduction band electron
E_{bg}	Bandgap energy. page 8
E_c	Conduction band energy. page 8
E_v	Valance band energy. page 8
EE/O	Electrical Energy per Order. [$\text{kWh}/(\text{m}^3 \text{ order})$]
eV	Electron Volts
$F_{95\%, \nu_1, \nu_2}$	95% confidence limit for F-distribution with ν_1 and ν_2 degrees of freedom
$F_{cal.}$	Calculated F-distribution. page 280
h	Planck's constant (6.6256×10^{-34} [J s photon ⁻¹]), see equation (2.3)
h^+	Semiconductor valance band hole

\underline{H}_i	Hessian matrix, see equation (4.14)
I	Molar photon flux, [Einstein $\text{m}^{-2} \text{s}^{-1}$]
I_T	Transmitted Molar photon flux. [Einstein $\text{m}^{-2} \text{s}^{-1}$]
\underline{J}_i	Jacobian matrix, see equation (4.18)
k	Reaction rate constant, [M s^{-1}]
k'	Adsorption rate constant. [s^{-1}], see equation (2.14)
k''	Desorption rate constant. [M s^{-1}], see equation (2.15)
k_L	Mass transfer coefficient. [m s^{-1}]
$K_{EDD,ads}$	EDD binding constant, see equation (5.64)
$k_{EDD,\bullet OH}$	Rate constant when EDD reacts with $\bullet\text{OH}$, see equation (5.64)
\bar{K}_i	Apparent binding constant. [M], see equation (2.18), page 19
k_i	Reaction rate constant. [M s^{-1}], see equation (2.18), page 19
k_s	Mass transfer coefficient at the liquid-solid interface, [m s^{-1}]
M	Molar (mol L^{-1})
M_B	Molecular weight of solvent, [kg kmol^{-1}], see equation (D.2)
m_p	Particle concentration in the solution, [kg m^{-3}]
n	Total number of species in the system; Total number of observation data; Total number of differential equations for a dynamic model

P	Lamp power. [kW]
pA	picoampere
Pr	Probability
\underline{q}_i	Gradient vector. see equation (4.16)
r_a	Rate of adsorption. see equation (2.14)
r_d	Rate of desorption. see equation (2.15)
r_{i0}	Initial reaction rate for component i
R_i	i^{th} run. page 278
r_i	Reaction rate for component i . [$M s^{-1}$]. see equation (2.18). page 19
Re	Reynolds Number. [dimensionless]
S_i	Initial concentration of 1,4-dioxane in the slurry photoreactor for the i^{th} run. page 278
Sc	Schmidt Number. [dimensionless]
Sh	Sherwood Number. [dimensionless]
T	Temperature. [K]
t	Time. [s] or [min]
t_{III}	Illumination time or the actual reaction time, [s] or [min], see equation (5.1)
t_{run}	Actual run time, [s] or [min], see equation (5.1)

- \underline{V}^* Covariance matrix
- V_{DIOX} Pure DIOX volume injected into V_{FDW} L of FDW [μ L]. see equation (B.2).
page 271
- V_{FDW} The volume of filtered deionized water [L]. see equation (B.2). page 271
- V_R The volume of the Illumination zone of the photoreactor. [L]
- V_s Sample solution volume. [mL]
- V_{THF} Pure THF volume injected into V_{FDW} L of FDW [μ L]. see equation (B.2).
page 271
- V_{TOL} Pure toluene volume injected into V_{FDW} L of FDW [μ L]. see equation (B.3).
page 271
- V_{tot} Total volume of the liquid in the photoreactor. [L]
- \underline{X}_i The vector of values of the independent variables at the i^{th} trial
- \underline{y}_i The vector of observations for the dependent variables at the i^{th} trial
- [] Designates concentration, units. or a dimensionless quantity

GREEK LETTERS

- α Proportionality constant, see equation (5.39)
- ϵ_i Vector of errors
- η The slope of the calibration curve, i.e., C_i versus $A_{r,i}$, see equation (3.1)

η_{EDD}	Calibration constant for EDD. see equation (5.65)
λ	the wavelength of the radiation. [m] or [nm]
λ_{max}	The wavelength at which maximum absorbance occurs. [nm]. see Table 5.1
μ	Solution viscosity. [kg m ⁻¹ s ⁻¹]
μM	Micromolar ($\mu\text{mol L}^{-1}$)
μS	MicroSiemens (the unit of conductivity). see Figures 5.13 and 5.17
ν	Frequency of the radiation. [s ⁻¹]. see equation (2.3)
ν_A	Solute molal volume at normal boiling point. [m ³ kmol ⁻¹]. see equation (D.2)
$\underline{\nu}_i$	The step direction(vector). see equation (4.12)
ν_p	Particle volume. [m ³]
ϕ	Association factor for solvent (=2.26 for water as solvent), see equation (D.2)
ϕ	Objective function. see equation (4.11)
ρ_{DIOX}	DIOX density (1.034 mg μL^{-1})
ρ_i	The step size (scalar), see equation (4.12)
ρ_p	Density of the particles. [kg m ⁻³]
ρ_{THF}	THF density (0.8892 mg μL^{-1})
ρ_{TOL}	Toluene density (0.866 mg μL^{-1})

σ	Standard deviation
σ^2	Variance
σ_D	Standard deviation for data
σ_D^2	Variance of data
σ_R	Standard deviation for runs
σ_R^2	Variance of runs
θ	Fraction of the catalyst surface covered by molecules (see Chapter 2). Also, the parameters in a dynamic model in Chapter 4.
$\underline{\theta}^*$	Vector of true parameter values

SUBSCRIPTS

+ and – Refers to the forward and backward reactions, for example, see equation (5.33), page 130

ν Number of observations, see equation (4.6)

ν_1, ν_2 Degrees of freedom in F-distribution, page 280

a Adsorption

ads Adsorbed organic species on the photocatalyst particles

Arabic numbers Refers to the equation numbers, for example, see equation (5.33)

D Data

<i>d</i>	Desorption
<i>i</i>	The i^{th} trial: also i^{th} component in the reaction rate equations
<i>io</i>	Initial condition for component <i>i</i>
<i>max</i>	Maximum
<i>o</i>	Initial condition
<i>P</i>	Photocatalyst
<i>p</i>	Number of parameters or Particles
<i>R</i>	Reactor
<i>R</i>	Runs
<i>run</i>	Run Time. see equation (5.1)
<i>s</i>	Sample
<i>std</i>	Standard solution
<i>tot</i>	Total

SUPERSCRIPTS

* Designates true values of the parameters

ACRONYMS

ANOVA Analysis of Variance

AOP Advanced Oxidation Process

Avg Average

CAS Chemical Abstract Service

DCA Dichloroacetate

DF Degree of Freedom

DIOX 1,4-Dioxane

DO Dissolved Oxygen

EDD 1,2-Ethanediol, diformate

EE/O Electrical Energy per Order

FDW Filtered Deionized Water, page 34

FID Flame Ionization Detector

GAC Granular Activated Carbon

GBL γ -Butyrolactone

GC Gas Chromatography

gpm Gallon Per Minute

HPLC High Performance Liquid Chromatography

I.S. Internal Standard

IC Ion Chromatography

LCL Lower Control Limit

LH Langmuir-Hinshelwood

LWL Lower Warning Limit

MEK Methyleneethyl ketone

MISA Municipal / Industrial Strategy for Abatement

MS Mass Spectrometry

MS Mean Square

PCE Perchloroethylene

PZC Point of Zero Charge. page 183

sample avg Sample Average

SEM Scanning Electron Microscope

SofS Sum of Squares

SPME Solid Phase MicroExtraction

THF Tetrahydrofuran

TIC Total Inorganic Carbon

TLV Threshold Limit Value

TOC Total Organic Carbon

TOL Toluene

TPBP Tellerette Packed Bed Photoreactor

UCL Upper Control Limit

UV Ultraviolet

UWL Upper Warning Limit

Chapter 1

INTRODUCTION

The presence of organic pollutants in drinking water, as well as in the waste waters of many industrial plants around the world, endangers human and animal health, i.e., the quality of the environment. Pollution in groundwater, streams, and lakes has manifold causes. The major sources are those from domestic and industrial discharges, chemical spills, and large scale applications of pesticides and herbicides.

Many of the organic pollutants are so toxic that even a trace amount of them could be enough to cause health problems among humans and animals. For example, PCBs enter the food chain and affect human health through bioaccumulation [135, 222]. Therefore, in the public mind, the management of toxic chemicals is becoming one of the most important issues facing any society. For instance, the Canadian government has a number of activities and responsibilities related to the control of toxic compounds. In this regard, many directives, such as the Environment Contaminant Act, the Clean Air

Act, the Pollution Provisions of the Fisheries Act, and the Ocean Dumping Control Act, all address these toxic components. In addition, a number of other federal departments and agencies have legislation and programs that address toxic chemicals and their control [60]. Generally speaking, Environment Canada has been developing a new federal environmental protection policy which will put forward the need for new federal legislation to protect the environment and human health against toxic chemicals and their hazards. As a result, on April 25, 1989, the Ontario Ministry of the Environment made the Effluent Monitoring Regulation for the Organic Chemical Manufacturing Sector as law [70]. In this regard, MISA (Municipal / Industrial Strategy for Abatement) formulated an abatement regulation which requires chemical plants to reduce toxic discharges to levels attainable by the best available pollution control technology that is economically achievable. The Ontario Environment Protection Act [70] has provided the enforcement of the regulation by which violators face fines of up to \$50,000 per day. Hence, MISA's ultimate goal is the virtual elimination of persistent toxic chemicals from discharges to Ontario waterways [70, 71, 175]. Consequently, we see that mineralization and complete degradation of all organic contaminants from water and wastewater is very desirable.

Many inorganic impurities are removed by conventional unit operations such as filtration, ion exchange, precipitation, flocculation / agglomeration, etc. which are not destructive. On the other hand, organic removal is often achieved by in-situ degradation of the substrates rather than by separation which would require further processing steps. Also, many organic pollutants

are resistant to biodegradation, such that their biodegradation reactions take much time. Photocatalysis, an advanced oxidation process (AOP), shows promise as a route to destroy organic pollutants completely to CO₂ and inorganic compounds. In photocatalysis, illuminated titanium dioxide produces hydroxyl and superoxide radicals which oxidize organic molecules at the solid surface of the catalyst. Therefore, of all processes for purification of water and wastewater, advanced oxidation processes offer an effective way to degrade them completely. Photocatalysis alone is not the only photoprocess capable of mineralizing organics. Other AOP's, capable of destroying many organics in water and wastewater, are UV/O₂, UV/H₂O₂, and UV/O₃ (for example see [31, 46, 93, 166]).

While numerous publications in photocatalysis deal with some organics in water and wastewater, few studies have been carried out on multicomponent systems. Tetrahydrofuran and 1,4-dioxane are two organic pollutants which are, for example, found in the landfill groundwater in the southern portion of the Ottawa Airport, Gloucester, Ontario, Canada. Moralejo [156] reported that this land, which is about twelve hectares, was used as a municipal dumpsite for the municipality of Gloucester between 1957 and 1974. Also this land was used to dump chemical wastes from various government agencies and laboratories between 1969 and 1980. The groundwater beneath this land contains many organic pollutants, which all cause serious health concerns. Moreover, tetrahydrofuran and 1,4-dioxane have been found in industrial wastewater. So far, there is virtually no work on the photocatalytic degradation of tetrahydrofuran (THF), 1,4-dioxane (DIOX), and their

mixture.

Furthermore, most of the studies have focused on the photocatalytic degradation of target contaminants in water and wastewater. However, in the real world there are some non-target components which may compete with oxidation reactions. For instance, the existence of carbonate and bicarbonate ions in the matrix may consume unacceptable amounts of hydroxyl radicals which are primarily responsible for the photocatalytic destruction of organics.

Regarding the importance of the destruction of toxic organics from water and wastewater, the objectives of this study are as follows:

1. *Nonlinear modelling and parameter estimation of a dynamic model in photocatalysis:*

To solve a set of non-linear differential equations for a dynamic model in photocatalytic reactions, a statistical approach based on the Box-Draper method is developed. This methodology will be used to solve non-linear dynamic models for the photocatalytic degradation of choice in the next part of this thesis.

The method of initial rates has been the customary approach to estimate the parameters in a photocatalytic reaction model. When there is more than one compound present in the system as well as some intermediates, the method of initial rate fails. One of the objectives of this study is to develop a robust method of parameter estimation for a dynamic model and explain the drawbacks of the method of initial rates.

2. *Investigate the photocatalytic degradation of tetrahydrofuran, 1,4-dioxane, and their mixture:*

Kinetic models which describe the time course of photocatalytic reactions are necessary to design photocatalytic reactors. Exploring possible intermediates, reaction mechanism pathways, and kinetic models for the photocatalytic degradation of tetrahydrofuran, 1,4-dioxane, and their mixture is the main objective of this study.

Another goal is to investigate the photoactivity of two available titanium dioxide photocatalysts, Degussa P25 and Hombikat UV 100.

In addition, studying the effects of carbonate and bicarbonate ions on the photocatalytic degradation of the mixture of tetrahydrofuran and 1,4-dioxane, is another objective of this study.

3. *Design and examine a novel packed bed photoreactor in order to enhance mass transfer between the liquid and photocatalyst surfaces while maintaining sufficient light penetration throughout the bed:*

1,4-Dioxane was chosen as a model compound to evaluate this photoreactor design.

The second chapter of this thesis summarizes the literature survey relevant to this study. Chapter 3 explains the materials and methods used in this study as well as the techniques involved in the experimental setup. Chapter 4 outlines a robust nonlinear parameter estimation method for a set of nonlinear differential equations. In Chapter 5, the experimental results for the degradation of tetrahydrofuran and 1,4-dioxane are discussed. Also,

possible intermediates, reaction mechanism pathways, and kinetic models for the photocatalytic degradation of these compounds are proposed. Chapter 6 explains the design of a novel packed bed photoreactor. Conclusions and recommendations for future work are presented in the last chapter of this thesis.

Chapter 2

LITERATURE REVIEW

In this chapter a general overview of photocatalysis and its fundamentals, mechanisms, and applications are reviewed. The literature related to the objectives of this thesis is given particular emphasis.

2.1 Photocatalysis and its Fundamental Concepts

A catalyst accelerates a reaction without being consumed. The catalyst can be organic or inorganic in transformation of redox-induced reactions. As long as the catalyst does not participate in bonding with the final products, the chemical nature of the catalyst is immaterial. Most catalysts are activated by heat and hence are called thermal catalysts [33, 72]. A photocatalyst is activated by photons rather than heat with the main chemical reactions occurring on the surface. In heterogeneous photocatalysis, light and a catalyst

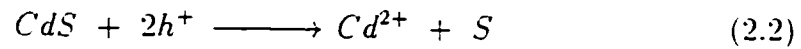
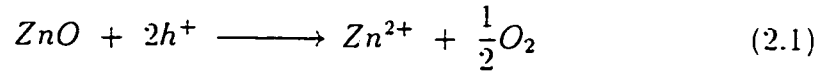
are essential to initiate or enhance the rate of a chemical reaction [118].

Because of the unique electronic characteristics of semiconductors, they have been widely used as photocatalysts. Bandgap energy is one of the most important characteristics of semiconductors. Its magnitude is the difference between valence band and conduction band energies, $E_{bg} = E_v - E_c$. The valence band is the upper of the filled bands while the conduction band is the lower of the unfilled bands. The strength of the chemical bonds strongly affects the E_{bg} [177].

There are some semiconductors which have been used in photocatalysis. A semiconductor used in photocatalysis must have the following general characteristics for pollution abatement technologies, that is, to be

1. photoactive when illuminated by radiation with energies greater than or equal to the bandgap energy
2. non-toxic
3. photostable
4. long-lived
5. inexpensive

Slight photoactivity for In_2O_3 , SrTiO_3 , ZrO_2 , and WO_3 has been reported [138, 192]. To date, titanium dioxide, cadmium sulfide, and zinc oxide have been the most commonly used semiconductor photocatalysts. However, CdS and ZnO, which have been used widely in photocatalysis, are not stable because of self-oxidation photocorrosion reactions [73, 96, 173]:



These reactions lead to the destruction of the photocatalyst as well as the production of some hazardous metal ions in solution. Due to the lack of photostability of ZnO and CdS, their photocatalytic applications are severely hampered.

To date, the n-type semiconductor titanium dioxide is the most commonly used photocatalyst in photocatalytic treatment of water and wastewater. TiO₂ has the following characteristics [12, 101, 153]: it is

1. photoactive
2. capable of utilizing UV light (absorbs UV light below 400 nm)
3. chemically and biologically inert; i.e., innocuous
4. photostable
5. inexpensive
6. free of chemical additives
7. capable of total degradation for many organic pollutants

Anatase, rutile, and brookite are the crystalline forms of titanium dioxide. Brookite is not commonly available and rutile is totally inactive. Anatase

is the only photoactive crystalline form of titanium dioxide. Although there are different sources of titanium dioxide, Degussa P25 TiO₂ has effectively become a research standard because of its well-defined nature and reasonably high photoactivity. It has a BET surface area of $55 \pm 15 \text{ m}^2\text{g}^{-1}$ with an average primary particle size of 30 nm. Also, Degussa P25 TiO₂ has a substantially higher photocatalytic activity than most of the other available samples of TiO₂ [75]. Degussa P25 TiO₂ contains 70% anatase and 30% rutile (see Table 3.1).

2.2 Mechanism of Photocatalysis

As mentioned previously, in a semiconductor there is a bandgap energy between the highest occupied and the lowest unoccupied energy bands. As Figure 2.1 depicts, a semiconductor is activated through the absorption of a photon of ultra-bandgap energy [69]. This results in the promotion of an electron, e^- , from the valence band into the conduction band generating a hole, h^+ , in the valence band, as shown in Reaction (2.3) [74, 85, 91, 128, 141, 165, 193].



where h = Planck's constant ($6.6256 \times 10^{-34} \text{ [J s photon}^{-1}\text{]}$);

ν = the frequency of radiation, [s^{-1}].

A photon has no mass but it has a specific energy. Planck's equation relates the energy of a photon to the frequency of the radiation, ν , as follows:

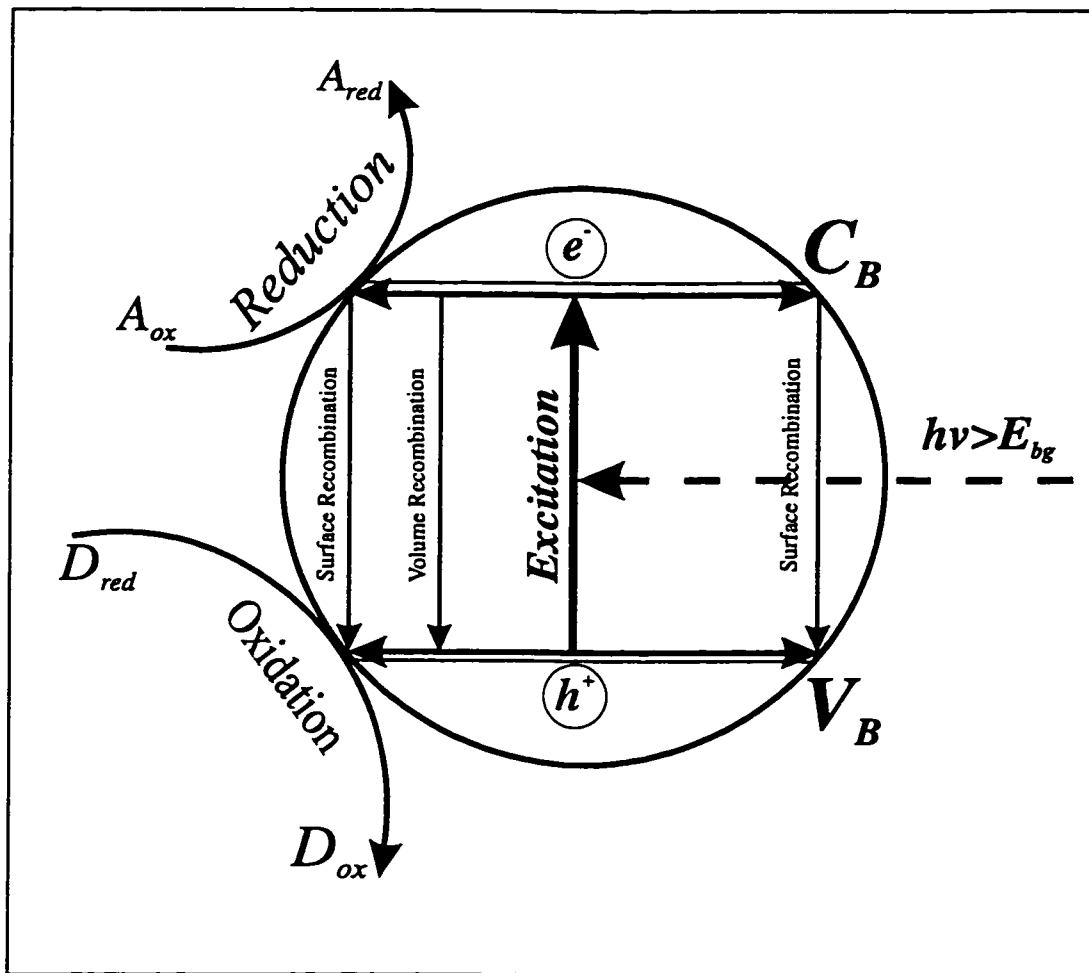


Figure 2.1: Schematic diagram of an illuminated semiconductor photocatalyst particle along with the oxidation and reduction reactions, adopted from Turchi [213].

$$E = h\nu \quad (2.4)$$

The electromagnetic radiation is described in terms of the frequency, the wavelength, and the velocity of light as follows:

$$c = \lambda\nu \quad (2.5)$$

where $c = 2.998 \times 10^8 \text{ m s}^{-1}$ is the velocity of light:

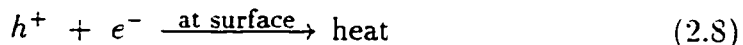
λ = the wavelength of the radiation, [m] or [nm].

By substituting Equation (2.4) into Equation (2.5), the wavelength of a photon may be defined as follows:

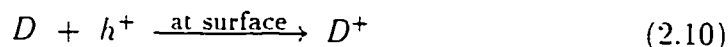
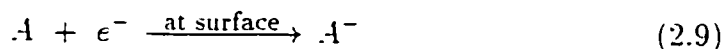
$$\lambda = \frac{hc}{E} \quad (2.6)$$

Anatase titanium dioxide has a bandgap energy of 3.2 eV [84]. By using Equation (2.6), photons with wavelength of 387.5 nm have 3.2 eV energy. Hence, the initiating step in photocatalysis is Reaction (2.3), which requires radiation sufficiently energetic ($\lambda < 387.5 \text{ nm}$ for anatase) to generate electron-hole pairs. As Figure 2.1 shows, some of the generated electrons and holes react in the bulk of the particle as well as at the surface. These undesired reactions, Reactions (2.7) and (2.8), reduce the photoactivity of the semiconductor.

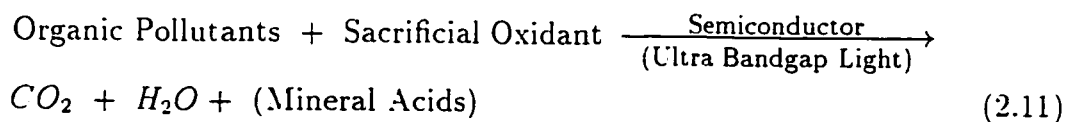




To prevent the recombination of electrons and holes, a sacrificial oxidant must be adsorbed on the photocatalyst surface. Its presence on the surface consumes electrons, thereby maintaining sufficient holes in the system to facilitate the oxidation reactions. Reaction (2.9) shows the reduction in which A is an electron acceptor such as oxygen, hydrogen peroxide, ozone, etc. On the other hand, Reaction (2.10) presents the general oxidation reaction in which D is the electron donor.



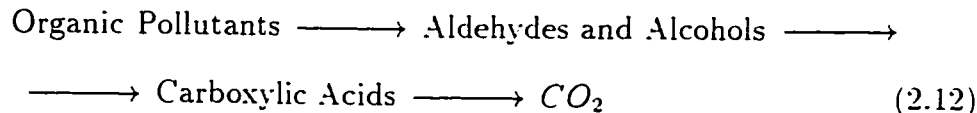
As mentioned before, the final goal of the photocatalytic process is to destroy organic pollutants completely, not just to remove them. The overall process in photocatalytic degradation of organic pollutants is as follows [153]:



As Equation (2.11) shows, the organic pollutants are degraded completely to CO₂ and some mineral acids, which depend on the kinds of organics.

When the semiconductor photocatalyst is continuously illuminated with an ultra bandgap light ($E_{bg}=3.2$ eV for TiO_2), the solid surface can oxidize large populations of hydroxide ions to hydroxyl radicals. These hydroxyl radicals are primarily responsible for oxidizing the majority of organics to CO_2 , water, and inorganic compounds [32, 137, 183, 206].

The general pattern of the organic destruction in photocatalysis and any other advanced oxidation technology can be summarized in Equation (2.12) [31]:



The last step in Reaction (2.12) is somehow slower than the other steps (for example see [53, 137]). Consequently, after degradation of the parent compounds, there are still some intermediates in solution that have to be taken into account. The total organic carbon (TOC) analysis can verify the existence of these intermediates in the system. While parent compounds disappear, there is still some TOC in the system.

2.3 Kinetic Studies of Heterogeneous Photocatalytic Degradation of Water Pollutants

In this section, a general overview of the photocatalytic kinetics is reviewed. The general background and the methods of reaction rate modelling

in photocatalysis are discussed.

2.3.1 General Background

Heterogeneous photocatalytic degradation of water and wastewater pollutants is a young technology which has only been investigated in the last couple of decades. In 1972, Fujishima and Honda [82] showed that water could be split (simultaneously oxidized and reduced) through illumination of titanium dioxide. In 1980, Childs and Ollis [58] through their paper came to the question "Is photocatalysis catalytic?". They not only demonstrated that photocatalytic reactions are indeed catalytic but also that their rates are comparable to biological and other reactions.

Ollis and co-workers [110, 178] showed that semiconductor photocatalysis can be used as a method of water purification. Since that time, photocatalytic reactions for different organic pollutants found in water and wastewater have been investigated. Most of the work to date has been focused on single component aqueous systems.

A sequence of steps occurs in heterogeneous catalysis in order to convert the reactants to products [107, 122, 202]:

1. transport of reactants from the bulk of the fluid to the exterior surface of the catalyst
2. intraparticle transport of reactants into the catalyst particle
3. adsorption of reactants
4. surface reactions

5. desorption of products
6. intraparticle transport of products to the exterior surface of the catalyst
7. transport of products from the surface of the catalyst to the bulk of the fluid

Heterogeneous photocatalysis can also be described via the following steps:

- I. photogeneration of electron-hole pairs by inducing an ultra-bandgap light on a semiconductor photocatalyst
- II. electron-hole pair separation by traps
- III. redox reaction
- IV. product evolution

Obviously steps 1 and 7 of the catalytic process must also occur in photocatalysis. Step IV of the photocatalytic process includes steps 5, 6, and 7 of the catalytic process. The only additional complexity contributed by the photocatalytic process is the surface reaction, step 4, which develops according to steps I, II, and III. Consequently, a photocatalytic process is the same as catalytic process except that the surface redox reaction occurs through a separated electron-hole, photogenerated by inducing a semiconductor photocatalyst.

Although it is commonly assumed that titanium dioxide is initiated at the liquid - solid interface, the exact mechanisms of photocatalysis and the location of the subsequent steps remains unclear. Literature shows that the reaction rates of most water pollutants, which have been photocatalytically degraded, follow the Langmuir-Hinshelwood (LH) isotherm form [75, 160, 161, 162, 164, 167, 168]. For instance, the reaction rates of benzene, perchloroethylene [212], dichloromethane [110], dichloroethane, dichloroacetic acid, and monochloroacetic acid [163] obey the Langmuir-Hinshelwood isotherm.

2.3.2 Conventional Langmuir-Hinshelwood (LH) isotherm

In the Langmuir-Hinshelwood isotherm, the reaction rate is proportional to the surface covered by adsorbed molecules. If θ is the fraction of surface which is covered by adsorbed molecules, we have:

$$rate = k\theta \quad (2.13)$$

where k is the rate constant. θ can be obtained using rate of adsorption and desorption. For adsorption:

$$r_a = k'C(1 - \theta) \quad (2.14)$$

and for desorption:

$$r_d = k''\theta \quad (2.15)$$

By equating r_a and r_d , the amount adsorbed at equilibrium can be obtained. Therefore,

$$\theta = \frac{k'C}{k'' + k'C} = \frac{KC}{1 + KC} \quad (2.16)$$

where $K (= k'/k'')$ is a binding constant. By substituting θ in equation (2.13), the rate of reaction is:

$$rate = \frac{kKC}{1 + KC} \quad (2.17)$$

2.3.3 Langmuir-Hinshelwood (LH) isotherm for a Multicomponent System in Photocatalysis

In the real world, water and wastewater are usually polluted with more than one contaminant. Even though the exact mechanisms of the photocatalytic reactions are not always clear and little information on multicomponent systems is available, the literature indicates that the Langmuir-Hinshelwood rate equation can predict the rate of reaction for component i which is adsorbed competitively with other species [5, 103, 146, 161, 211, 212]. In other words, the following expression has been suggested to account for reactions in which there are some competitive adsorbing species such as reactants and intermediates for a single adsorption site [164]:

$$r_i = \frac{k_i K_i C_i}{1 + K_i C_i + \sum_{j=1}^n (j \neq i) K_j C_j} \quad (2.18)$$

where k_i = the rate constant, a function of catalytic properties, reactants, sacrificial oxidant, and light intensity:

K_i = the apparent binding constant, which is a function of the catalyst surface, reactants, and solvent properties:

n = number of competing species.

In 1990, Turchi and Ollis [212], by studying a mixture of benzene and perchloroethylene, showed that the degradation obeyed the Langmuir - Hinshelwood form considering two significant intermediates for benzene. Deberry et al. [63] showed qualitatively that photocatalysis has the ability to treat real wastewater including propanol, pyridine, methylethyl ketone (MEK), 1,2,3-trichloropropane, and methanol.

2.3.4 Langmuir-Hinshelwood (LH) Model in Photocatalysis

Although, the conventional LH model is the most probable form of the photocatalytic reaction mechanisms, the parameters in this model have different meanings. Turchi and Ollis [212, 213] demonstrated that there are four possible routes in which hydroxyl radicals attack organics in photocatalysis process. These possible mechanisms are as follows:

1. The reactions take place between the adsorbed organic pollutants and hydroxyl radicals on the photocatalyst surface.
2. Adsorbed organic pollutants react with the free hydroxyl radicals.
3. Free organic pollutants react with the adsorbed hydroxyl radicals.

4. Both organic pollutants and hydroxyl radicals react in the bulk phase.

After deriving the LH form with all four possible mechanisms, all models are similar in the general form of Equation (2.18). These results have been used to develop the models for the photocatalytic destruction of 1,4-dioxane and tetrahydrofuran in Chapter 5.

There is also evidence that direct oxidation of organics by holes occurs, as well as direct reduction by electrons for some compounds such as tetrachloride [105].

2.3.5 Photocatalysis and Effective Parameters

Sacrificial oxidants, usually oxygen, have an important role in the rate of photocatalytic reactions. Okamoto et al. [160, 161] studied the role of oxygen in degradation of phenol over TiO_2 powder. They found that photocatalytic reaction rates depend on the light irradiance and the oxygen concentration in the solution.

Another factor which may affect TiO_2 is pH [42, 67, 75, 76, 80, 90, 97, 101, 153, 186, 188, 189]. Literature shows that degradation rates of reactions for some organics are high at low pH whereas for others at high pH. Nevertheless, there are small changes, often less than one order of magnitude, for the photocatalytic activity from one end of the pH range to the other [75]. To determine the influence of pH on the reaction rate, the reagents used to adjust the pH must contain co-ions which have no effect on the rate. NaOH, HNO_3 , and buffer solutions are typically used to adjust the pH in various ranges.

Temperature and pressure are two other factors which usually affect the rate of the reaction. One advantage of photocatalytic water and wastewater purification is that operation takes place at ambient temperature and pressure. Studies show that by increasing temperature up to 70°C , the photocatalytic reaction rate increases [6]. On the other hand, at higher temperatures ($> 70^{\circ}\text{C}$), the photocatalytic reaction rate decreases and therefore, the activation energy becomes negative and the adsorption of organics onto the surface of the photocatalyst becomes the rate limiting step [176]. It has been reported that the activation energy in photocatalysis processes is small ($5\text{--}16\text{ kJ mol}^{-1}$) [99, 153]. This is due to the fact that the photocatalysis processes are activated by photons. The working temperature for photocatalytic reactions is between 20 to 80°C [99]. Therefore, appropriate commercial reactor design must allow for suitable temperature control. In some studies, Arrhenius behavior was observed in the photodetoxification of phenol and salicylic acid [144, 161] although a linear dependence of reaction rate on temperature in photocatalyzed degradation of chloroform has been reported [18]. Therefore, operation at ambient temperature and atmospheric pressure is one of the advantages of photocatalysis.

2.4 Effects of Carbonate and Bicarbonate Ions on Photocatalysis

The presence of some inorganic impurities may affect the photocatalytic destruction of organics in water or wastewater. It is believed that these anions

scavenge hydroxyl radicals [23, 87, 88, 119, 207, 218], which are responsible for attacking organics. To date there is little information regarding the effects of these impurities on photocatalysis. Although there are some studies which include the effects of these ions in advanced oxidation processes (AOP) [23, 87, 88, 119, 207, 218], these effects are neglected in photocatalysis. Therefore, this can be an area which needs to be addressed.

Bicarbonate and carbonate ions are commonly found in surface waters, groundwaters, or wastewaters. For instance, the bicarbonate ions in the Gloucester landfill groundwater are about $150\text{--}300\text{ mg L}^{-1}$ ($\sim 2.5\text{--}5\text{ mM}$) [156]. Due to the fact that these anions are hydroxyl radical scavengers, their effects on the photocatalytic degradation of organics should be explored.

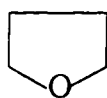
2.5 Tetrahydrofuran and 1,4-Dioxane: Their Environmental Fate and Physical Properties

Tetrahydrofuran (THF) and 1,4-dioxane (DIOX) are two kinds of water pollutants which are used in large quantities as solvents and chemical bulk products. The existence of these contaminants in water may cause severe health problems. Tetrahydrofuran and 1,4-dioxane are industrial solvents used for dyes, oils, waxes, resins, cellulosic esters and ethers, and polyvinyl polymers [45, 98, 203, 204]. These compounds are also found in some contaminant groundwaters [156]. Painter and King [170] reported that tetrahydrofuran is classified as a chemical which is not readily biodegradable. Bern-

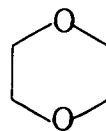
hardt and Diekmann [25] also confirmed that the biodegradation of these pollutants is very slow or they are not biodegradable. The aqueous aerobic half-life of DIOX biodegradation is 672–4320 h, which is based on unacclimated aerobic aqueous screening test data with confirmed resistance to biodegradation [109, 116, 191]. In addition, its aqueous anaerobic half-life is 2688–17280 h, which is based on estimated aqueous aerobic biodegradation half-life [109].

It can be seen that the biodegradation of these pollutants is very slow and an additional process may be necessary to degrade these contaminants. As an advanced oxidation process, photocatalysis is capable of destroying organic pollutants in less time.

The chemical structures of tetrahydrofuran and 1,4-dioxane are illustrated in Figure 2.2. Also, physical properties of these compounds are summarized in Table 2.1.



Tetrahydrofuran (THF)



1,4-Dioxane (DIOX)

Figure 2.2: Chemical structures of tetrahydrofuran and 1,4-dioxane.

Table 2.1: Physical properties of tetrahydrofuran and 1,4-dioxane [133].

CHEMICAL NAME	SYNONYM	MOLECULAR WEIGHT	M.P. (°C)	B.P. (°C)	DENSITY @20°C (g cm ⁻³)	WATER SOLUBILITY	HENRY'S LAW CONSTANT (atm m ³ mol ⁻¹)
Tetrahydrofuran (THF)	1,4-Epoxybutane, Diethylene oxide, Oxacyclopentane, Tetramethylene-Oxide	72.11	-108.39	66	0.8892	∞	9.63×10^{-3}
1,4-Dioxane (1,4-DIOX)	1,4-Diethylenedioxi- de, p-Dioxane, Glycoethylenether	88.12	11.8	101.1	1.0336	∞	4.88×10^{-6}

2.6 Photoreactor Design in Photocatalysis

Although there is substantial research in the area of photocatalysis, most of it deals with the kinetics of a variety of organics. On the other hand, information is scarce regarding photoreactor configuration, design, and scale-up. This area of research has been a matter of great attention in recent years.

2.6.1 Photoreactors and Their Configurations

There are two major categories of photoreactors, which have been designed, built, and eventually used on at least a laboratory scale:

1. **Slurry photoreactors:** In this type of photoreactor, the photocatalyst particles are dispersed into slurry solutions. While slurry photoreactors have the advantage of high efficiency, high mass transfer, are well mixed and simple to make, they suffer from a major drawback in industrial applications. The solid particles must be separated in the downstream photocatalytic processes, making them cost ineffective. However, these photoreactors are the best choice for kinetic studies in photocatalysis. Slurry photoreactors have been designed with different geometries on the laboratory scale. Tubular slurry photoreactors, annular slurry photoreactor, and beakers are among the configurations which have been used (for example see [7, 22, 29, 151, 206, 211]). UV sources are inserted into the center and/or around the outer walls of the photoreactors.

2. **Immobilized photoreactors:** In the second category of photoreactors, the photocatalyst, usually titanium dioxide, is immobilized onto the surface of a support as a stationary phase. There is no need to separate the solid particles in the downstream process, which is the main advantage of these photoreactors.

Different reactor configurations with various supports have been used in immobilized photoreactors. The supports used for the immobilization of titanium dioxide on their surface are listed in Table 2.2. Table 2.3 lists some examples of immobilized photoreactors with different configurations which have been previously studied. Although different configurations have been considered in the design of photoreactors, they suffer from potential mass transfer limitations, low surface area-to-volume ratios, and inefficiencies caused by absorption and scattering of light by the reaction medium [105]. Therefore, there is still much to investigate and learn about different photoreactor configurations in order to establish a design which maintains both high mass transfer and sufficient light penetration.

2.6.2 Photoreactor Modelling

In the last decade, there has been a great attention to photocatalysis and its kinetics. However, there is scarce work done on photoreactor modelling. There are at least two phases in a photoreactor, liquid and solid. In photoreactors, it is sometimes necessary to introduce a gas phase such as oxygen or air into the system, and in such cases, there are three phases involved in the

Table 2.2: Summary of different supports on which titanium dioxide was immobilized.

SUPPORT MATERIALS	REFERENCES
glass mesh	Valladares et al. [215]
3–4 mm glass beads	Serpone et al. [198]
inside tubes of either Teflon or glass	Low and Matthews [129], Matthews et al. [143], Matthews [144]
silica gel	Matthews [140]
fiberglass	Al-Ekabi et al. [4], Matthews [145]
fused silica glass fibers	Hofstadler et al. [106]
cellulose and polyester membranes	Bellobono et al. [24]
glass walls	Sabate et al. [187, 188]
woven mesh	Murabayashi et al. [157], Robertson and Henderson [184]
porous alumina-silica ceramic	Kato et al. [115]
activated carbon	Yoneyama et al. [225]
alumina	Fujishima [77]
ceramic tile	Anderson [11], Fujishima [77]
sand	Lee [121], Matthews [142]
stainless steel	Wilkinson [220], Ha and Anderson [94], This study

Table 2.3: Examples of different immobilized photoreactor configurations studied previously.

PHOTOREACTOR	UV LIGHT POSITION	REFERENCES
packed bed (1% Pt-TiO ₂ supported on silica gel)	1 cm from outside	Crittenden et al. [61]
fixed bed falling film	above (solar or artificial)	Bockelmann and Bahnemann [28], Puma and Yue [179]
annular packed bed	center	Raupp et al. [180]
packed bed (glass beads)	outside	Serpone et al. [198]
flat plate	above, solar	Augugliaro et al. [15], Wilkinson [220]
fluidized bed	inside or outside	Haarstrick et al. [95], Lee [121]
flat fluidized bed	outside	Brucato et al. [44], Iatridis et al. [111]
series conical basket	center	Valladares [216]
spiral glass tube	center	Matthews [139]
packed bed (fiber optic bundles)	end	Hofstadler et al. [106]
monolithic (TiO ₂ coated on honeycomb support)	external	Suzuki [208]

photoreactor. To model a photoreactor, the following formulations must be developed [228]:

1. mass balance equations
2. kinetic equations
3. radiation equations

Depending on the number of species present in the system, reactor configuration, and particular hydrodynamic behavior including momentum balances, the mass balance equations are set up. The kinetic equations are found experimentally as a function of concentrations. Finally, the radiant energy conservation equations which are the vital key to the modelling of a photoreactor should be formulated. The radiation equation depends on the following factors [226]:

1. reactor geometry
2. optical thickness
3. UV source type and position in the photoreactor
4. wavelengths of irradiation
5. mixing characteristics and hydrodynamic behavior of the system

To design a proper photoreactor, the equations for mass, momentum, energy, and radiation energy balances, as well as the kinetic equations, should be coupled together and solved simultaneously.

2.7 Photocatalysis Applications

During the past decade, photocatalysis has been examined for potential applications in various fields. However, the actual number of applications to date is small. Although the primary goal of photocatalysis is mineralization of organics in water and wastewater, it has other significant potential applications as summarized below:

- Complete mineralization of a variety of organics in air and water to CO_2 , H_2O , and associated inorganic components such as HCl , HBr , SO_4^{2-} , NO_3^- , etc. have been reported in various technical reports and publications [5, 19, 27, 29, 75, 105, 151, 153, 155, 164, 205, 212]. The complete lists of organic pollutants that have been investigated by various research groups are summarized in review papers [101, 105, 153].
- In addition to organic species, a wide variety of inorganic compounds have been the subject of great attention for photocatalysis processes. Sensitivity of inorganic species to photocatalysis processes has created significant potential applications in the field of metal recovery for either valuable or toxic metals.

Borgarello et al. [34, 35, 197] and also other researchers [8, 20, 83, 112, 199, 221] have shown that gold (Au^{3+}) could be recovered by titanium dioxide photocatalysis using methanol as a hole scavenger in the presence of cyanide. Also, Herrmann et al. [100] investigated the recovery of silver (Ag^+). Recovery of other inorganic species such as copper [26, 47, 174], iron [47, 171], platinum [34, 102, 136, 199].

cyanide [41, 152, 200], manganese [47, 130], rhodium [36, 199], and sulfur [65] are also among others which have been reported. After the photocatalysis process in which the metals are photochemically being plated onto the titanium dioxide surface, the metals could be recovered by subsequent acid wash. As a promising route, the removal of toxic metals such as mercury, arsenic, cadmium, and lead using photocatalysis has been reported in the literature [196, 199].

- To produce ultrapure water for pharmaceutical and electronic industries [227].
- To convert solar to chemical energy [114].
- To convert light to electricity [158].
- Photoelectrochemical detector (photocurrent measured) for flow injection analysis and liquid chromatography [43].
- Photocatalytic oxidation system for total organic carbon analysis [143].
- Photodeodorizer for living environment such as office room, underground market, inside of vehicle, etc. [81].
- Decolorization of wastewater dyes [62, 124].
- Regeneration of spent adsorbents such as granular activated carbon (GAC) is another interesting application of photocatalysis [159]. Due to the air and water pollution, the conventional methods of disposal by incineration or landfill are not desirable.

- Cai et al. [49, 50, 51] and Fujishima et al. [78, 79] demonstrated another interesting application of photocatalysis in killing cancer cells in both vitro and vivo. By using photoexcited titanium dioxide, a large cell killing effect was observed not only in vitro but also in vivo. Hopefully, this method can be applied as one of the possible anti-cancer modalities due to the strong ability of illuminated TiO_2 to oxidize cancerous cells in both vitro and vivo. Although the light with 300-400 nm used in this type of research cannot penetrate the human body deeply, this possible modality could be used for the treatment of superficial tumors in an organ appropriate for light exposure such as skin, oral cavity, trachea, and urinary bladder. If a fiber-transmitted laser is used as a light source, the fiber can be inserted into subcutaneous tumor tissues, and irradiation of light can be carried out frequently without surgical opening of the skin. Therefore, it is possible to apply this modality to several tumors of other organs.

Although these may be the main applications of photocatalysis, the use of photocatalysis has been increasing in different areas. Since photocatalysis is a young technology, most of its applications have been investigated only in the laboratories around the world.

2.8 Concluding Remarks

A review of the literature concludes that a number of insights into photocatalysis have been obtained, yet some important unresolved issues need to

be investigated. There is a lack of information for some of the water pollutants which may degrade easily by photocatalysis. For instance, few studies are found for the photocatalytic degradation of THF and DIOX. Furthermore, most of studies have been carried out using a single component system. Hence, the photocatalytic destruction of multicomponent systems and their kinetic modelling is an area which is worthy of investigation. In addition, there are few studies examining the effects of carbonate and bicarbonate ions on photocatalysis. These anions, which are hydroxyl radical scavengers, are found in most of the waters and may affect the photocatalytic reaction rates. Since photocatalysis is a relatively new technology, there are some unsolved problems such as unclear mechanisms of photocatalytic reactions, photoreactor design and scale-up, and kinetic studies for multicomponent systems which need to be investigated. Although there are other unresolved issues in photocatalysis, this study will focus on these problems mentioned above.

Chapter 3

MATERIALS AND METHODS

In this chapter, materials and methods used in this study are explained in detail. The experimental setup for the slurry photoreactor, the packed bed photoreactor, the immobilization of titanium dioxide on the tellerette packings, and the analytical techniques are also explained.

3.1 Materials

The materials used in this study are described as follows:

- The water used for the whole sets of the experiments was filtered deionized water (FDW) . The deionized water provided in the lab entered into three column ion exchange cartridges consecutively. The disposable columns were Bion ExchangerTM model made by PIERCE Chem-

ical Company, Rockford, IL., U.S.A. Their model numbers were 19710, 19720, and 19720, respectively.

- The test water samples with different concentrations were prepared in the lab using organic materials purchased directly from Sigma Chemical Company (St. Louis, MO). The organic materials used without any further prepurification are listed as follows:
 1. Tetrahydrofuran (THF) was HPLC grade with the purity of 99+%. Its CAS number was 109-99-9.
 2. 1,4-Dioxane (1,4-DIOX) was HPLC grade with the purity of 99.9%. Its CAS number was 123-91-1.
 3. Gamma-Butyrolactone (GBL) was also HPLC grade with the purity of 99+%. Its CAS number was 96-48-0.
- Two different types of photocatalysts were used in this study. P25 titanium dioxide and Hombikat UV 100. P25 titanium dioxide, CAS number 13463-67-7, was provided by Degussa Corporation (Akron, OH). The other photocatalyst used in this study was titanium dioxide Hombikat UV 100 provided by Sachtleben Chemie GmbH (Duisburg, Germany). They were used without any further prepurifications. The properties and supplemental information of these two different photocatalysts are shown in Table 3.1.

Table 3.1: Physical properties and supplemental information for two different photocatalysts, titanium dioxide, used in this work. This information was provided by the suppliers.

PROPERTIES	DEGUSSA P25 TITANIUM DIOXIDE	HOMBIKAT UV 100 TITANIUM DIOXIDE
TiO ₂ Content	> 99.5%	> 99%
Composition	70% Anatase 30% Rutile	100% Anatase
Primary Particle Size	21 nm	< 10 nm
Specific Surface Area	36–65 m ² g ⁻¹	> 250 m ² g ⁻¹
Density	3.8 g cm ⁻³	3.9 g cm ⁻³
Solubility in Water	Insoluble	0.01 g L ⁻¹

3.2 Slurry Photoreactor Setup

It is preferable for a kinetic study to be carried out under conditions such that mass transfer and other complicating effects are absent [185]. The major type of photoreactor used for kinetic studies has been a stirred slurry photoreactor. However, to study the destruction of volatile organics, the photoreactor should be completely sealed. Moreover, since oxygen plays an important role in photocatalysis and the reaction rate is dependent on the dissolved oxygen concentration in the system, a suitable photoreactor must be designed to maintain dissolved oxygen concentration constant. Amongst the photoreactors used in kinetic studies, a recirculating annular batch photoreactor similar to that used previously by Pruden and Ollis [178] and Turchi and Ollis [211] is believed to be the most suitable.

To achieve the goals of this work, an annular slurry photoreactor setup was designed and built. In this manner, a true and intrinsic kinetic reaction has been carried out in the slurry photoreactor. The schematic diagram of the experimental setup is shown in Figure 3.1.

Among the photoreactors used in kinetic studies, this type of reactor is preferable because of the following advantages, i.e., it offers

1. high mass transfer between liquid phase and solid particles
2. high catalyst surface area
3. potentially high reaction rates per unit volume of the reactor
4. excess oxygen availability in the headspace

5. the use of higher light irradiance
6. uniform concentrations of compounds throughout the system due to mixing
7. enhancement of mixing due to the tangential entrance flow

The slurry photoreactor was made annular by two concentric borosilicate glass tubes. The outer glass cylinder had 105 mm internal diameter (ID) and the internal glass cylinder had 48 mm outer diameter and 44 mm inner diameter. The total volume of the reactor including the reservoir and the tubes was approximately 9.0 L. The volume of the reactor zone was 3.8 L.

As discussed in Chapter 2, dissolved oxygen (DO) is a common sacrificial oxidant used in photocatalysis to capture the electrons from the valence band. Therefore, by leaving a headspace (~2 L), a reservoir was made to provide the required oxygen.

The tubing used in this setup was C-FLEX provided by Cole-Parmer. Based on the information provided by the manufacturer, it has an excellent chemical resistance against weak and strong acids and bases. The tubing used had 1/2 inches ID, 3/4 inches OD with a wall thickness of 1/8 inches.

In this photoreactor, the slurry was recirculated through the system using a 1/3 hp, 3450 rpm, magnetic drive pump (Fluids Control Division, Hamden, Connecticut, USA).

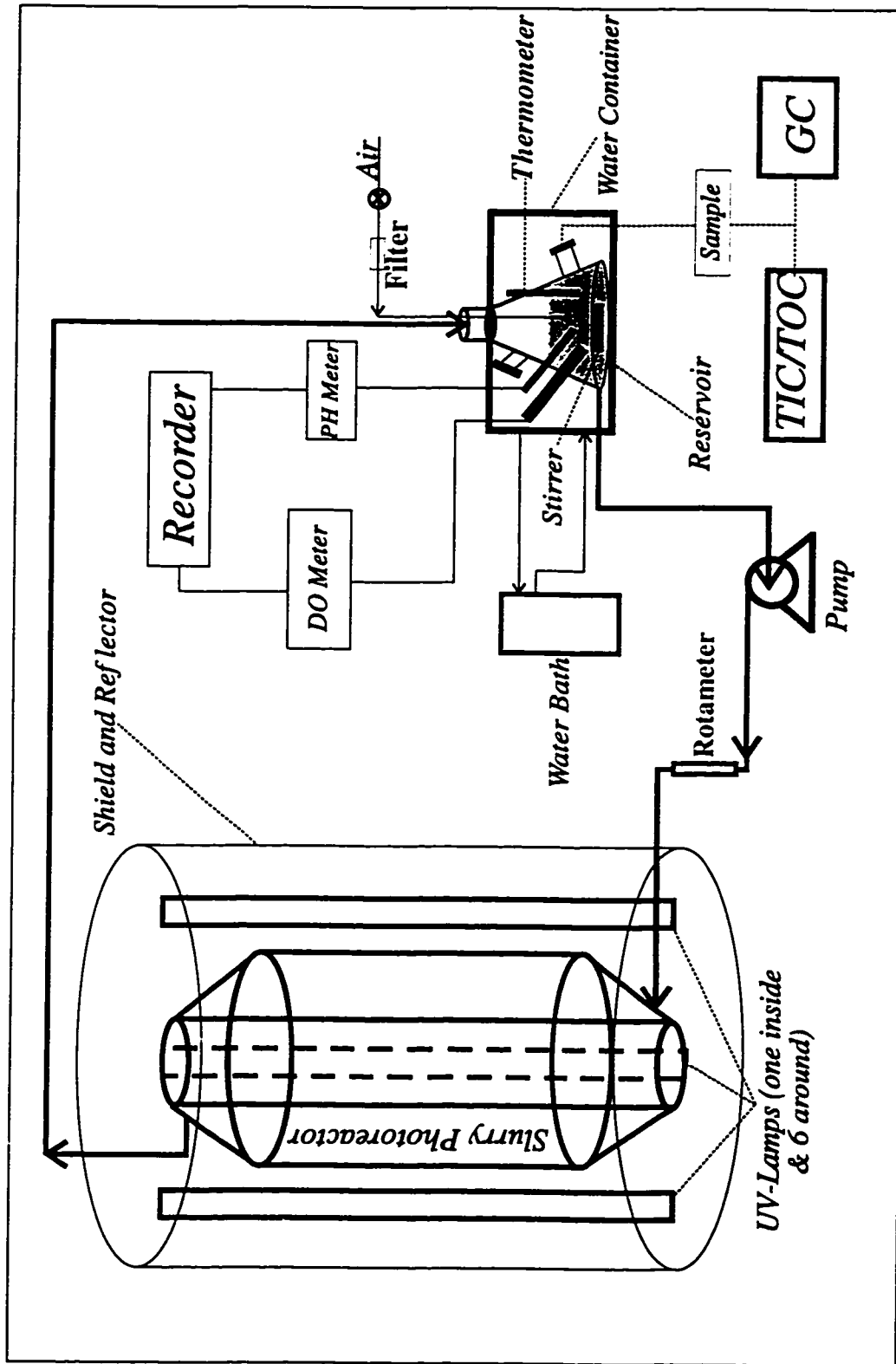


Figure 3.1: Schematic diagram of the slurry photoreactor set-up.

The temperature throughout the experiments was kept at $25 \pm 2^\circ\text{C}$ with a circulating water bath (NESLAB RTE 111). The reservoir section of the setup was put in a water container. The water surrounding the reservoir was recirculated through two water pumps that were already installed inside the water bath. The water bath controlled the water temperature around the reservoir; therefore, the temperature of the liquid inside the system was controlled. Due to heat transfer between the water in the container and the ambient, the temperature of the water inside the bath remained constant at $12 \pm 2^\circ\text{C}$.

Light was provided by a UV lamp inside and six UV lamps around the photoreactor. These tubular low-pressure mercury-vapour fluorescent lamps emitting long-wave ultraviolet radiation were provided by Philips. The UV lamps used were type 'TL' 20 W/09 N with a nominal wattage of 20 watts each and a current of 0.37 ampere. The UV lamps were 61 cm in length and 38 mm in diameter. They emit highly concentrated radiation between 320 and 390 nm with a maximum peak at 350 nm. According to the manufacturer information, these UV lamps are also branded UV-A in which the ratio of UV-B/UV-A is lower than 1:200. Also, no radiation with a wavelength below 300 nm was emitted. The light irradiance was measured using a Spectroline Digital Radiometer (DRC-100X) with a 320–380 nm electromagnetic wavelength sensor (DIX-365).

The liquid in the reservoir was stirred magnetically to increase the mass transfer between the headspace and the liquid as well to provide a homogeneous system.

Before starting each run, the water was aerated to a saturation level using the air line provided in the lab. A gas filter was installed in order to filter the air.

Dissolved oxygen (DO) was measured with a dissolved oxygen meter YSI model 57 (Yellow Springs Instrument Company, Ohio). The DO probe was mounted in the reservoir on line in order to monitor dissolved oxygen during the runs. The dissolved oxygen meter was calibrated by air saturated water before initiating each run. A volume of 500 mL water was stirred while it was aerated. The DO probe was placed in the water sample in a relatively constant temperature for about 15 min until the dissolved oxygen concentration no longer changed. The calibration was made by considering the local altitude, i.e., the atmospheric pressure reported by the Weather Bureau. Depending on the atmospheric pressure, a correction factor was used to calibrate the DO probe [194]. The DO was recorded using a recorder on line.

The pH was monitored using a pH meter manufactured by Barnant Company in Barrington, IL. The pH was monitored on line by placing the pH probe in the reservoir. The pH probe was also calibrated before each run using three different buffer solutions of pH 4, 7, and 10. The monitored pH was recorded using a recorder on line.

Samples were periodically taken from the sample ports for analysis. The samples were collected in the 2 mL headspace-free vials. Prior to testing, the liquid samples were centrifuged by Centrifuge IEC Centra-HN (International Equipment Company) at about 4500 rpm. The samples were then analyzed

through a 5890 Series II Gas Chromatograph (GC). The total inorganic and organic carbon (TIC/TOC) were measured with an Astro Model 2001 System 2 Analyzer. The analytical techniques are discussed in detail in Section 3.5.

3.3 Photoreactor Operation

The aim of this section is to explain the photoreactor operation method for all experimental runs. A stock solution for the purpose of the runs was prepared using pure organic compounds based on a method described in Appendix B. For instance, a stock solution with pure tetrahydrofuran was prepared and it was used when tetrahydrofuran was needed in the runs. These stock solutions were prepared from time to time on demand. Filtered deionized water was used for all stock solution preparations. Prior to each run the photoreactor was cleaned by circulating deionized water. Also, after finishing each run, water was also recirculated through the photoreactor for about a half hour while a small amount of detergent was added in order to clean the equipment properly. Then the photoreactor was rinsed with deionized water for another half hour in order to remove any possible detergent or material attached to the equipment. In the stage of rinsing the equipment, water was passed through the system continuously.

For the purpose of kinetic runs, 7.0 L of filtered deionized water was fed to the photoreactor. Oxygen is one of the important elements in any photocatalysis process. As shown in Section 2.3 of Chapter 2, oxygen was used as a sacrificial oxidant in photocatalysis in order to capture electrons. Therefore, the water was aerated for half an hour using bench air while the

water was recirculating in the system. An air filter was installed in the air line to ensure that the air was free of impurities (see Figure 3.1). During this period, all UV lights were turned on in order to clear any possible trace of organic background either left from the previous runs or present in the filtered deionized water. Then a certain amount of titanium dioxide, for instance, 10.5 grams Degussa P25 in the case of most kinetic runs, was added to the photoreactor. The system was sealed completely by the caps installed on the reservoir. The slurry was then recirculated for another 15 min while the UV lights remained on. During this time, the slurry was homogenized, and it was also possible to remove any trace of organics as a result of the photocatalysis process. Then the lights were turned off and depending on the initial concentration needed in the system, a certain amount of stock solution prepared for the runs was injected into the system using a gas-tight microliter syringe (Hamilton Microliter[®] Syringe). Safety precautions during the experimental runs were considered. For instance, the solutions were prepared in the fumehood (see Section 3.6). In addition, a Wilson 1200 series Respirator, Wilson[®] Safety Products (PA, USA) was employed while preparing the runs.

The system was then allowed to circulate while the lights were off for another 15 min. During this time, the system was homogenized. Samples were taken at this point in order to determine whether or not adsorption of organics on the catalyst surface had occurred. At this point, the UV lights were turned on and the photocatalytic reactions started. The samples were then taken periodically and analyzed. Upon completion of the run, the

equipment was cleaned as explained previously and prepared for the next run.

Prior to each run, DO and pH probes were calibrated. Also, the water bath temperature was adjusted in order to maintain constant temperature. Slurry flow rate was adjusted by the rotameter as needed.

3.4 Packed Bed Photoreactor Set-Up

As the research in the relatively new area of photocatalysis is progressing, there have been issues in photoreactor design. Although, various reactor configurations for different reactions and phases in chemical engineering have been customary (see Chapter 2), photoreactors with the following specifications still need to be addressed, so as to have photoreactors that are

1. capable of maximum mass transfer between liquid phase and the photocatalyst surface
2. capable of maximum light distribution throughout the photoreactor
3. cheap and easy to make.

In the following sections, the details of the packed bed photoreactor and immobilization technique are explained.

3.4.1 Packings

In order to design a packed bed photoreactor with the proper internal light distribution, and high mass transfer between the bulk liquid and the

solid surface, tellerette packings were designed. Since no companies make metal tellerettes to our knowledge, the packing was made manually using stainless steel welding wire (see Figure 3.2).

The raw stainless steel wires (ER316L), made by HH Rigby-Mary Land (stainless) Ltd., were purchased from Handy and Harman Company, Canada, as one meter long with a diameter of 1.6 mm.

The following describes the procedure involved to create the tellerettes:

1. The wires were roughened using sand paper (grit number 100) in order to ease the attachment of titanium dioxide on their surfaces.
2. After roughening, the wires were wound around a rotating dowel, held in slow spinning lathe. This produced pieces of wire resembling long springs.
3. Each "long spring" was then cut into small springs with six loops each. These "small springs" had total length of 233 mm each.
4. The final step involved manually bending the "small springs" to bring the ends together, to form the tellerette shape.

These packings were used to support titanium dioxide on their surfaces. Figure 3.2 demonstrates a sample of tellerette packings made by this method.

3.4.2 Immobilization Technique

In this section, the immobilization technique used to attach titanium dioxide to the surfaces of the stainless steel tellerette packings is described.

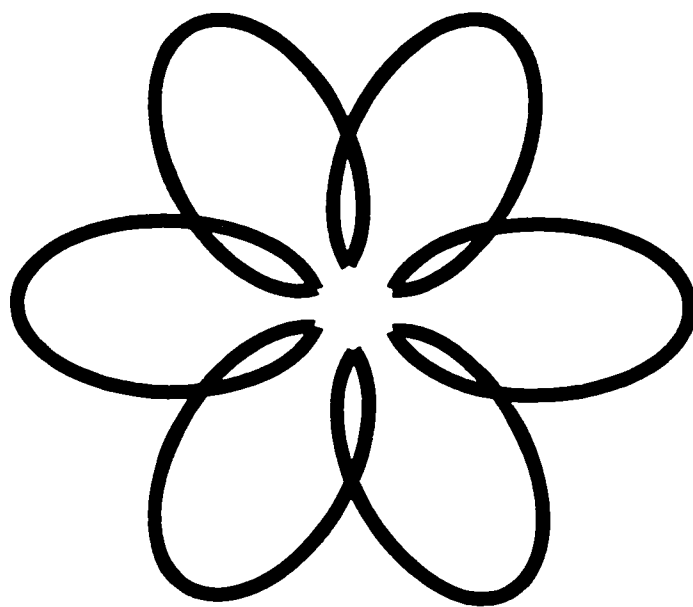


Figure 3.2: The configuration of tellerette packings made by the stainless steel wire.

Since the recovery of micron size particles from the slurry solutions in the treated water may be an awkward process, immobilization techniques for the attachment of titanium dioxide on different supports have been practiced in previous studies (see Chapter 2).

Although, there is documentation [220, 94] on the stainless steel support on a flat plate, there is a lack of information on the immobilization technique on the surface of a thin wire packing supports such as tellerettes. The following describes the procedure involved to immobilize the titanium dioxide on the the surfaces of the tellerette packings:

1. The packings were immersed into a 15% hydrochloric acid solution for one and half hours in order to clean any possible grease or any other

impurities that might be on the surfaces. The hydrochloric acid was prepared using concentrated HCl and filtered deionized water (FDW).

2. The packings were then rinsed a few times with deionized water to remove any possible solid impurity remaining on the surfaces.
3. The cleaned packings were allowed to air-dry for a few hours.
4. Ha and Anderson [94] showed that if a metal is fired at high temperature, an oxide film would be produced on the metal surface. This metal oxide film is more compatible for bonding to titanium dioxide particles than the metal support itself.

The packings were then fired at 400°C in the oven for 2 h in order to create the metal oxide film and to remove any possible organic impurities left on the surfaces of the packings.

5. After firing, the packings were allowed to air-dry.
6. A 30 g L⁻¹ slurry titanium dioxide (Degussa P25) was prepared using 25% (v/v) methanol in filtered deionized water. Valladares [216] showed that the methanol would help in the attachment of titanium dioxide to the surface. This may be due to the fact that methanol acts as a dispersant and reduces the particle segregation in the slurry. Therefore, methanol enhances the distribution of titanium dioxide particles on the support surface.
7. The packings were spread out into a few shallow pans containing the slurry solution made in the previous step. The pans were then put in

an oven overnight set at 50°C.

8. Another 30 g L⁻¹ titanium dioxide slurry solution with just deionized water was made. The packings were then put in the second slurry solution in the shallow pans for the second coating. The pans were put in the oven in the same temperature (50°C) and left in the oven overnight. This step was done to make sure the uncovered surfaces are also immobilized with titanium dioxide.
9. The immobilized tellerette packings were then air-dried and rinsed with deionized water for a few times in order to remove any unattached solid particles.
10. The tellerette packings were then baked in an oven at 300°C for 4 h and then allowed to air-dry.
11. The tellerette packings were then ready to put into the photoreactor to test. The results of these packings are described in Chapter 6.

3.4.3 Packed Bed Experimental Setup

In this study, a novel packed bed photoreactor was designed and built. The degradation of 1,4-dioxane as a model compound was examined. Degradation results in this photoreactor will be discussed in Chapter 6. The same experimental setup explained in previous section was used except the fact that the photoreactor was modified and was filled with special immobilized tellerette packings. The inside cylindrical tube including the inner UV lamp was removed and the top and the bottom of the photoreactor were sealed

using a hollow Plexiglas screw with a rubber stopper inside. A Teflon disk was mounted on top of the rubber stopper in order for the adsorption of the pollutants to be minimized. The schematic diagram of the packed bed experimental setup is shown in Figure 3.3. The photoreactor had 105 mm internal diameter (ID) and 51 cm height.

3.5 Analytical Techniques

In this section, the analytical techniques used in this study are described. A gas chromatograph available in the lab was used in order to analyze samples. A GC/MS apparatus in the Civil Engineering Department was used in order to identify intermediates produced during the course of the reactions. GC/MS analyses were carried out using the method of Solid Phase MicroExtraction (SPME). Also, total organic and inorganic carbon analyses as well as absorbance analyses are described.

3.5.1 Gas Chromatography (GC)

The analysis was carried out using a Hewlett Packard (Avondale, PA) 5890 Series II gas chromatograph, which was equipped with a flame ionization detector (FID). The column was an RTX-502.2 fused silica megabore column with $30\text{ m} \times 0.53\text{ mm}$ ID and $3.0\text{ }\mu\text{m}$ film thickness (Chromatographic Specialties Inc.). One of the advantages of this kind of column is that the sample can be injected directly in aqueous phase without any further pretreatment aside from centrifugation to separate the solid particles.

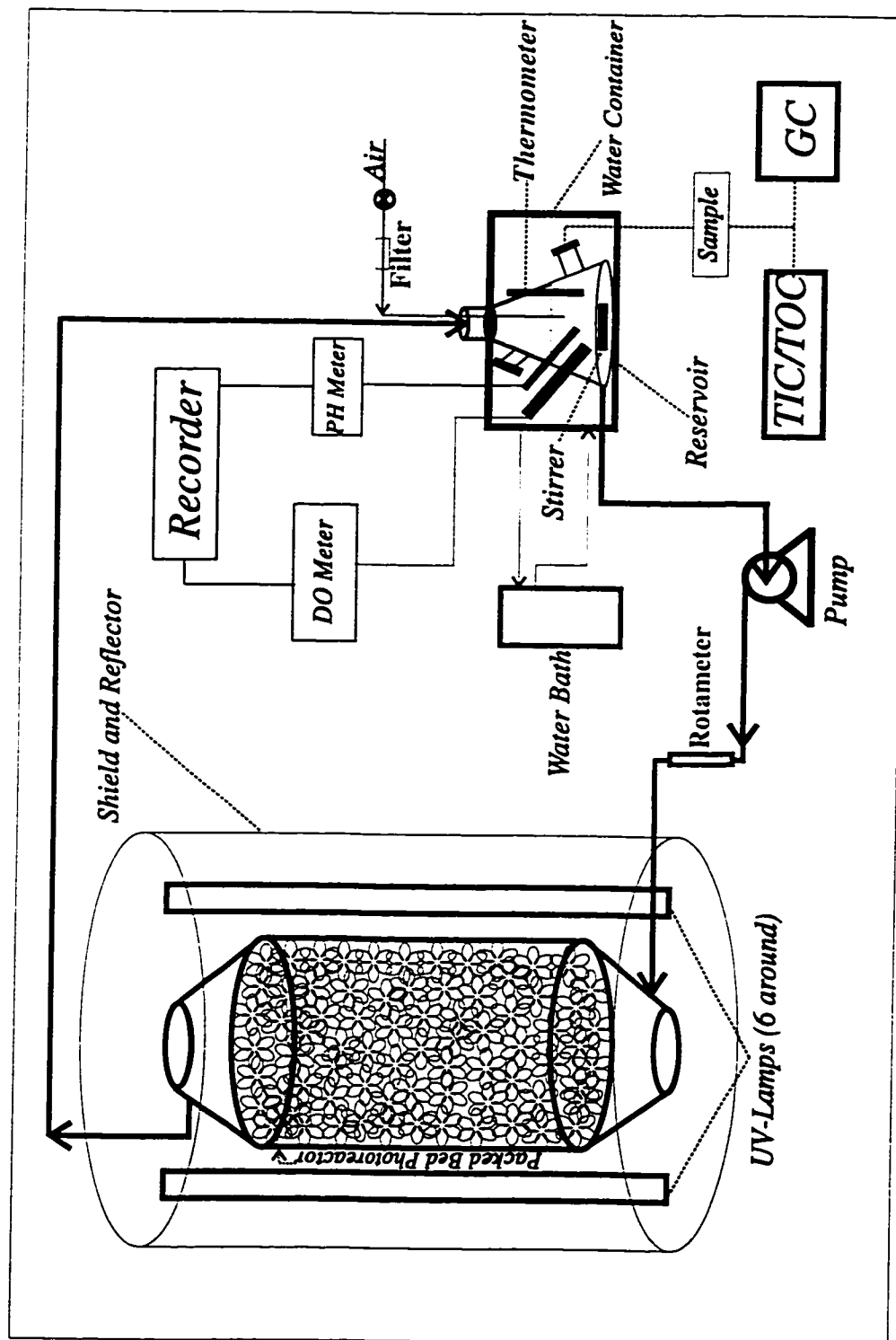


Figure 3.3: Schematic diagram of the packed bed photoreactor set-up.

The samples were collected in the small 2 mL vials capped with Teflon face septa (Chromatographic Specialties Inc.). After centrifuging the samples, 0.6 μL was injected into the GC manually using a sandwich method to avoid possible evaporation of volatile organics. The carrier gas used in this GC was helium and the flow of carrier in the column was set to be 15 mL min^{-1} . The auxiliary gas was nitrogen. A split/splitless technique as well as a temperature program were used for analysis such that the initial oven temperature was 30°C which was held for 3 min. After one and one half minutes splitless flow, the purge valve was then automatically turned on to provide a split flow. After this time, a ramp of 2°C/min was then initiated until 35°C was reached and held for 10 min. The second ramp of 3°C/min was applied until the oven temperature of 55°C. Finally, a ramp of 20°C/min was applied until the final oven temperature of 245°C was reached and held for 5 min. The injector and detector (FID) were set at 180°C and 250°C, respectively. The FID sensitivity used for the purpose of these analyses was set at 1.0×10^3 pA. Data was automatically acquired and integrated by the software package Peaksimple II (Peak Simple Chromatography Data System, SRI Instruments, Torrance, CA) installed on a personal computer.

To obtain the concentration of samples, a calibration curve was prepared prior to the experiments. To reduce the error in sample injection as well as other sources of error, toluene with a concentration of 40 mg L^{-1} in both standards and samples was added as an internal standard (I.S.). A plot of peak area ratios for each constituent i and the internal standard (I.S.), i.e., $A_{r,i} = A_i/A_{I.S.}$, against the amount of each constituent of interest was

built as a calibration curve. Figure 3.4 shows a typical calibration curve for 1,4-dioxane.

Thus the concentration of the constituent of interest was calculated from the following equation:

$$C_i = \eta \cdot A_{r,i} \quad (3.1)$$

where C_i = the concentration of the component of interest, [mg L^{-1}];

$A_{r,i}$ = the GC peak area ratio for component of interest.

η = The slope of the calibration curve, i.e.. C_i vs. $A_{r,i}$.

Before each run two samples of known concentration of the constituent of interest were injected into the GC. If the measured concentration deviated significantly from the 95% confidence interval, another calibration curve for that particular constituent was prepared (see Appendix C). The sample was then chromatographed and the peak area ratios were measured. From these ratios, values of the amount of each constituent in the unknown sample may be calculated.

3.5.2 Solid Phase MicroExtraction (SPME)

GC/MS was used to identify the intermediates formed during the course of the reactions (see Section 3.5.3). All reactions took place in the aqueous phase and the concentrations of the organics in the system were in the mg L^{-1} levels and below. Therefore, the samples contained more than 99% water. Since no water could be introduced into the mass spectrometer, further preparation was required before performing GC/MS analysis on the

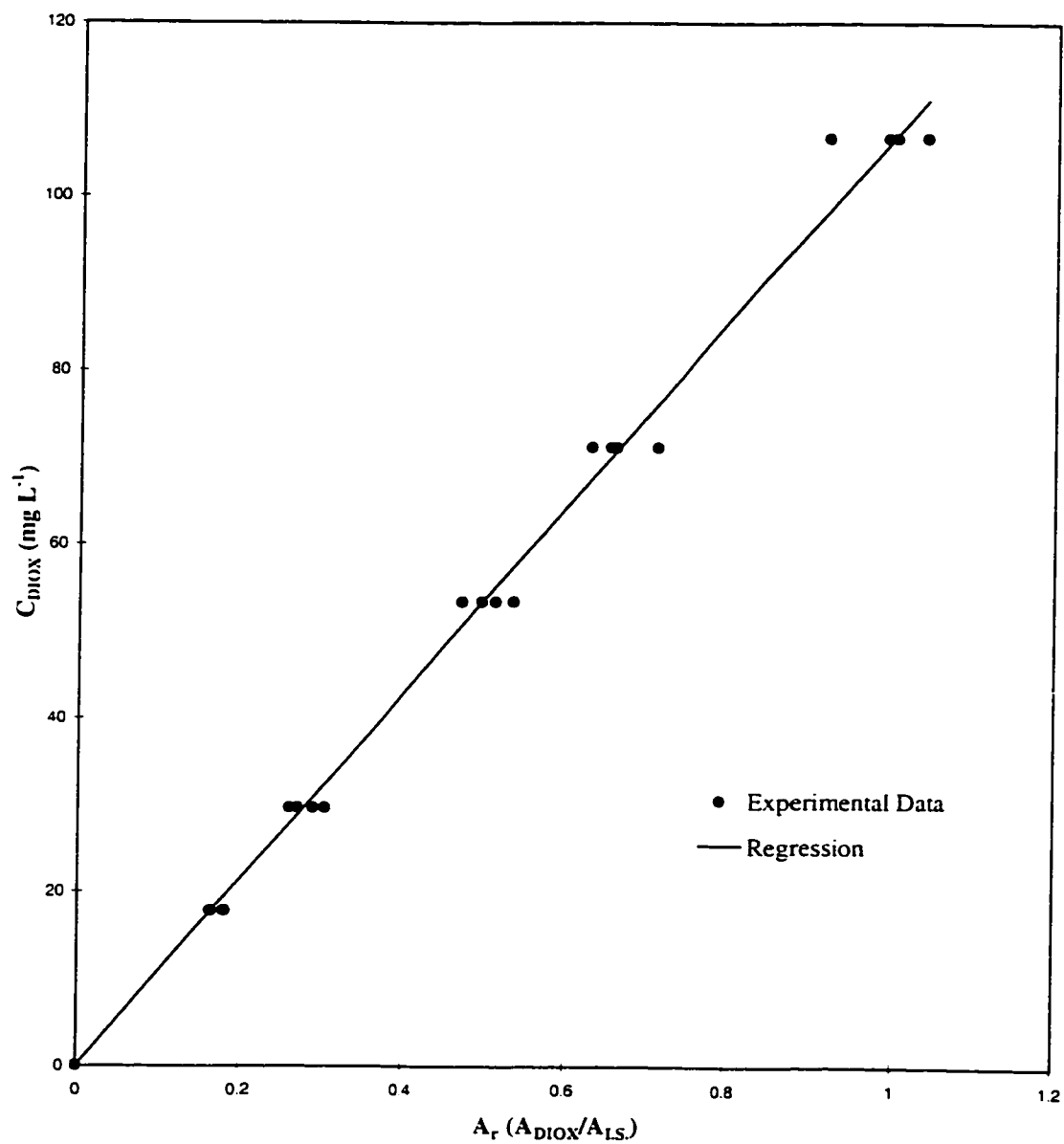


Figure 3.4: A typical calibration curve for 1,4-dioxane, $C_{DIOX} = (107.19 \pm 2.32) \times A_r \text{ [mg L}^{-1}\text{]}$ where $A_r = A_{DIOX}/A_{IS}$; $R^2 = 0.9923$.

samples. The method of Solid Phase MicroExtraction (SPME) was used in order to extract organics out of the aqueous phase.

Solid Phase MicroExtraction (SPME) is a solventless extraction in which a phase-coated fused silica fiber is immersed in a liquid sample and after a short time the analytes establish equilibria between the solid phase and the liquid sample. Generally speaking, the SPME is an equilibrium process between the solid phase, fiber, and the liquid phase or the gas phase in the case of headspace [223, 230]. After adsorption of the organic compounds on the fiber, the compounds are thermally desorbed into the GC column due to the high temperature of the injection port. All injections in the GC/MS were performed manually.

The SPME holder and the SPME fiber were purchased from Supelco Canada Ltd. The stationary phase used was 65 μm carbowax/divinylbenzene which was partially crosslinked. The fiber is carefully mounted to a septum piercing needle of the holder syringe. The needle of the syringe is a hollow cylinder in which the fiber is held. By depressing the plunger on the holder, the fiber is pushed out.

In order to extract the organics, the samples were kept in 5 mL vials with open screw caps sealed with aluminum foil for the ease of puncturing by SPME syringe. Prior to extraction, the samples were centrifuged to separate the suspended titanium dioxide particles. The aluminum foil on the sample vials was pierced by the needle and the plunger pushed down. The fiber was contacted with the sample for a period of 30 min at room temperature. After the time had elapsed, the fiber was retracted into the needle. The needle was

immediately injected into the GC and the plunger depressed exposing the fiber to the injection port. The depth guide had been adjusted such that the fiber was exposed to the hottest part of the injection port. The injection port of the GC was adjusted to 200°C. After 1.5 min. the fiber was retracted into the needle and the needle removed from the injection port.

This method was successful in extracting organic intermediates. Reproducibility of detectable peaks with respect to peak shapes, retention times, and peak height was demonstrated.

Before using the fiber, it was conditioned at 250°C for 1 h as recommended by the supplier to ensure that all monomers used in the glue to attach the fiber were released. Because of this, some initial extraneous peaks primarily from the glue were detected. After conditioning the fiber, no significant peaks were observed as confirmed by a blank injection. Before analyzing each series of samples, a blank injection was made to make sure the fiber was free of extraneously adsorbed compounds or any other material which might contaminate the fiber.

3.5.3 Gas Chromatography/Mass Spectrometry (GC/MS)

Identification of the intermediates produced during the course of reactions was carried out using the GC/MS in the water research group of the Civil Engineering Department at the University of Waterloo. The GC was a Hewlett Packard 5890 Series II (Avondale, PA). The column was a Restek fused silica capillary column RTX-502.2 purchased from Chromatographic Specialties.

The column was coated with crossbonded phenylmethyl polysiloxane with 1.4 μm film thickness. It had a length of 30 m with 0.25 mm inner diameter.

The mass spectrometer was a Hewlett Packard 5971 Series with mass selective detector. The software used in mass spectrometer was a Hewlett Packard MS ChemStation, DOS Series by which the signals were integrated. After analyzing each sample, every single peak obtained by the integrator was carefully analyzed using the search library in order to identify the compound with the best match in the library. The greater the probability of correctly identifying the compound, the higher the acceptance confidence interval obtained. Generally speaking, there is no statistical limit to accept a compound with the one identified in the library. However, a probability greater than 80% is generally agreed to be a good indication of a likely match.

The samples prepared by the method of SPME explained in the previous section were introduced into the GC and then directly transferred into the MS. The carrier gas used in the GC was helium and the flow of carrier in the column was set to be 1 mL min⁻¹. A split/splitless technique as well as a special temperature program were used for analysis. The initial oven temperature was 35°C which was held for 1 min. Before each run started, the purge valve was automatically turned off to provide a splitless flow. After 5 min of splitless flow into the GC, the purge valve was automatically turned on for a split flow. After this time, a ramp of 3°C/min was then initiated up to 150°C. The second ramp of 35°C/min was then applied until a final oven temperature of 240°C was reached. The oven temperature was then held at 240°C for 5 min in order to bake the column and to desorb any possible

compounds that might exist in the system. The injector and detector were set at 200°C and 250°C, respectively.

3.5.4 Ion Chromatography Analysis (IC)

The method of ion chromatography (IC) was used to identify possible organic acid intermediates during the photocatalytic reactions. The ion chromatography analyses were done using the IC system, Dionex, Sunnyvale, CA, USA. The IC system was equipped with an autosampler, an advanced gradient pump, a high-pressure, three way injection valve (BF-2), and a relatively large sample loop. The sample loop had capacity of 740 μL which was equivalent to 370 cm PEEK tubing with 0.51 mm I.D. The anion-exchange column used in the IC system was AS 10, 250 \times 4 mm I.D. and composed of 8.5 μm ethylvinylbenzene-divinylbenzene substrate agglomerated with the 65 nm completely aminated anion-exchange latex particles. The anion exchange column had a capacity of 170 μeq . The IC analyses were performed based on the method developed by Peldszus et al. [172]. In this method, after preparing standards with 50 $\mu\text{g L}^{-1}$ for each organic acid, the samples were qualitatively analyzed based on their relative retention times and peak shape. The sample chromatograms were then compared with the standard chromatogram.

3.5.5 Total Organic Carbon (TOC) and Total Inorganic Carbon (TIC) Analyses

TIC and TOC were analyzed using an Astro Model 2001 System 2 Analyzer (Astro International Corporation, League City, TX). It was equipped with an ultraviolet promoted persulfate oxidation followed by non-dispersive infrared CO₂ detection. The TOC analyzer was equipped with an automatic sampler. A personal computer attached to the analyzer integrated the results using a 2001 software package supplied by Astro International Corporation. The eluents, 1.5 M sodium persulfate solution, Na₂S₂O₈, supplied by Sigma Chemical Company (St. Louis, MO), and 1.0 M phosphoric acid solution, H₃PO₄, supplied by BDH Inc. (Toronto, Ontario), were prepared according to the Astro International Manual [14]. The TOC standards employed was anhydrous potassium biphthalate, HOCOC₆H₄COOK, supplied by Fisher Scientific (Fair Lawn, New Jersey). Its assay was 99.97%. TIC Standards were also prepared with anhydrous sodium bicarbonate, NaHCO₃, supplied by BDH Inc. (Toronto, Ontario), and sodium carbonate, Na₂CO₃, supplied by BDH Inc. (Toronto, Ontario), in carbon free water according to the procedure outlined by Greenberg et al. [92]. The 40 mL samples taken from the photoreactor were centrifuged using a DAMON IEC B-20A Centrifuge at 9000 rpm to separate suspended titanium dioxide particles. The compartment temperature of the centrifuge was set at 5°C. Due to the large volume of the sample (40 mL) taken from the photoreactor, no further dilution was necessary.

3.5.6 UV Absorbance and Transmittance Analyses

An HP ultraviolet/visible spectrophotometer was used to measure the absorbance and transmittance of the solutions with suspended titanium dioxide particles. After putting a sample in a 1 mL quartz cuvette, the absorbance and transmittance of the solution were measured automatically by a personal computer as an integrator attached to the spectrophotometer. The computer used a HP software package. The spectrophotometer was set to measure the absorbance and the percent transmittance in the wavelength range of 300 to 400 nm. Filtered deionized water (FDW) was used as a blank for the analyses.

3.6 Safety Precautions

Safety is one of the most important necessities in any work place. Due to toxicity, use of organics may cause severe health problems such as respiratory complications, cancer, heritable genetic damage, etc.. Care was taken to work under the fumehood during the preparation of the organic solutions to avoid possible hazards. A special mask, Wilson 1200 series Respirator, Wilson® Safety Products, PA, USA, was used while preparing the solutions.

Due to the potential danger of the optical radiation for the eyes and skin, each of these should be appropriately protected [201]. As continuously staring at the sun for one minute can induce permanent blindness, the same effect such as conjunctivitis and inflammation of the cornea can result from exposure to a UV light. Although, these effects may be reversible, eventual

formation of cataracts may develop from repeated exposure to strong doses of UV rays. Therefore, a pair of UV protective goggles were worn while working and running the experiments. Also, a pair of gloves was worn while doing the experiments. For the near UV spectra (320–400 nm), it has been reported that the total irradiance incident for unprotected eyes should not exceed 1.0 mW cm^{-2} for a period more than 16 min and for exposure times less than that should not exceed 1.0 J cm^{-2} [59]. In general, for unprotected eyes and skin in a period of 8 h, the threshold limit value (TLV) of total near UV exposure at 350 nm should not exceed 15 J cm^{-2} [59]. In order to avoid UV hazards, the photoreactor was covered with a stainless steel shield. This UV shield also helped in the reflection of the UV rays back to the photoreactor. The equipment setup was completely sealed while running the experiments. Samples were taken with a gas-tight syringe without any need to open the system.

Chapter 4

NON-LINEAR PARAMETER ESTIMATION FOR A DYNAMIC MODEL

In this chapter, a non-linear parameter estimation method for a dynamic model in photocatalytic reaction engineering is explained. Advantages and disadvantages of the non-linear modelling and the conventional method of initial rates are also explained. The results for the two methods are compared using published data. The method described in this chapter may be applied to other chemical reactions with n non-linear differential equations. However, the emphasis here is on the non-linear parameter estimation in photocatalysis processes. An example with literature data is described.

4.1 Introduction

As discussed earlier, heterogeneous photocatalysis on TiO_2 is a promising method for the degradation of organic pollutants in both water and air [5, 75, 164, 212]. Most research has focused on single components in water. As shown in Equation (4.1), it has been documented that many photocatalytic reactions follow the Langmuir-Hinshelwood (LH) form [75, 160, 161, 162, 164, 167, 168, 212]:

$$-r_i = -\frac{dC_i}{dt} = \frac{k_i K_i C_i}{1 + K_i C_i} \quad (4.1)$$

where $-r_i$ = the reaction rate of the component i to be degraded, $[\text{M s}^{-1}]$;

C_i = the concentration of the component, i $[\text{M}]$;

k_i = the reaction rate constant, $[\text{M s}^{-1}]$;

K_i = the binding constant, $[\text{M}]$.

To estimate the parameters, it has been customary in the last decade to write Equation (4.1) in reciprocal form and then to plot the reciprocal initial reaction rate, $\frac{1}{-r_{i0}}$, versus the reciprocal initial concentration, $\frac{1}{C_{i0}}$, as shown in Equation (4.2).

$$\frac{1}{-r_{i0}} = \frac{1}{k_i} + \frac{1}{k_i K_i} \left(\frac{1}{C_{i0}} \right) \quad (4.2)$$

where $-r_{i0}$ = the initial reaction rate of the component i to be degraded, $[\text{M s}^{-1}]$;

C_{i0} = the initial concentration of the component i , $[\text{M}]$.

This method is called the method of initial rates [122]. To estimate the parameters in Equation (4.2) using the method of initial rates, a series of concentration-time runs is made using different initial conditions. Then each run is extrapolated back to the initial concentration to find an estimate for the initial reaction rate [122]. Runs having different r_{i0} and C_{i0} are tabulated. Then $\frac{1}{-r_{i0}}$ versus $\frac{1}{C_{i0}}$ are plotted, and using linear regression the kinetic parameters are found. Figure 4.1 shows an example of the initial rate estimations versus reciprocal concentrations in the conventional method.

The raw data for this example which were representative of the photocatalytic degradation of perchloroethylene (PCE) in an annular slurry photoreactor have been adopted from Turchi [213]. Although the conventional method in photocatalytic reaction data analysis may sometimes give approximate point estimates of the kinetic parameters, it has significant faults. The faults involved in using conventional method are as follows:

1. By taking the reciprocal of the LH equation, the error structure is distorted because of the $-r_{i0}$ in the denominator. The error in $-r_{i0}$ is magnified when the values of $-r_{i0}$ are small.
2. In the theory of linear regression, it is assumed that the independent variables are perfectly known [21, 39, 40]. On the other hand, in Equation (4.2), there is error involved in the measurement of C_{i0} ; in addition, since C_{i0} is in the denominator, the error in $\frac{1}{C_{i0}}$ is also magnified when C_{i0} is small.

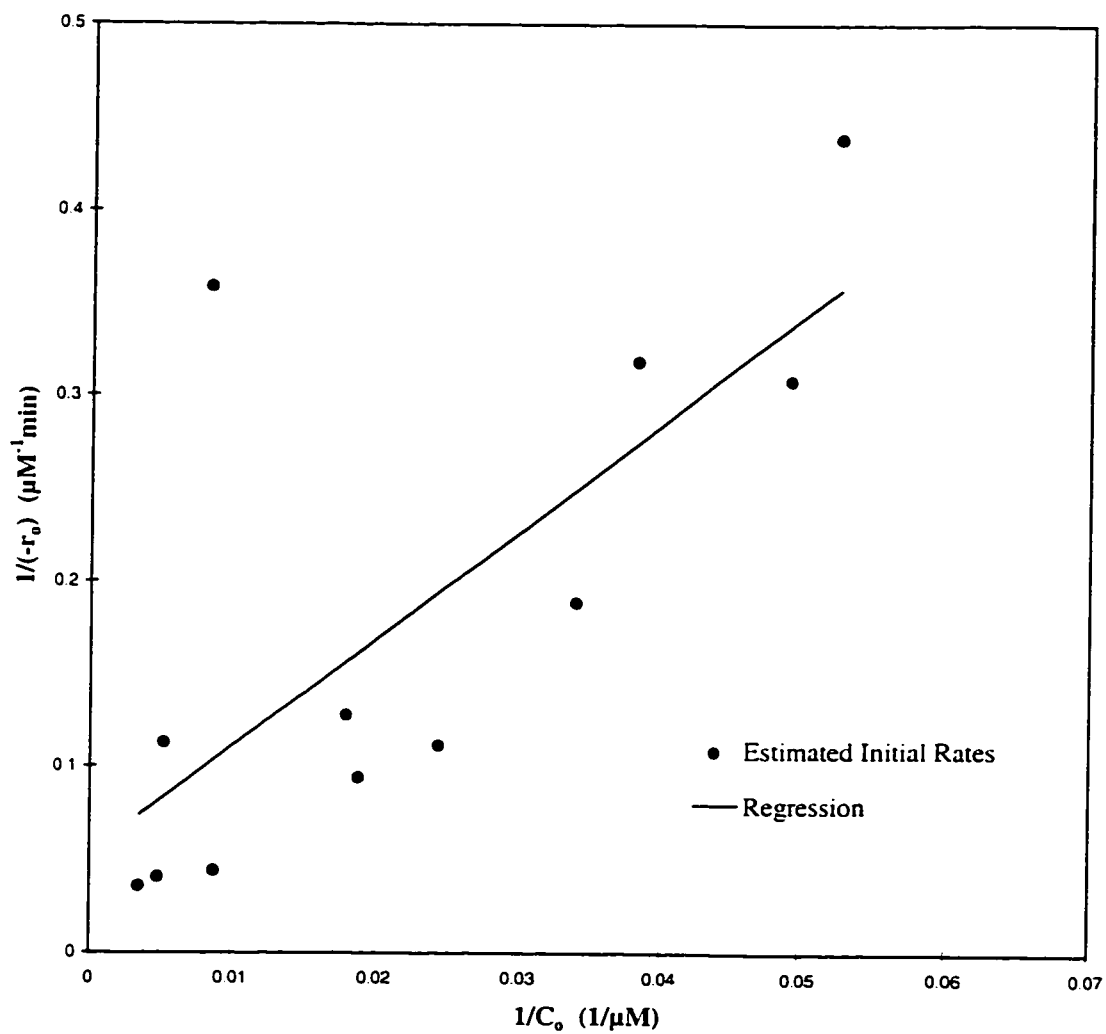


Figure 4.1: The initial rate data plot for perchloroethylene (PCE) (raw data adopted from Turchi [213]).

3. To find $\frac{1}{-r_{i0}}$ one has to plot C_i versus t for each run and then get the best tangential line at $t=0$. Obviously, this method is tedious and not reproducible.
4. In the method of initial rates, little data from each run are used. This could cause the misinterpretation of the reaction orders or mechanisms.
5. The conventional method is only applicable for single component systems and cannot predict multicomponent mixtures. In addition, it fails when intermediate species are produced as their initial concentrations are zero.
6. Even if the errors in finding initial rates are low, sometimes the reaction orders, i.e., the kinetic parameters, obtained by the initial rates differ from those found by the analysis of a full run. Levenspiel [122] indicated that this is a strong indication of complex kinetics in which some products or intermediates influence the rate.

All of the above faults and deficiencies may be avoided by applying the technique of non-linear regression analysis to all the data at once. The estimates so obtained are reproducible and are more accurate because of the use of all the data.

A general procedure for the modelling of the photocatalytic destruction of organics is outlined in Figure 4.2. Using this procedure, a systematic approach for the kinetic studies in photocatalysis can be followed.

As the first objective of this chapter, we show that an elegant non-linear regression method, such as the Box-Draper method [21, 38, 181], can be

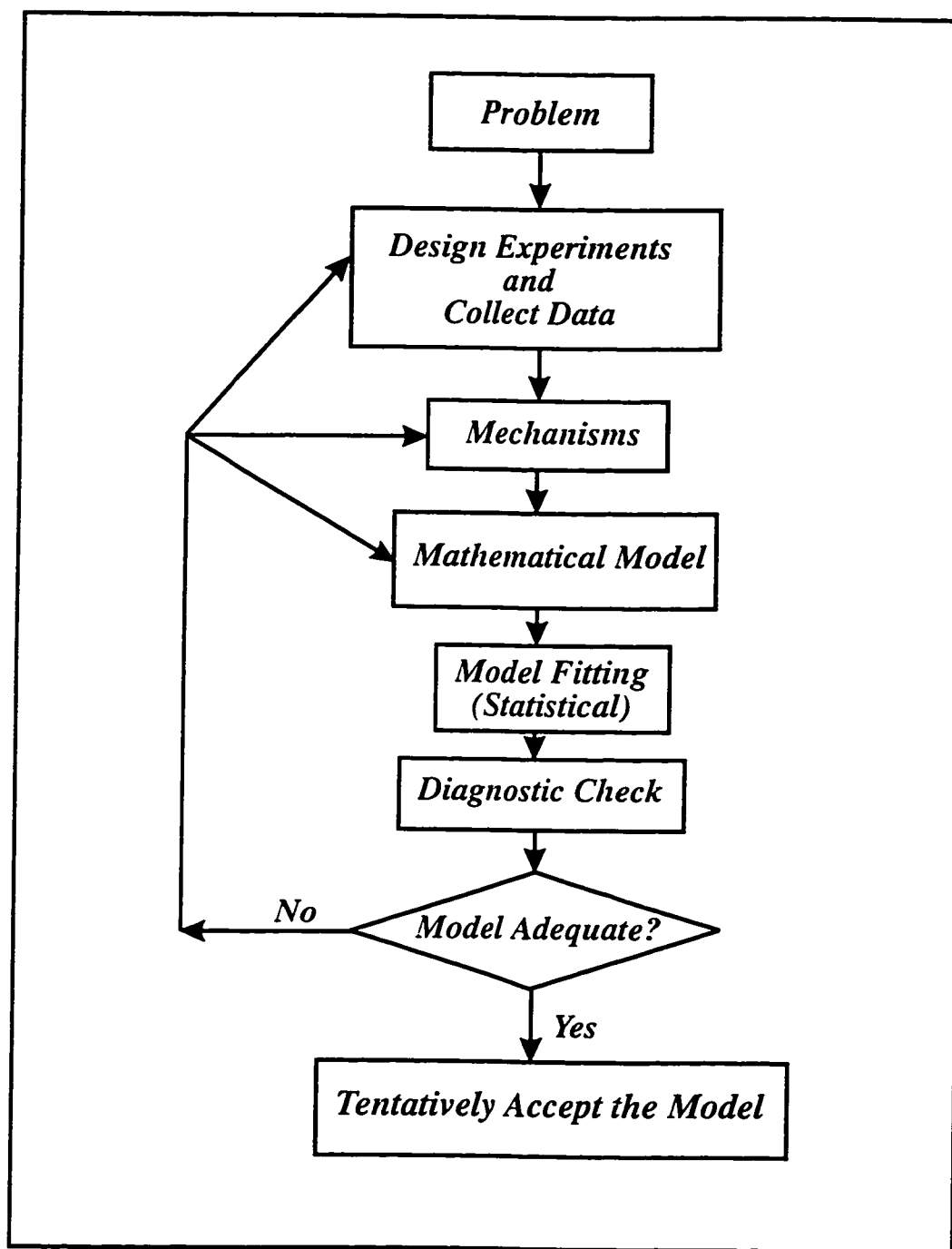
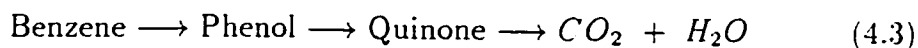


Figure 4.2: General algorithm for studying the kinetic modeling.

applied to find the point estimates. The results of this method and the conventional method are compared. We further show how to design experiments when more than one component is involved, i.e., a general experimental design for multicomponent systems. Finally, we discuss the effects of errors in measurements.

4.2 Problem Definition

Depending on the reaction paths, any chemical or photochemical reaction involves one or more differential equations. For instance, the photocatalytic degradation of benzene in water has at least two intermediates, phenol and quinone [16, 160, 161, 213]. Therefore, there are at least three simultaneous first-order ordinary differential equations in the dependent variables C_1 , C_2 , and C_3 where C_1 , C_2 , and C_3 are the concentrations of benzene, phenol, and quinone, respectively [212]. Equation (4.4) shows these differential equations which can be written based on the LH isotherm form as well as the following reaction mechanism path:



$$\begin{aligned} -\frac{dC_1}{dt} &= \frac{k_1 K_1 C_1}{1 + K_1 C_1 + K_2 C_2 + K_3 C_3} \\ -\frac{dC_2}{dt} &= \frac{k_1 K_1 C_1 - k_2 K_2 C_2}{1 + K_1 C_1 + K_2 C_2 + K_3 C_3} \\ -\frac{dC_3}{dt} &= \frac{k_2 K_2 C_2 - k_3 K_3 C_3}{1 + K_1 C_1 + K_2 C_2 + K_3 C_3} \end{aligned} \quad (4.4)$$

As shown in Equation (4.5), if n species including intermediates are present in the course of a photocatalytic reaction, a system of n simultaneous first-order ordinary differential equations in the dependent variables C_1, C_2, \dots, C_n describes the behavior of the photocatalytic degradation of these species.

$$\begin{aligned}
 -\frac{dC_1}{dt} &= f_1(t, C_1, C_2, \dots, C_n, \theta_1, \theta_2, \dots, \theta_p) \\
 -\frac{dC_2}{dt} &= f_2(t, C_1, C_2, \dots, C_n, \theta_1, \theta_2, \dots, \theta_p) \\
 &\vdots \\
 -\frac{dC_n}{dt} &= f_n(t, C_1, C_2, \dots, C_n, \theta_1, \theta_2, \dots, \theta_p)
 \end{aligned} \tag{4.5}$$

The initial conditions for these differential equations are given at a common point, usually initial concentrations at $t=0$.

Equation (4.5) is a standard dynamic model in photocatalysis with the following definitions:

1. The independent variable t , referred to as time.
2. The vector of unknown parameters, $\underline{\theta}^*$, which is the final goal of parameter estimation. Also $\underline{V}(\underline{\theta}^*)$ is the covariance matrix of the estimates of these parameters.
3. A vector of dependent variables, $\underline{\hat{C}}$, are concentrations which are functions of t , $\underline{\theta}$, and other species concentrations. The functionalities of the dependent variables are defined implicitly by means of Equation (4.5)

and their initial conditions.

4. A vector of observations, \underline{C} , are measured experimentally in the course of the photocatalytic reactions at different times for different runs. The dynamic model is a function of t , \underline{C} and $\underline{\theta}$ as shown in Equation (4.5).

4.3 Statistical Analysis

The goal of data analysis is to obtain the best point estimates for the parameters in the dynamic model. Equation (4.5). Since most photocatalytic reactions appear to obey the LH isotherm [75, 160, 161, 162, 164, 167, 168, 212], which is non-linear in the parameters, the dynamic models in photocatalysis are non-linear. Therefore, a suitable non-linear parameter estimation method should be used.

As mentioned in the previous section, in almost all the photocatalytic reaction problems that have so far been considered in the literature, observations, and thus data analyses, are made of a single unidimensional response or output C_i with respect to time. However, in practice, there is more than one component in the system and also there are some significant intermediates during the course of the reactions that should be considered. In other words, we should deal with a vector of observations implying a multivariate approach [38].

Suppose a number of experimental runs with different initial concentrations are carried out in a photocatalytic reaction and the j^{th} run consists of n observations at a specific time and fixed set of initial conditions. This

situation is common in a multicomponent system. There are p parameters in the dynamic model that have to be estimated. In this case we assume that the error covariance matrix is unknown. The general model is:

$$\underbrace{y_i}_{\nu \times 1} = \underline{f}_i(\underline{X}_i; \underline{\theta}^*) + \underline{\epsilon}_i \quad \text{where } i = 1, 2, \dots, n \quad (4.6)$$

$$\underline{\epsilon}_i : N(\underline{0}; \underline{V}^*)$$

where \underline{y}_i = the vector of observations for the dependent variables at the i^{th} trial;

\underline{X}_i = the vector of values of the independent variables at the i^{th} trial;

$\underline{\epsilon}_i$ = the vector of errors, which is normally distributed with mean zero and covariance matrix \underline{V}^* for each i ;

ν = the number of observations;

$\underline{\theta}^*$ = the vector of true parameter values;

n = the total number of data.

Error vectors $\underline{\epsilon}_i$ and $\underline{\epsilon}_j$ are independent if $i \neq j$. The underlined letters designate matrices or vectors.

The Box-Draper method used [38, 181] is a Bayesian approach. Assuming the uniform Jeffrey's prior, the density function for the elements of the \underline{V}^* is given by Equation (4.7).

$$DF(\underline{V}^*) \propto |\underline{V}|^{-\frac{(\nu+1)}{2}} \quad (4.7)$$

in which ν is the number of observations, i.e., the outputs. From Equation (4.6) the likelihood function is:

$$DF(\underline{Y}|\underline{\theta}, \underline{V}) = (2\pi)^{-\frac{n\nu}{2}} |\underline{V}|^{-\frac{n}{2}} \exp \left\{ -\frac{1}{2} \sum_{i=1}^n [\underline{y}_i - \underline{f}(\underline{X}_i, \underline{\theta})]' \underline{V}^{-1} [\underline{y}_i - \underline{f}(\underline{X}_i, \underline{\theta})] \right\} \quad (4.8)$$

By combining equations 4.7 and 4.8 and using Bayes' theorem [38], the joint probability density function can be written as Equation (4.9):

$$DF(\underline{\theta}^*, \underline{V}^{*-1} | \underline{Y}) \propto |\underline{V}^{-1}|^{\frac{1}{2}(n-\nu-1)} \exp \left\{ -\frac{1}{2} \sum_{i=1}^n (\underline{z}_i' \underline{V}^{-1} \underline{z}_i) \right\} \quad (4.9)$$

where $\underline{z}_i = \underline{y}_i - \underline{f}(\underline{X}_i, \underline{\theta})$ is the error vector.

By comparing the Wishart distribution [21, 38], the posterior probability density function of $\underline{\theta}^*$ is:

$$DF(\underline{\theta}^* | \underline{Y}) \propto \left| \sum_{i=1}^n \underline{z}_i \underline{z}_i' \right|^{-\frac{n}{2}} \quad (4.10)$$

In order to find the point estimation for $\underline{\theta}^*$, it is convenient to minimize the negative natural logarithm of proportionality statement (4.10), i.e., the objective function ϕ as shown in Equation (4.11).

$$\phi = -\ln [DF(\underline{\theta}^* | \underline{Y})] = \frac{n}{2} \ln |\underline{R}|$$

where $n \geq \nu$, $-\infty < \underline{\theta}^* < \infty$ (4.11)

and $\underline{R} = \sum_{i=1}^n \underline{z}_i \underline{z}_i'$
 $\nu \times \nu$

This simple objective function is general since in its derivation it is not assumed either that the parameters $\underline{\theta}_i$ or any of the input variables was or was not common to more than one output or that the expectation functions were linear or non-linear in the parameters [38].

To minimize the objective function in Equation (4.11), an iterative scheme with an initial guess $\underline{\theta}_1$ is used. The general iterative scheme for all methods is shown in Equation (4.12):

$$\underline{\theta}_{i+1} = \underline{\theta}_i + \rho_i \underline{\nu}_i \quad (4.12)$$

where ρ_i = the step size (scalar):

$\underline{\nu}_i$ = the step direction(vector).

The various methods described in the literature differ only in the way of choosing ρ_i and $\underline{\nu}_i$. However, the final goal of all methods is that the i^{th} step should be improved in such a way that:

$$o_{i+1} < o_i \quad (4.13)$$

To solve the dynamic model, the Marquardt method described by Bard [21, pages 94-95] was used in which

$$\underline{\nu}_i = -(\underline{A}_i + \lambda_i \underline{B}_i^2)^{-1} \underline{q}_i \quad (4.14)$$

where \underline{A}_i is an approximation to the Hessian matrix defined by

$$\underline{H}_i = \frac{\partial^2 \phi}{\partial \underline{\theta}_i \partial \underline{\theta}_j} \quad (4.15)$$

and

$$\underline{q}_i = \frac{\partial o}{\partial \underline{\theta}} \quad (4.16)$$

\underline{B}_i^2 in Equation (4.14) is a diagonal matrix whose elements coincide with the absolute values of the diagonal matrix \underline{A}_i in which zero elements are replaced by ones. Also, λ_i in Equation (4.14) is a constant, whose sufficiently large values make the term $\underline{A}_i + \lambda_i \underline{B}_i^2$ positive definite regardless of \underline{A}_i . The values of λ_i were selected according to the Marquardt's suggestion [21, pages 94–95]. λ_i was started with the value of 0.01 and then it was replaced with the maximum value between $0.1\lambda_i$ and ϵ where ϵ is a small positive number, about 10^{-7} [21, page 95]. The step size ρ_i is determined by the algorithm described by Bard [21, pages 112–113].

In addition, by using Equation (4.17), the gradient vector \underline{q}_i is determined in each step [181]:

$$\underline{q}_i = \frac{\partial o}{\partial \underline{\theta}} = -n \sum_{i=1}^n \underline{J}'_i \underline{R}^{-1} \underline{z}_i \quad (4.17)$$

where \underline{J}_i is the Jacobian matrix defined by

$$\underbrace{\underline{J}_i}_{\nu \times p} = \left(\frac{[\partial \underline{f}(\underline{X}_i, \underline{\theta})]_c}{\partial \theta_d} \right)_{c,d \text{ element}} \quad (4.18)$$

The elements of the Jacobian matrix are estimated by solving the sensitivity equations. For a dynamic model with ν observations and p parameters, $\nu \times p$ sensitivity equations must be written and solved numerically. An example of sensitivity equations is given in Appendix A.

Since the second derivatives of the objective function are tedious to calculate, especially when the number of outputs is higher, the Hessian matrix is estimated in each iteration by the use of a variable metric method as described by Bard [21]. As pointed out by Bard [21], the covariance matrix of the posterior distribution of the parameters is approximated by the inverse of the Hessian matrix: i.e.,

$$\underline{\theta} : N[\hat{\underline{\theta}} : \underline{H}^{-1}] \quad (4.19)$$

where $\hat{\underline{\theta}}$ = the point estimate of the parameters found by minimizing the objective function:

\underline{H} = the Hessian matrix at the minimum.

After finding a point estimate, it is useful to draw the contours of the constant posterior probability. By using Equation (4.20), the contours are drawn [37]:

$$\ln [DF(\underline{\theta})] \geq \ln [DF(\hat{\underline{\theta}})] - \frac{1}{2} \chi^2_{p,\alpha} \quad (4.20)$$

where p = the number of parameters;

$\chi^2_{p,\alpha}$ = the value of χ^2 with p degrees of freedom such that

$$Pr\{\chi^2_p \leq \chi^2_{p,\alpha}\} = \alpha \quad [182].$$

A FORTRAN coded program based on the theory explained in this section was written to obtain the point estimates for the parameters in the dynamic model. The algorithm for such a program is illustrated in Figure 4.3.

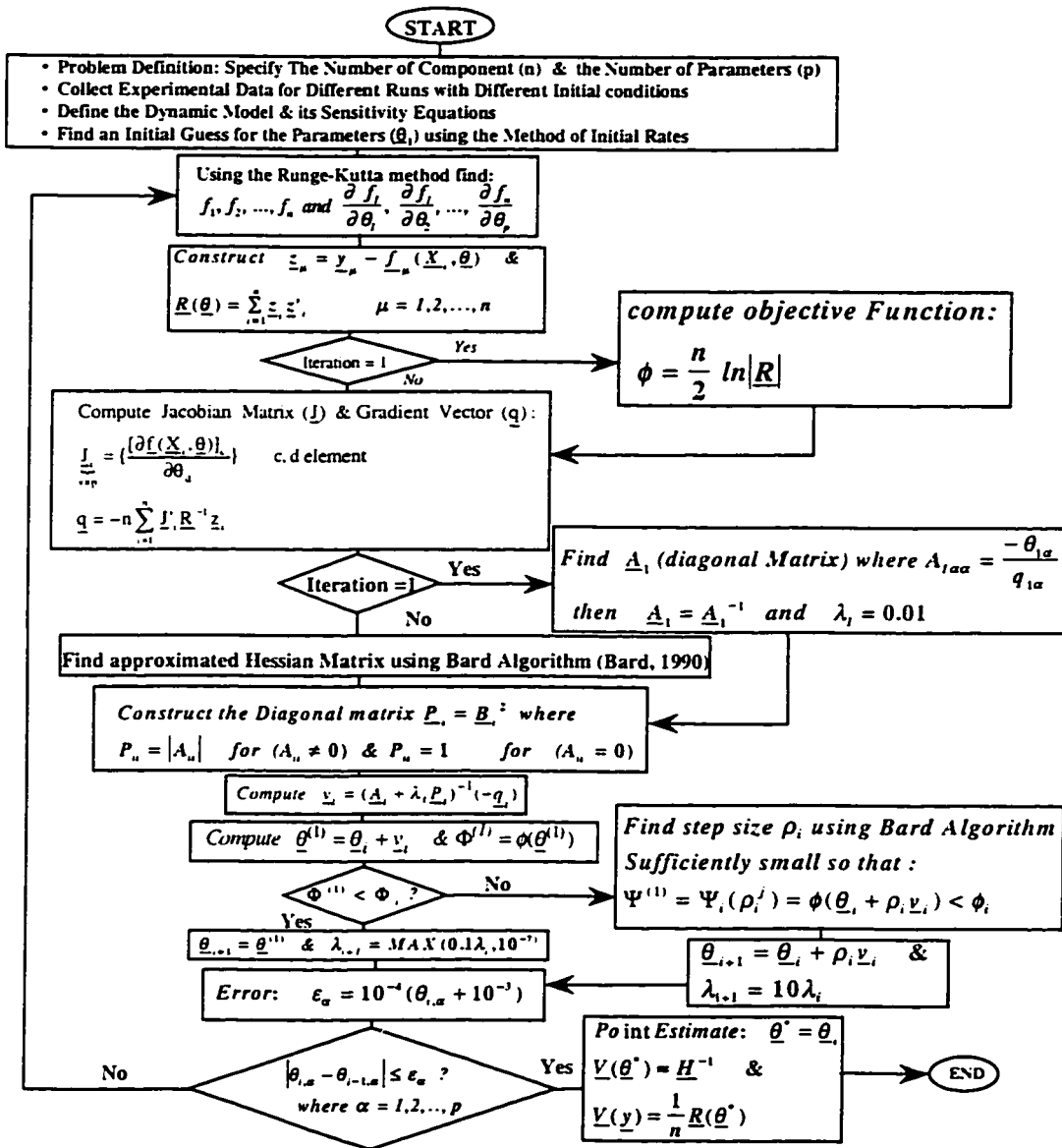


Figure 4.3: The algorithm of the nonlinear parameter estimation of a dynamic model in kinetic studies.

Also, another FORTRAN coded program was written in order to draw the contours of the constant posterior probability described by Equation (4.20). The algorithm for the contours, i.e., joint confidence intervals of the parameters, is shown in Figure 4.4. The FORTRAN coded program was written based on this algorithm to find the joint confidence intervals of 50, 75, and 95%.

Since the dynamic model described by Equation (4.5) consists of n simultaneously coupled first order differential equations for which there is no analytical solution, the fourth-order Runge-Kutta method was used to find the vector of \underline{f} , the values of the variables estimated by the model [52]. In this numerical method, Gill's constants [86] were used.

In the next section, the results of an example of a photocatalytic reaction are explained.

4.4 An Example

Due to the lack of a complete data set for photocatalytic degradation of a multicomponent system in the literature, we present a simple example for which the data are available. The example presented here is the photocatalytic degradation of perchloroethylene (PCE) [213]. Literature shows that PCE is photocatalytically clean; that is, it proceeds without generation of measurable intermediates [138, 163, 211, 212]. It is also found that PCE follows the Langmuir-Hinshelwood form [163]. Therefore, we here deal with one component in the system, meaning that there is only one observation or output at any specific time. The raw data are taken from Turchi [213].

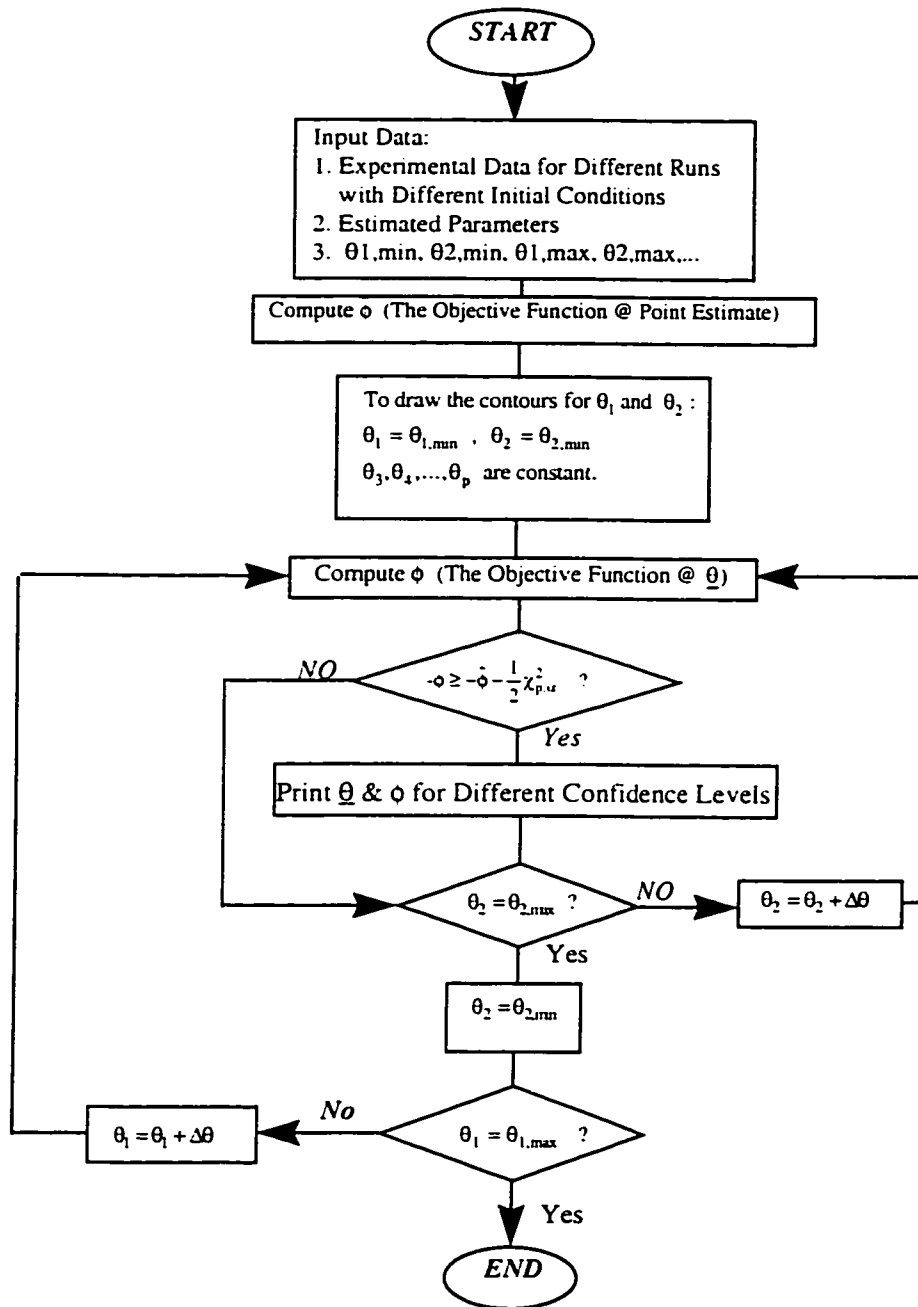


Figure 4.4: The algorithm of the contours for the joint confidence of the parameters in the dynamic model.

These data consist of twelve runs with different initial conditions that represent the photocatalytic degradation of PCE in pure water using a slurry photoreactor. The model derived by the reaction mechanism follows the Langmuir-Hinshelwood isotherm as shown in Equation (4.21).

$$-r = -\frac{dC}{dt} = \frac{\theta_1 \theta_2 C}{1 + \theta_2 C} \quad (4.21)$$

in which $\theta_1 = k$ and $\theta_2 = K$ are the reaction rate constant and binding constant, respectively. The method of initial rates was used to find the kinetic parameters in Equation (4.21). The data analysis using this conventional method showed that the values of the parameters are $\theta_1 = 18.7 \pm 21.0 \mu\text{M min}^{-1}$ and $\theta_2 = 0.00923 \pm 0.0278 \mu\text{M}^{-1}$. On the other hand, Turchi [213] found that the parameters have the values of $\theta_1 = 34 \mu\text{M min}^{-1}$ and $\theta_2 = 0.0086 \mu\text{M}^{-1}$. Since Turchi used the conventional method as we did, it is obvious that it does not give consistent results when used by different researchers and therefore should not be considered reliable. As mentioned before, Figure 4.1 depicts the plot of $\frac{1}{-r_{i0}}$ versus $\frac{1}{C_{i0}}$, and it is obvious from $R^2 = 0.534$ that the data are poorly explained by the model. In addition, the plot of residuals for linear regression against the observed data in Figure 4.5 shows that there is a serial correlation among the data.

Since the residuals are not well behaved, it is concluded that the method of initial rates is inadequate. For comparison, the application of the non-linear parameter estimation described in the previous section was used employing all 133 data points in the analysis. Using the FORTRAN coded program, the parameters with 95% confidence limits were determined to be:

$$\theta_1 = 27.0 \pm 1.4 \mu M \text{ min}^{-1}$$

and

$$\theta_2 = (9.7 \pm 1.1) \times 10^{-3} \mu M^{-1}$$

By plotting the residuals against the observed data in this method, about five outliers were detected, i.e., those data that have much more uncertainty and experimental errors. After excluding these five data, and analyzing the remaining 128 data points, the point estimates for the parameters with 95% confidence limits are:

$$\theta_1 = 24.9 \pm 1.0 \mu M \text{ min}^{-1}$$

and

$$\theta_2 = (1.07 \pm 0.09) \times 10^{-2} \mu M^{-1}$$

The plot of residuals for these data points is shown in Figure 4.6.

As Figure 4.6 shows, a random scatter with no discernible pattern about $\epsilon_i = 0$ is seen. Therefore, the model with these parameters explains the experimental data very well.

Also, the plots of concentration-time data for all runs show that the non-linear parameter estimation describes the model more accurately than the method of initial rates. For instance, Figure 4.7 shows the concentration-time data for one of the runs, and it is obvious that the non-linear analysis

explains the experimental data better.

As mentioned before, one of the advantages of the non-linear data analysis is that one is not required to find initial rates that are often highly inaccurate. In addition, data obtained through the whole course of the experimental run are used in this method. Thus, far better evaluation of the model in terms of the data is obtained. It should be emphasized that the method of initial rates fails for multicomponent systems, in which some of the components may be intermediates with zero initial concentrations. In this case, a dynamic model describes the behavior of the reaction system and non-linear data analysis using all run-time data must be used.

The joint 95, 75, and 50% posterior probability regions of the parameters for both non-linear and linear models are drawn in Figures 4.8 and 4.9, respectively.

The outside contour in Figures 4.8 is the 95% confidence region. By comparing Figures 4.8 and 4.9, it is obvious that the contour area in the non-linear model is much smaller than that in the linear model. This indicates that the non-linear model is much more precise. In addition, as Figure 4.9 demonstrates, the contours of the confidence regions in the linear model are banana-shaped showing a wide range of values for the parameters. This indicates the higher level of uncertainty in the parameters determined by the conventional method.

Using Equation (4.2), the parameters, $(\theta_1\theta_2)^{-1}$ and $(\theta_1)^{-1}$, are lumped together in order to make the regression. By drawing the 95% confidence region for the lumped parameters in Equation (4.2), one can judge the val-

idation of the parameter estimation. Figure 4.10 shows the 95% confidence region for the PCE kinetic lumped parameters. Also, by comparing Figures 4.8 and 4.10, it is obvious that linear regression for such data gives a broad range of parameters. This is an indication that non-linear parameter estimation provides better point estimates than linear regression using the method of initial rates.

4.5 Concluding Remarks

It is customary that data analysis in photocatalytic and many other chemical reactions is performed by the method of initial rates. It has been illustrated here that this method has serious disadvantages especially when a dynamic model describes the kinetic reactions. One of the major faults in this method is the error involved in finding the initial rates, given that the estimation of the initial rates can be highly subjective. The plot of residuals in the linear (initial rate) analysis confirms that there is a pattern among the data, which indicates a lack of constant variance amongst the data. Most importantly, the method of initial rates fails in the multicomponent systems, in which some intermediates or products are present with no initial concentrations.

The method of non-linear data analysis described in this chapter addresses these deficiencies. It can be applied to multicomponent system including models in which intermediate and product species are considered. It does not require subjective estimates of initial reaction rates for model development but rather utilize all available data to compute the best point estimate of the

parameters. The approach developed in this chapter will be used to solve non-linear dynamic models in Chapter 5.

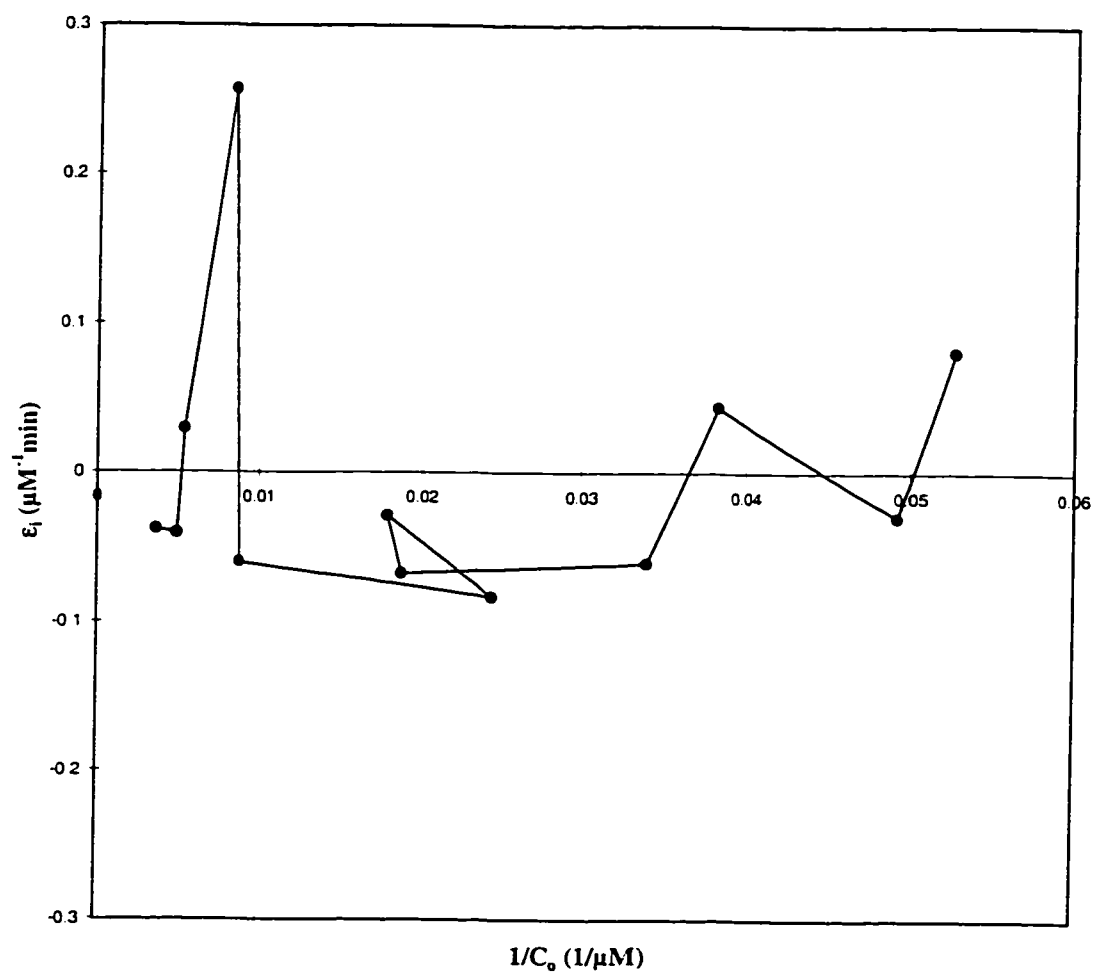


Figure 4.5: The residuals in the linear (initial rate) model.

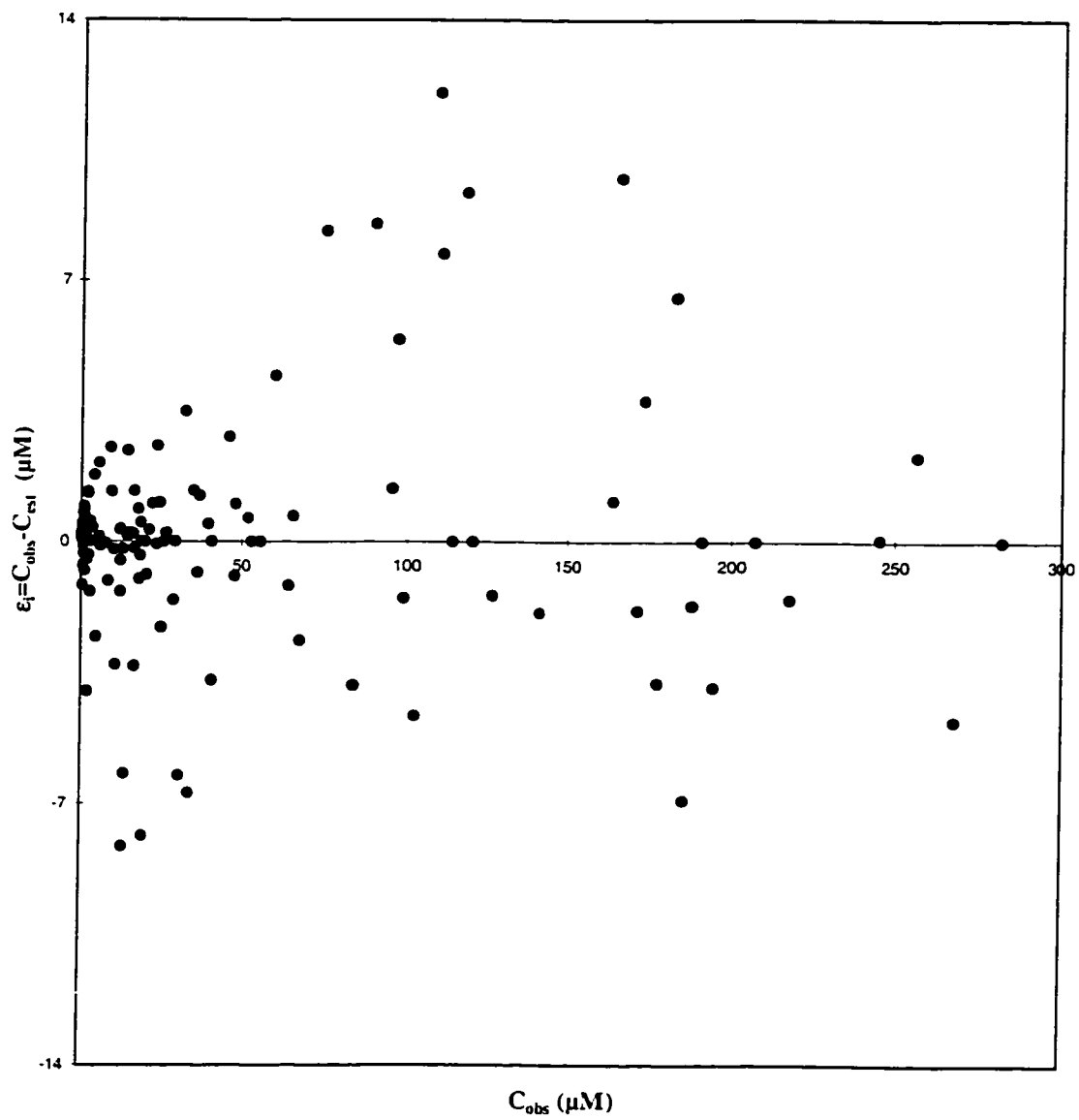


Figure 4.6: The residuals in the non-linear parameter estimation for PCE data (experimental data were adopted from Turchi [213]).

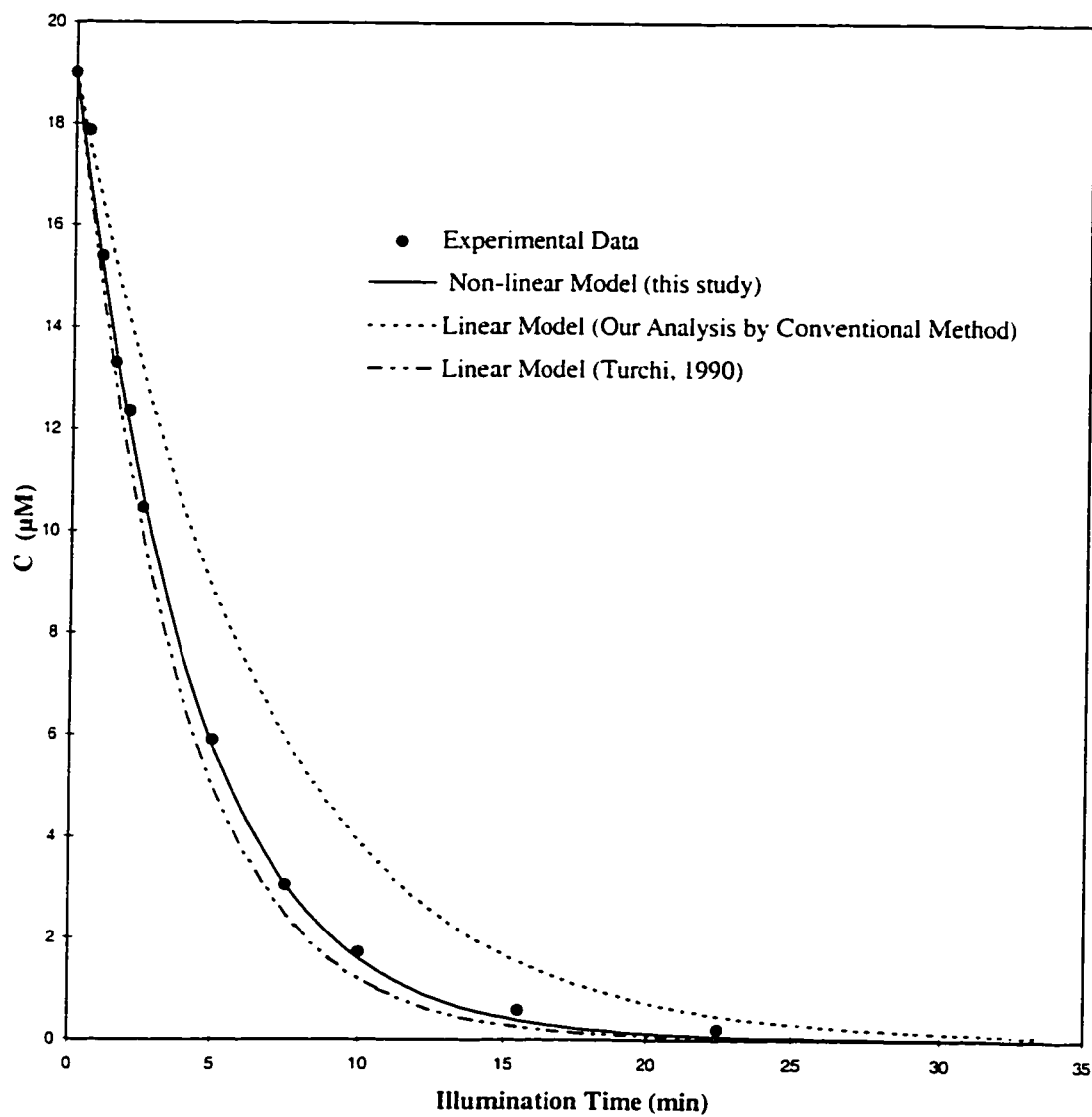


Figure 4.7: The Concentration-Time plot for the Photocatalytic Degradation of PCE (experimental data were adopted from Turchi [213]).

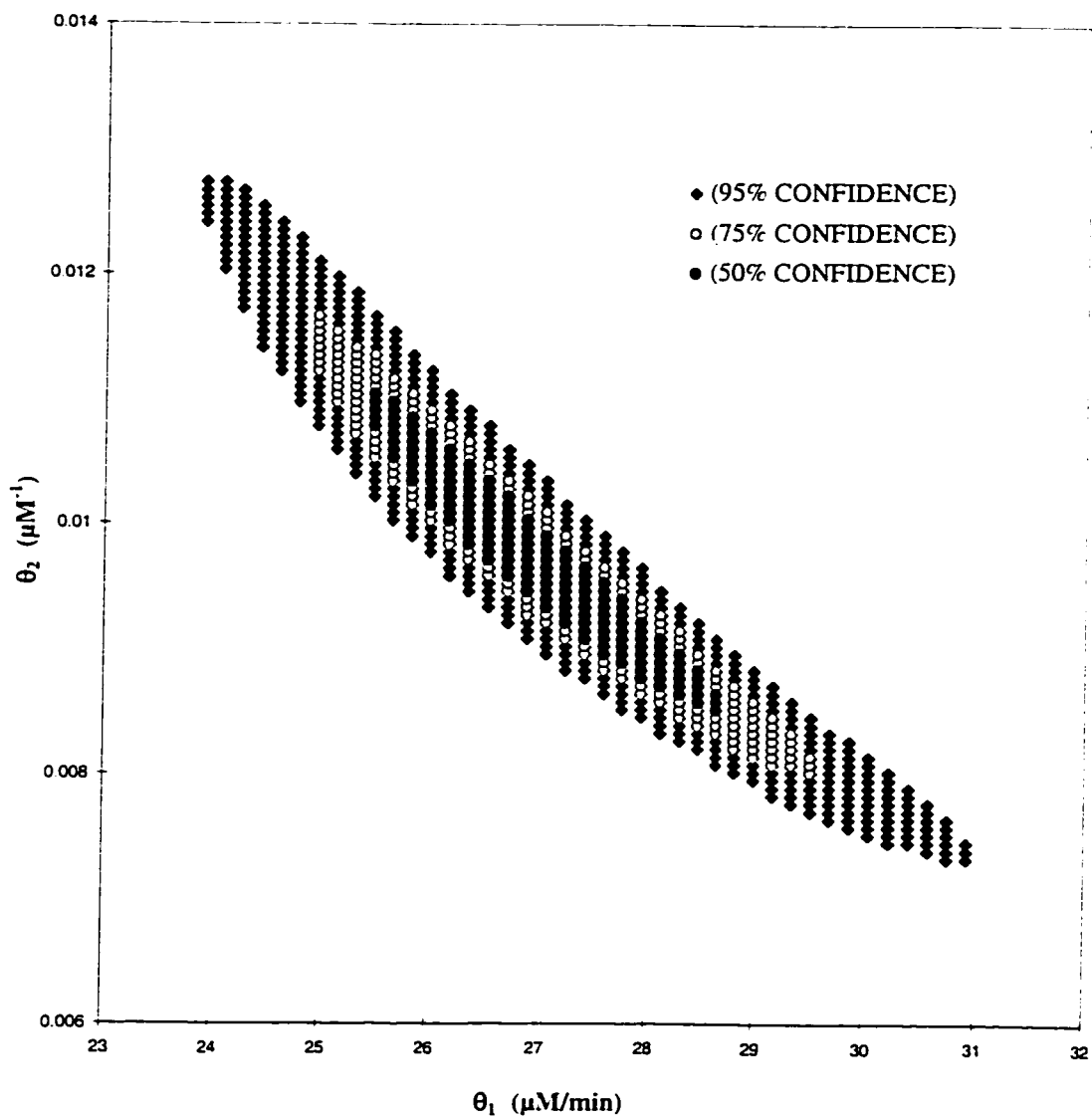


Figure 4.8: Joint confidence interval for the PCE kinetic parameters in the non-linear model.

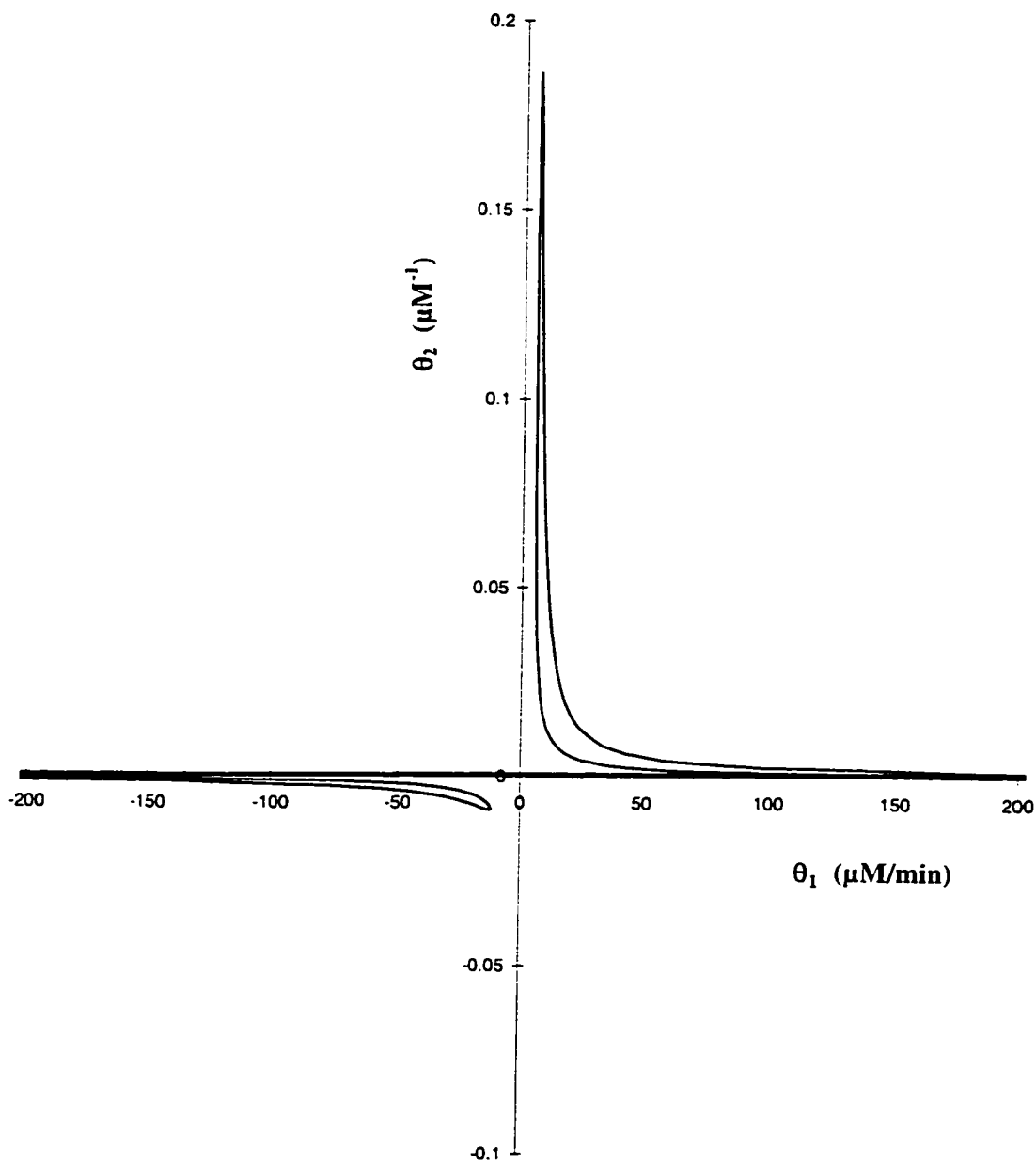


Figure 4.9: Joint 95% confidence interval for the PCE kinetic parameters in the linear (initial rate) model.

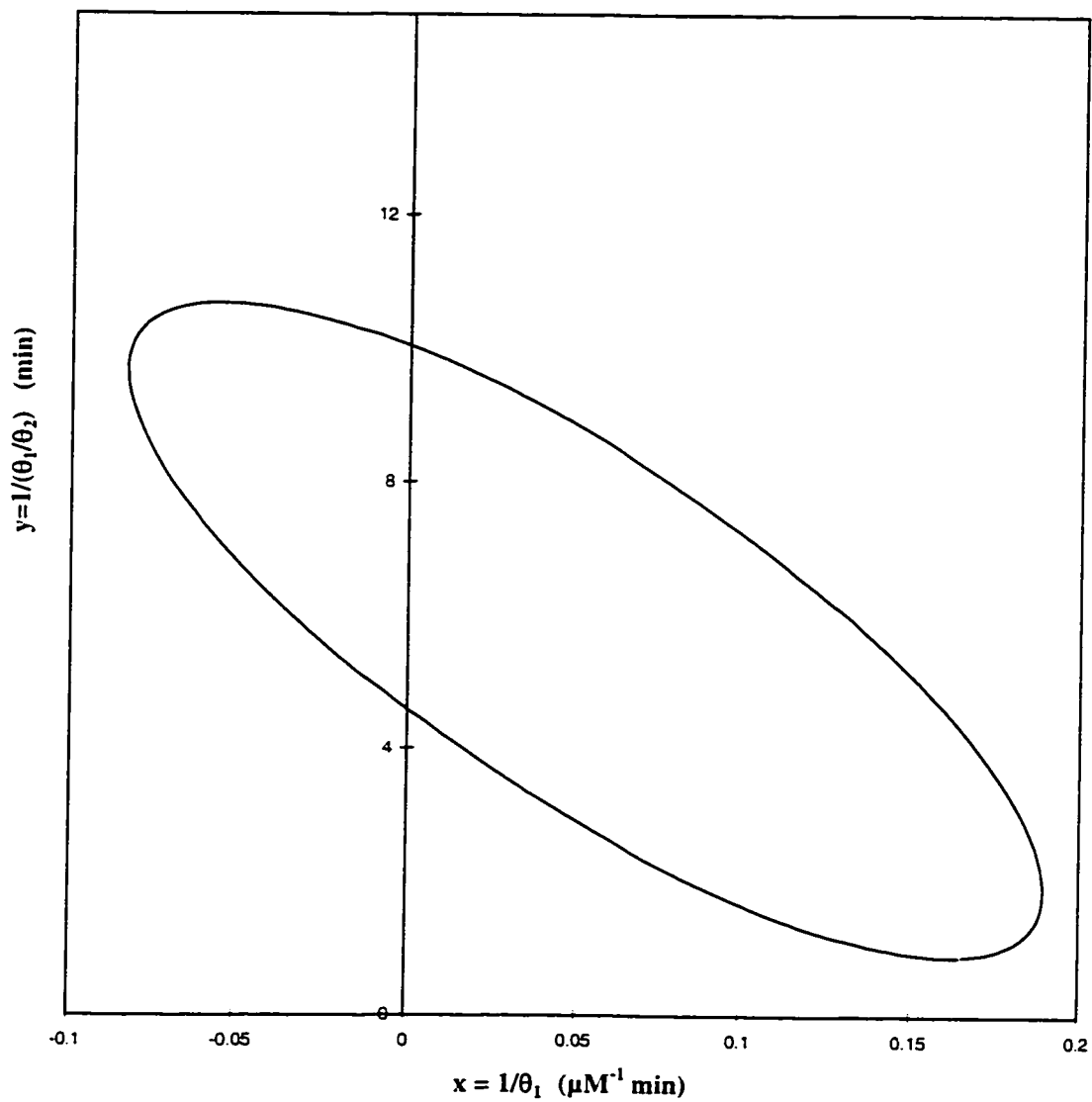


Figure 4.10: Joint 95% confidence interval for the PCE kinetic lumped parameters in the linear (initial rate) model.

Chapter 5

PHOTOCATALYTIC DEGRADATION OF TETRAHYDROFURAN, 1,4-DIOXANE, AND THEIR MIXTURE

5.1 Introduction

In this chapter, the results of the kinetic studies of a binary system are presented and discussed. The results focus on the organic pollutants tetrahydrofuran (THF) and 1,4-dioxane (DIOX). The reaction mechanisms and kinetic models are presented. The kinetic models have been developed based

on the reaction mechanisms proposed. The reaction rate constants are estimated using the experimental data and the method outlined in Chapter 4.

5.2 Illumination Time

For all kinetic rate determinations, the illumination time was used in the model equations. The illumination time is defined as the actual reaction time which indicates how long each element of the liquid is in the illumination zone of the photoreactor. Therefore, the illumination time or the actual reaction time can be estimated as follows:

$$t_{Ill} = \frac{V_R}{V_{tot}} t_{run} \quad (5.1)$$

where t_{Ill} = the illumination time or the actual reaction time, [s] or [min];

t_{run} = actual run time, [s] or [min];

V_R = the volume of the illumination zone of the photoreactor, [L];

V_{tot} = total volume of the liquid in the photoreactor, [L].

In the recirculating slurry photoreactor used in this study, the illumination zone of the photoreactor was 3.8 L and the total liquid used was 7.0 L. Using Equation (5.1), the illumination time in this slurry photoreactor may be estimated as follows:

$$\begin{aligned} t_{Ill} &= \frac{3.8 \text{ L}}{7.0 \text{ L}} (t_{run}) \\ &= 0.543 (t_{run}) \end{aligned} \quad (5.2)$$

Therefore, in the kinetic model equations, the illumination time (t) is calculated using Equation (5.2).

The slurry photoreactor used in this study (see Chapter 3) had a flow rate of 12.1 L min^{-1} . Since the total liquid used in this photoreactor was 7.0 L for each run, the time required for a pass was 0.58 min. This slurry photoreactor was a recycling differential reactor since the conversion per pass in all cases was small ($< 1\%$). This means that there could be no appreciable concentration gradient throughout the recycling system at any instant. Because of no through flow in this slurry photoreactor, this was essentially a batch photoreactor: and Equation(5.1) is valid.

5.3 Mass Transfer Effects in the Slurry Photoreactor

In this photoreactor, mass transfer effects were minimized; therefore, the system was controlled only by reaction kinetics. The Damköhler number (Da), the ratio of the maximum possible reaction rate to the maximum possible mass transfer rate, can be used as a criteria for the influence of the mass transfer rate on the reaction rate [164]. This dimensionless number is defined as follows:

$$Da = \frac{k}{k_s a C_0} \quad (5.3)$$

where k = reaction rate constant, $[\text{mol m}^{-3} \text{s}^{-1}]$;

k_s = mass transfer coefficient at the liquid-solid interface, $[\text{m s}^{-1}]$;

a = specific surface area of the particles in solution, $[\text{m}^2 \text{m}^{-3}]$;

C_0 = bulk solution concentration of organic species. [mol m^{-3}].

If $Da \ll 1$, no mass transfer limitation exists and if $Da \gg 1$, it indicates of a reaction with mass transfer control.

The mass transfer coefficient for very fine spherical particles can be estimated by the following equation [160]:

$$k_s a = \frac{12 D m_p}{\bar{d}_p^2 \rho_p} \quad (5.4)$$

where D = diffusion coefficient, [$\text{m}^2 \text{s}^{-1}$];

m_p = particle concentration in the solution, [kg m^{-3}];

\bar{d}_p = average particle diameter, [m];

ρ_p = density of the particles. [kg m^{-3}].

For example, for 1,4-dioxane, using a typical rate constant of $9.3 \mu\text{M min}^{-1}$, 50 mg L^{-1} initial concentration, $D_{DIOX-H_2O} = 8.694 \times 10^{-10} \text{ m}^2 \text{ s}^{-1}$ (see Appendix D), $[\text{TiO}_2] = 1.5 \text{ g L}^{-1}$, $\bar{d}_p = 21 \text{ nm}$, and $\rho_p = 3.8 \text{ g cm}^{-3}$, the value of Da is evaluated to be 2.93×10^{-8} using Equations (5.4) and then (5.3). This number is significantly less than 1 implying that, mass transfer is not a factor in this slurry photoreactor. Ollis et al. [164] estimated that the maximum typical Damköhler number for a slurry photoreactor with fine particles is about 2.5×10^{-4} . Similarly, Turchi and Ollis [210] estimated that in a slurry photoreactor with 1 g L^{-1} Degussa P25 titanium dioxide, the maximum diffusion distance of the reactant to the catalyst surface is half the mean particle spacing ($0.5 \mu\text{m}$). Again mass transfer is not controlling in the slurry photoreactor. This contrasts with systems such as an immobilized tube or

glass beads which are frequently limited by mass transfer. For instance, in a coated tubular reactor of 2 mm radius, the maximum transport distance is 2 mm (2000 μm) which is significant in comparison to that of the slurry photoreactor.

5.4 Dark Reactions and Photolysis

To verify that the reactions occurring in this system were solely a result of photocatalysis, a run without any TiO_2 and UV light was carried out, the so-called “dark reaction”. In another set of experiment, photolysis was examined in this particular system. The results of these experiments are discussed in the following.

5.4.1 Dark Reaction

To prove photocatalysis was the main source of disappearance in these experiments, the dark reaction was carried out. In this experiment, no TiO_2 was used and also UV lights were off during the run. Figure 5.1 reveals the results of dark reaction experiment.

As this figure shows, there is no significant change in the concentration of 1,4-dioxane. The slight reduction of 1,4-dioxane concentration in about 5 h could be due to adsorption of the organic on different surfaces, experimental and analytical error, and the escape of some organic material into the gas phase. Dietz and Singley [64] also showed that the reduction of such typical organics in the dark reaction might be due to the slow leakage of organics

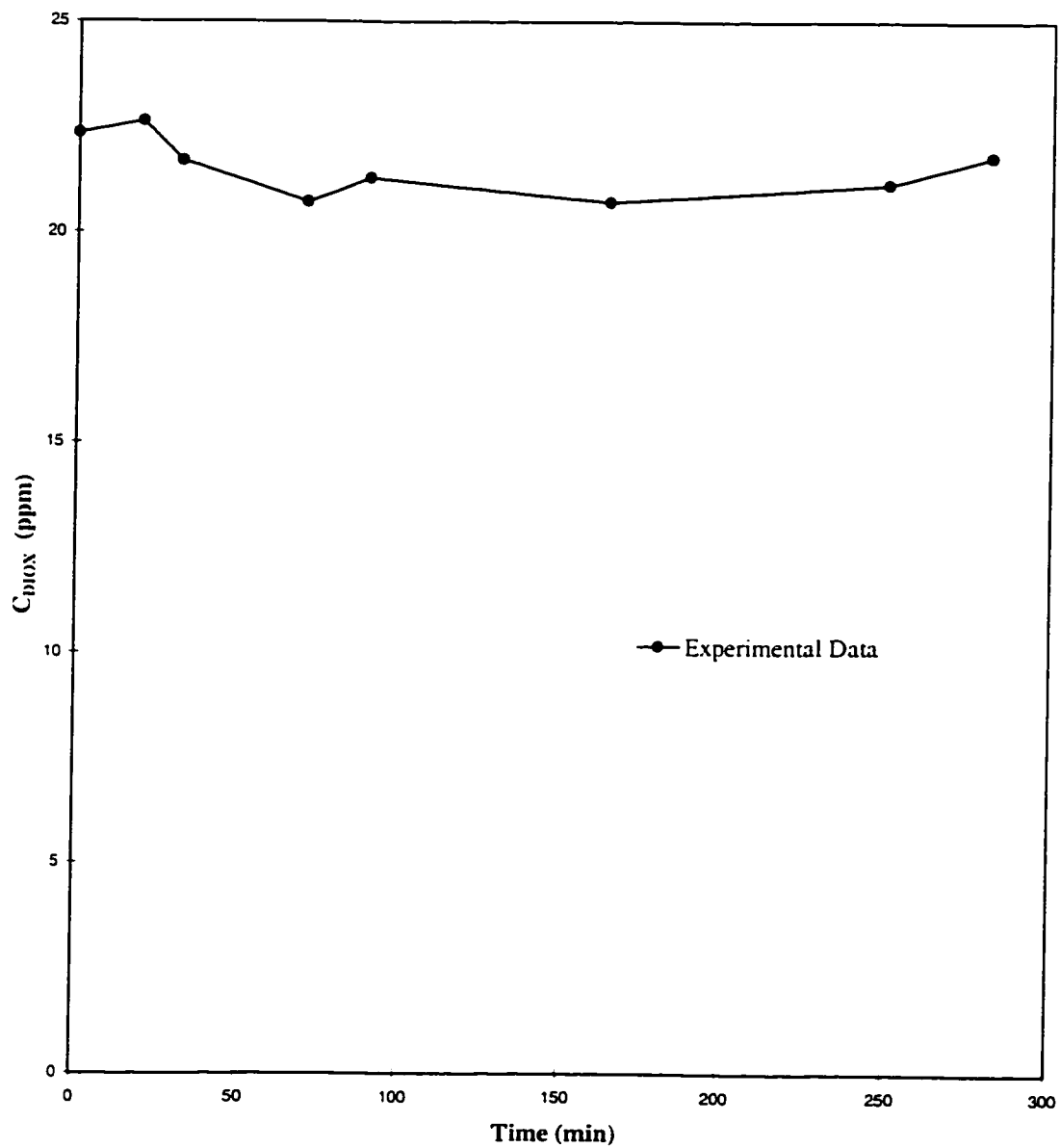


Figure 5.1: Dark reaction for 1,4-dioxane in the slurry photoreactor, no photocatalyst and no UV light.

through the photoreactor seals and the punctured Teflon septum. Although the Henry's constants for tetrahydrofuran and 1,4-dioxane are low due to their high solubilities in water (see Table 2.1), it is still possible that a slight amount of organics escape into the headspace section of the reservoir. Therefore, it is concluded that adsorption of organics was not significant in this system. In another words, the disappearance of organics in the dark reaction was not significant in comparison to the decrease in the presence of illumination and photocatalyst. For instance as Figures 5.3 and 5.4 will show in subsequent sections, 1,4-dioxane disappeared almost completely in about 1 h when illuminated in the presence of a photocatalyst. The disappearance time in photocatalytic reactions (Figures 5.3 and 5.4) was significantly smaller in comparison to the time required by the dark reaction (Figure 5.1).

5.4.2 Photolysis

Organics can be destroyed photolytically by near UV light if they absorb light in that region. Although near UV light can in principle degrade organics, photolytic reactions do not occur to a significant extent. Most organics do not absorb UV light sufficiently in the near UV region, and therefore, in most cases photolytic processes do not occur significantly.

Table 5.1 shows the absorption spectra characteristics for the organic compounds used or found in this study [125, 126]. Although it has been reported that tetrahydrofuran and 1,4-dioxane can absorb UV light in the range of 350–400 nm, their maximum absorbance at this range is only 0.005 in comparison to their maximum absorbance of 1.000 at 212 nm for THF and

180 and 215 nm for DIOX [120, 125]. As Table 5.1 shows, the maximum UV absorbance for tetrahydrofuran, 1,4-dioxane, and γ -butyrolactone (GBL) occurs at lower wavelengths which are not in the range of UV-A (320–400 nm). Therefore, it is not expected that photolysis contributes to the disappearance of these organics.

In this study, a photolytic experiment for 1,4-dioxane was examined in the annular photoreactor while the UV lights were on and there was no titanium dioxide present (see Figure 5.2). As expected, photolysis did not cause significant disappearance of 1,4-dioxane. Therefore, it can be concluded that almost all disappearance of organics in this study was solely a result of photocatalysis.

Table 5.1: Absorption spectra characteristics of tetrahydrofuran, 1,4-dioxane, and γ -butyrolactone.

CHEMICAL NAME	λ_{max} [nm]	REFERENCE
Tetrahydrofuran (THF)	212	[125]
1,4-Dioxane (1,4-DIOX)	180, 215	[125, 126]
γ -Butyrolactone (GBL)	209	[126]

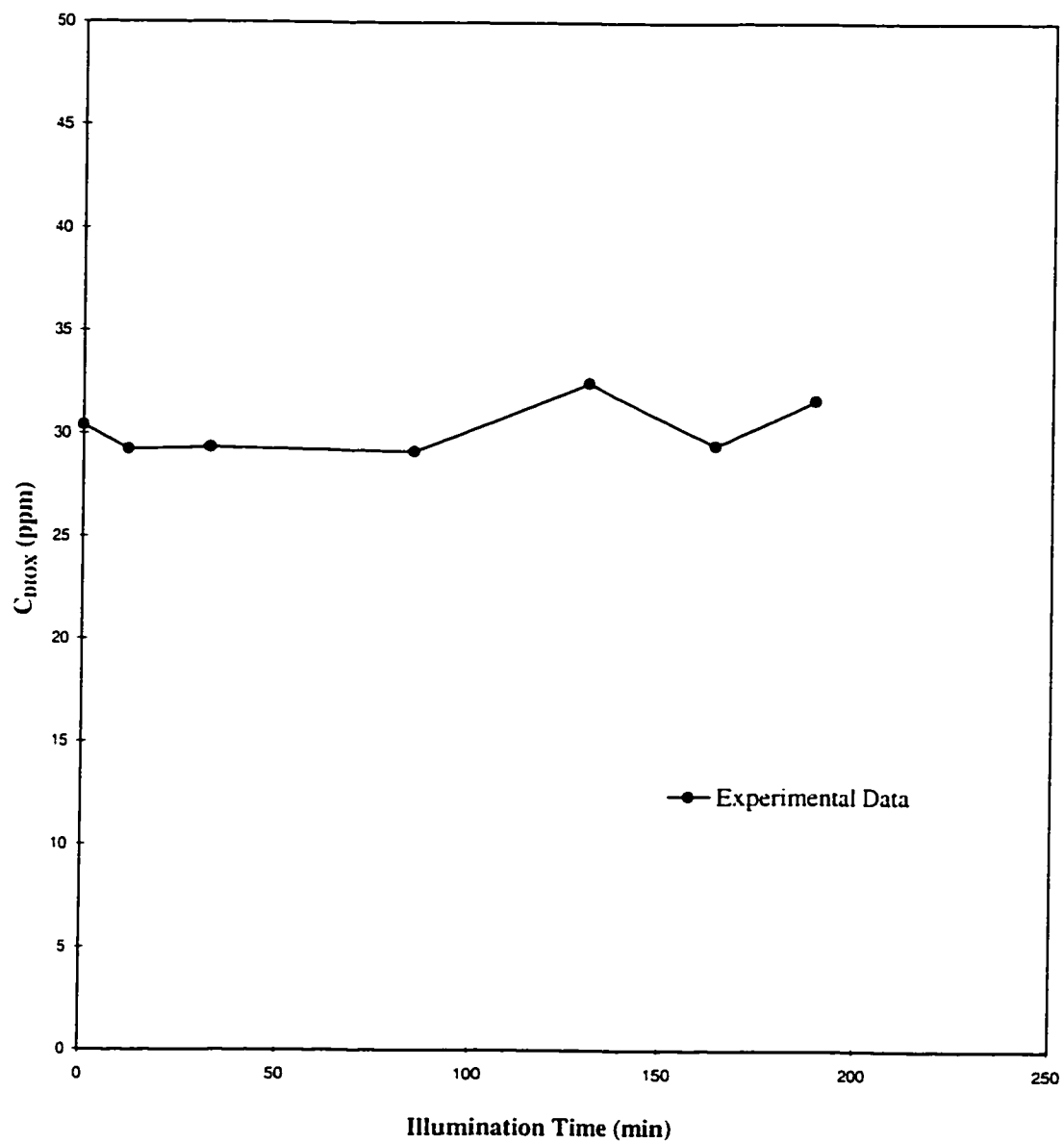


Figure 5.2: Photolytic degradation of 1,4-dioxane (lights on, no photocatalyst), $C_{o,DIOX} = 30.4 \text{ mg L}^{-1}$.

5.5 Photocatalyst Optimization

Photocatalyst optimization in the annular photoreactor was the next step in studying the intrinsic photocatalytic kinetics of tetrahydrofuran and 1,4-dioxane. The main goal of this section is to optimize the photocatalyst loading for the purpose of kinetic studies. Another main goal of this section is to compare two titanium dioxides, Degussa P25 and Hombikat UV 100, in terms of photoactivity, catalyst loadings, UV extinction, and hydrodynamic effects. As mentioned in Section 3.1, these two photocatalysts were provided by Degussa Corporation and Sachtleben Chemie GmbH, in Duisburg, Germany, respectively. In the following, the results for these two catalysts are discussed.

5.5.1 P25 Titanium Dioxide

The sequence of the experimental runs began with a single component system in order to optimize the photocatalyst loading. For the purpose of this phase of the study, 1,4-dioxane was chosen as an organic model compound for the optimization runs. To optimize P25 titanium dioxide, the photoreactor was loaded with different slurry concentrations. The system was aerated prior to each run to provide enough oxygen for the entire course of the reaction. At specific time intervals, samples were taken from the reactor and analyzed by GC.

Figure 5.3 depicts the time-concentration plot of photocatalytic degradation of 1,4-dioxane using Degussa P25 TiO₂ in the slurry photoreactor. In these experiments, all conditions remained constant except the TiO₂ concen-

trations. The initial concentration of 1,4-dioxane for all experimental runs was 27.8 mg L^{-1} ($316 \text{ }\mu\text{M}$). Although all degradation curves are close to each other as depicted in Figure 5.3, it can be demonstrated that an optimum catalyst loading exists. This can be done either by estimating initial rates or by finding reaction rate constants. The details are discussed in Section 5.5.3.

5.5.2 Hombikat UV 100 Titanium Dioxide

Another set of experiments was carried out using a relatively new titanium dioxide, called Hombikat UV 100, provided by Sachtleben Chemie GmbH. In these experiments, 1,4-dioxane was also used as the organic compound model. For the ease of comparison, the initial concentration for all experimental runs was kept the same as the initial concentration in the Degussa P25 experiments (27.8 mg L^{-1}). Also, the photoreactor was aerated prior to each run in order to provide ample oxygen in the system.

Figure 5.4 reveals the concentration-time profile of a series of similar experiments in which photocatalytic degradation of 1,4-dioxane was examined using Hombikat UV 100 photocatalyst. A range of $0.5\text{--}7.5 \text{ g L}^{-1}$ of UV 100 titanium dioxide slurry was examined. As depicted in Figure 5.4, at the lowest titanium dioxide loading, i.e., 0.5 g L^{-1} , the photocatalytic degradation rate is somewhat slower than those with higher titanium dioxide loadings. It is obvious from this figure that as the loading of titanium dioxide increases, the degradation rate is enhanced. However, the degradation curves are getting closer as the slurry loading increases. At the highest loading, it is difficult to distinguish between the photocatalytic degradation rates. The details are

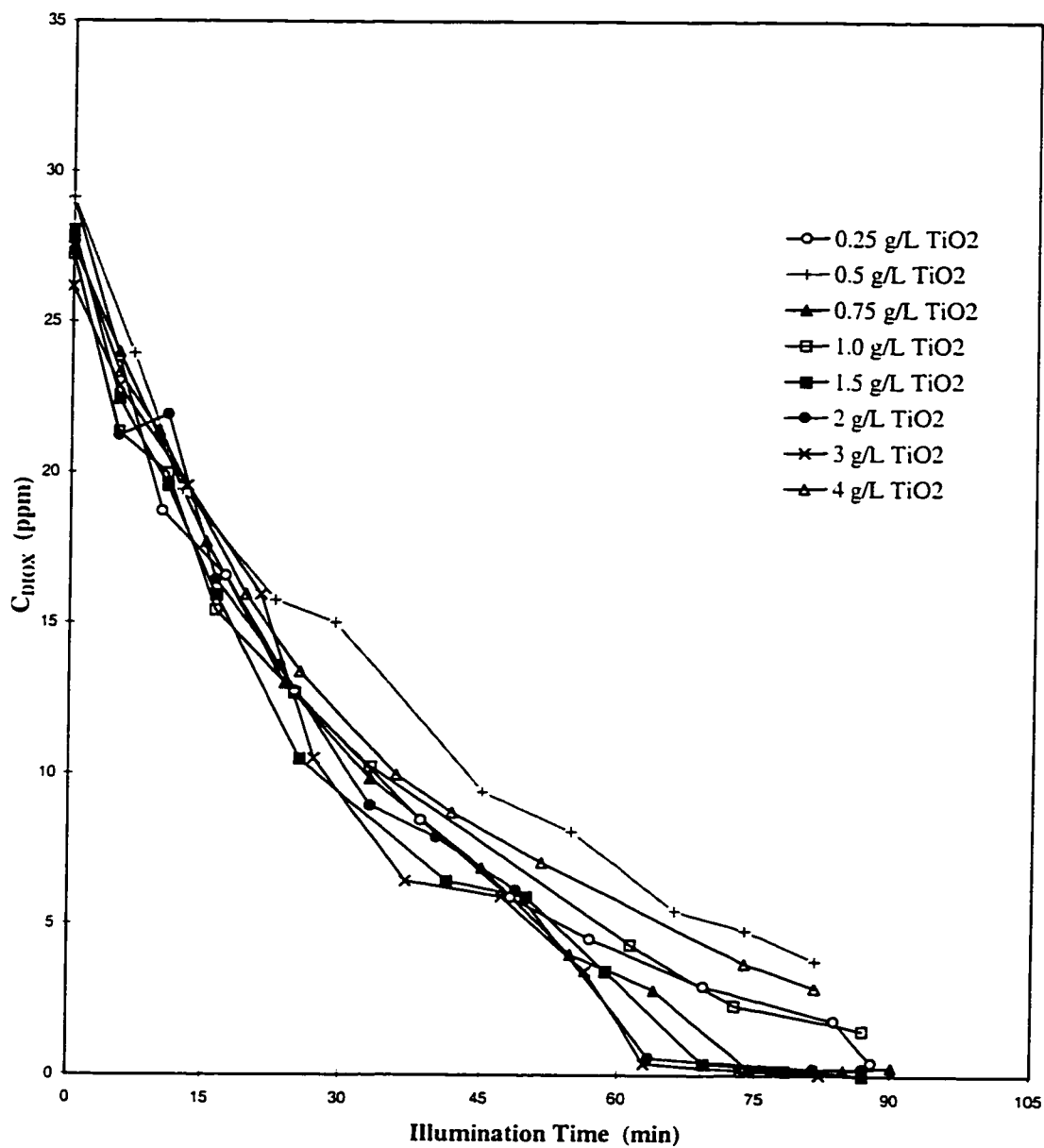


Figure 5.3: Photocatalytic degradation of 1,4-dioxane in the slurry photoreactor with different Degussa P25 TiO₂ photocatalyst loadings, $C_{0,DIOX} = 27.8 \text{ mg L}^{-1}$. The system was aerated before runs.

discussed in the following section.

5.5.3 Comparison Between Degussa P25 and Hombikat UV 100 Titanium Dioxides

In order to optimize the photocatalyst loading and to compare the results, two simple but informative methods were used to analyze the data. In the first method, the first order rate constant for individual runs was estimated. Although the error involved in the first order rate estimation in some runs was high, this kind of analysis is still informative. Figure 5.5 depicts the first order rate constants versus slurry loadings of the two different titanium dioxides.

As illustrated in Figure 5.5, similar behaviors are seen for the two photocatalysts. As catalyst loading increases, the first order rate constants for both titanium dioxides increase. This increase reached a plateau at a loading of around 1.5 g L^{-1} for Degussa P25 and $3.0\text{--}4.0 \text{ g L}^{-1}$ for Hombikat UV 100 titanium dioxide. When the loading of Degussa P25 TiO_2 increased to 4.0 g L^{-1} , a decrease in the first order rate constant was observed. This observation is depicted in both Figures 5.3 and 5.5. This decrease in the rate constant for P25 TiO_2 at 4.0 g L^{-1} can be explained easily by the fact that the light cannot penetrate inside the photoreactor zone easily due to the high particle loading. A similar result was observed with UV 100 TiO_2 at loading of 7.5 g L^{-1} .

In the second analysis, the conventional method of initial rate for each individual run was estimated by the initial slope of the concentration-time

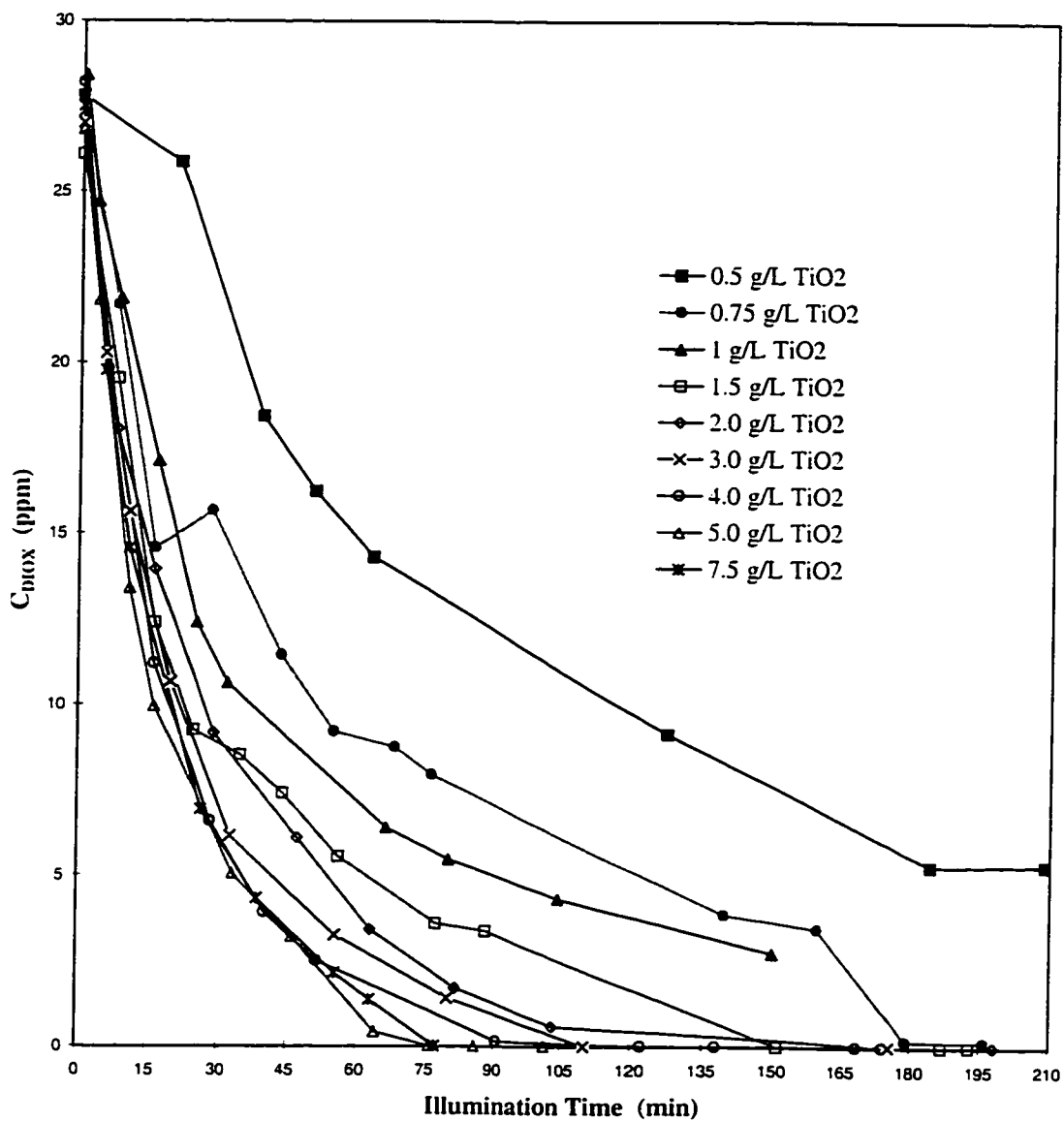


Figure 5.4: Photocatalytic degradation of 1,4-dioxane in the slurry photoreactor with different UV-100 TiO_2 photocatalyst loading, $C_{0,DIOX} = 27.8 \text{ mg L}^{-1}$. The system was aerated before runs.

profiles. Although Mehrvar et al. [148] showed that the method of initial rates had some drawbacks such as sensitivity, this method is still sufficient for comparative purposes. The method of initial rates was applied to these experimental runs and the results for both titanium dioxide photocatalysts are revealed in Figure 5.6.

Similar behaviors are seen for both photocatalysts in Figure 5.6 as observed in Figure 5.5. At lower loadings of titanium dioxide, Degussa P25 had more activity than UV 100. However, at higher loadings of titanium dioxide, Hombikat UV 100 was more active. The activities of both photocatalysts reached a plateau at a loading of 1.5 g L^{-1} for Degussa P25 and $3.0\text{--}4.0 \text{ g L}^{-1}$ for UV 100 titanium dioxide. As depicted in Figures 5.5 and 5.6, the photoactivity of UV 100 titanium dioxide was almost twice as high as that of Degussa P25 titanium dioxide. Cabrera et al. [48] also showed that the photoactivity of UV-100 titanium dioxide is better than that of Degussa P25 titanium dioxide.

The high efficiency for Hombikat UV 100 at high titanium dioxide loadings may be due to its higher specific surface area and therefore site availability (see Table 3.1). Also, higher photoactivity of UV 100 photocatalyst can be explained by the fact that it contains 100% anatase whereas Degussa P25 contains 70% anatase and 30% rutile.

As the loading of titanium dioxide reaches an optimal level, the efficiency of both photocatalysts remains constant up to a certain loading. Figures 5.3 and 5.4 also show that the degradation curves are getting closer. This phenomenon can be explained by the hydrodynamic behavior of the slurry in the

photoreactor. As the loading of titanium dioxide increases, the transparent layer close to the walls of the photoreactor becomes narrower, i.e., the depth of the light penetration decreases. This results in decreasing illuminated slurry volume at high TiO_2 loadings. Therefore, the compensating effect of more surface area is no longer able to make up for rapidly reducing illuminated slurry volume. This transparent layer will shrink by increasing the slurry loading up to a point that the slurry is becoming very viscous. The efficiency of the photocatalysts drops and therefore, the degradation rates dramatically decrease. At the extreme, the reaction ceases entirely.

With different photoreactor geometries, similar behavior was observed for both photocatalysts by Lindner et al. [127]. By estimating photonic efficiency, Lindner et al. [127] showed that the maximum photonic efficiency obtained by Hombikat UV 100 was about four times higher than that of Degussa P25 titanium dioxide. The same photocatalysts were used in Lindner's research [127] as in this study.

To better understand the behavior of the system for different photocatalysts, a series of experiments was carried out to examine the extinction and transmittance of light through the photoreactor. These experiments were performed at a wavelength of 350 nm, that being the wavelength of maximum emission from the UV lamps. Different titanium dioxide slurries were prepared for both photocatalysts in a 500-mL beaker. Immediately prior to the precipitation of the particles in the beaker, the samples taken from the beakers were analyzed using a UV spectrophotometer. Extinction and transmittance for different samples were measured at 350 nm in a 1 cm cell

(Figure 5.7).

As illustrated in Figure 5.7, Degussa P25 titanium dioxide absorbs almost all light going through the photoreactor. Therefore, the light transmittance is negligible. On the other hand, light extinction in Hombikat UV 100 titanium dioxide rises as the loading of the slurry increases. This increase in extinction continues to a loading of about 2.0 g L^{-1} , while transmittance also drops to zero at the same loading.

Lewis and Rosenbluth [123] noted that for sufficiently small particles, the band structure will not be developed completely. Therefore, the continuum of levels is not approximated by the orbitals in any given band and therefore, the electronic absorption is affected by the change of energy distribution. Figure 5.7 supports this theoretical phenomenon. For lower loadings of titanium dioxide ($[\text{TiO}_2] < 2 \text{ g L}^{-1}$), light extinction at 350 nm by UV 100 photocatalyst was significantly less than that by Degussa P25.

In the case of UV 100 photocatalyst, the small particles ($< 10 \text{ nm}$) resulted in a blue-shifted absorption spectrum and therefore, higher photocatalyst loading was needed in order to achieve higher particle size by agglomeration and therefore, higher light absorption. A secondary agglomeration with $1 \mu\text{m}$ diameter particles for UV 100 is reported [127].

The optimum loading of Degussa P25 was found to be 1.5 g L^{-1} and for Hombikat UV 100 between $3.0\text{-}4.0 \text{ g L}^{-1}$ (see Figures 5.6 and 5.6). Lindner et al. [127] found that the optimum loading for P25 titanium dioxide was 0.5 g L^{-1} while for Hombikat UV 100 titanium dioxide, it was 5.0 g L^{-1} . This discrepancy could be due to differences in reactor geometries and the model

compound employed. Lindner et al. [127] used dichloroacetate (DCA) as the model compound.

Figures 5.8 through 5.10 compare the photocatalytic degradation of 1,4-dioxane at low, high, and optimum loadings of titanium dioxide, respectively. At low loadings (0.5 g L^{-1}) of titanium dioxide, the degradation rate of 1,4-dioxane for the P25 photocatalyst is significantly higher than that of UV 100 photocatalyst (see Figure 5.8). This trend is reversed at higher loadings (4.0 g L^{-1}) of titanium dioxide (see Figure 5.9) in which the degradation rate of 1,4-dioxane is higher with Hombikat UV 100 photocatalyst than with Degussa P25 titanium dioxide. Figure 5.10 shows that at optimum loading for both photocatalysts, the degradation rate for Hombikat UV 100 seems slightly higher than that of Degussa P25 titanium dioxide.

5.6 Experimental Procedures for the Kinetic Studies

The kinetic studies began with single component runs (either tetrahydrofuran or 1,4-dioxane) followed by their mixture. The optimum loading of Degussa P25 titanium dioxide (1.5 g L^{-1}) found in Section 5.5 was used in both single and binary system experiments. For all trials, a slurry of titanium dioxide was made based on the procedure explained in Chapter 3.

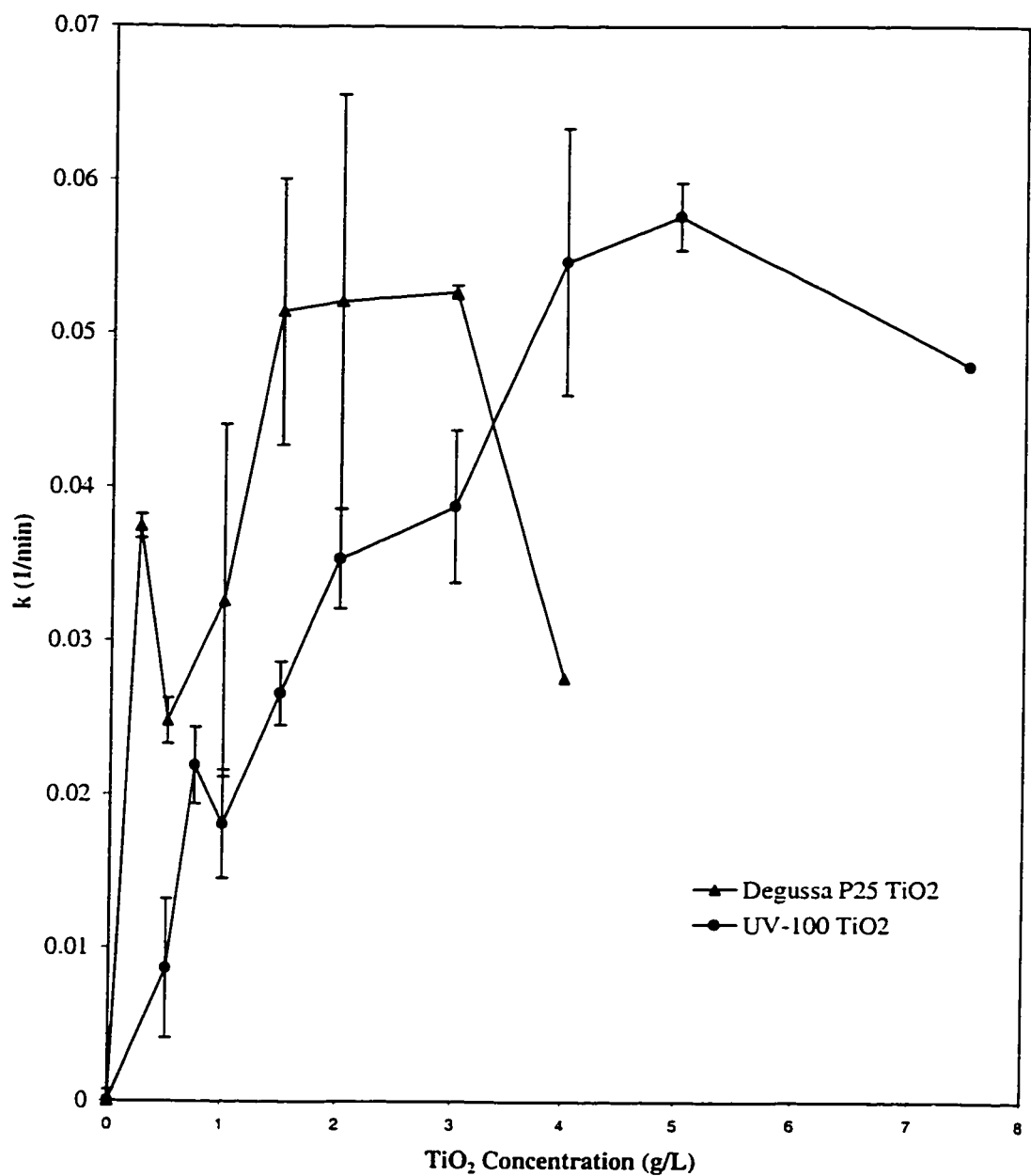


Figure 5.5: Comparison between first order rate constants for UV-100 and Degussa P25 TiO₂ catalysts in the slurry photoreactor for different TiO₂ loadings, $C_{0,DIOX}=27.8 \text{ mg L}^{-1}$. Error bars indicate the 95% confidence intervals.

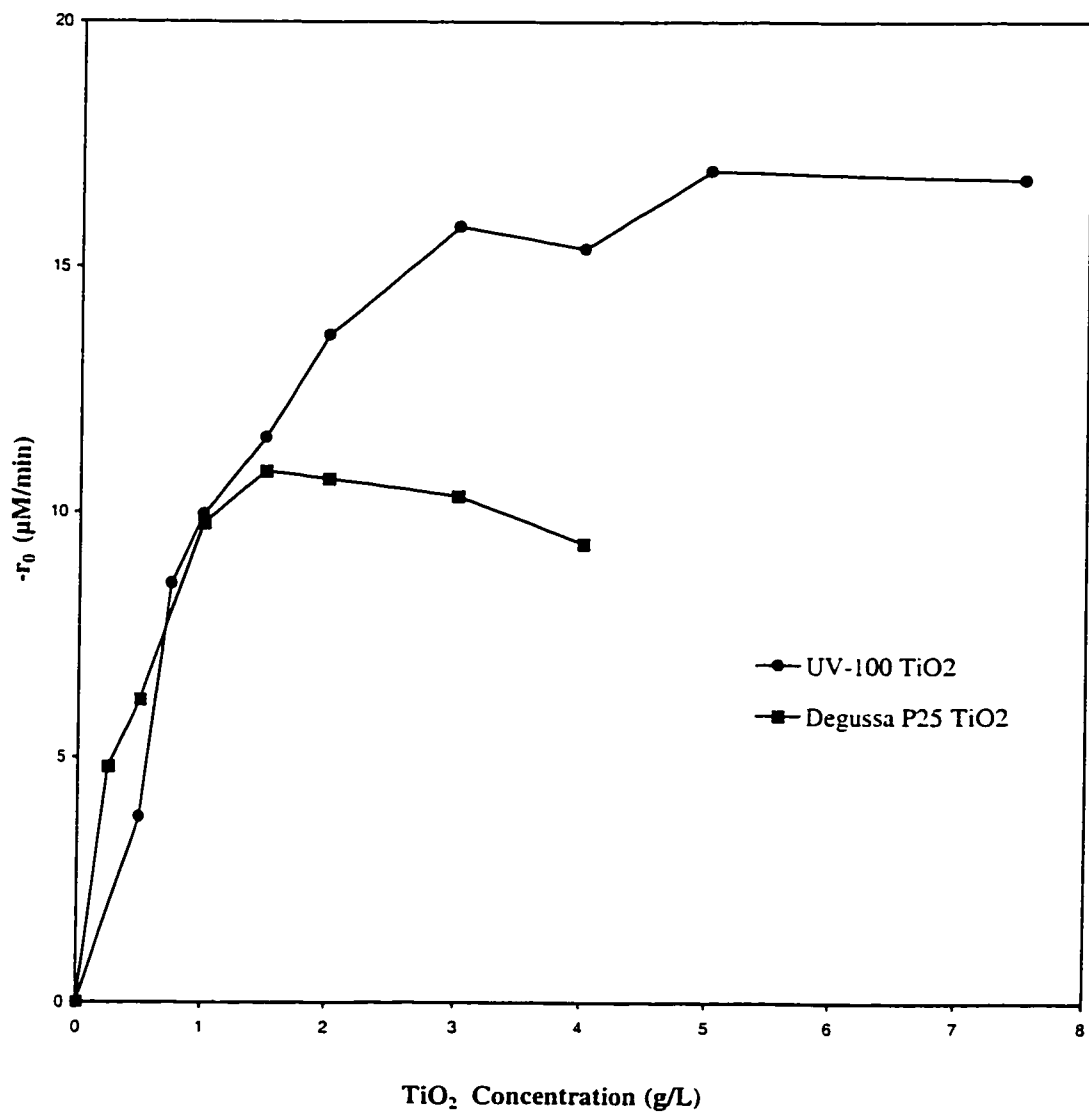


Figure 5.6: Comparison between initial rates for UV-100 and Degussa P25 TiO_2 catalysts in the slurry photoreactor for different TiO_2 loadings, $C_{0,DIOX}=27.8 \text{ mg L}^{-1}$.

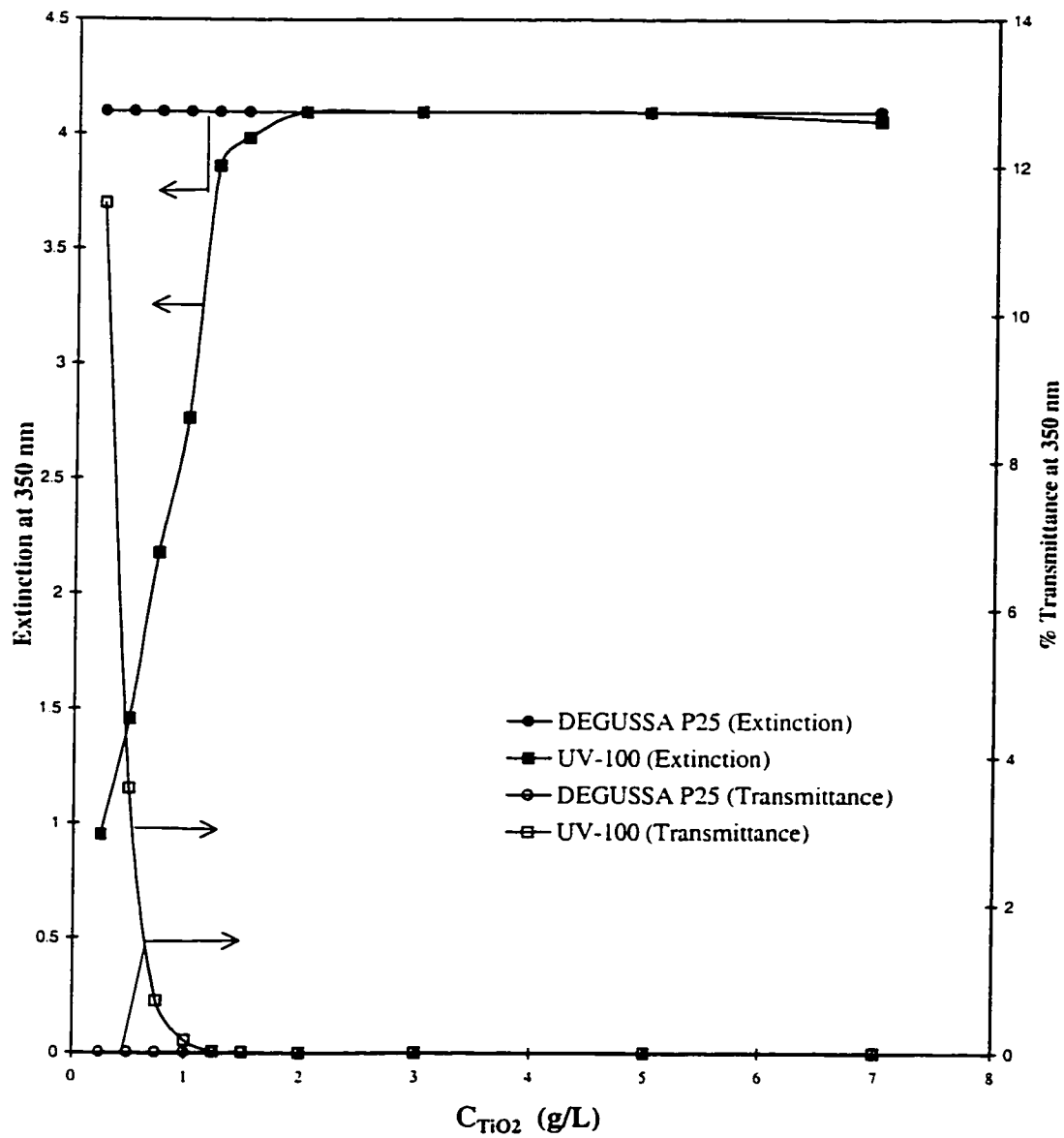


Figure 5.7: Light extinction and transmittance at 350 nm for different TiO₂ slurry solutions in a 1 cm cell.

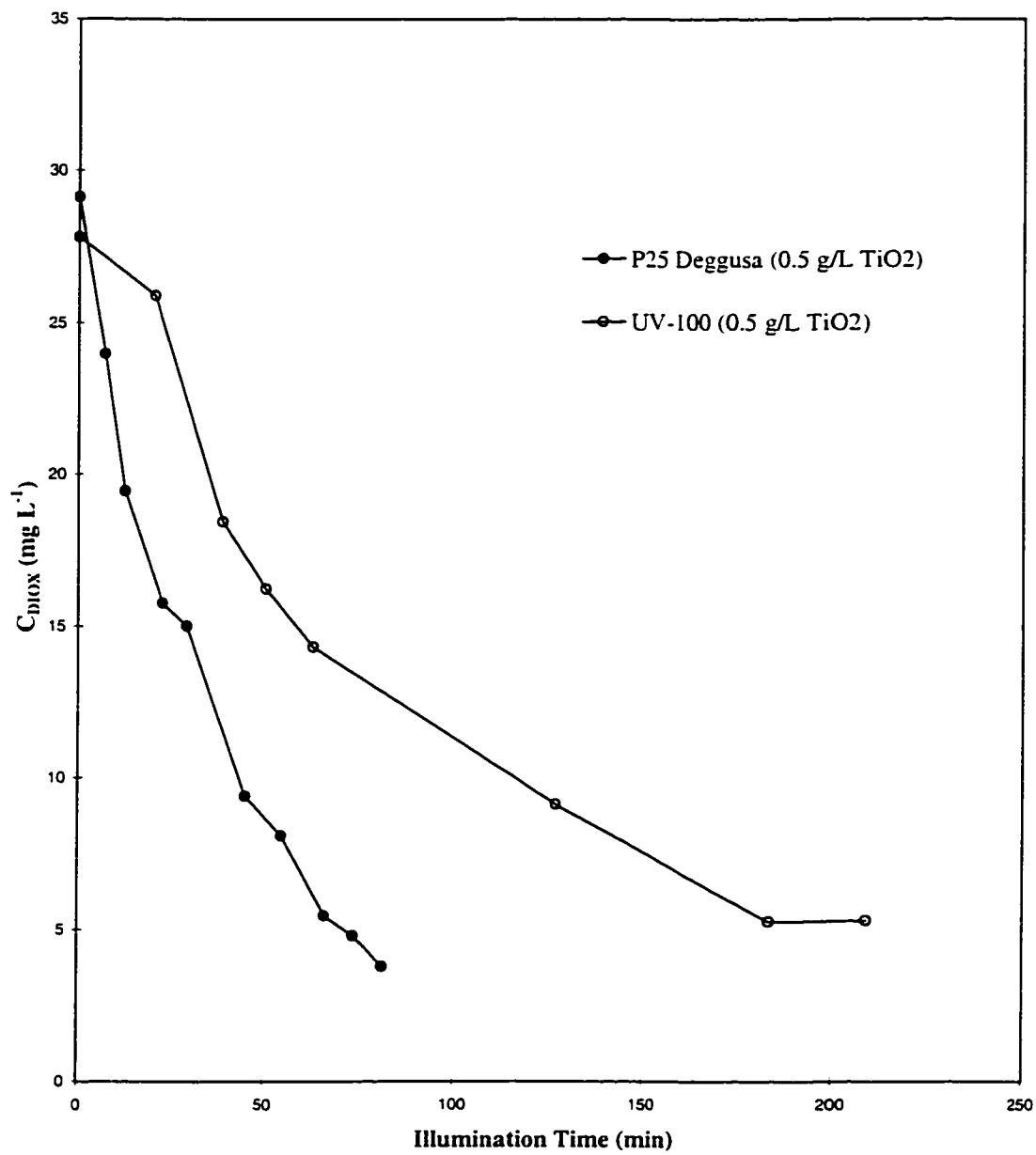


Figure 5.8: Comparison between UV-100 and Degussa P25 TiO₂ photocatalysts in the slurry photoreactor at low TiO₂ loading, [TiO₂]=0.5 g L⁻¹ and C_{0,DIOX}=27.8 mg L⁻¹.

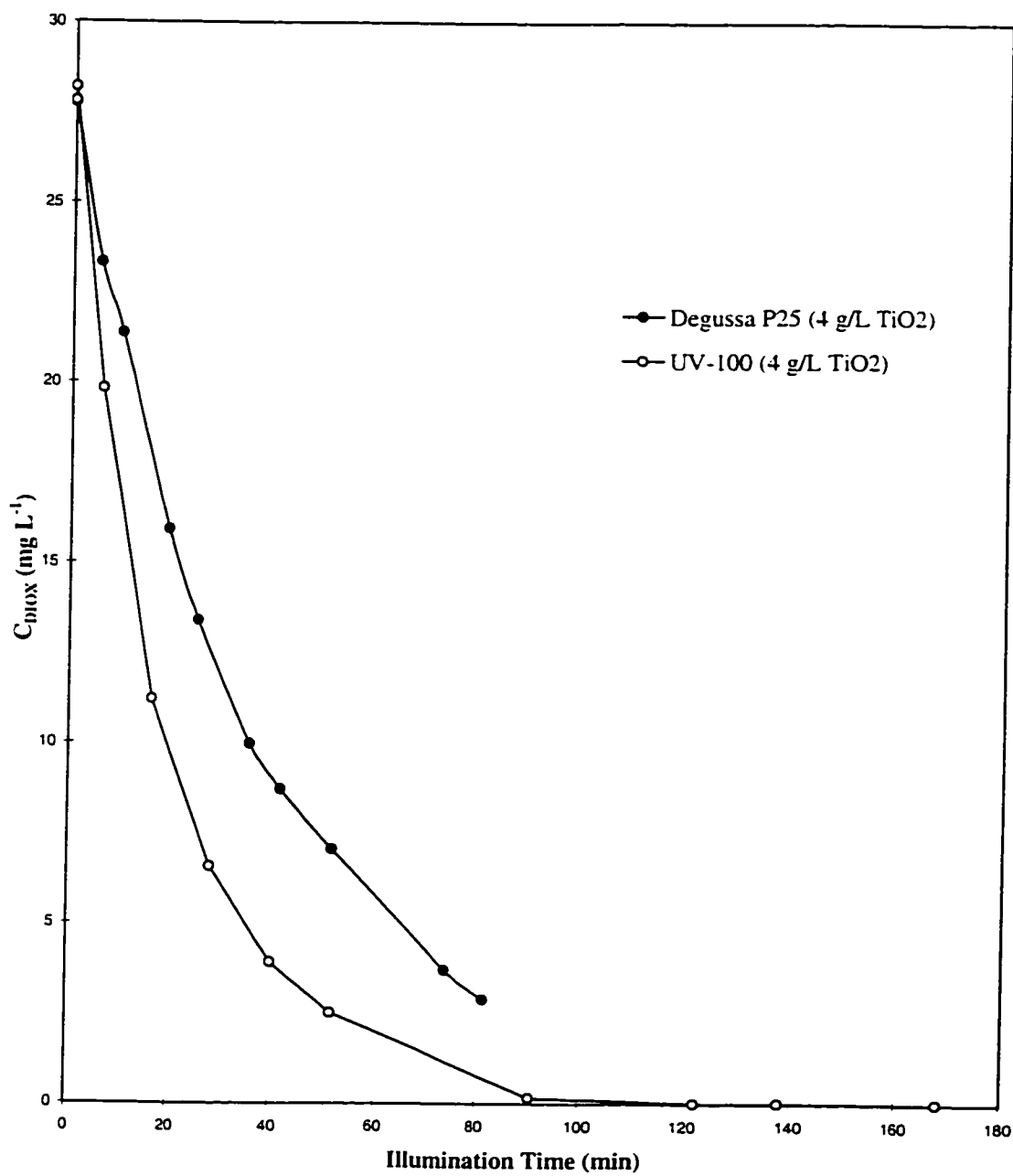


Figure 5.9: Comparison between UV-100 and Degussa P25 TiO₂ photocatalysts in the slurry photoreactor at high TiO₂ loading, [TiO₂]=4.0 g L⁻¹ and C_{0,DIOX}=27.8 mg L⁻¹.

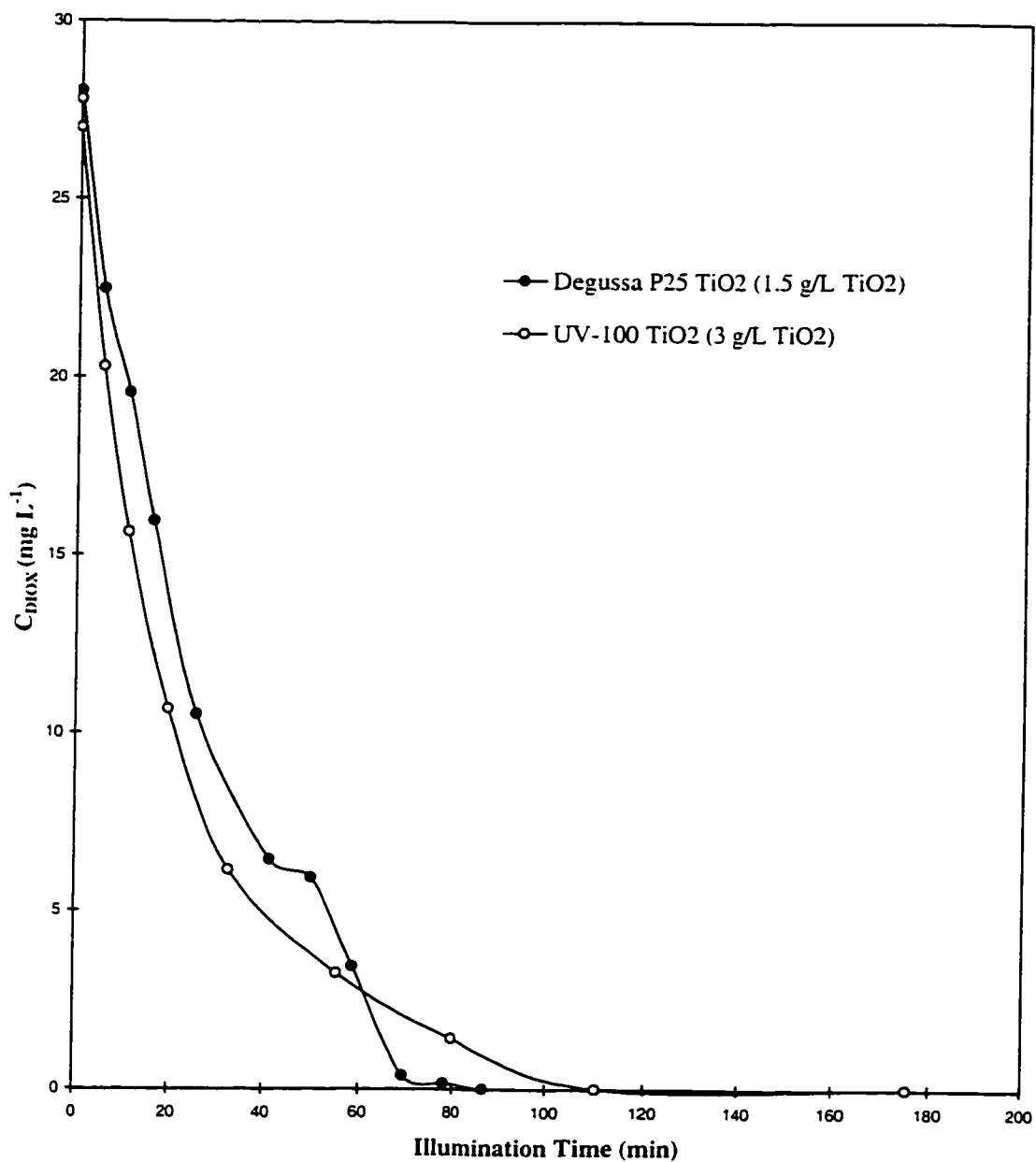


Figure 5.10: Comparison between UV-100 and Degussa P25 TiO₂ photocatalysts for the photocatalytic degradation of 1,4-dioxane in the slurry photoreactor at the optimum TiO₂ loadings, $C_{0,DIOX}=27.8 \text{ mg L}^{-1}$.

5.7 Reaction Mechanisms for the Photocatalytic Degradation of THF and DIOX

In this section, the reaction mechanisms for the photocatalytic degradation of tetrahydrofuran and 1,4-dioxane are proposed based on analyses from experimental trials and basic principles of photocatalysis. Using experimental data and the reaction mechanisms proposed in this section, the kinetic models are developed.

5.7.1 Photocatalytic Reaction Mechanisms for THF

The intermediates produced during the photocatalytic degradation of tetrahydrofuran are speculated based on analyses from experimental runs. The photocatalytic reaction of tetrahydrofuran along different reaction pathways is proposed.

5.7.1.1 GC/MS Results for THF Degradation

Different samples were taken during the experimental trials and stored in 5-mL vials for the purpose of GC/MS analyses (see details in Chapter 3).

Since the samples contained more than 99.9% water, it was impossible to inject the samples directly for GC/MS analyses. Methods of extraction, such as liquid-liquid solvent extraction using hexane, failed due to low organic concentrations as well as high solubilities of the compounds of interest.

Although the pH and ionic strength of the solvent extraction was adjusted using HCl and KCl, this method still failed.

The viability of Solid Phase MicroExtraction (SPME) was investigated in which the proper fiber was chosen to detect different organics that may be present in the samples (see Chapter 3 for details). This method was verified by analyzing known organic solutions such as tetrahydrofuran and 1,4-dioxane. Samples from different runs at different times were analyzed and the results obtained were very consistent and reproducible. As presented before [151, 150], the intermediates in the photocatalytic degradation of THF detected by GC/MS and ion chromatography are summarized in Table 5.2. A few intermediates that have not been detected but are believed to exist are also listed. Figure 5.11 depicts the molecular structures of tetrahydrofuran and all of possible intermediates.

5.7.1.2 Ion Chromatography Results for THF Degradation

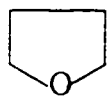
Recall in Reaction (2.12) of Chapter 2 that organic acids are important intermediates produced during photocatalytic reactions. Therefore, identification of these intermediates helps to achieve a better understanding of the mechanism of the photocatalysis processes.

In this section, the results of the ion chromatography (IC) analyses for the photocatalytic degradation of tetrahydrofuran are discussed. The basic principles of ion chromatography were explained in Chapter 3. Based on these results, organic acid intermediates during the photocatalytic degradation of THF are deduced.

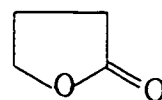
Table 5.2: Possible intermediates for the photocatalytic degradation of tetrahydrofuran.

INTERMEDIATE	DETECTION METHOD	CAS No. ¹	GC/MS PROBABILITY (%)
2(3H)-Furanone, dihydro- (γ -Butyrolactone)	GC/MS	96-48-0	90
Succinic acid	GC/MS	110-15-6	78
Acetic acid	GC/MS & IC	64-19-7	80
Formic acid	IC	64-18-6	N/A
β -Hydroxybutyric acid	IC	625-71-8	N/A
Glycolic acid	IC	79-14-1	N/A
2-Hydroxytetrahydrofuran	Not Detected	5371-52-8	N/A
Dihydro-5-hydroxy-2(3H)-furanone	Not Detected	50768-69-9	N/A
4-Oxobutanoic acid	Not Detected	692-29-5	N/A

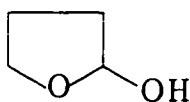
¹ Chemical Abstract Service Number



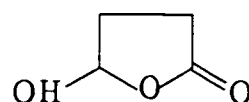
Tetrahydrofuran



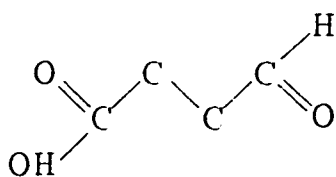
γ -Butyrolactone



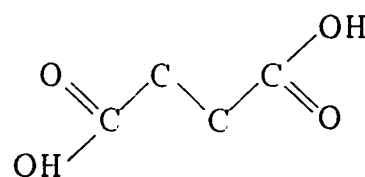
2-Hydroxytetrahydrofuran



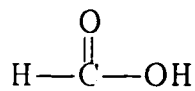
Dihydro-5-hydroxy-2(3H)-furanone



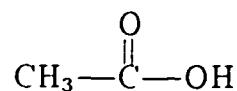
4-Oxobutanoic acid



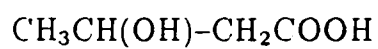
Succinic acid



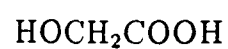
Formic acid



Acetic acid



β -Hydroxybutyric acid



Glycolic acid

Figure 5.11: Molecular structures of tetrahydrofuran and its possible intermediates in the photocatalysis of tetrahydrofuran.

The ion chromatography analysis was based on the method developed by Peldszus et al. [172]. According to this method some carboxylic acids, including hydroxy- or oxo- substituted acids, such as β -hydroxybutyric, acetic, glycolic, butyric, formic, α -ketobutyric, and pyruvic acid could be identified even at low $\mu\text{g L}^{-1}$ concentrations. Although not all of these organic acids are expected in our case study, this method is capable of identifying the compounds of interest.

A standard solution of the seven organic acids mentioned above, each at a concentration of $50 \mu\text{g L}^{-1}$, was made. Tap water was used in preparing the standard solution. Figure 5.12 depicts the standard IC chromatograph for the organic acids. Note that some inorganic salts of the most common anions were added.

Figure 5.13 shows the results of a sample taken from one of the THF runs with an initial THF concentration of 1.25 mM. The sample was withdrawn from the photoreactor at 940 min actual run time (510.3 min illumination time). All of the parent compound, THF, and some of its intermediates, especially GBL, had disappeared by this time. However, formic acid is one of the major organic acids detected in the sample. The first peak in Figure 5.13 is postulated to be acetic acid which is another major organic acid detected in the THF sample using GC/MS analysis method. Acetic acid in the standard chromatograph in Figure 5.12 eluted at a retention time of about 11 min while formic acid eluted at 15 min. The slight differences in retention times of the same organic acids in the standard versus the sample may be due to differences in ionic strength and the type of water employed. The water used

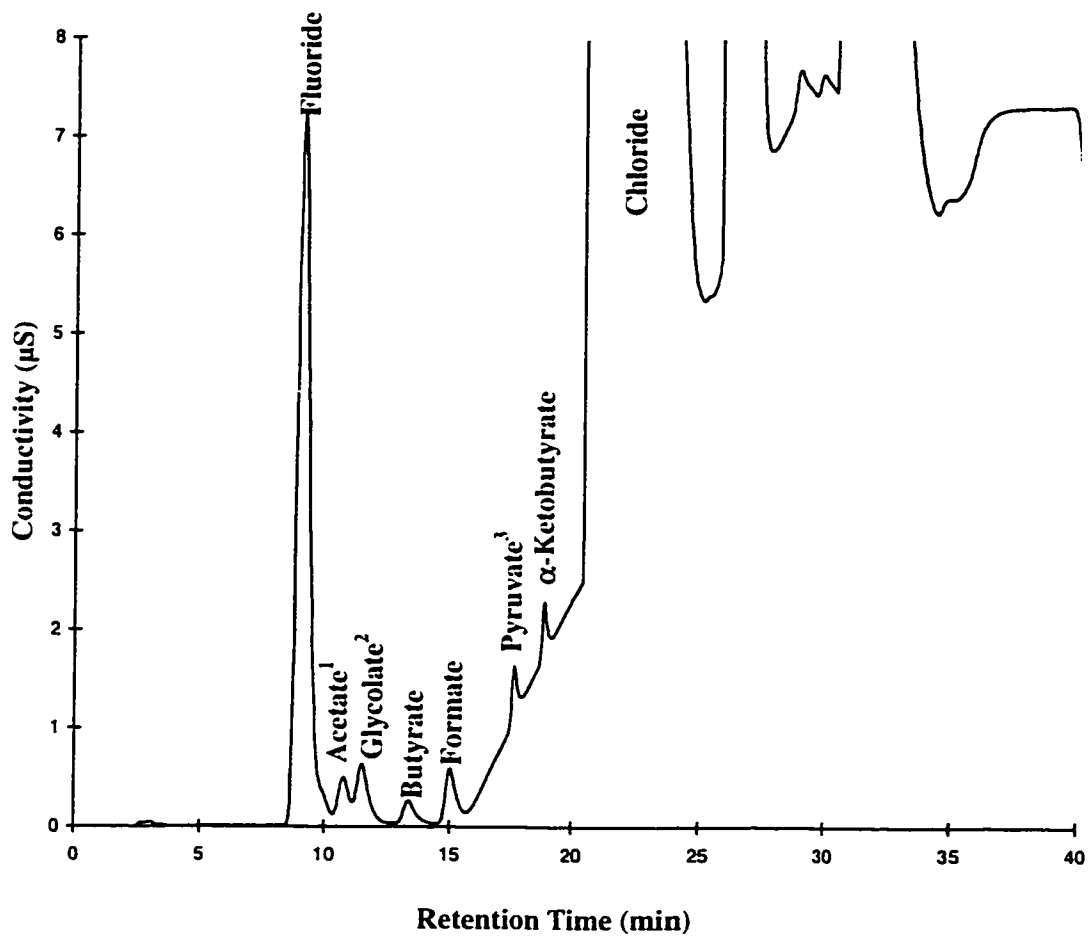


Figure 5.12: Typical Ion Chromatogram of standard solution containing organic acids at $50 \mu\text{g L}^{-1}$ concentration in tap water; superscripts indicate coelution: 1. with lactate and glycerate. 2. with propionate. 3. with oxalacetate.

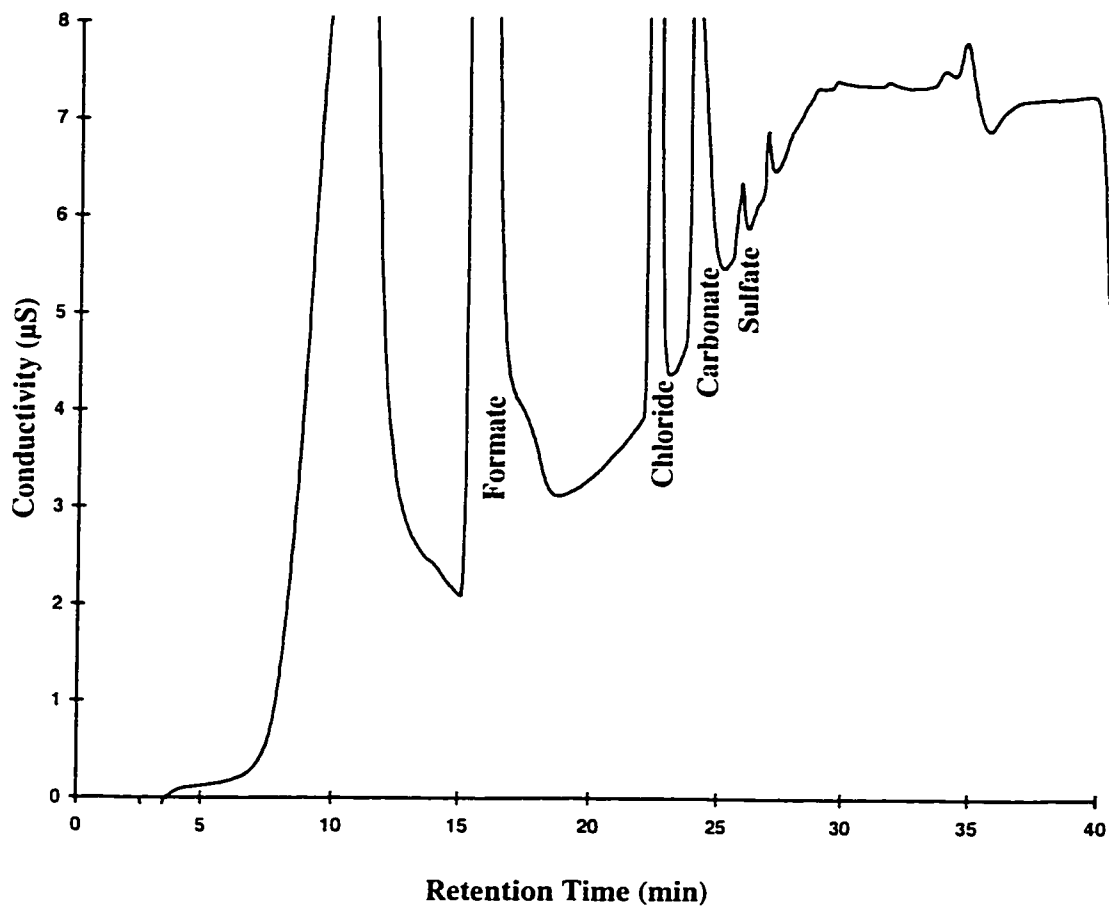


Figure 5.13: Typical Ion Chromatogram of sample taken from photocatalytic reaction of tetrahydrofuran.

for the standard was tap water whereas filtered deionized water was utilized in the experimental runs from which samples were taken.

By comparing Figures 5.12 and 5.13, the difference in the peak shapes indicates that the amount of acetic acid and formic acid present in the sample was in the range of mg L^{-1} . Acetic acid was also detected by GC/MS. Since the first peak in Figure 5.13 is broad, other organic acids such as β -hydroxybutyric acid and glycolic acid may coelute with acetic acid. Therefore, these two organic acids, β -hydroxybutyric acid and glycolic acid, might also be considered as THF intermediates.

5.7.1.3 THF Reaction Mechanisms

Identification of the intermediates in the photocatalytic degradation of THF leads us to propose a degradation pathway. Referring to the general pattern of the photocatalysis processes, Equation (2.12), a photocatalysis process may produce aldehydes, alcohols, carboxylic acids, and other hydroxylated compound intermediates. These, in turn, are attacked by hydroxyl or other active radicals. The hypothetical reaction pathways for the photocatalytic degradation of tetrahydrofuran are depicted in Figure 5.14.

In this mechanism, tetrahydrofuran is readily oxygenated to γ -butyrolactone. γ -Butyrolactone, in turn, is attacked by a hydroxyl radical, $\bullet\text{OH}$, produced during the illumination of the titanium dioxide. Succinic acid and other organic acids such as formic and acetic acids are produced during the process, which are then eventually converted to CO_2 . The details of the reaction mechanisms are discussed below:

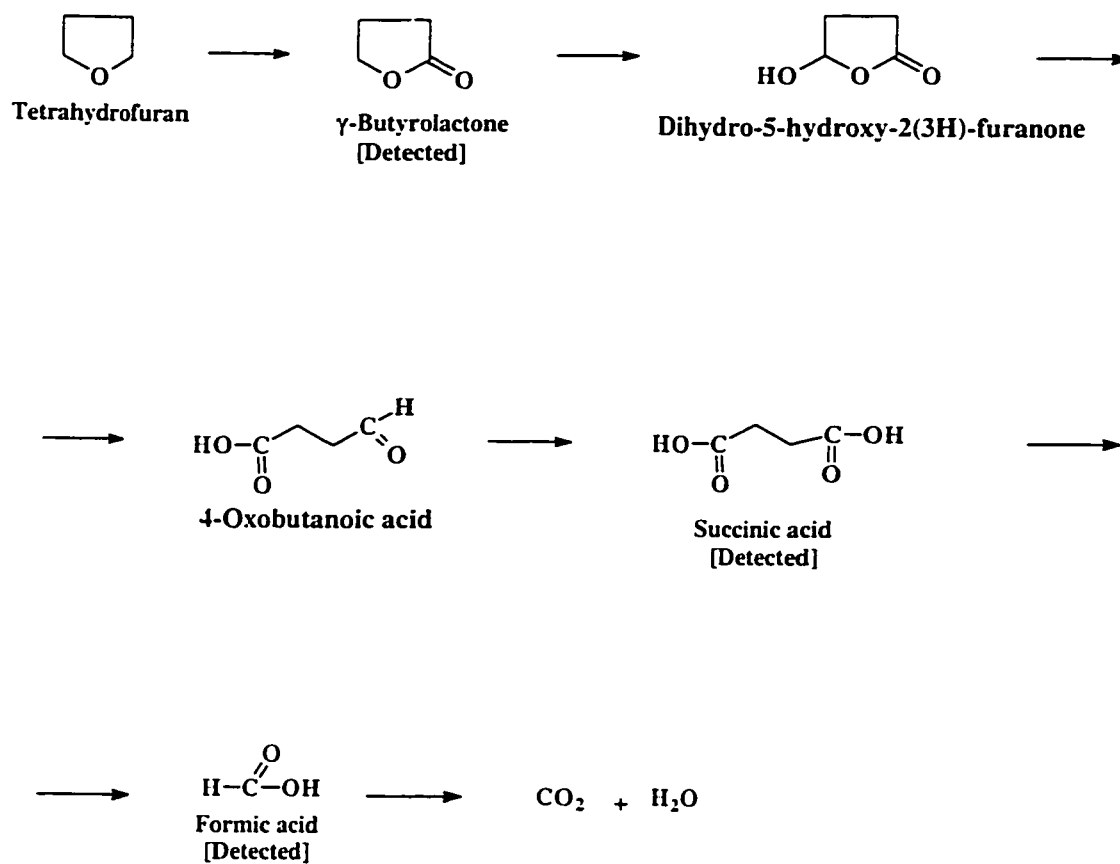


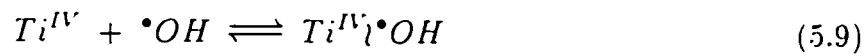
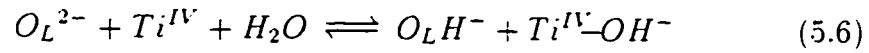
Figure 5.14: Proposed reaction mechanism for the photocatalytic degradation of tetrahydrofuran.

Turchi [213] summarized the general reactions occurring in all photocatalysis processes (see Reactions (5.5) through (5.17)). Any photocatalysis process has four major steps. In the excitation step, illumination of the photocatalyst with an energy bandgap greater than the semiconductor bandgap, causes separation of electrons resulting in the production of holes (Reaction (5.5)). During the adsorption process (see Reactions (5.6)–(5.9)), water is adsorbed onto the catalyst surface and after ionization, produces hydroxyl radicals. These hydroxyl radicals can migrate in the vicinity of the photocatalyst surface into the bulk phase in the form of an equilibrium reaction, as shown in Reaction (5.9). At this stage, organic compounds are also adsorbed onto the photocatalyst surface. Organic species are attacked by hydroxyl radicals either on the surface or in the bulk phase. One of the disadvantages of the photocatalysis process is its low efficiency due to the recombination of the separated electrons and holes as depicted in Reaction (5.10). In the trapping step, H_2O which is also adsorbed may become oxidized by a hole, h^+ , to produce more hydroxyl radicals. Other radical reactions which are also possible are listed in Reactions (5.15)–(5.17).

Excitation



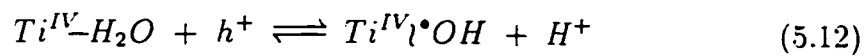
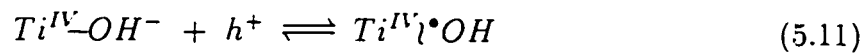
Adsorption



Recombination

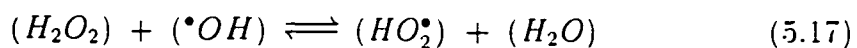
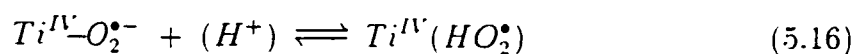
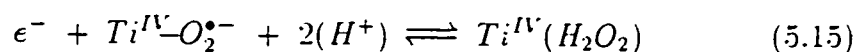


Trapping





Other radical reactions



Potential reaction mechanisms for the degradation of tetrahydrofuran are shown in Reactions (5.18) through (5.32). Since reaction mechanisms in photocatalysis are very complicated, each proposed reaction mechanism in the following may be involved in different intermediate pathways. As a result, only the global reaction mechanism in each step is considered. For example, the production of γ -butyrolactone (GBL) may have several extra steps as shown in Figure 5.15.

After adsorption of THF onto the catalyst surface (Reaction (5.18)), it

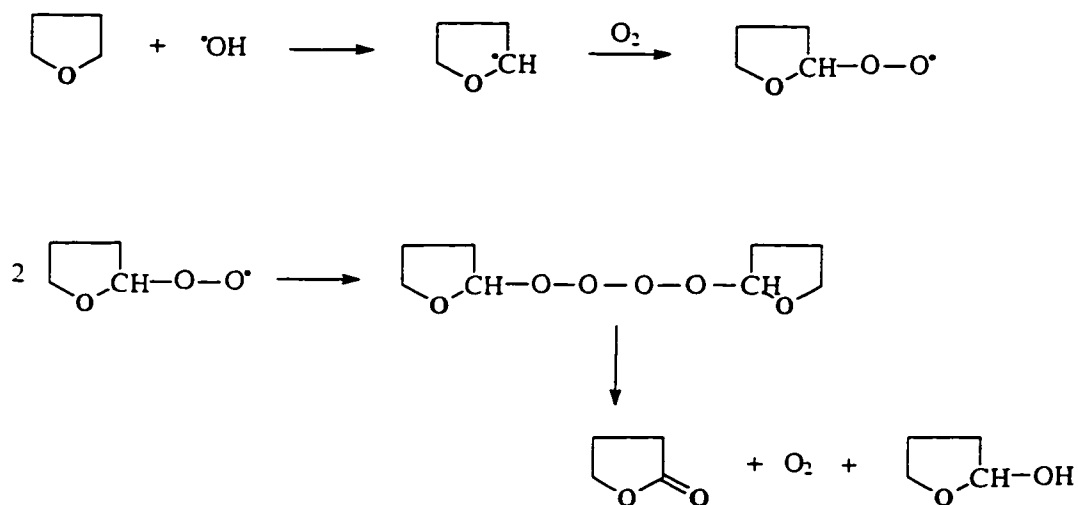
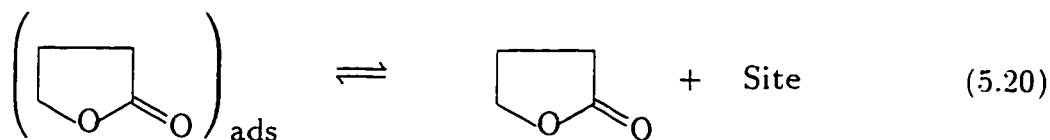
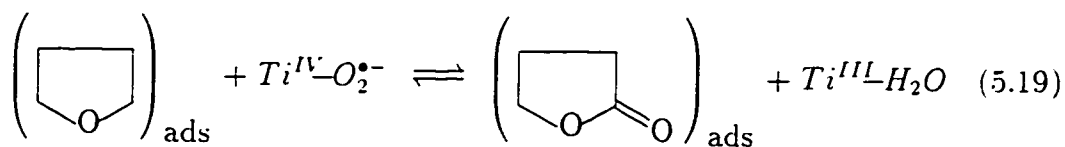
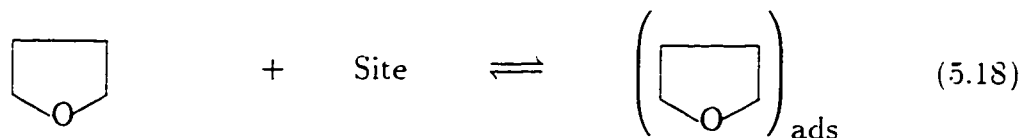
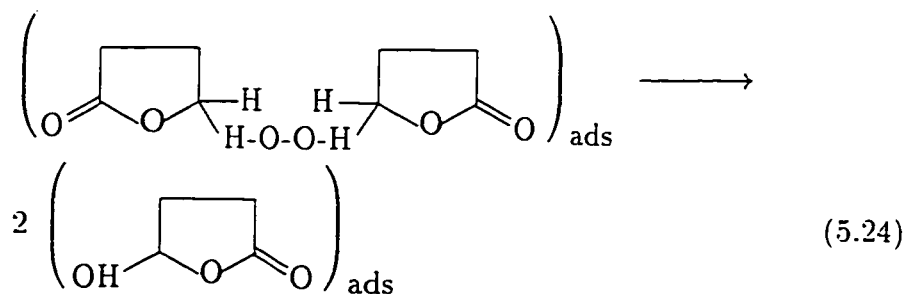
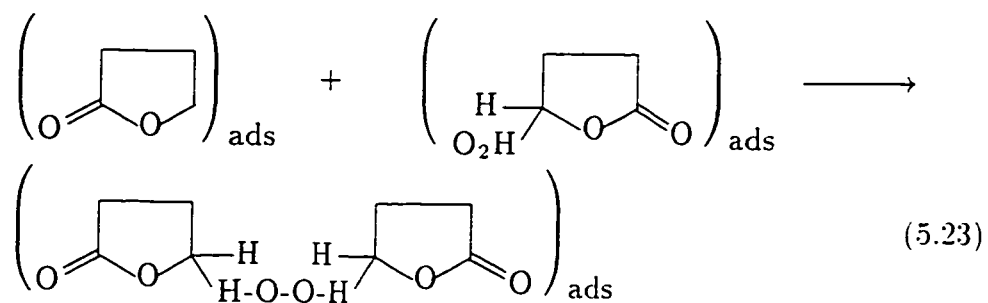
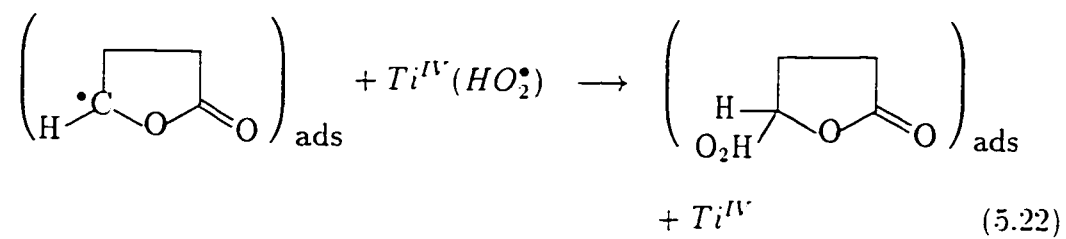
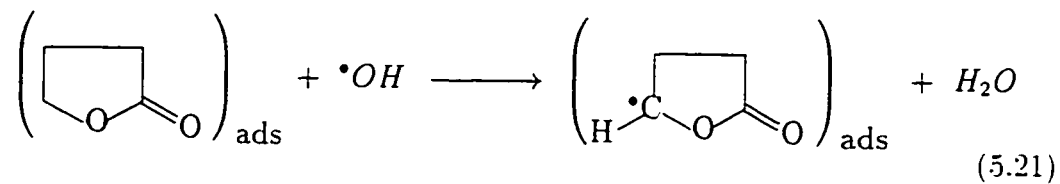


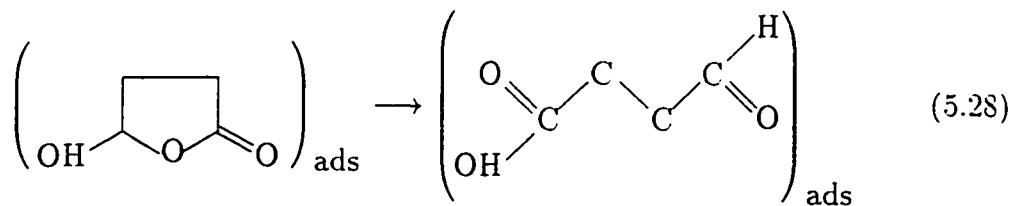
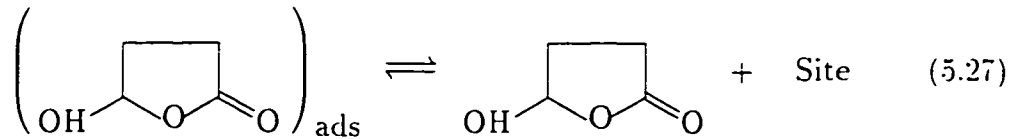
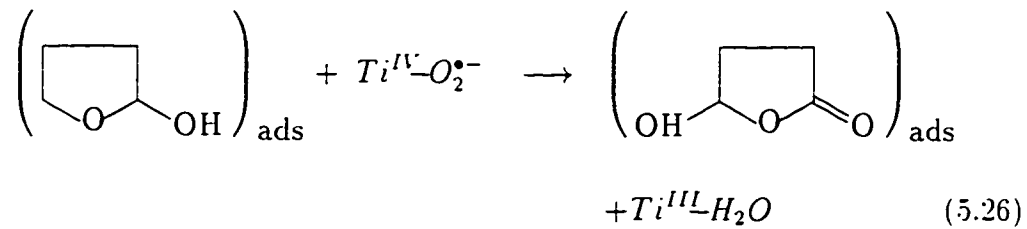
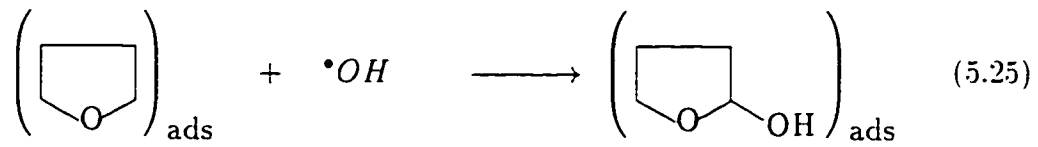
Figure 5.15: Details of the tetrahydrofuran oxidation by hydroxyl radical attack.

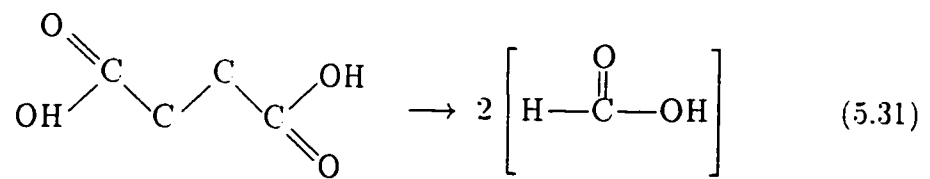
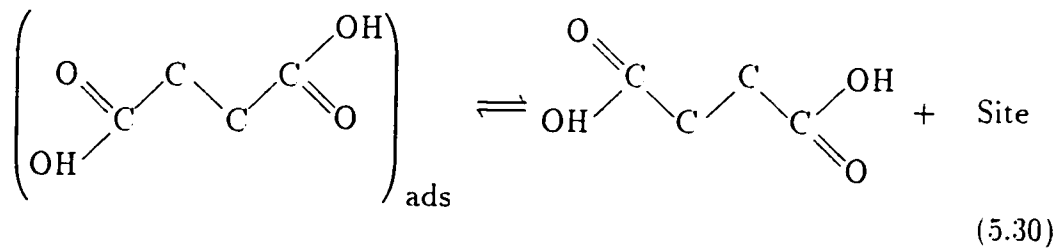
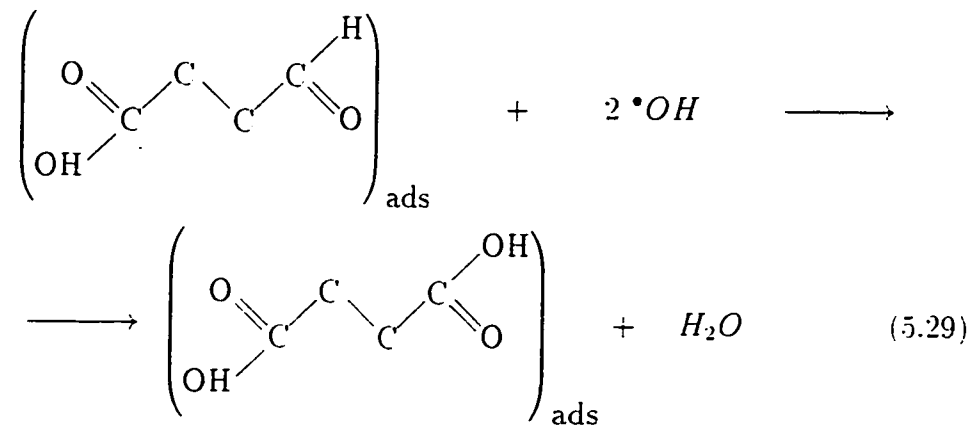
is oxygenated through an adsorbed oxygen, $\text{Ti}^{IV}\text{-O}_2^{\bullet-}$, as shown in Reaction (5.19). During this reaction, γ -butyrolactone is produced as the most significant and measurable intermediate. Adsorbed GBL, in turn, must reversibly desorb and migrate into the bulk phase (see Reaction (5.20)). The detection and, therefore, the measurement of GBL is possible due to its desorption into the liquid bulk phase. Since plentiful hydroxyl radicals are produced during the process, most probably all organic species get attacked by hydroxyl radicals either on the surface of the photocatalyst or in the liquid bulk phase. Hence, adsorbed GBL can react with $\cdot\text{OH}$ to produce 5-hydroxy-2(3H)furanone, dihydro- (see Reactions (5.21) through (5.24)). Alternatively, hydroxyl radicals can attack THF resulting in the formation of 2-hydroxytetrahydrofuran although this species was not detected in this study. Dihydro-5-hydroxy-2(3H)-furanone may also be produced through

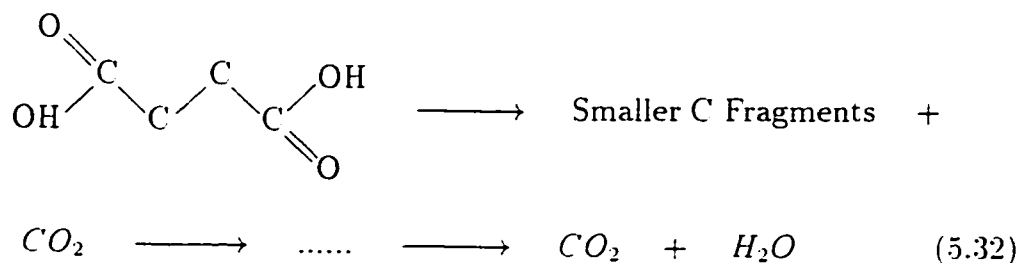
oxygenation of 2-hydroxytetrahydrofuran as shown in Reaction (5.26). This intermediate can also desorb into the liquid phase. Dihydro-5-hydroxy-2(3H)-furanone is unstable whereby the ring opens to produce 4-oxobutanoic acid as another intermediate (see Reaction (5.28)). 4-Oxobutanoic acid is attacked by another hydroxyl radical resulting in the formation of succinic acid. This organic acid was detected in the samples by GC/MS. Succinic acid may desorb into the bulk phase and convert to formic acid (see Reactions (5.30) and (5.31)). The general reaction in which succinic acid breaks down into smaller C fragments is depicted in Reaction (5.32).











5.7.1.4 THF Rate Equations

Based on the reaction mechanisms proposed in Section 5.7.1.3, the rate equations for the photocatalytic degradation of tetrahydrofuran in water were developed.

From Reactions (5.19) and (5.25), the rate of disappearance of adsorbed THF may be written as:

$$-\frac{d[\text{THF}]_{ads}}{dt} = k_{5.19} a_s [\text{THF}]_{ads} [\text{Ti}^{IV}\text{O}_2^{\bullet-}] + k_{5.25} a_s [\bullet\text{OH}] [\text{THF}]_{ads} \quad (5.33)$$

Assuming that Reactions (5.13), (5.14), and (5.18) quickly approach equilibrium, the following equations can be derived:

$$[\text{Ti}^{III}] = K_{5.13} [\text{Ti}^{IV}] [\epsilon^-] \quad (5.34)$$

$$[Ti^{IV}-O_2^{\bullet-}] = K_{5.14}[Ti^{III}][O_2] \quad (5.35)$$

$$[THF]_{ads} = K_{5.18}[Site][THF] \quad (5.36)$$

By substituting Equation (5.34) into Equation (5.35) and considering that $[e^-] = [h^+]$, the concentration of the titanium dioxide radical, $[Ti^{IV}-O_2^{\bullet-}]$, is simplified as follows:

$$[Ti^{IV}-O_2^{\bullet-}] = K_{5.13}K_{5.14}[Ti^{IV}][h^+][O_2] \quad (5.37)$$

By combining Equations (5.33), (5.36), and (5.37), the following reaction rate for THF may be derived.

$$\begin{aligned} -\frac{d[THF]}{dt} = & \frac{k_{5.19} + K_{5.13}K_{5.14}a_s}{K_{5.18}[Site]} [Ti^{IV}][h^+][O_2][THF]_{ads} \\ & + \frac{k_{5.25}a_s}{K_{5.18}[Site]} [\bullet OH][THF]_{ads} \end{aligned} \quad (5.38)$$

The pH throughout all experimental runs was monitored and found to be 4 ± 0.5 . The pH did not change significantly during any experiments. Considering the low pH range for the runs, Reaction (5.12) is more likely to proceed than Reaction (5.11) under these conditions. Using this assumption and by applying steady state approximation method for the $\bullet OH$ concentration at low pH, the following rate equation can be derived:

$$\begin{aligned}
\frac{d[\bullet OH]}{dt} = & \alpha k_{5.12+} [Ti^{IV}-H_2O] [h^+] a_s - k_{5.12-} a_s [Ti^{IV}\{\bullet OH\}] [H^+] \\
& - k_{5.25} a_s [\bullet OH] [THF]_{ads} - k_{5.21} a_s [\bullet OH] [GBL]_{ads} \\
& - \sum_{j=3}^n k_j [\bullet OH] [R_{j,ads}] a_s \approx 0
\end{aligned} \tag{5.39}$$

where j = the other components which are attacked by hydroxyl radicals: in this case $j \neq THF$ & GBL ;

n = the total number of different organic species present in the system;

α = the proportionality constant;

$[H^+] = 10^{-pH}$;

a_s = particle surface area, $[m^2]$.

GC analyses revealed that the concentrations of certain intermediates were either not measurable or present at very low concentration levels. Therefore, the last term in Equation (5.39), which is related to the other intermediates with relatively low concentrations, can be assumed to be negligible.

As shown by other researchers [212, 213], hole trapping is the most probable source of hydroxyl radical generation. Therefore, Reactions (5.12+) and (5.9-) together are the possible mechanisms for producing the hydroxyl radicals. Reaction (5.9) will be used to determine the adsorption constant as follows:

$$[Ti^{IV}\{\bullet OH\}] = K_{5.9} [Ti^{IV}] [\bullet OH] \tag{5.40}$$

As pH does not fluctuate during the course of the reaction, $[H^+]$ can

be assumed to be constant. The $[Ti^{IV}-H_2O]$ is the surface concentration of bound H_2O at low pH and is assumed to remain relatively constant.

By considering these assumptions and substituting Equation (5.40) into Equation (5.39), the hydroxyl radical concentration is simplified as follows:

$$[{}^{\bullet}OH] = \frac{\alpha k'_{5.12+}[h^+]}{k'_{5.12-} K_{5.9}[Ti^{IV}] + k_{5.25}[THF]_{ads} + k_{5.21}[GBL]_{ads}} \quad (5.41)$$

where $k'_{5.12-} = k_{5.12-}10^{-pH}$;

$$k'_{5.12+} = k_{5.12+}[Ti^{IV}-H_2O].$$

Similarly using the steady state approximation, the hole concentration, $[h^+]$, at high photon flux can be simplified as follows:

$$[h^+] = \left(\frac{k_{5.5} I a_c}{k_{5.10} \nu_p} \right)^{1/2} \quad (5.42)$$

where $I =$ Molar photon flux. $[Einstein\ m^{-2}\ s^{-1}]$;

$\nu_p =$ Particle volume. $[m^3]$;

$a_c =$ Titanium dioxide particle area normal to illumination. $[m^2]$.

The kinetic rate equation for GBL can be written as follows:

$$\frac{d[GBL]}{dt} = k_{5.19+} a_s [THF]_{ads} [Ti^{IV}-O_2^{\bullet-}] - k_{5.21} a_s [{}^{\bullet}OH][GBL]_{ads} \quad (5.43)$$

By substituting Equations (5.41) and (5.42) into Equations (5.38) and (5.43), the final dynamic model for THF considering GBL as its major kinetic

intermediate is as follows:

$$-\frac{d[THF]}{dt} = k_{app}[THF] + \frac{k_{THF}K_{THF}[THF]}{1 + K_{THF}[THF] + K_{GBL}[GBL]} \quad (5.44)$$

$$\frac{d[GBL]}{dt} = k_{app}[THF] - \frac{k_{GBL}K_{GBL}[GBL]}{1 + K_{THF}[THF] + K_{GBL}[GBL]}$$

where:

$$k_{app} = k_{5.19+} K_{5.13} K_{5.14} a_s [Ti^{IV}] [O_2] \left(\frac{k_{5.5} I a_c}{k_{5.10} \nu_p} \right)^{1/2} \quad (5.45)$$

$$k_{THF} = \frac{\alpha k'_{5.12+} a_s \left(\frac{k_{5.5} I a_c}{k_{5.10} \nu_p} \right)^{1/2}}{K_{5.18} [Site]} \quad (5.46)$$

$$k_{GBL} = \alpha k'_{5.12+} a_s \left(\frac{k_{5.5} I a_c}{k_{5.10} \nu_p} \right)^{1/2} \quad (5.47)$$

$$K_{THF} = \frac{k_{5.25} K_{5.18} [Site]}{k'_{5.12-} K_{5.9} [Ti^{IV}]} \quad (5.48)$$

$$K_{GBL} = \frac{k_{5.21} [Site]}{k'_{5.12-} K_{5.9} K_{5.20} [Ti^{IV}]} \quad (5.49)$$

Equations (5.44) together construct a simplified dynamic model of the kinetic rate equations for the photocatalytic degradation of THF in water. These two equations must be solved simultaneously in order to estimate the

parameters. Applying experimental data for different trials and using the statistical method outlined in Chapter 4, the best point estimate kinetic parameters in the dynamic model for THF may be computed.

Although, the kinetic rate equations were derived on the assumption that adsorbed organic compounds react with the hydroxyl radicals in the bulk phase, similar results may be obtained if other cases in Section 2.3.4 are considered. In these cases, the parameters may differ slightly.

In comparison to the LH model described in Equation (2.18), it can be seen that Equation (5.44) has one extra term. Although the model is LH, a first order term for THF has been obtained in the derivation of these equations. Depending on the nature of the compounds and their reaction pathways, the LH model may be modified. In this case since THF is oxygenated through the adsorbed oxygen to produce GBL, this extra term appears. This means that the disappearance of THF is either a consequence of the attack by hydroxyl radicals (Reaction (5.25)) or due to oxidation of THF by adsorbed oxygen (Reaction (5.19)). On the other hand, Turchi [213] in his derivations assumed that the disappearance of organics is solely due to hydroxyl radical attacks. Experimental results also support the validity of the proposed model for the photocatalytic degradation of tetrahydrofuran as well as the mixture of THF and DIOX.

5.7.2 Photocatalytic Reaction Mechanisms for DIOX

Intermediates found during the photocatalytic destruction of 1,4-dioxane are presented in this section. Reaction mechanisms and pathways are pro-

posed based on these observations. As with THF, two analytical methods, GC/MS and IC, were performed in order to identify DIOX intermediates.

5.7.2.1 GC/MS Results for DIOX Degradation

GC/MS analyses for DIOX were performed similar to those done for THF analyses. As presented before [151, 150], Table 5.3 summarizes the results of possible intermediates identified for DIOX by both analytical procedures. The molecular structure of 1,4-dioxane and all of its possible intermediates are illustrated in Figure 5.16.

1,2-Ethanediol, diformate (EDD) was one of the significant intermediates detected in the photocatalytic mineralization of DIOX. This intermediate was also found as the significant intermediate of 1,4-dioxane by two other research groups, whose papers were published recently [104, 147]. However, its peak area ratio and hence, its concentration in all runs was low in comparison to the parent compound. 1,2-Ethanediol, diformate was needed to calibrate the GC. Unfortunately this compound was not available through different suppliers in North America, making GC calibration impossible. Acetic acid was another DIOX intermediate found through both GC/MS and IC analyses.

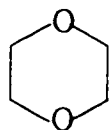
5.7.2.2 Ion Chromatography Results for DIOX Degradation

Similar to IC analyses for THF, DIOX samples taken during the run were analyzed. Figure 5.17 depicts a typical IC analysis for a DIOX sample. The water used in the experimental runs for DIOX was filtered deionized water (FDW) whereas the standard solution employed was tap water. Therefore,

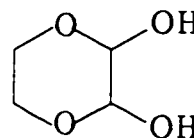
Table 5.3: Possible intermediates for the photocatalytic degradation of 1,4-dioxane.

INTERMEDIATE	DETECTION METHOD	CAS No. ¹	GC/MS PROBABILITY (%)
1,2-Ethanediol, diformate	GC/MS	629-15-2	83
Acetic acid	GC/MS & IC	64-19-7	78
Formic acid	IC	64-18-6	N/A
3-Hydroxybutyric acid	IC	625-71-8	N/A
Glycolic acid	IC	79-14-1	N/A
1,4-Dioxane-2,3-diol (2,3-dihydroxy-1,4-dioxane)	Not Detected	4845-50-5	N/A
[1,2-Ethanediy]bis(oxy)]bis[methanol]	Not Detected	3586-55-8	N/A

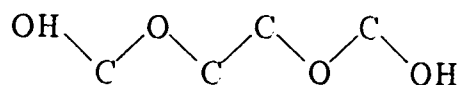
¹ Chemical Abstract Service Number



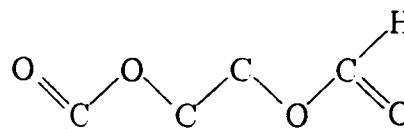
1,4-Dioxane



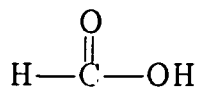
2,3-Dihydroxy-1,4-dioxane



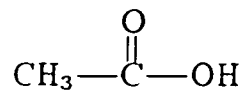
[1,2-Ethanediy]bis(oxy)]bis[methanol]



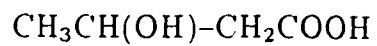
1,2-Ethanol. diformate



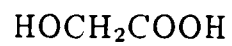
Formic acid



Acetic acid



β -Hydroxybutyric acid



Glycolic acid

Figure 5.16: Molecular structures of 1,4-dioxane and its possible intermediates in photocatalytic DIOX degradation.

slight differences in the retention times between the two IC chromatograms may be present. Comparing Figure 5.12 to Figure 5.17, the broad peak for formic acid suggests that it is present in the sample in the mg L^{-1} level. Therefore, it is one of the significant intermediates produced during the photocatalytic destruction of DIOX. Moreover, other organic acids such as acetic, glycolic, and β -hydroxybutyric acids are also detected as intermediates. By comparing Figures 5.12 and 5.17, it was concluded that the concentrations of acetic, glycolic, and β -hydroxybutyric acids are in the $\mu\text{g L}^{-1}$ range.

5.7.2.3 DIOX Reaction Mechanisms

Applying the identified intermediates in the photocatalytic degradation of DIOX, a hypothetical pathway for its mineralization may be proposed. Equations (5.5) through (5.17) in Section 5.7.1.3 represent the general reactions in photocatalysis processes. Recalling the general pattern of photocatalytic reactions in Equation (2.12), the hypothetical reaction pathway for the photocatalytic degradation of 1,4-dioxane is depicted in Figure 5.18. It is assumed that 1,4-dioxane converts to hydroxylated 1,4-dioxane causing the ring to open. Some organic acids are produced which ultimately convert to CO_2 , the final product of photocatalysis.

Similar to reaction mechanism pathways for THF, only global reactions are considered in order to model the photocatalytic degradation of 1,4-dioxane. Each global reaction may have different intermediate pathways. The details of the reaction mechanisms for the photocatalytic destruction of 1,4-dioxane can be summarized as follows:

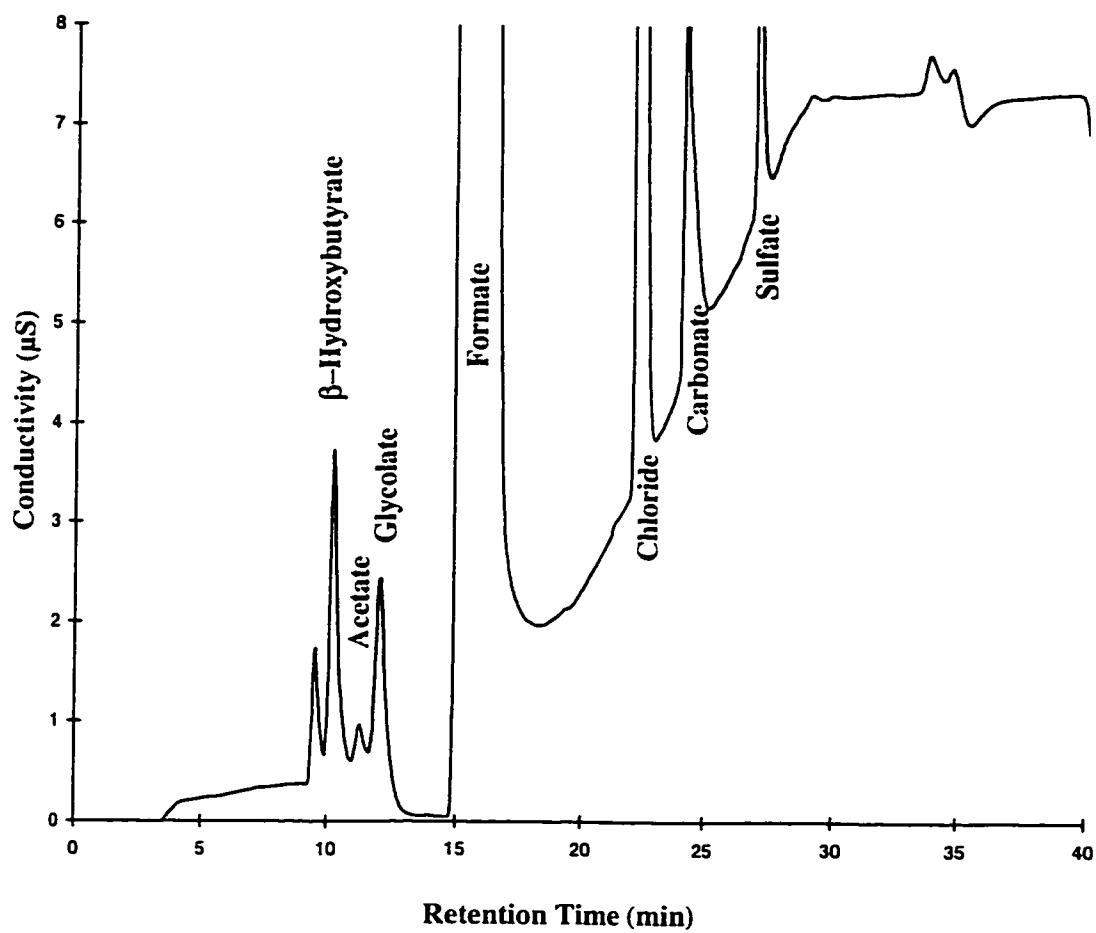


Figure 5.17: Typical Ion Chromatogram of 1,4-dioxane sample in the photocatalysis reaction.

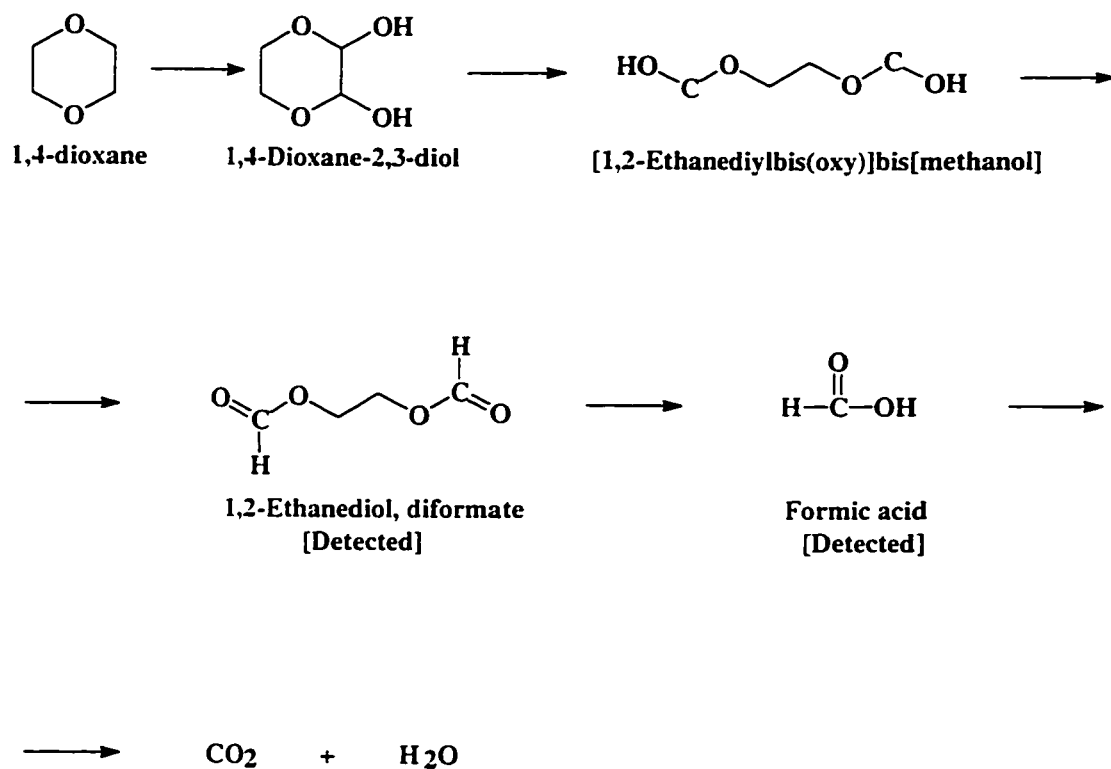
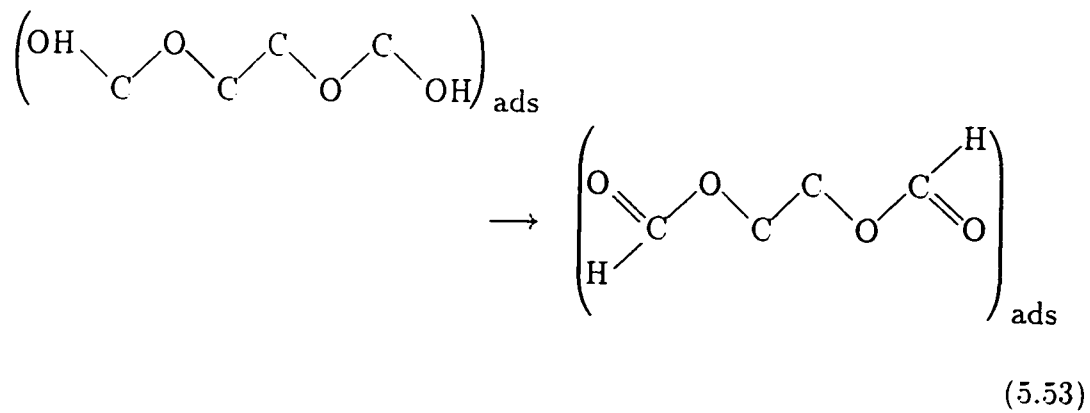
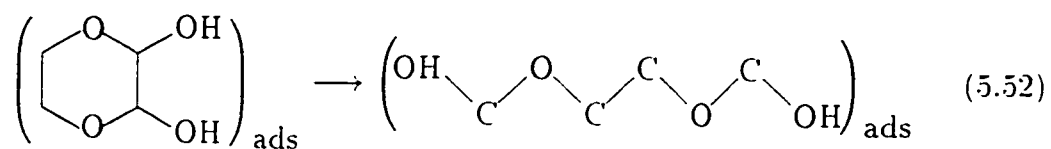
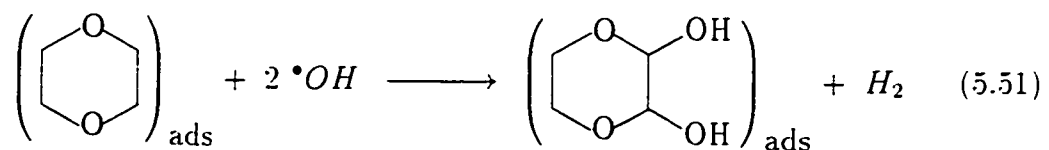
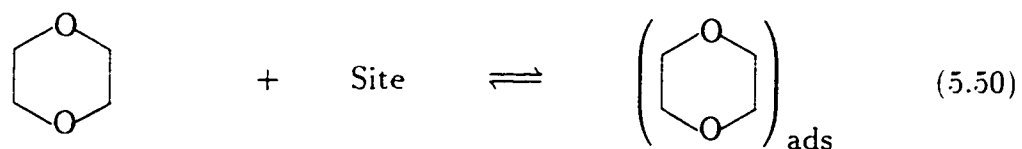
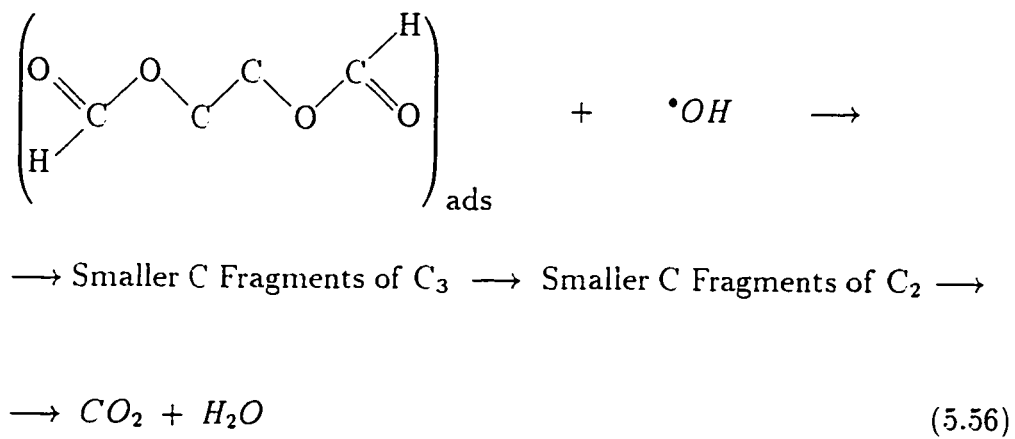
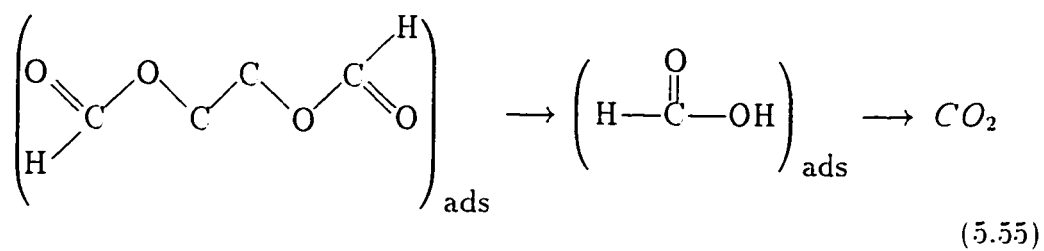
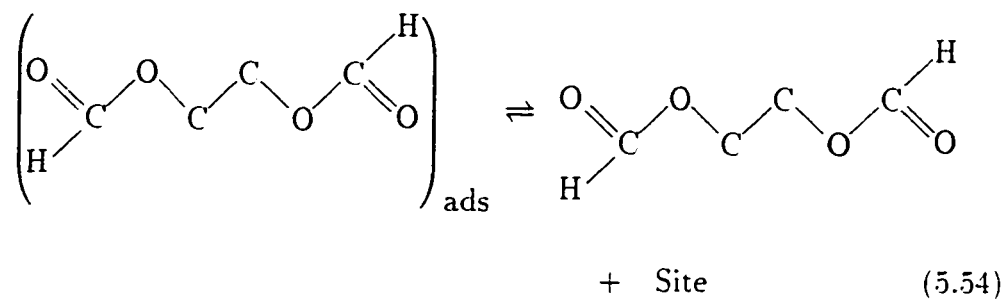


Figure 5.18: Proposed reaction mechanism for the photocatalytic degradation of 1,4-dioxane.

1,4-Dioxane adsorbs onto the surface of the photocatalyst as shown in Reaction (5.50). Hydroxyl radicals attack 1,4-dioxane producing the intermediate, 1,4-dioxane-2,3-diol (see Reaction (5.51)). This intermediate was not detected in the analyses. There is a possibility that some intermediates are tightly bound to the photocatalyst or their concentration in the solution are below the extraction limit of SPME. Another possibility is that the SPME fiber was unable to pick up particular intermediates. Also, the intrinsic reaction rate constants for some of the intermediates might be too high that their detection was impossible.

Alternatively, there is a possibility that 1,4-dioxane-2,3-diol ring opens as shown in Reaction (5.52). This would produce the intermediate, 1,2-ethanediol, diformate (see Reaction (5.53)), which was detected by GC/MS. Then 1,2-ethanediol, diformate either desorbs into the bulk phase or converts to formic acid (Reactions (5.54) and (5.55)). It is also possible that hydroxyl radicals attack 1,2-ethanediol, diformate thereby converting it to smaller C fragments. These smaller C fragments eventually lead to the final product of photocatalysis, CO₂, as revealed in Reaction (5.56).





5.7.2.4 DIOX Rate Equations

The dynamic model for the photocatalytic degradation of 1,4-dioxane in water was developed similar to the approach taken for THF (see Section 5.7.2.3). Since the DIOX intermediate was unavailable for GC calibration, the dynamic model of DIOX has an extra parameter, the calibration constant for 1,2-ethanediol, diformate (EDD).

1,4-Dioxane disappearance in the system is due to hydroxyl radical attacks. Therefore, the rate equation for 1,4-dioxane is:

$$-\frac{d[DIOX]_{ads}}{dt} = k_{5.51}a_s[{}^{\bullet}OH][DIOX]_{ads} \quad (5.57)$$

Assuming the concentrations of all other intermediates in the photocatalytic degradation of 1,4-dioxane except 1,2-ethanediol, diformate are negligible, the concentration of the hydroxyl radicals is:

$$[{}^{\bullet}OH] = \frac{\alpha k'_{5.12+} [h^+]}{k'_{5.12-} K_{5.9} [Ti^{IV}] + k_{5.51} [DIOX]_{ads} + k_{EDD,{}^{\bullet}OH} [EDD]_{ads}} \quad (5.58)$$

where $k'_{5.12-} = k_{5.12-} 10^{-pH}$;

$$k'_{5.12+} = k_{5.12+} [Ti^{IV} - H_2O];$$

$k_{EDD,{}^{\bullet}OH}$ = rate constant in reaction EDD with ${}^{\bullet}OH$.

Assuming that Reaction (5.50) is in equilibrium, we have:

$$[DIOX]_{ads} = K_{5.50} [Site] [DIOX] \quad (5.59)$$

By writing a similar rate equation for EDD and substituting Equations (5.58) and (5.59) into Equation (5.57), the dynamic model for the photocatalytic degradation of 1,4-dioxane obtained is as follows:

$$-\frac{d[DIOX]}{dt} = \frac{k_{DIOX}K_{DIOX}[DIOX]}{1 + K_{DIOX}[DIOX] + K_{EDD}[EDD]} \quad (5.60)$$

$$\frac{d[EDD]}{dt} = \frac{k_{DIOX}K_{DIOX}[DIOX] - k_{EDD}K_{EDD}[EDD]}{1 + K_{DIOX}[DIOX] + K_{EDD}[EDD]}$$

in which:

$$k_{DIOX} = \frac{\alpha k'_{5.12} + a_s \left(\frac{k_{5.5} I a_c}{k_{5.10} \nu_p} \right)^{1/2}}{K_{5.50}[Site]} \quad (5.61)$$

$$k_{EDD} = \frac{\alpha k'_{5.12} + a_s \left(\frac{k_{5.5} I a_c}{k_{5.10} \nu_p} \right)^{1/2}}{K_{EDD,ads}[Site]} \quad (5.62)$$

$$K_{DIOX} = \frac{k_{5.51} K_{5.50}[Site]}{k'_{5.12} - K_{5.9}[Ti^{IV}]} \quad (5.63)$$

$$K_{EDD} = \frac{k_{EDD \cdot OH} K_{EDD,ads}[Site]}{k'_{5.12} - K_{5.9}[Ti^{IV}]} \quad (5.64)$$

and $K_{EDD,ads}$ is the *EDD* binding constant.

It is obvious from Equation (5.60) that DIOX degradation follows the LH form; and unlike THF, it does not include an extra term in its dynamic model. As mentioned earlier, this is due to the hypothesis that DIOX disappears only through hydroxyl radicals attack.

Since 1,2-ethanediol, diformate (EDD) was unavailable to calibrate the GC, its concentration may be expressed in terms of a GC peak area ratio which was experimentally measured during the trials. Hence:

$$[EDD] = \eta_{EDD} \cdot A_{r,EDD} \quad (5.65)$$

where η_{EDD} = calibration constant for EDD;

$A_{r,EDD}$ = GC peak area ratio for EDD.

By substituting Equation (5.65) into Equation (5.60), the dynamic model for 1,4-dioxane can be obtained:

$$-\frac{d[DIOX]}{dt} = \frac{k_{DIOX} K_{DIOX} [DIOX]}{1 + K_{DIOX} [DIOX] + K'_{EDD} \cdot A_{r,EDD}} \quad (5.66)$$

$$\frac{dA_{r,EDD}}{dt} = \left(\frac{1}{\eta_{EDD}} \right) \frac{k_{DIOX} K_{DIOX} [DIOX] - k_{EDD} K'_{EDD} \cdot A_{r,EDD}}{1 + K_{DIOX} [DIOX] + K'_{EDD} \cdot A_{r,EDD}}$$

in which:

$$K'_{EDD} = \eta_{EDD} K_{EDD} \quad (5.67)$$

The parameters in this dynamic model will be estimated statistically in the following sections using the experimental data.

5.8 Biodegradability of Intermediates

Photocatalysis has been well known in degrading many organics. However, during this process some intermediates such as carboxylic acids are produced whose photocatalytic degradation rates are usually slow. In cases where the concentrations of these intermediates are low ($\mu\text{g L}^{-1}$ level), they might be accepted if they are below detection limits. However, if their concentrations are significant, these intermediates must be degraded. One possibility for degradation of these organics is the combined photocatalysis and biological treatment [195].

Although biological degradation data are not available for all intermediates, published data shows that some of the intermediates produced during the photocatalytic degradation of THF and DIOX are biologically degradable.

Elkins et al. [66] showed that acetic acid was biologically degradable by activated sludge. With original concentration of 500 mg L^{-1} , it could be degraded to about 50% of theoretical oxidation by phenol acclimated sludge after 12 h aeration. Also, literature shows that acetic acid degraded by more than 90% using an activated sludge inoculum [108, 132, 217]. Ludzack [131] demonstrated that formic acid is also biologically degradable using activated sludge. The concentrations after 6, 12, and 24 h dropped to 28.3, 45.4, and 70.0% of theoretical oxygen demand, respectively. Similarly, Malaney [134] showed that succinic acid was also biologically degradable using activated sludge. It was shown that its concentration decreased to 11.2, 27.2, and 42.2% of theoretical oxygen demand after 6, 12, and 24 h, respectively.

5.9 Photocatalytic Degradation of Tetrahydrofuran

The experimental results for the photocatalytic degradation of tetrahydrofuran in the single component system are presented in this section. Also, the kinetic parameters for different models are estimated and compared.

Figure 5.19 depicts the dissolved oxygen concentration profiles during the photocatalytic degradation of THF. In the initial part of the reaction, the DO concentration decreased dramatically and then it remained almost constant for the remainder of the experiment. Based on the reaction mechanisms discussed in Section 5.7.1.3, THF was oxygenated to produce γ -butyrolactone. Also, some of the oxygen was consumed to scavenge electrons in the conduction band of the semiconductor particles.

Although a few THF intermediates were observed in the GC analyses, there was only one significant and quantifiable intermediate during the process. γ -Butyrolactone was the only significant intermediate which could be integrated reliably with good reproducibility using GC analysis. However as discussed in Section 5.7.1.3, there were a few other intermediates such as succinic acid, acetic acid, formic acid, β -hydroxybutyric acid, and glycolic acid which were detected. Although some of these intermediates did not appear in the GC analyses, it is possible that their levels were below detection limits. For this reason, it was assumed that the last term in Equation (5.39) related to the intermediates was negligible and these intermediates were not taken into account for the modelling purposes. Moreover, it was also assumed that

there were few undetected intermediates such as 2-hydroxytetrahydrofuran, dihydro-5-hydroxy-2(3H)-furanone, and 4-oxobutanoic acid in the photocatalytic destruction of THF.

To find the parameters in Equations (5.44), a set of experimental trials with different initial concentrations for THF degradation was carried out. All of the experimental data were used to solve the dynamic models. The method of Box-Draper explained in Chapter 4 was applied to estimate the parameters. Table 5.4 lists the parameter values estimated for the dynamic model in Equations (5.44).

Table 5.4: THF kinetic parameters in dynamic model Equations (5.44).

COMPOUND	PARAMETERS WITH 95% CONFIDENCE LEVELS
Tetrahydrofuran	$k_{app} = (1.71 \pm 0.08) \times 10^{-2}$ [min ⁻¹]
	$k_{THF} = 5.24 \pm 0.51$ [μ M min ⁻¹]
	$K_{THF} = (3.16 \pm 0.13) \times 10^{-2}$ [μ M ⁻¹]
γ -Butyrolactone	$k_{GBL} = 1.67 \pm 0.30$ [μ M min ⁻¹]
	$K_{GBL} = (3.3 \pm 1.4) \times 10^{-2}$ [μ M ⁻¹]

Figure 5.20 shows a typical result for one of the runs in which tetrahydrofuran followed the modified LH form in Equations (5.44). The modified LH form described the experimental data for THF and its significant intermediate, GBL, well.

To compare the LH and its modified form, the LH model was applied to the experimental data. Equation 5.68 describes a simplified LH model in which no intermediates are considered in the photocatalytic degradation of component i (where $i = THF$).

$$-r_i = -\frac{dC_i}{dt} = \frac{k_i K_i C_i}{1 + K_i C_i} \quad (5.68)$$

where $-r_i$ = the reaction rate of the component i to be degraded. [$M s^{-1}$];

C_i = the concentration of the component i , [M];

k_i = the reaction rate constant. [$M s^{-1}$];

K_i = the binding constant. [M^{-1}].

Equation (5.68) was applied to the THF experimental data and the parameters were estimated. Table 5.5 shows the results of the estimated parameters for THF degradation in LH model neglecting intermediate involvement. For comparison, the conventional LH model considering one intermediate in the model as shown in Equation (5.69) was also applied to the THF experimental data. The estimated parameters are summarized in Table 5.6. In the derivation of Equations (5.69), it has been assumed that THF degradation occurs only via hydroxyl radical attacks while in the development of the modified LH model in Equations (5.44), it had been assumed that

THF disappearance proceeded via both hydroxyl radical attacks and direct oxidation.

$$\begin{aligned}
 -r_{THF} &= -\frac{dC_{THF}}{dt} = \frac{k_{THF}K_{THF}C_{THF}}{1 + K_{THF}C_{THF} + K_{GBL}C_{GBL}} \\
 r_{GBL} &= \frac{dC_{GBL}}{dt} = \frac{k_{THF}K_{THF}C_{THF} - k_{GBL}K_{GBL}C_{GBL}}{1 + K_{THF}C_{THF} + K_{GBL}C_{GBL}}
 \end{aligned}
 \tag{5.69}$$

Table 5.5: THF kinetic parameters considering no intermediates in the LH model Equations (5.68).

COMPOUND	PARAMETERS WITH 95% CONFIDENCE LEVELS
Tetrahydrofuran	$k_{THF} = 13.5 \pm 2.6$ $[\mu\text{M min}^{-1}]$
	$K_{THF} = (5.3 \pm 1.9) \times 10^{-3}$ $[\mu\text{M}^{-1}]$

Although the modified LH model worked well for the photocatalytic mineralization of THF, it described the experimental data only in the lower concentration ranges (for example, $C_{0,THF}=0-500 \mu\text{M}$). However, this is within the range of the organic pollutants found in water and wastewater. Figures 5.21 and 5.22 compare different models for THF destruction. These figures illustrate that the LH model without any intermediates also describes the data well. This might be due to the fact that the concentrations of inter-

Table 5.6: THF kinetic parameters in LH model Equations (5.69) considering GBL as its intermediate.

COMPOUND	PARAMETERS WITH 95% CONFIDENCE LEVELS
Tetrahydrofuran	$k_{THF} = 46.3 \pm 7.8$ $[\mu\text{M min}^{-1}]$
	$K_{THF} = (8.84 \pm 0.60) \times 10^{-4}$ $[\mu\text{M}^{-1}]$
γ -Butyrolactone	$k_{GBL} = 6.80 \pm 0.86$ $[\mu\text{M min}^{-1}]$
	$K_{GBL} = (1.16 \pm 0.37) \times 10^{-2}$ $[\mu\text{M}^{-1}]$

mediates were low in low initial concentration ranges. On the other hand, the LH model in Equations (5.69) underestimated the data. For the higher concentration of THF, neither the modified LH model nor the LH model without any intermediates describe the experimental data well. In the higher concentration ranges for THF, the concentration of intermediates are sufficiently high such that the intermediate term in the denominator is necessary in the model. Also, in the higher concentration ranges, the disappearance of THF tends to be a zero order reaction. Consequently, the first term, which contributes the first order kinetics in the dynamic model of Equations (5.44), was excluded. As Figure 5.23 depicts, the LH model with GBL as its intermediate (Equations (5.69)), represented the experimental data in the higher concentration range. In contrast, the modified LH model and the LH model without any intermediates overestimated the experimental data.

5.10 Photocatalytic Degradation of 1,4-Dioxane

In the next set of the experiments, 1,4-dioxane alone was examined in the slurry photoreactor. The kinetic parameters were estimated using the data obtained in different trials. The only significant and measurable intermediate in the photocatalytic destruction of DIOX was 1,2-ethanediol, diformate. Due to their low concentrations of the other intermediates listed in Table 5.3, the reproducibility of the GC peak areas for these compounds was very poor. Therefore for the purpose of modelling, these intermediates

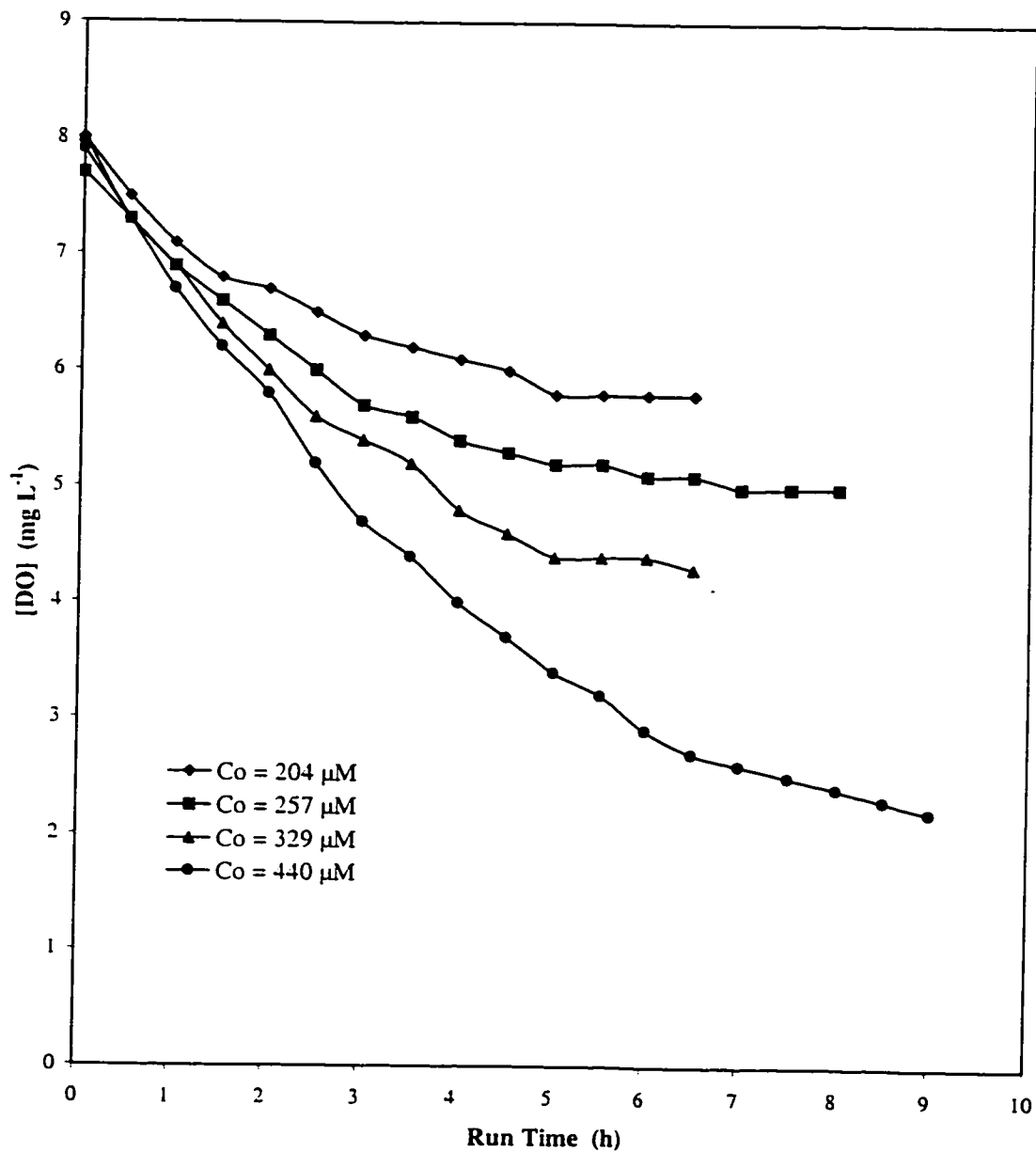


Figure 5.19: Dissolved oxygen profile for the photocatalytic degradation of THF in the slurry photoreactor.

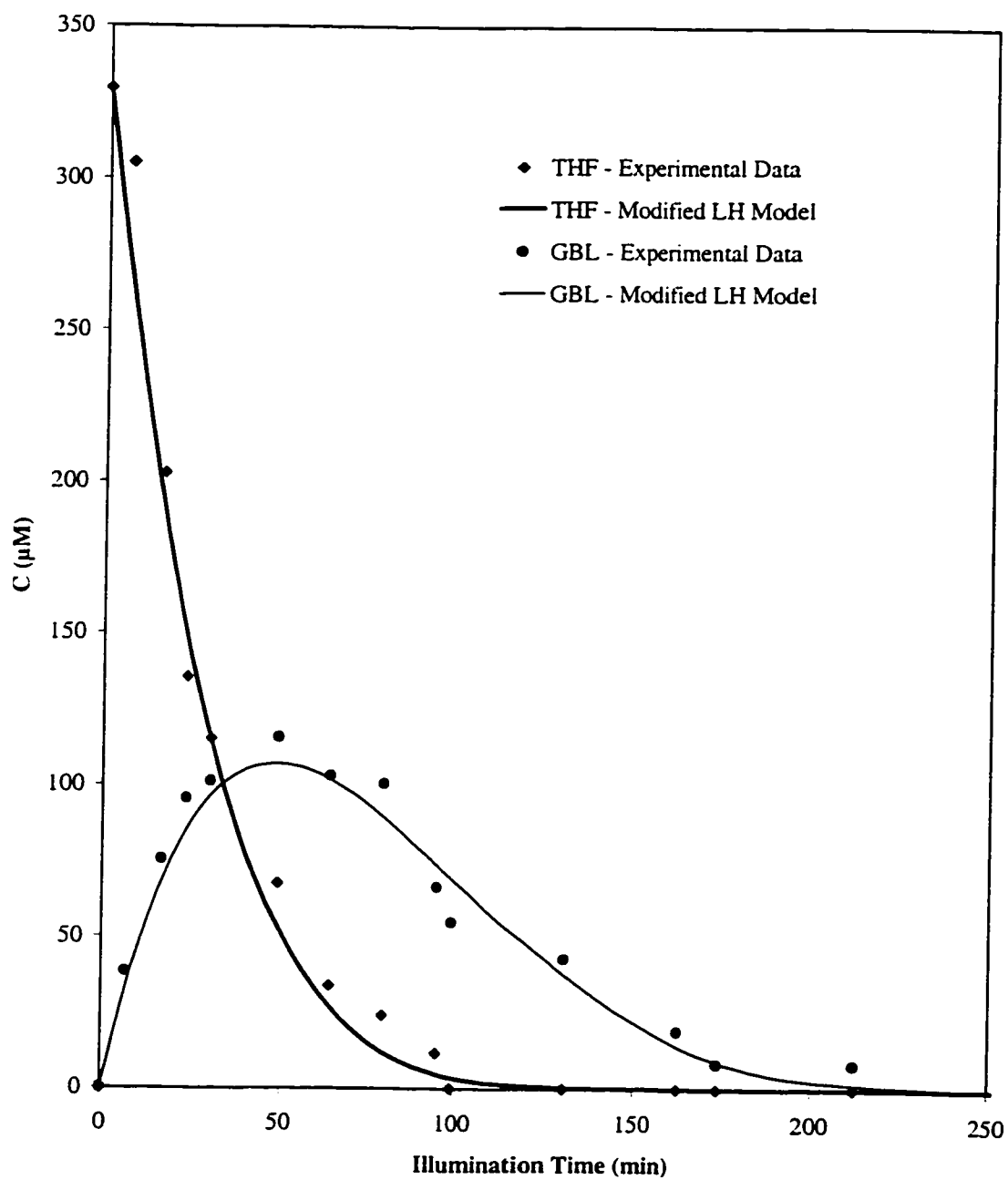


Figure 5.20: Photocatalytic degradation of THF along with its intermediate, γ -butyrolactone (GBL), in the slurry photoreactor; $C_{0,THF}=329 \mu\text{M}$.

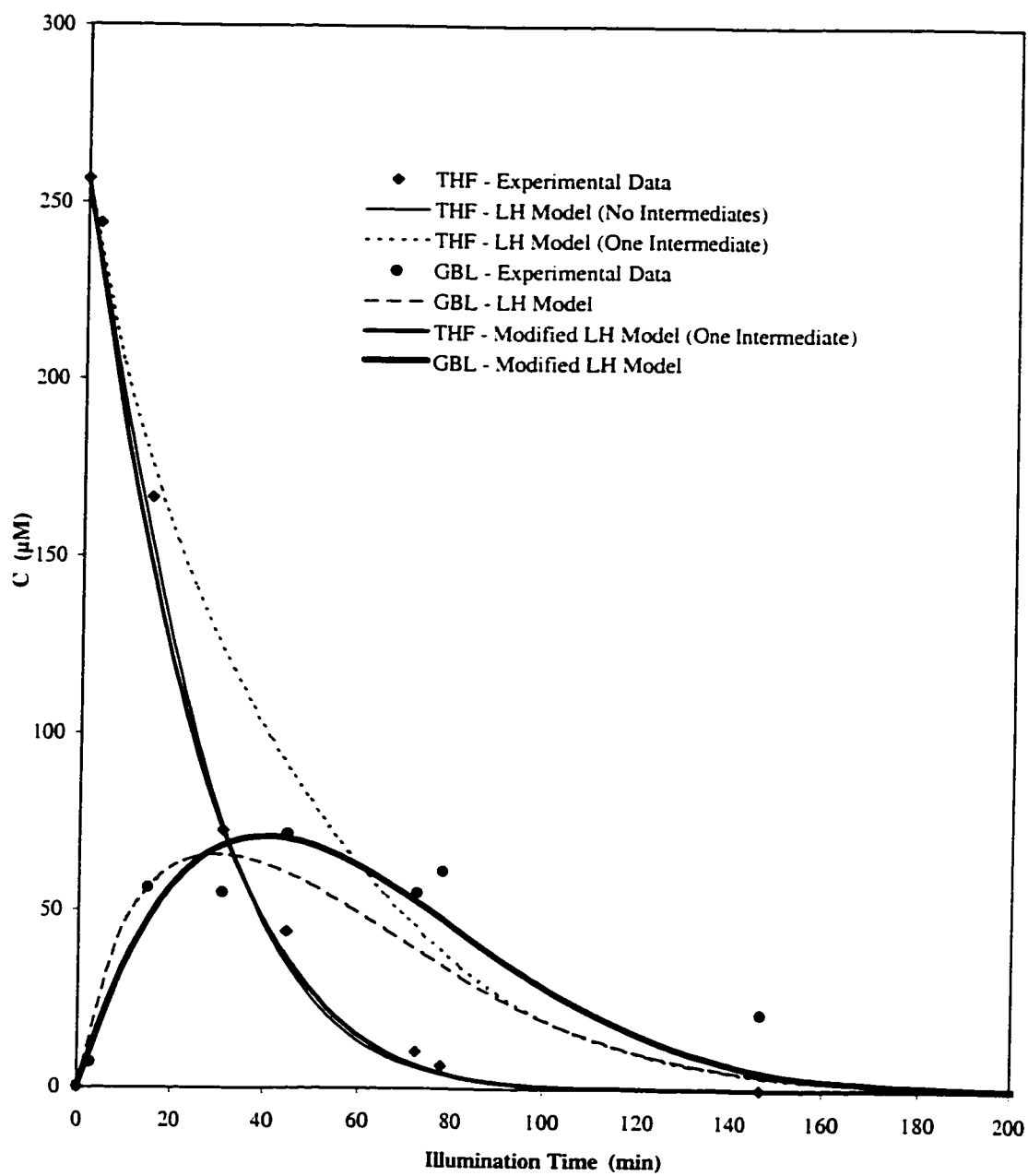


Figure 5.21: Comparison of the different models for the photocatalytic degradation of THF along with its intermediate, γ -butyrolactone (GBL), in the slurry photoreactor; $C_{0,THF}=257 \mu\text{M}$.

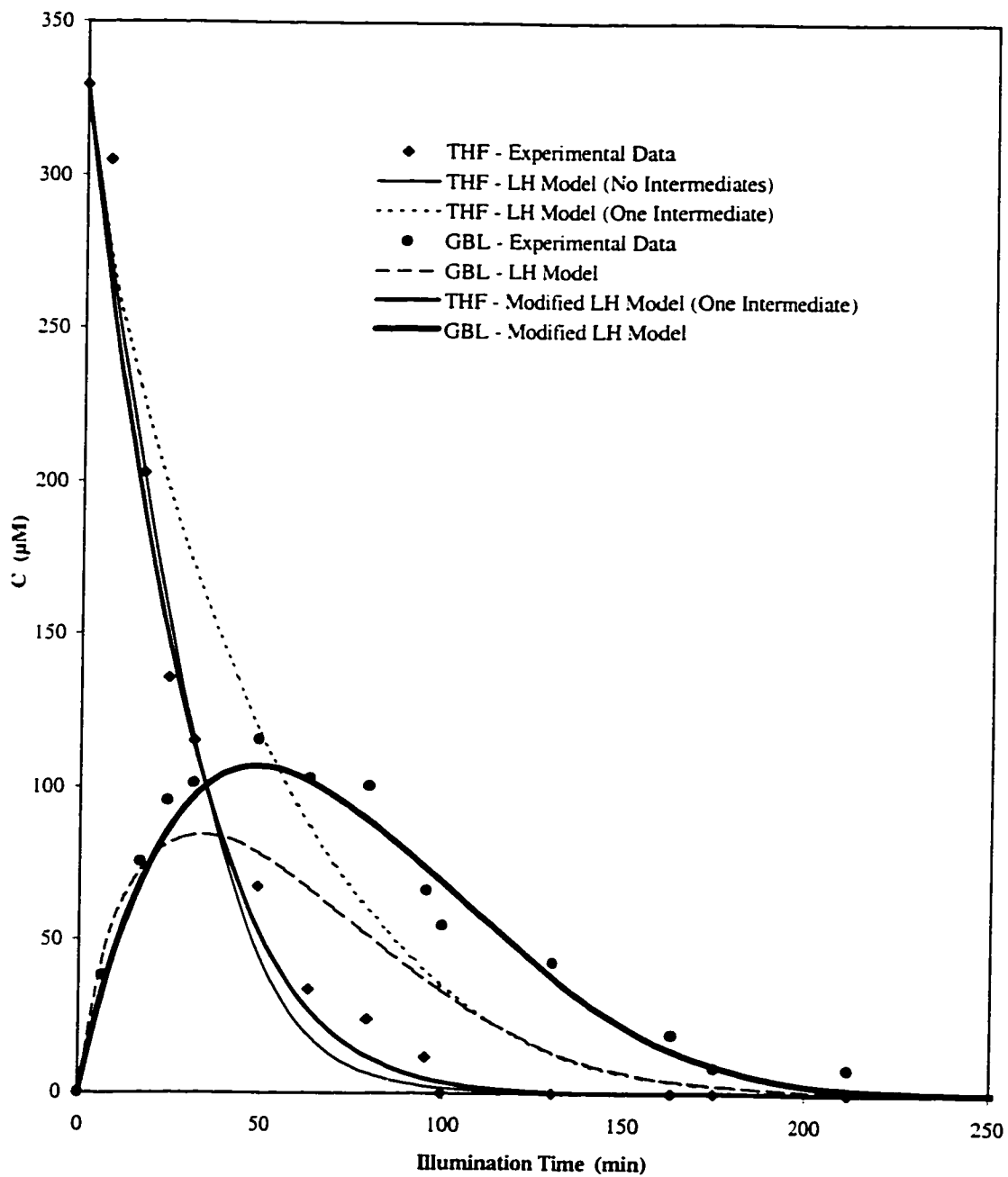


Figure 5.22: Comparison of the different models for the photocatalytic degradation of THF along with its intermediate, γ -butyrolactone (GBL), in the slurry photoreactor; $C_{0,THF}=329 \mu\text{M}$.

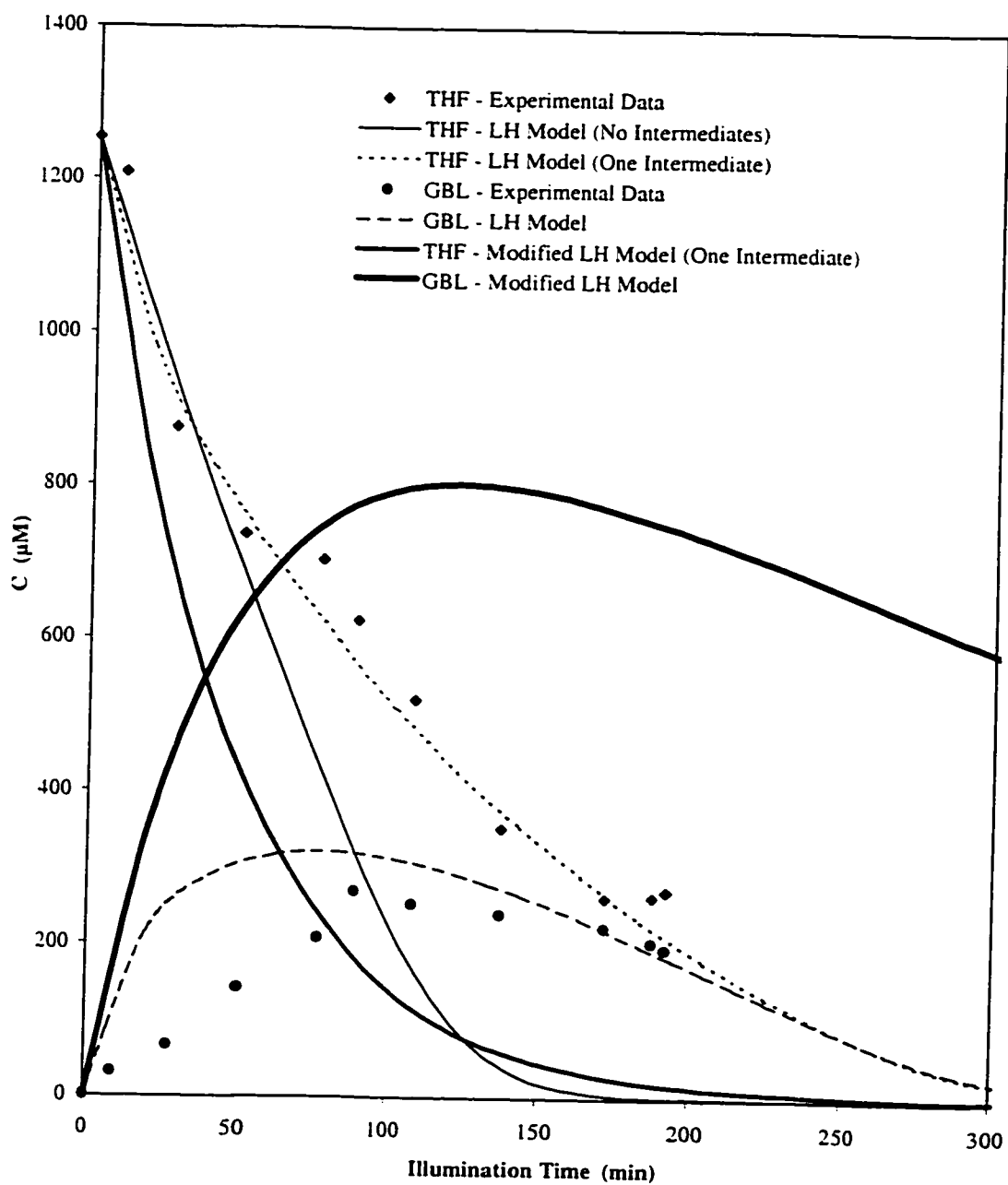


Figure 5.23: Comparison of the different models for the photocatalytic degradation of THF along with its intermediate, γ -butyrolactone (GBL), in the slurry photoreactor: $C_{0,THF}=1.25$ mM.

were not taken into account. Similar to THF rate equation in which the last term in Equation (5.39) was neglected, the term related to the other intermediates for DIOX was also neglected. Although, 1,2-ethanediol, diformate was considered in the model, this compound was not available for purchase. Therefore, an extra parameter, the GC calibration constant, was estimated in the dynamic model Equations (5.66). The dynamic model for DIOX using all experimental runs was solved by the method described in Chapter 4. The estimated parameter values at a 95% confidence interval are listed in Table 5.7. The estimated parameter η_{EDD} had the same order of magnitude as other GC calibration constants. Figure 5.24 shows a typical result for the degradation of 1,4-dioxane. This figure demonstrates that the LH model with one intermediate describes the experimental data well.

The LH model with no intermediate (Equation (5.68)), was also applied to the experimental data. Table 5.8 depicts the estimated parameters for the photocatalytic degradation of 1,4-dioxane in which no intermediates were considered. Figures 5.25, 5.26, and 5.27 show the comparison between the LH model with zero and one intermediate. As these figures illustrate, there was no significant change between these two models in all concentration ranges. Perhaps the concentration of EDD was so low during the photocatalytic degradation of 1,4-dioxane that it did not affect the denominator of Equations (5.66) to any significant extent.

Table 5.7: DIOX kinetic parameters in dynamic model Equations (5.66).

COMPOUND	PARAMETERS WITH 95% CONFIDENCE LEVELS
1.4-Dioxane	$k_{DIOX} = 9.27 \pm 0.83$ $[\mu\text{M min}^{-1}]$
	$K_{DIOX} = (6.4 \pm 1.8) \times 10^{-3}$ $[\mu\text{M}^{-1}]$
1.2-Ethanediol. diformate	$k_{EDD} = 67.7 \pm 6.2$ $[\mu\text{M min}^{-1}]$
	$K'_{EDD} = 1.10 \pm 0.21$ $[]^1$ (or $K_{EDD} = 9.34 \times 10^{-4}$ $[\mu\text{M}^{-1}]$)
	$\eta_{EDD} = (1.18 \pm 0.12) \times 10^3$ $[\mu\text{M}]$

¹ $[]$ designates dimensionless.

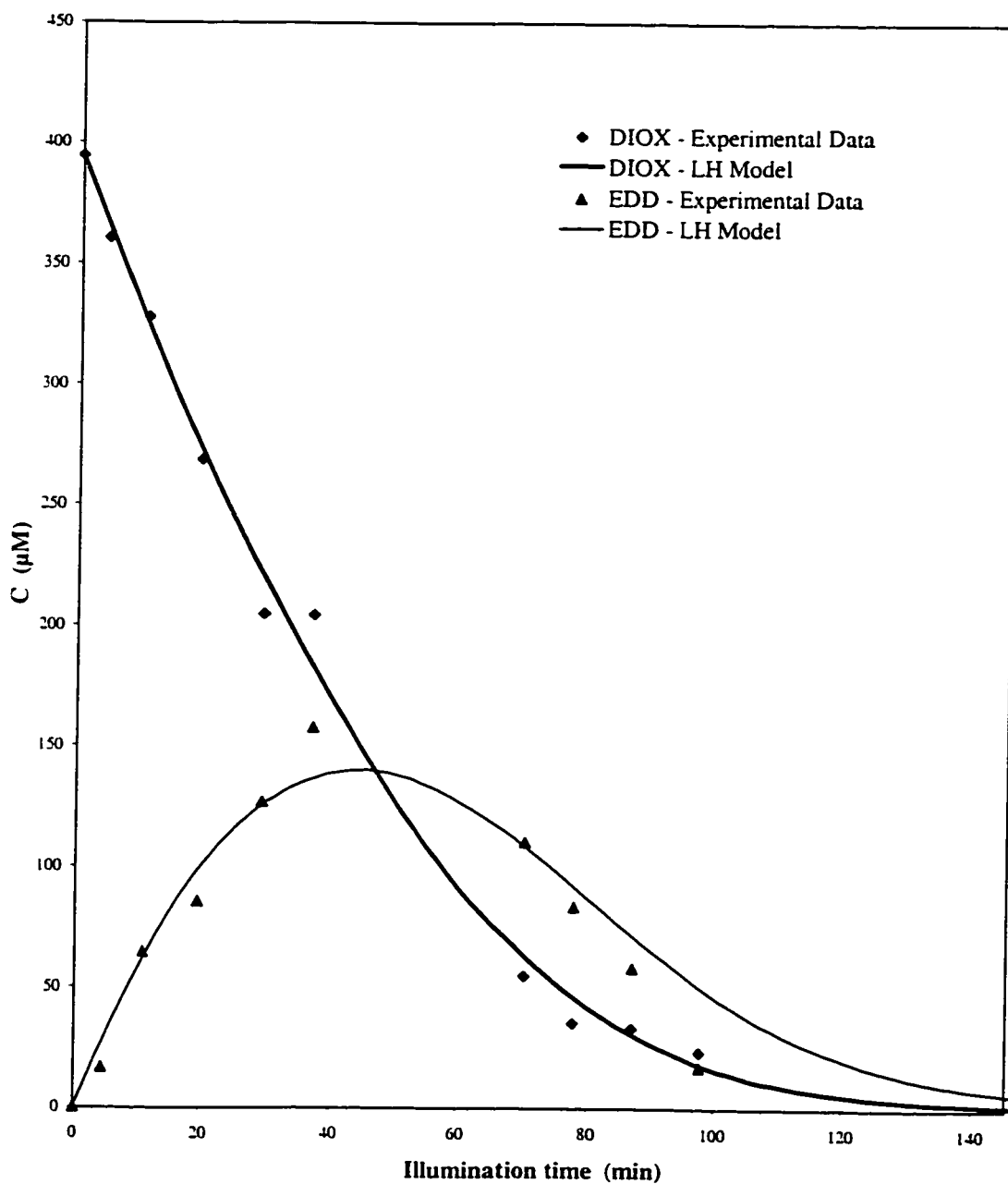


Figure 5.24: Photocatalytic degradation of DIOX along with its intermediate, 1,2-ethanediol, diformate (EDD), in the slurry photoreactor; $C_{o,DIOX} = 394 \mu\text{M}$.

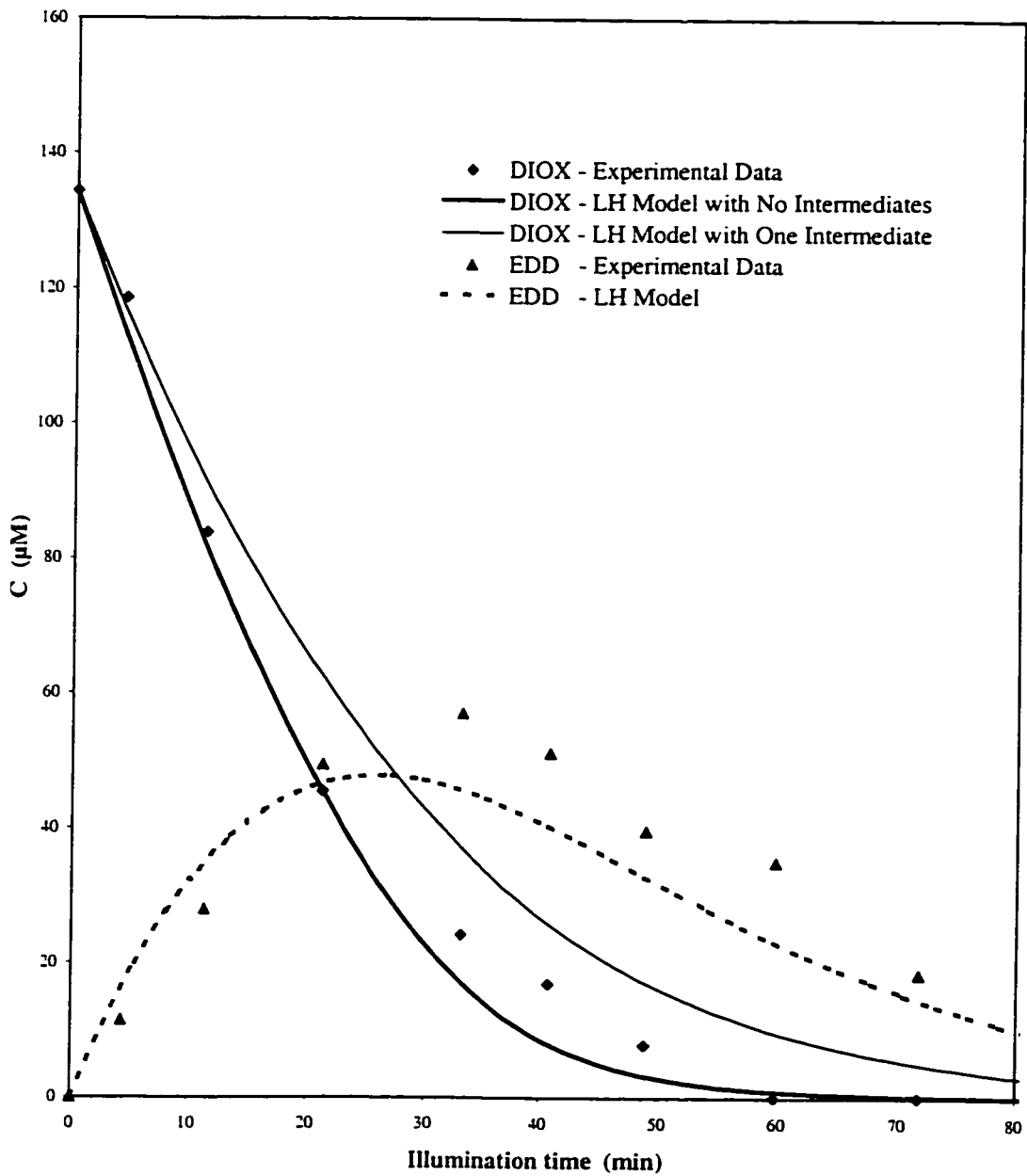


Figure 5.25: Comparison of the different models for the photocatalytic degradation of DIOX along with its intermediate, 1,2-ethanediol, diformate (EDD), in the slurry photoreactor; $C_{o,DIOX}=134 \mu\text{M}$.

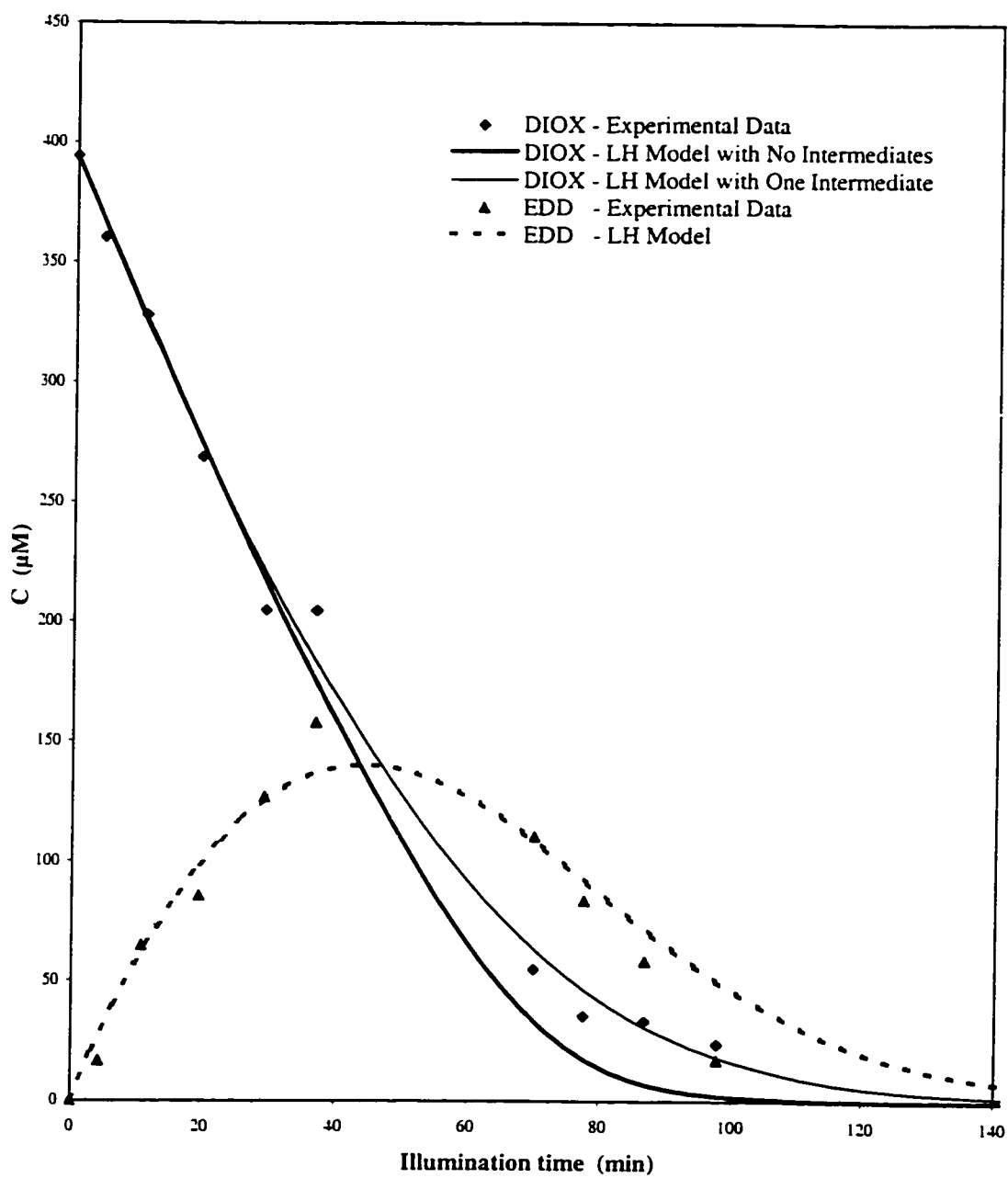


Figure 5.26: Comparison of the different models for the photocatalytic degradation of DIOX along with its intermediate, 1,2-ethanediol, diformate (EDD), in the slurry photoreactor; $C_{o,DIOX}=394 \mu\text{M}$.

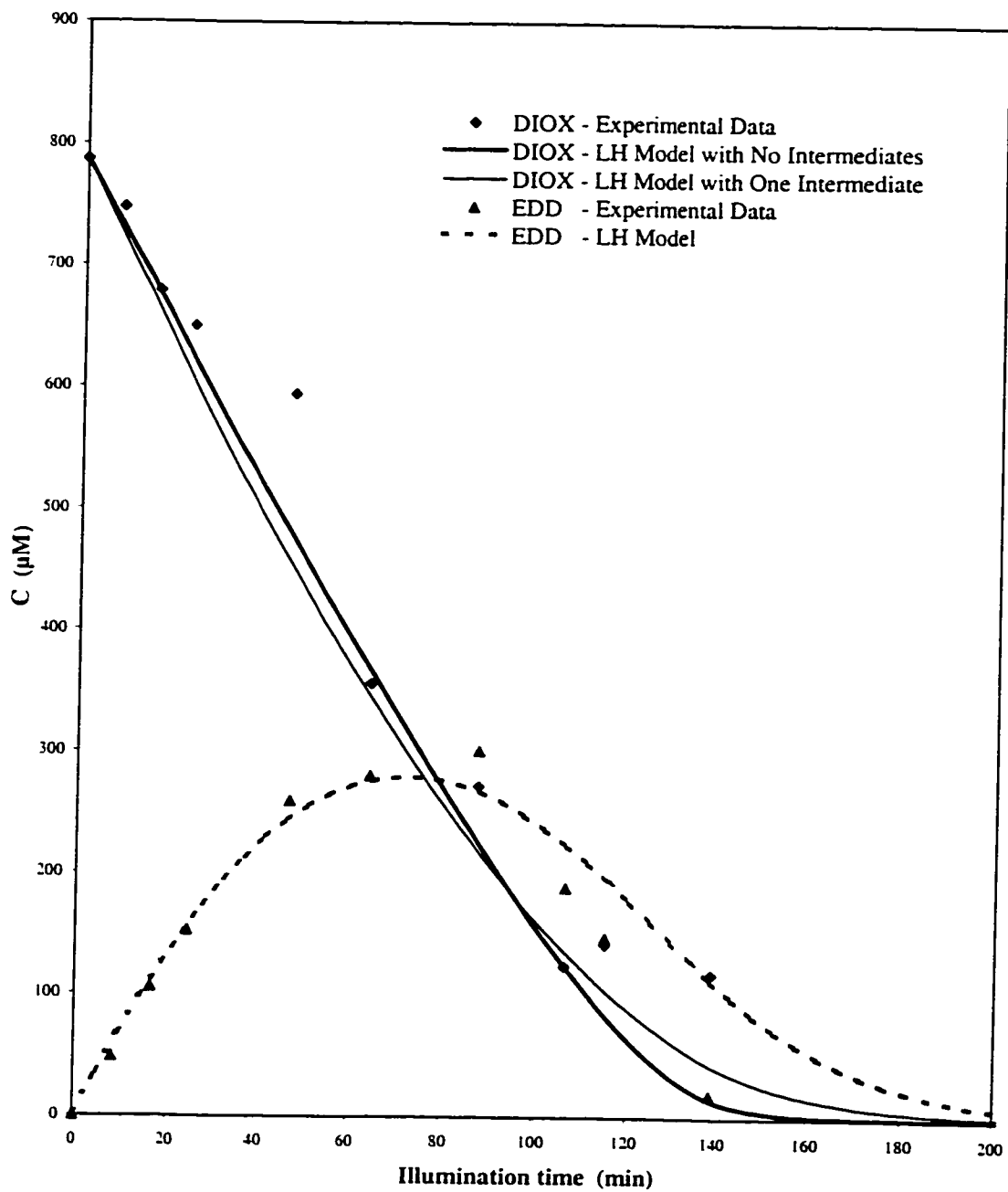


Figure 5.27: Comparison of the different models for the photocatalytic degradation of DIOX along with its intermediate, 1,2-ethanediol, diformate (EDD), in the slurry photoreactor; $C_{o,DIOX}=787 \mu\text{M}$.

Table 5.8: DIOX kinetic parameters for the LH model in Equation (5.68) without any intermediates.

COMPOUND	PARAMETERS WITH 95% CONFIDENCE LEVELS	
1,4-Dioxane	$k_{DIOX} = 7.26 \pm 0.60$	$[\mu\text{M min}^{-1}]$
	$K_{DIOX} = (1.62 \pm 0.87) \times 10^{-2}$	$[\mu\text{M}^{-1}]$

5.11 Photocatalytic Degradation of γ -Butyrolactone (GBL)

Photocatalytic degradation of γ -butyrolactone was also investigated in a single component system. Its degradation followed first order kinetics as depicted in Figure 5.28. The estimated first order rate constant for GBL was $k'_{GBL} = 0.0194 \text{ min}^{-1}$.

Figure 5.29 reveals no significant change in the dissolved oxygen concentration within the GBL runs. However in THF degradation, the dissolved oxygen concentration dropped which indicates the oxidation of THF to GBL (see Figure 5.19). Figure 5.30 shows the time-concentration profile for the GBL degradation in a single component system which obeyed first order kinetics. Also, Figure 5.31 depicts the TIC/TOC profile for the photocatalytic degradation of GBL. The TOC disappeared to a level close to zero while

TIC increased during the reaction. The decrease in TC is assumed to be a result of escaping CO₂ into the headspace. Also, adsorption of organics to the catalyst surface could be another explanation for the drop in the TC. A few tiny GC peaks were observed during the course of the reaction, but their GC areas were very small compared to those for GBL. Although few intermediates were observed during the reaction, it is possible that their degradation rates are sufficiently rapid, making them not detectable.

5.12 Photocatalytic Degradation of a Binary System (Mixture of THF and DIOX)

The results of the photocatalytic degradation of a binary system are presented and discussed in this section. Tetrahydrofuran and 1,4-dioxane, whose photocatalytic degradations in single component systems were discussed previously, were used as the model compounds. Based on the significant and quantifiable intermediates for both THF and DIOX, the following dynamic model in Equations (5.70) satisfactorily described the behavior of the binary system. Figure 5.32 depicts the results of a typical binary run. The estimated kinetic parameters of the binary dynamic model in Equations (5.70) are summarized in Table 5.9.

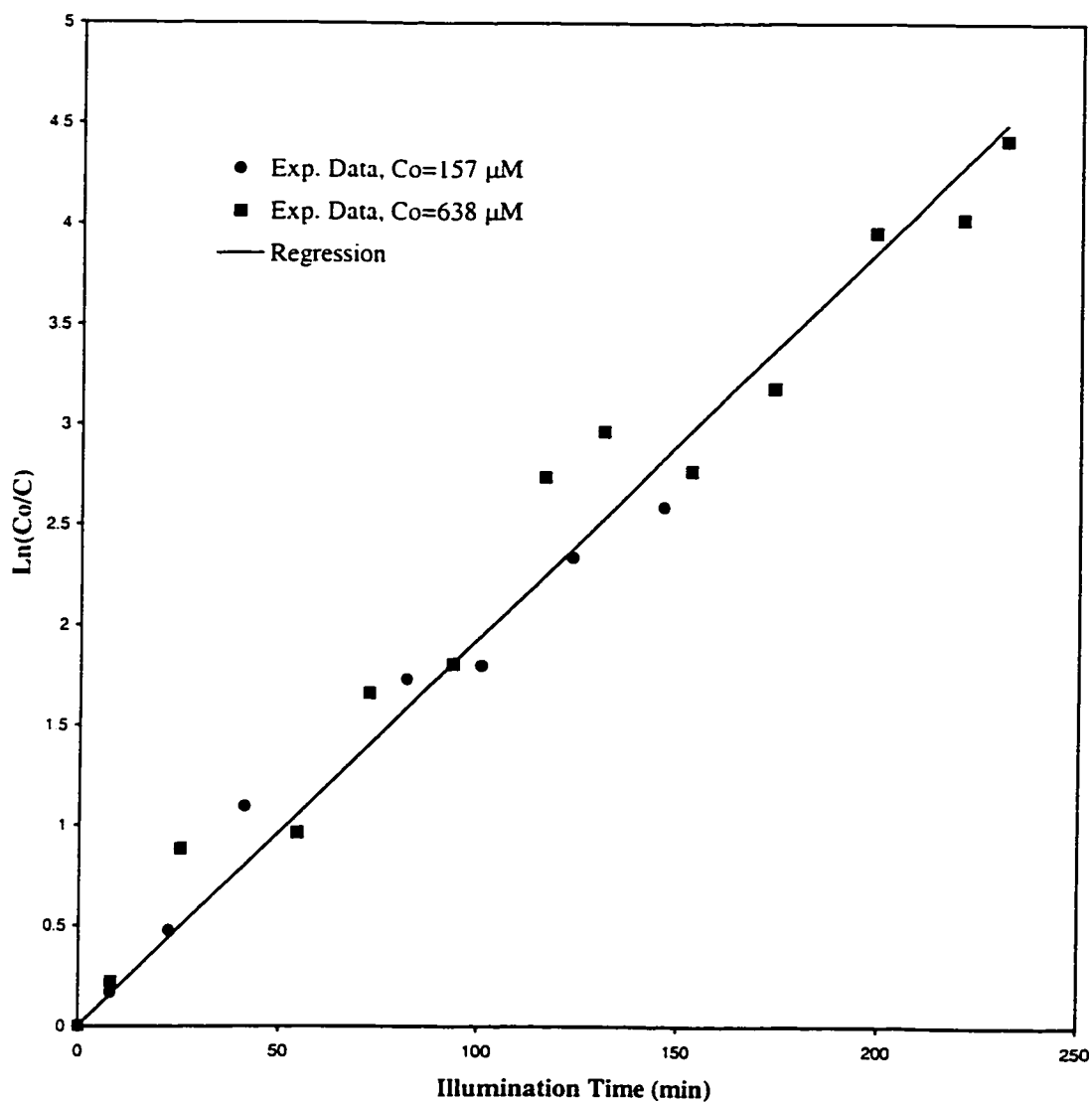


Figure 5.28: First order kinetic test for the photocatalytic degradation of γ -butyrolactone in the slurry photoreactor; $k'_{GBL}=0.0194 \text{ min}^{-1}$ and $R^2=0.973$.

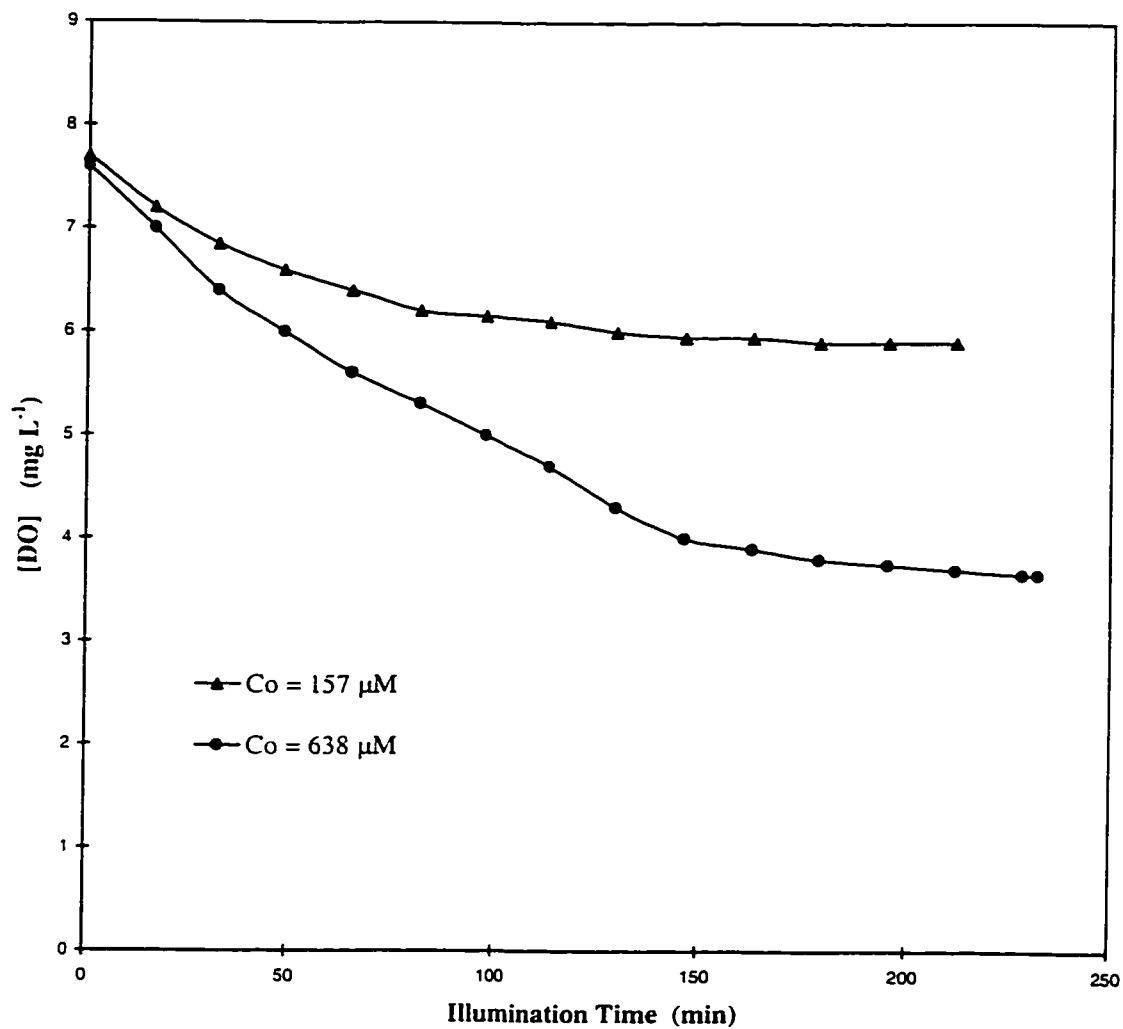


Figure 5.29: Dissolved oxygen (DO) profile for the photocatalytic degradation of γ -butyrolactone in the slurry photoreactor.

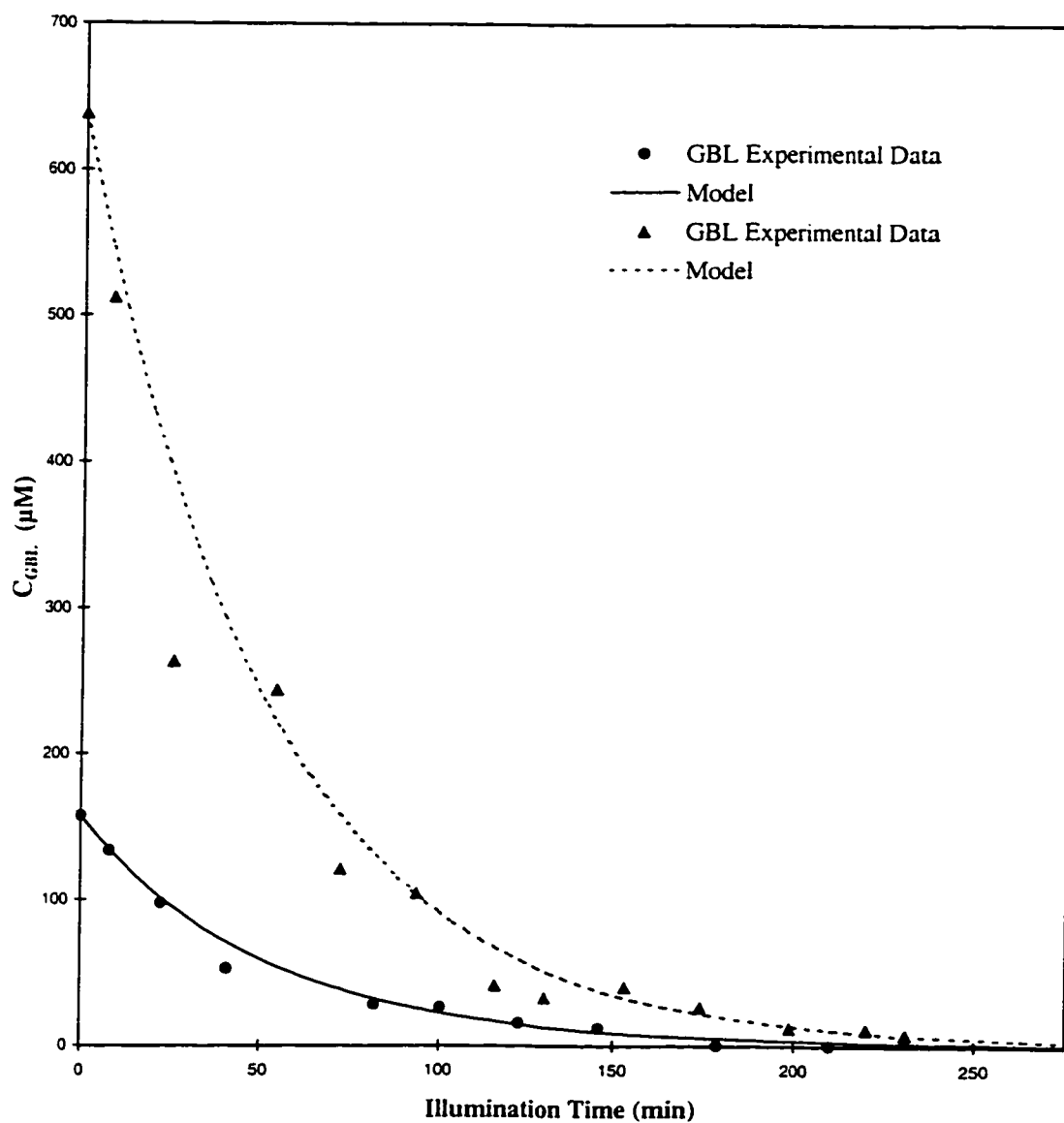


Figure 5.30: First order kinetics for the photocatalytic degradation of γ -butyrolactone in the slurry photoreactor; $k = 0.0194 \text{ min}^{-1}$.

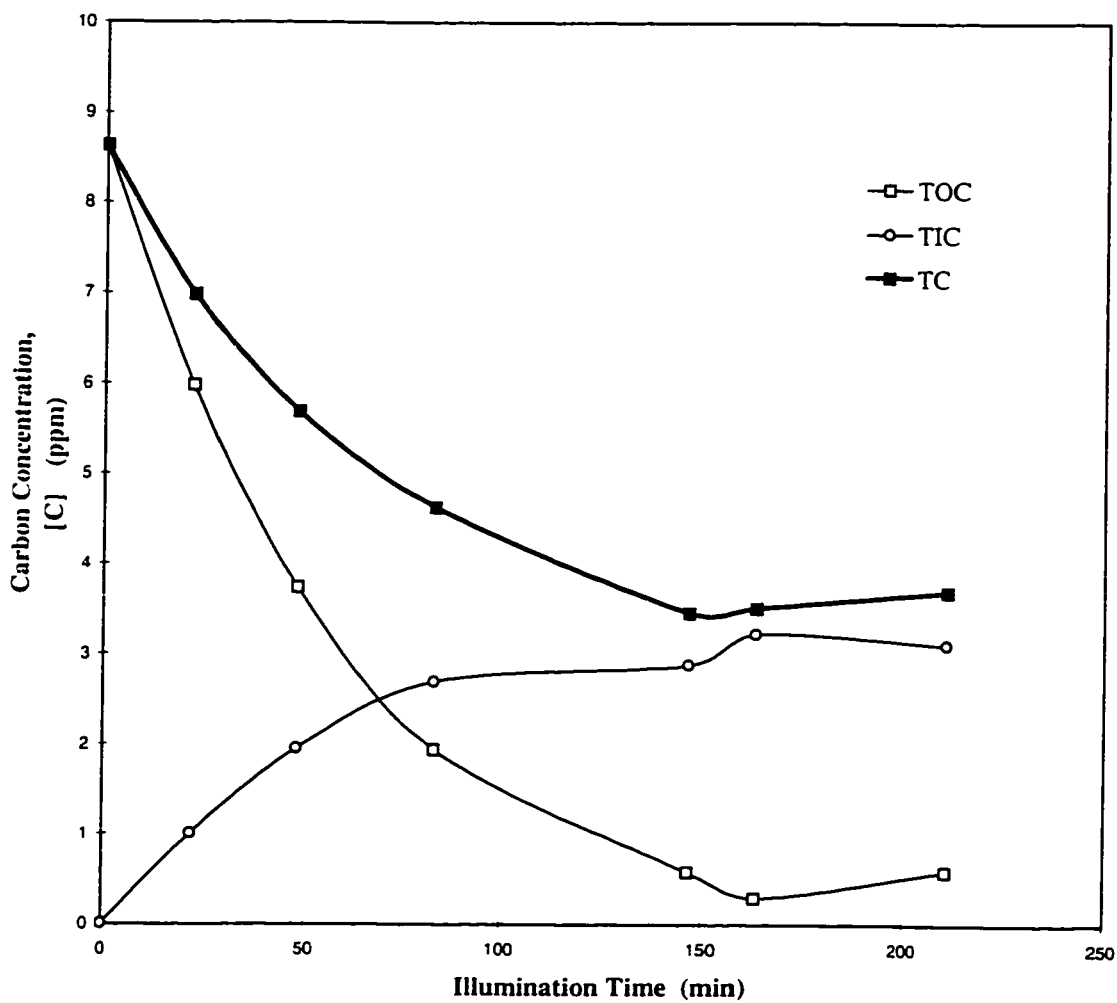


Figure 5.31: TIC/TOC profile for the photocatalytic degradation of γ -butyrolactone in the slurry photoreactor.

$$\begin{aligned}
-\frac{d[THF]}{dt} &= k_{app}[THF] \\
&\quad + \frac{k_{THF}K_{THF}[THF]}{1 + K_{THF}[THF] + K_{GBL}[GBL] + K_{DIOX}[DIOX]} \\
\frac{d[GBL]}{dt} &= k_{app}[THF] \\
&\quad - \frac{k_{GBL}K_{GBL}[GBL]}{1 + K_{THF}[THF] + K_{GBL}[GBL] + K_{DIOX}[DIOX]} \\
-\frac{d[DIOX]}{dt} &= \frac{k_{DIOX}K_{DIOX}[DIOX]}{1 + K_{THF}[THF] + K_{GBL}[GBL] + K_{DIOX}[DIOX]}
\end{aligned} \tag{5.70}$$

Other models were also examined for the binary system. The LH model with no intermediate (see Equations (5.71)) was tested. The estimated parameters for this model are shown in Table 5.10.

$$\begin{aligned}
-\frac{d[THF]}{dt} &= \frac{k_{THF}K_{THF}[THF]}{1 + K_{THF}[THF] + K_{DIOX}[DIOX]} \\
-\frac{d[DIOX]}{dt} &= \frac{k_{DIOX}K_{DIOX}[DIOX]}{1 + K_{THF}[THF] + K_{DIOX}[DIOX]}
\end{aligned} \tag{5.71}$$

In addition, the LH model considering one intermediate for THF was tested for the binary system (see Equations (5.72)) and the estimated parameters are shown in Table 5.11.

$$\begin{aligned}
-\frac{d[THF]}{dt} &= \frac{k_{THF}K_{THF}[THF]}{1 + K_{THF}[THF] + K_{GBL}[GBL] + K_{DIOX}[DIOX]} \\
\frac{d[GBL]}{dt} &= \frac{k_{THF}K_{THF}[THF] - k_{GBL}K_{GBL}[GBL]}{1 + K_{THF}[THF] + K_{GBL}[GBL] + K_{DIOX}[DIOX]} \\
-\frac{d[DIOX]}{dt} &= \frac{k_{DIOX}K_{DIOX}[DIOX]}{1 + K_{THF}[THF] + K_{GBL}[GBL] + K_{DIOX}[DIOX]}
\end{aligned}
\tag{5.72}$$

Figure 5.33 compares different models for the binary system. Both LH models with no intermediates or one intermediate overestimate the kinetic rates. This indicates that the dynamic model for the binary system needs at least one intermediate to satisfy the experimental data. Therefore, the modified LH model in which THF disappears via two routes, hydroxyl radical attack and oxidation to GBL, displays the best agreement with the experimental data.

Figures 5.34 and 5.35 respectively compare the photocatalytic degradation of THF and DIOX in single and binary systems. Although the initial concentrations of THF and DIOX in the single component system were higher, their degradation rates were much faster in comparison to their degradation in the binary system. The decrease in the rate of the binary system was a result of competition for active sites between different species available in the system.

The kinetic parameters estimated in the single trials (see Tables 5.4

and 5.8) were applied to the binary dynamic model shown in Equations (5.70). Figure 5.36 illustrates the results of the binary model with single system parameters. This figure indicates that the parameters in the single trials cannot be used in the binary system models simply because the degradation rates are not additive. Therefore, separate tests are needed in order to model a binary system.

Table 5.9: Binary kinetic parameters in dynamic model (Equations (5.70)).

COMPOUND	PARAMETERS WITH 95% CONFIDENCE LEVELS
Tetrahydrofuran	$k_{app} = (8.1 \pm 1.0) \times 10^{-3}$ [min ⁻¹]
	$k_{THF} = 2.40 \pm 0.63$ [μ M min ⁻¹]
	$K_{THF} = (1.18 \pm 0.34) \times 10^{-2}$ [μ M ⁻¹]
γ -Butyrolactone	$k_{GBL} = 7.7 \pm 5.2$ [μ M min ⁻¹]
	$K_{GBL} = (1.8 \pm 1.0) \times 10^{-3}$ [μ M ⁻¹]
1,4-Dioxane	$k_{DIOX} = 5.4 \pm 3.5$ [μ M min ⁻¹]
	$K_{DIOX} = (5.4 \pm 3.9) \times 10^{-3}$ [μ M ⁻¹]

Table 5.10: Kinetic parameters in binary model Equations (5.71); no intermediates were included in the model.

COMPOUND	PARAMETERS WITH 95% CONFIDENCE LEVELS	
Tetrahydrofuran	$k_{THF} = 12.7 \pm 1.4$	$[\mu\text{M min}^{-1}]$
	$K_{THF} = (8.9 \pm 2.3) \times 10^{-2}$	$[\mu\text{M}^{-1}]$
1,4-Dioxane	$k_{DIOX} = 2.87 \pm 0.21$	$[\mu\text{M min}^{-1}]$
	$K_{DIOX} = (1.36 \pm 0.22) \times 10^{-1}$	$[\mu\text{M}^{-1}]$

5.13 Effects of Carbonate and Bicarbonate Ions on Photocatalysis

Most water and wastewater samples will have a few inorganic compounds which can potentially act as hydroxyl radical scavengers during photocatalysis processes. Carbonate and bicarbonate ions are well known as hydroxyl radical scavengers (see Section 2.4) in processes such as flash photolysis and pulse radiolysis [1, 2, 3, 23, 89, 218]. Other anion species such as phosphates, sulfates, and nitrates may also be present in water and their effects

Table 5.11: Binary kinetic parameters in LH model Equations (5.72) considering one intermediate for THF.

COMPOUND	PARAMETERS WITH 95% CONFIDENCE LEVELS	
Tetrahydrofuran	$k_{THF} = 6.28 \pm 0.45$	$[\mu\text{M min}^{-1}]$
	$K_{THF} = (5.7 \pm 1.1) \times 10^{-3}$	$[\mu\text{M}^{-1}]$
γ -Butyrolactone	$k_{GBL} = 7.9 \pm 1.4$	$[\mu\text{M min}^{-1}]$
	$K_{GBL} = (5.0 \pm 1.0) \times 10^{-3}$	$[\mu\text{M}^{-1}]$
1,4-Dioxane	$k_{DIOX} = 67 \pm 18$	$[\mu\text{M min}^{-1}]$
	$K_{DIOX} = (4.1 \pm 1.5) \times 10^{-4}$	$[\mu\text{M}^{-1}]$

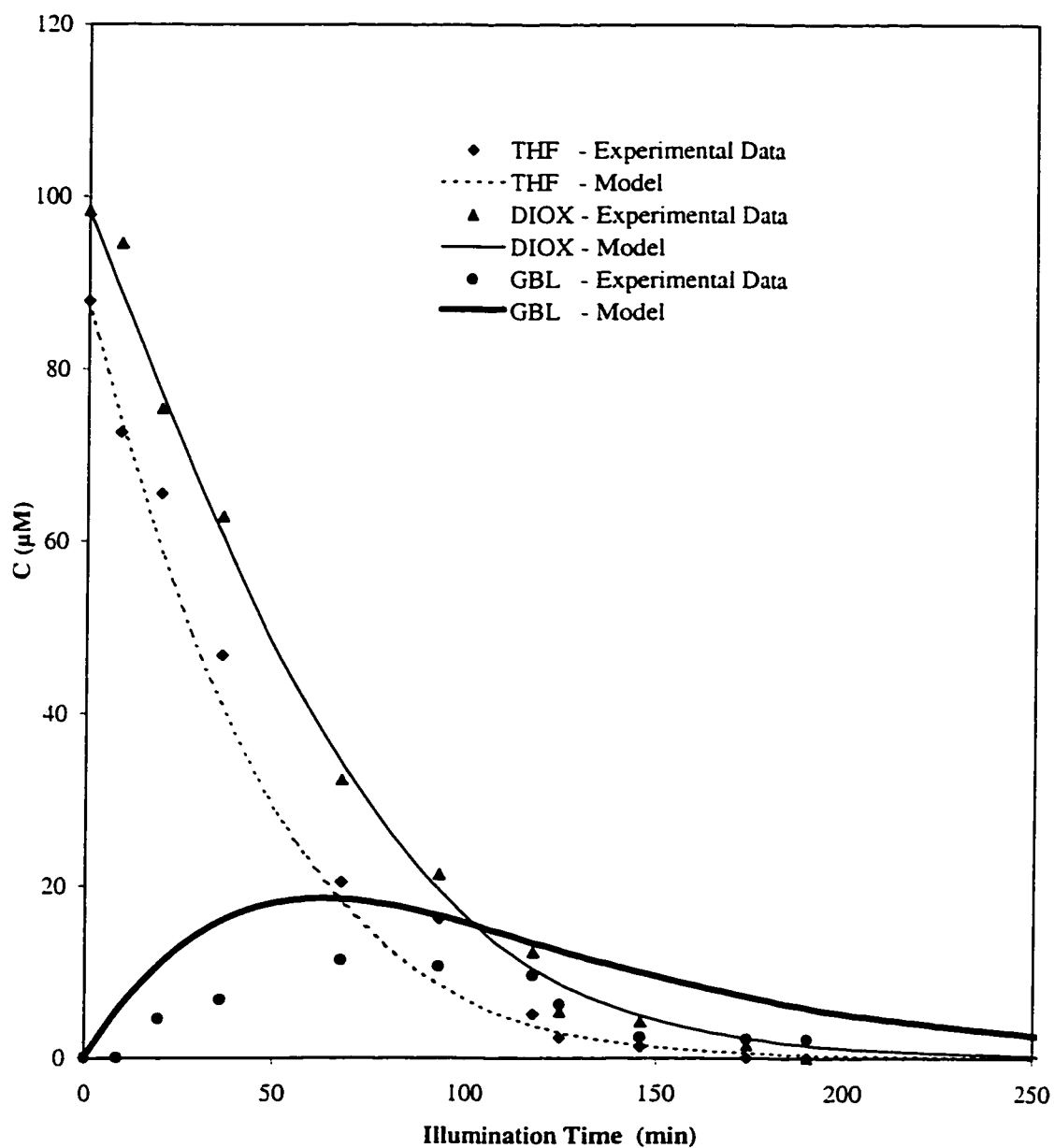


Figure 5.32: Photocatalytic degradation of the mixture of THF and DIOX along with THF intermediate, γ -butyrolactone (GBL), in the slurry photoreactor; $C_{0,THF}=87.9 \mu\text{M}$ and $C_{0,DIOX}=98.4 \mu\text{M}$; Models are based on the modified LH forms.

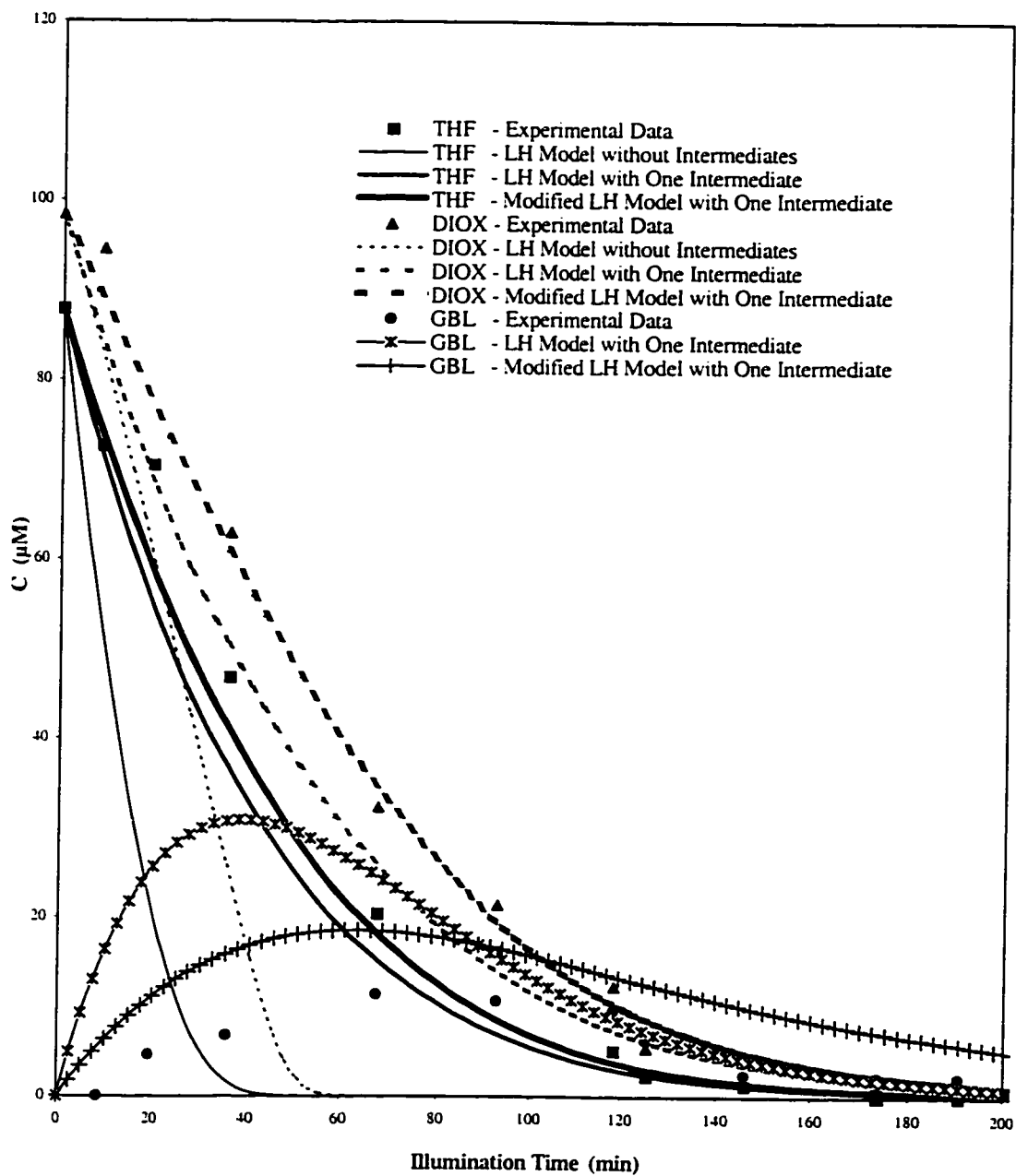


Figure 5.33: Comparison of the different models for the photocatalytic degradation of the mixture of THF and DIOX along with THF intermediate, γ -butyrolactone (GBL), in the slurry photoreactor; $C_{0,THF}=87.9 \mu\text{M}$ and $C_{0,DIOX}=98.4 \mu\text{M}$.

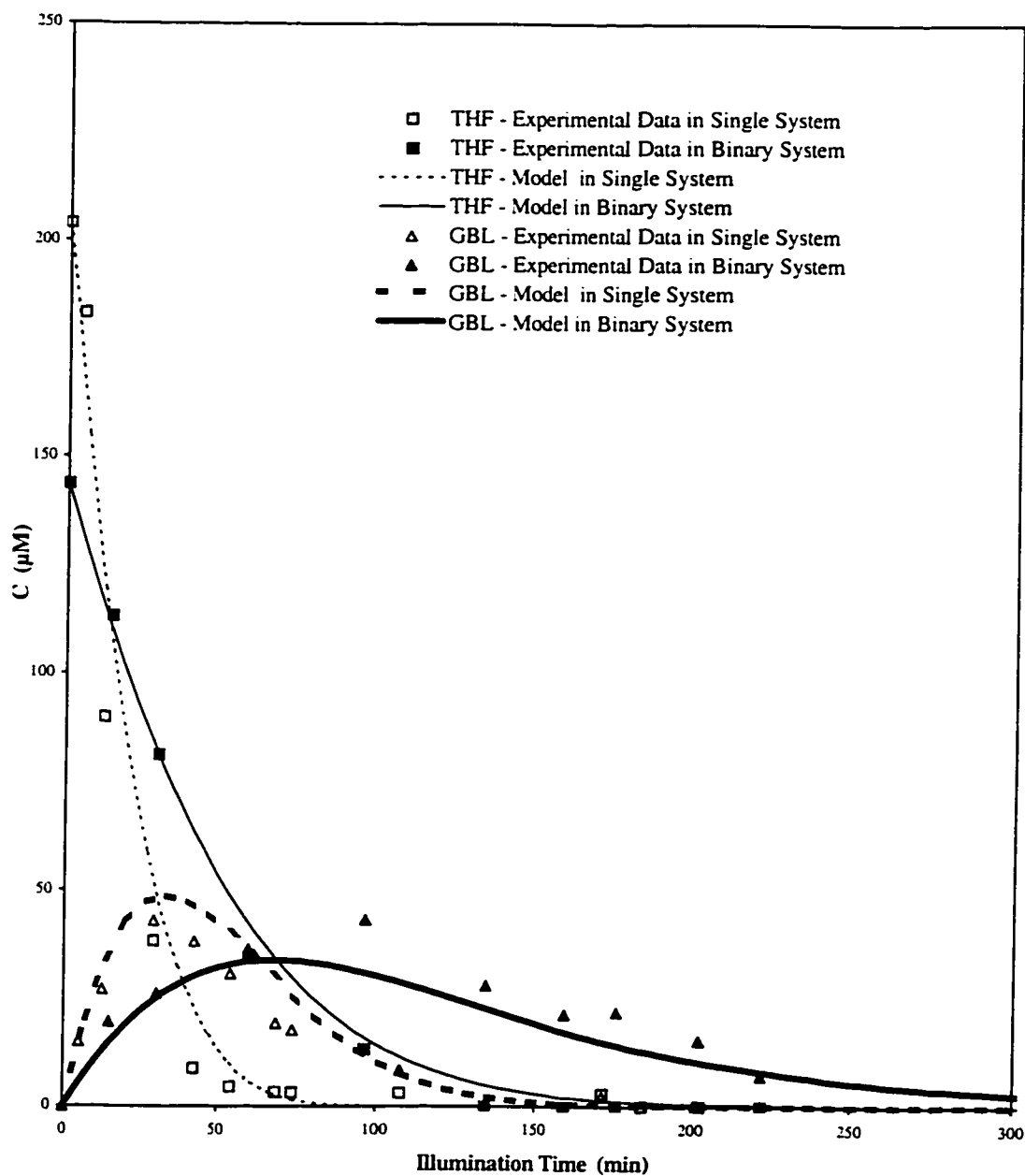


Figure 5.34: Comparison between single and binary systems for the photocatalytic degradation of THF in the slurry photoreactor; $C_{0,THF}=204 \mu\text{M}$ in single system and $C_{0,THF}=144 \mu\text{M}$ in binary system.

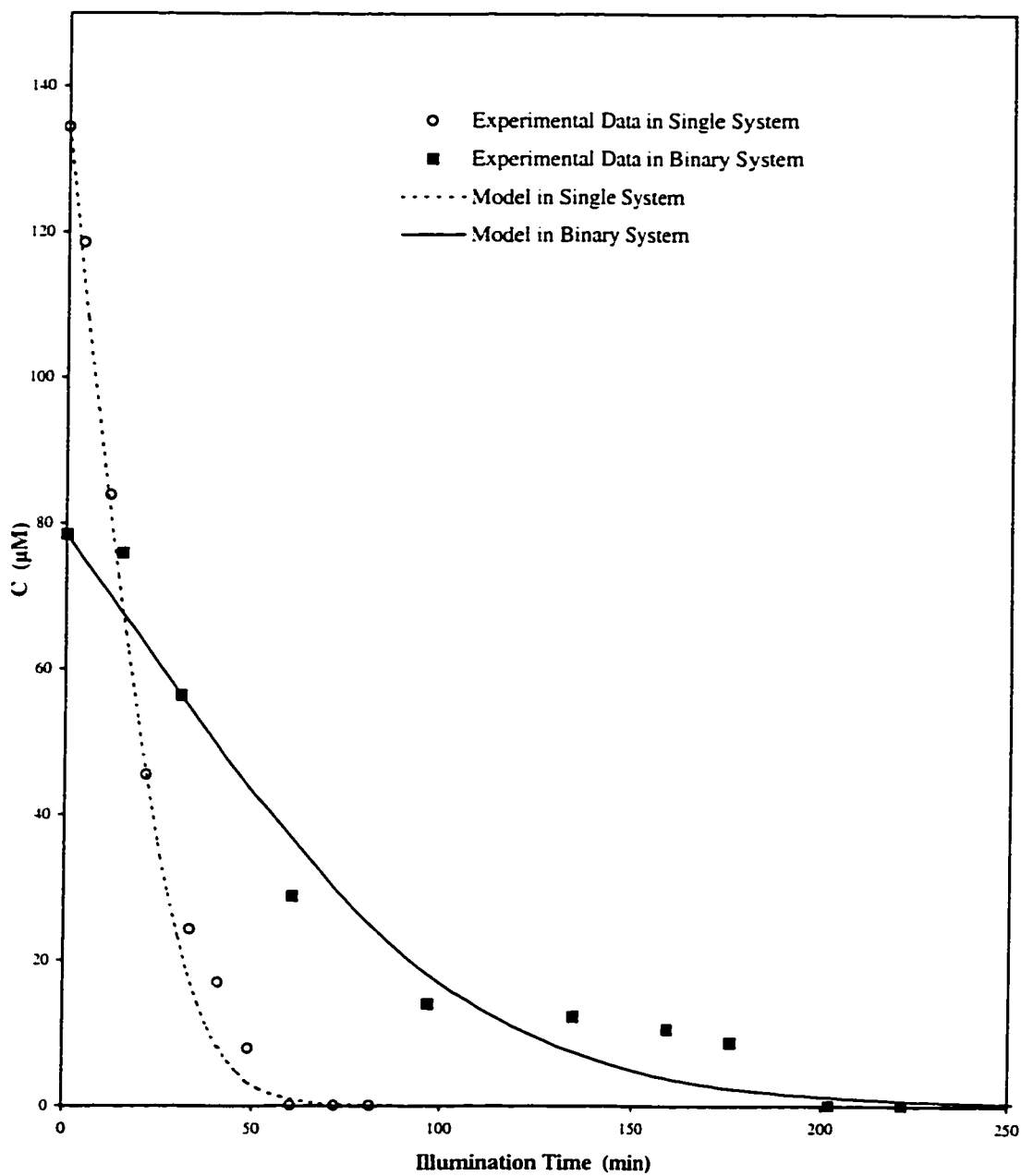


Figure 5.35: Comparison between single and binary systems for the photocatalytic degradation of DIOX in the slurry photoreactor; $C_{0,DIOX}=134 \mu\text{M}$ in single system and $C_{0,DIOX}=78.5 \mu\text{M}$ in binary system.

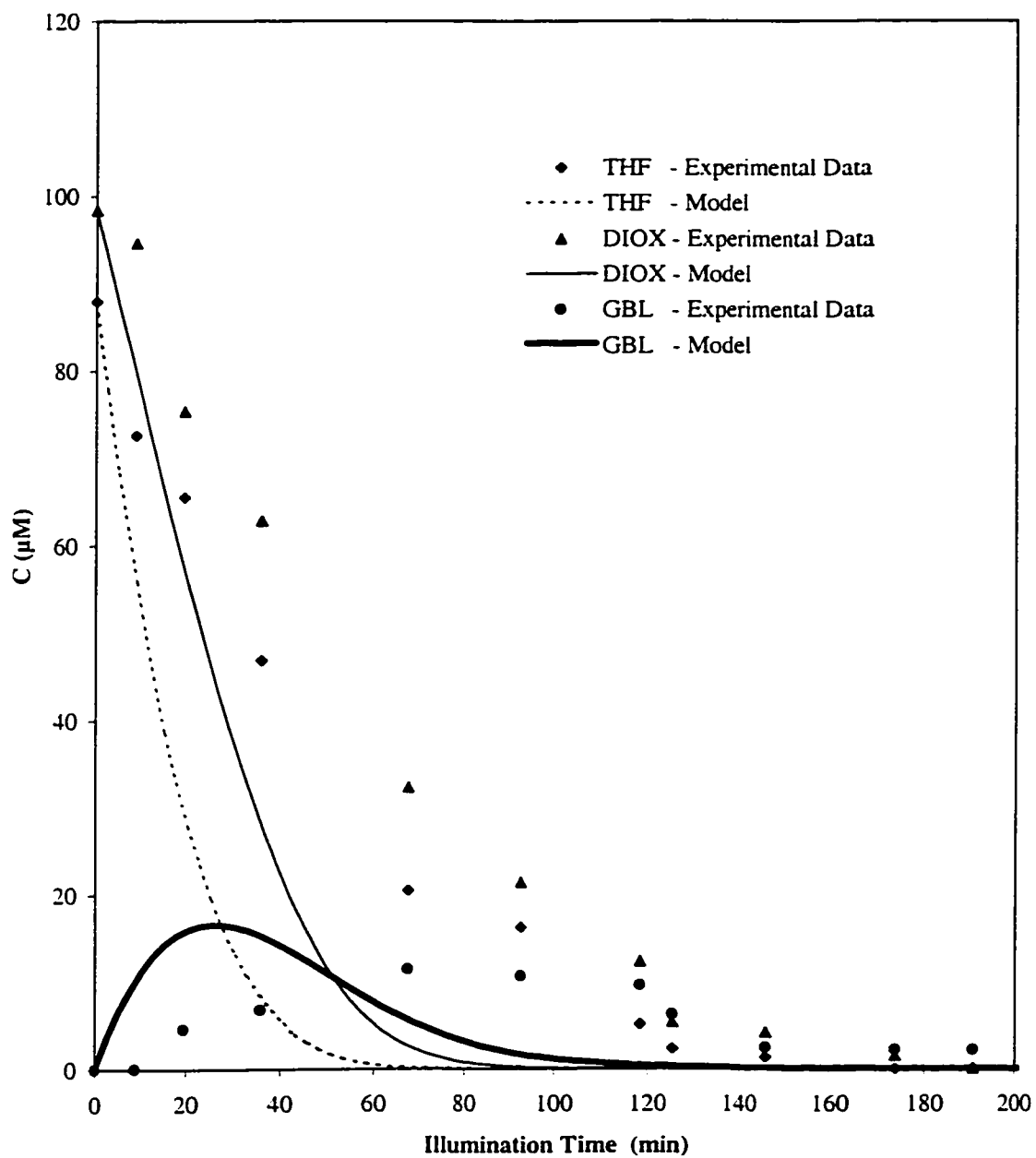
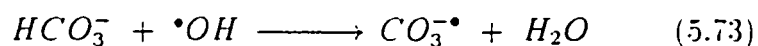


Figure 5.36: Binary model using kinetic parameters from single runs: $C_{0,THF}=87.9 \mu\text{M}$ and $C_{0,DIOX}=98.4 \mu\text{M}$.

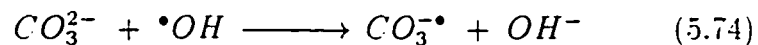
on photocatalysis need to be addressed. In this section, the effect of sodium bicarbonate on the photocatalytic degradation of the mixture of THF and DIOX is explored.

Behar et al. [23] and other researchers [1, 2, 3, 89, 218] showed that in pulse radiolysis, bicarbonate and carbonate ions react with hydroxyl radicals to produce carbonate radical ions via the following reactions:

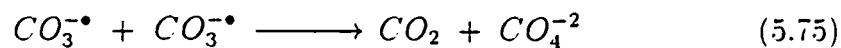
at low pH



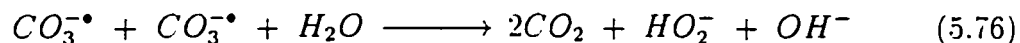
at high pH



Although the exact mechanism of the formation of these carbonate radicals is not clear, Weeks and Rabani [218] demonstrated that the decay of these carbonate radical ions may occur through the following reactions:



or



In order to study the effects of carbonate and bicarbonate anions on

the photocatalytic degradation of the mixture of THF and DIOX, a few runs with different initial concentrations of sodium bicarbonate (BDH grade) were performed.

Figure 5.37 depicts the pH changes during the trials. In the pH range of 5.5–8, both bicarbonate and carbonate anions are present with bicarbonate ions predominating. Hence, Reaction (5.73) most likely occurs in this range of pH.

Figures 5.38 and 5.39 compare two identical runs with different initial NaHCO_3 concentrations. It was expected that bicarbonate ions scavenge hydroxyl radicals and reduce the degradation rate of both THF and DIOX. In contrast, Figures 5.38 and 5.39 show that the degradation rate of THF was slightly enhanced with increasing NaHCO_3 concentration while the degradation rate of DIOX decreased. The slight increase in THF degradation rate may be due to the increase in pH. The pH change in the binary runs without sodium bicarbonate was 3.5–4.5. The pH changes for the two binary runs in the presence of sodium bicarbonate were in the ranges of 5.5–7 ($[\text{NaHCO}_3]=76.4 \text{ mg L}^{-1}$) and 6.5–8 ($[\text{NaHCO}_3]=214 \text{ mg L}^{-1}$), respectively.

Ortyl and Peck [169] demonstrated that both organic adsorption and particle suspension depend on the pH of the suspension and the point of zero charge (PZC) of titanium dioxide. PZC determines the charge characteristics of the solid surface, which is the pH at which the net surface charge is zero. The net surface charge is positive below the PZC and negative above the PZC. During sampling from the reactor in the presence of sodium bicarbonate, it was observed that the titanium dioxide particles settled down in

the vials completely after a few minutes. On the other hand, the particles did not precipitate after hours in the samples taken from the runs without sodium bicarbonate. This observation indicates that the PZC of titanium dioxide was within the working pH range of the runs with sodium bicarbonate, 5.5–8. The net surface charge of the particles becomes zero at PZC and therefore, the particles settle down easily.

Ortyl and Peck [169] found that the PZC of titanium dioxide containing anatase and rutile with $0.03 \mu\text{m}$ particle size is 6.83. Therefore, it seems that at a pH below the PZC, the THF degradation rate is enhanced (Figure 5.38). On the other hand, by almost tripling the NaHCO_3 concentration to 214 mg L^{-1} and elevating the pH above the PZC, the THF degradation rate was not significantly different from that without NaHCO_3 . This suggests that the degradation of THF is enhanced within the pH range of 5.5–7, whereas it did not show a significant change at higher pH levels. It is also possible that within the pH range of 5.5–7, THF adsorption was greater than that at pH levels above the PZC.

Although the decrease of DIOX degradation rate may be due to the shortage of hydroxyl radicals, it is possible that the DIOX degradation is favoured by lower pH conditions. Therefore, there are two factors which may play important roles in describing the degradation changes in the presence of sodium bicarbonate. These factors are:

1. Scavenging hydroxyl radicals by bicarbonate and carbonate ions
2. pH changes

Figures 5.40 and 5.41 respectively depict the total organic carbon (TOC)

and total inorganic carbon (TIC) of the binary runs in the presence of sodium bicarbonate. Figure 5.40 shows that during the initial part of the reaction, the TOC increases for the first 50 min of the illumination time and then decreases. At the same time, Figure 5.41 reveals that the TIC decreases in the initial part of the reaction and then increases.

The TOC increase in the initial part of the reaction may be due to the desorption of organic species from the catalyst surface into the liquid phase. Alternatively, it is also possible that some carbonate and bicarbonate ions convert to organics which could also explain the initial increase in TOC. Previous studies support this observation. Chandrasekaran et al. [57] and Monheit et al. [154] showed that carbonate ions could be photochemically reduced to formaldehyde. Also, Khalil [117] showed that it is likely that photocatalytically produced electrons reduce carbonate ions initially to formate, HCOO^- , and then to formaldehyde, HCHO , and methanol, CH_3OH . In addition, Aurian-Blajeni et al. [17] and Inoue et al. [113] demonstrated that CO_2 may be photocatalytically reduced to organic species such as formaldehyde and methanol over semiconductor materials. The dramatic decrease in pH during the initial stages of the reaction may indicate that bicarbonate and carbonate ions are scavenged by hydroxyl radicals and also reduced to organic species (see Figure 5.37). The increase in TIC in the second part of the reduction may be a result of CO_2 formation.

Figure 5.42 shows a typical carbon balance profile in the photocatalytic degradation of THF and DIOX in the presence of sodium bicarbonate. A slight decrease in the total carbon (TC) may be due to the fact that some

CO₂ formed during the photocatalysis process releases into the headspace. It is also possible that some of the organics and carbon dioxide produced escape from the reactor through the punctured septa.

To verify the reduction of carbonate and bicarbonate ions to organic species, a run with 214 mgL⁻¹ NaHCO₃ in the absence of organics was performed. The results of this run are depicted in Figure 5.43. The total inorganic carbon decreased dramatically in the first few minutes of the run while at the same time a slight amount of organic carbon was produced. Although the amount of total organic carbon produced was low, it is possible that the organics degraded immediately after their formation. The high degradation rate of organics produced could be easily explained by the abundance of active sites available in the system and the low concentrations of organics formed. This results in a high active site to reactant species ratio, a condition which favours a rapid reaction.

5.14 Concluding Remarks

In this chapter, the photocatalytic degradation of two compounds found in industrial wastes as well as groundwater was explored. The experimental results showed that these compounds are photocatalytically degradable. Two different photocatalysts, Degussa P25 and Hombikat UV 100, were examined and their photoactivities and optimized loads were compared.

The intermediates formed during the course of the reactions for both THF and DIOX were identified using both GC/MS and IC methods. Based on detected intermediates, hypothetical reaction mechanism pathways were

proposed and the corresponding kinetic models developed. It was shown that the photocatalytic rate equation for THF and the binary systems followed the modified LH model. It was also demonstrated that the photocatalytic degradation rates of THF and DIOX were slower in a binary system.

Finally, the effect of sodium bicarbonate on the photocatalytic degradation of the binary system was examined. It was shown that bicarbonate and carbonate ions act as hydroxyl radical scavengers which slowed down the DIOX degradation rate but did not significantly affect the THF degradation rate. The slight enhancement in the THF degradation rate in the presence of sodium bicarbonate may be due to the increase in pH. Also, there is a possibility that bicarbonate and carbonate ions reduce to other organic species during the photocatalytic reaction. Therefore, the presence of these anions should be taken into account in photocatalysis processes.

It may be a good idea to remove these anions from water or wastewater before the photocatalysis process in order to eliminate their effects. Another alternative is that in practice the effects of carbonate and bicarbonate anions are eliminated by lowering the pH to about 5 before the photocatalysis treatment [13]. This way, many of these anions are removed as CO_2 gas.

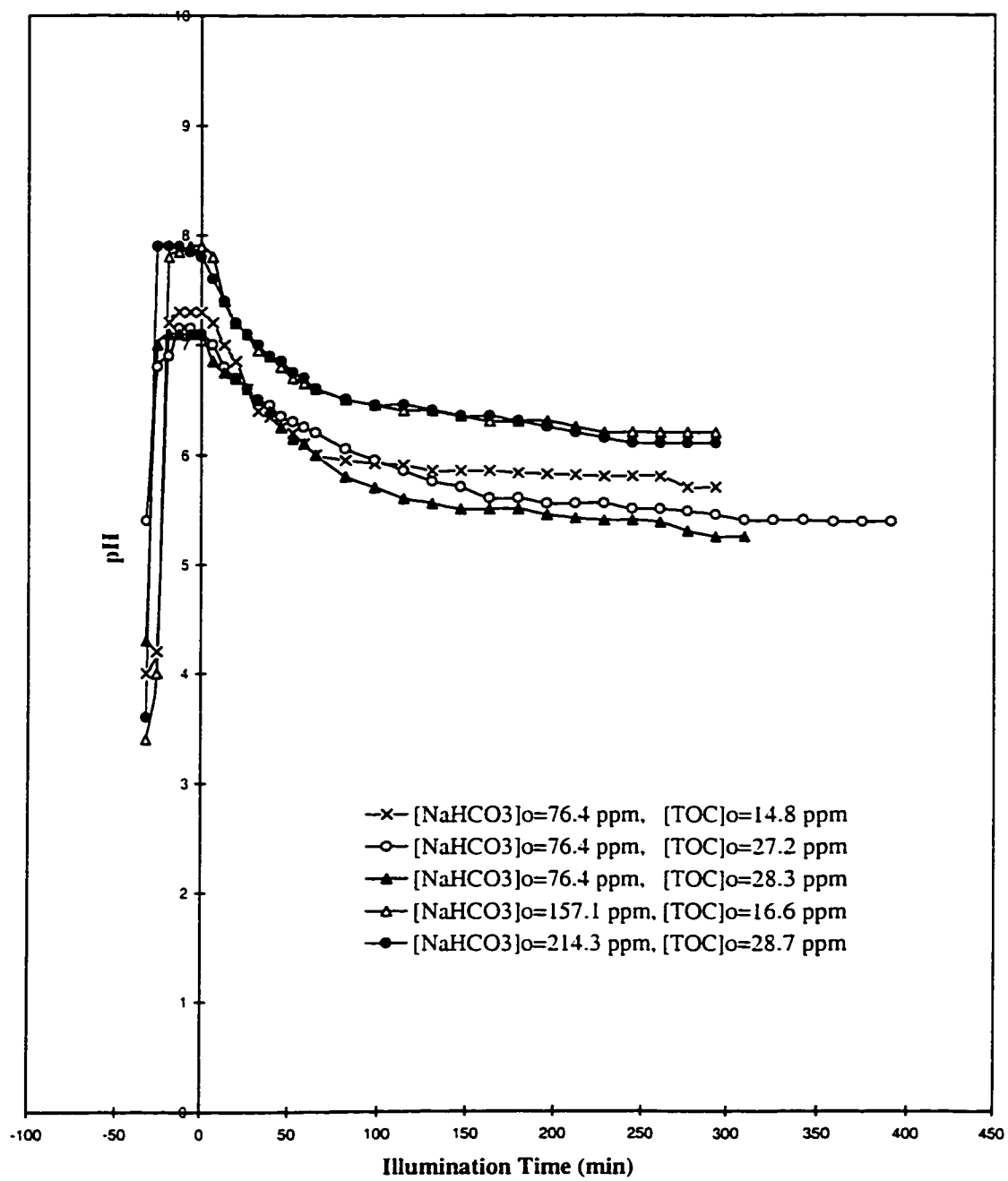


Figure 5.37: pH profile for the photocatalytic degradation of the binary system (THF and DIOX) in the presence of NaHCO_3 in the slurry photoreactor.

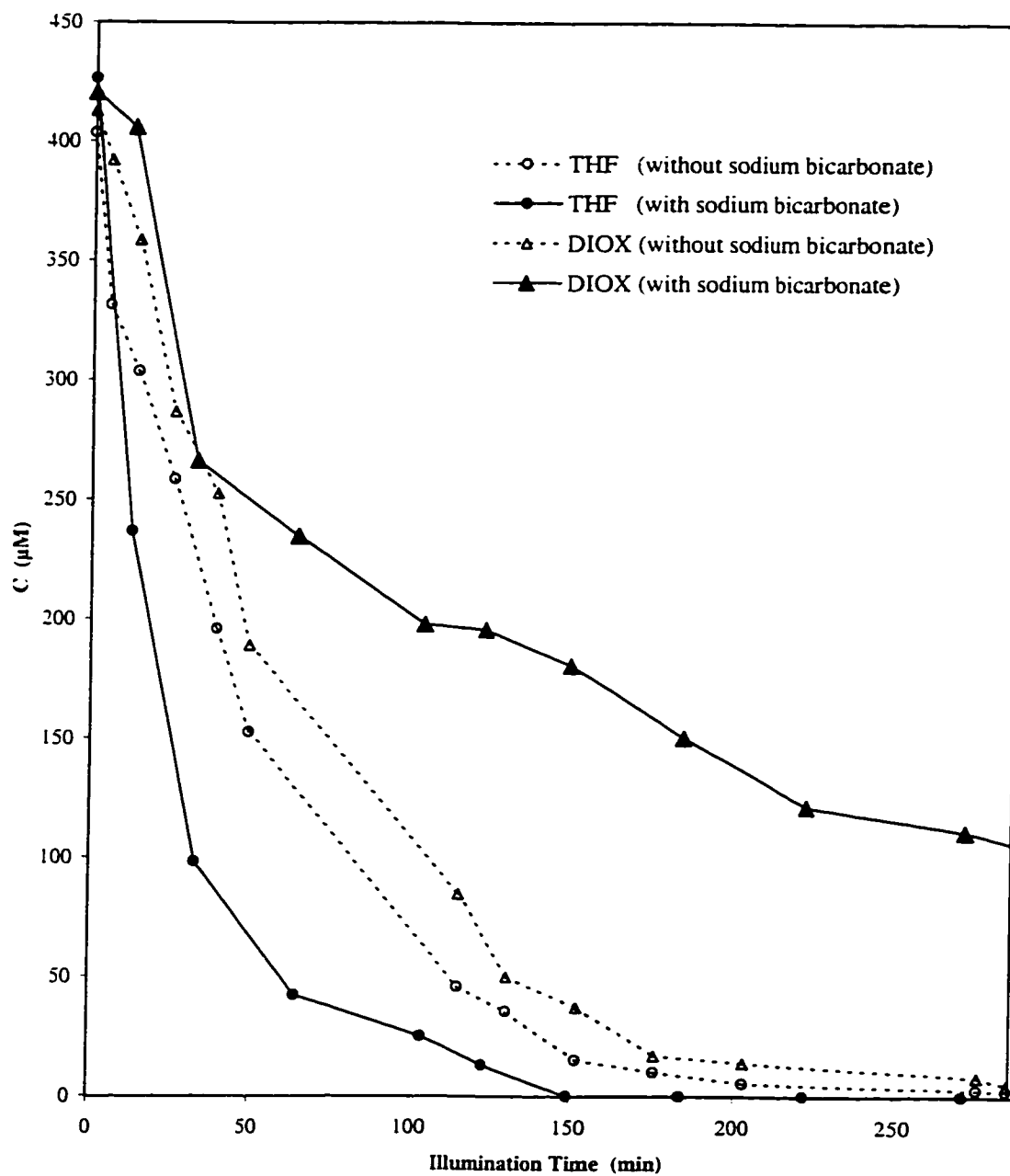


Figure 5.38: Effect of sodium bicarbonate on the photocatalytic degradation of the binary system (THF and DIOX) in the slurry photoreactor, for the run with sodium bicarbonate: $[\text{NaHCO}_3]=76.4 \text{ mg L}^{-1}$.

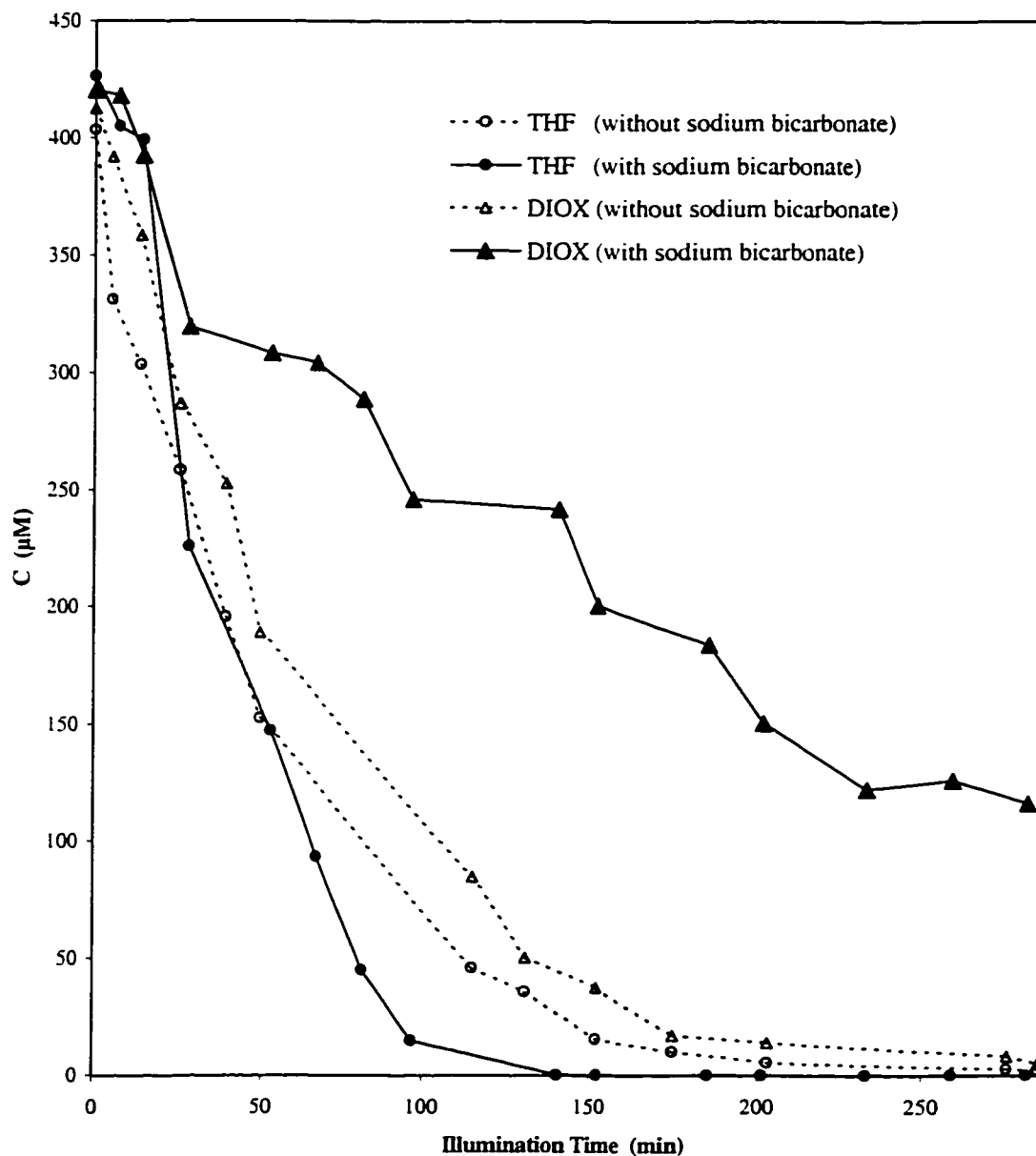


Figure 5.39: Effect of sodium bicarbonate on the photocatalytic degradation of the binary system (THF and DIOX) in the slurry photoreactor, for the run with sodium bicarbonate: $[\text{NaHCO}_3]=214 \text{ mg L}^{-1}$.

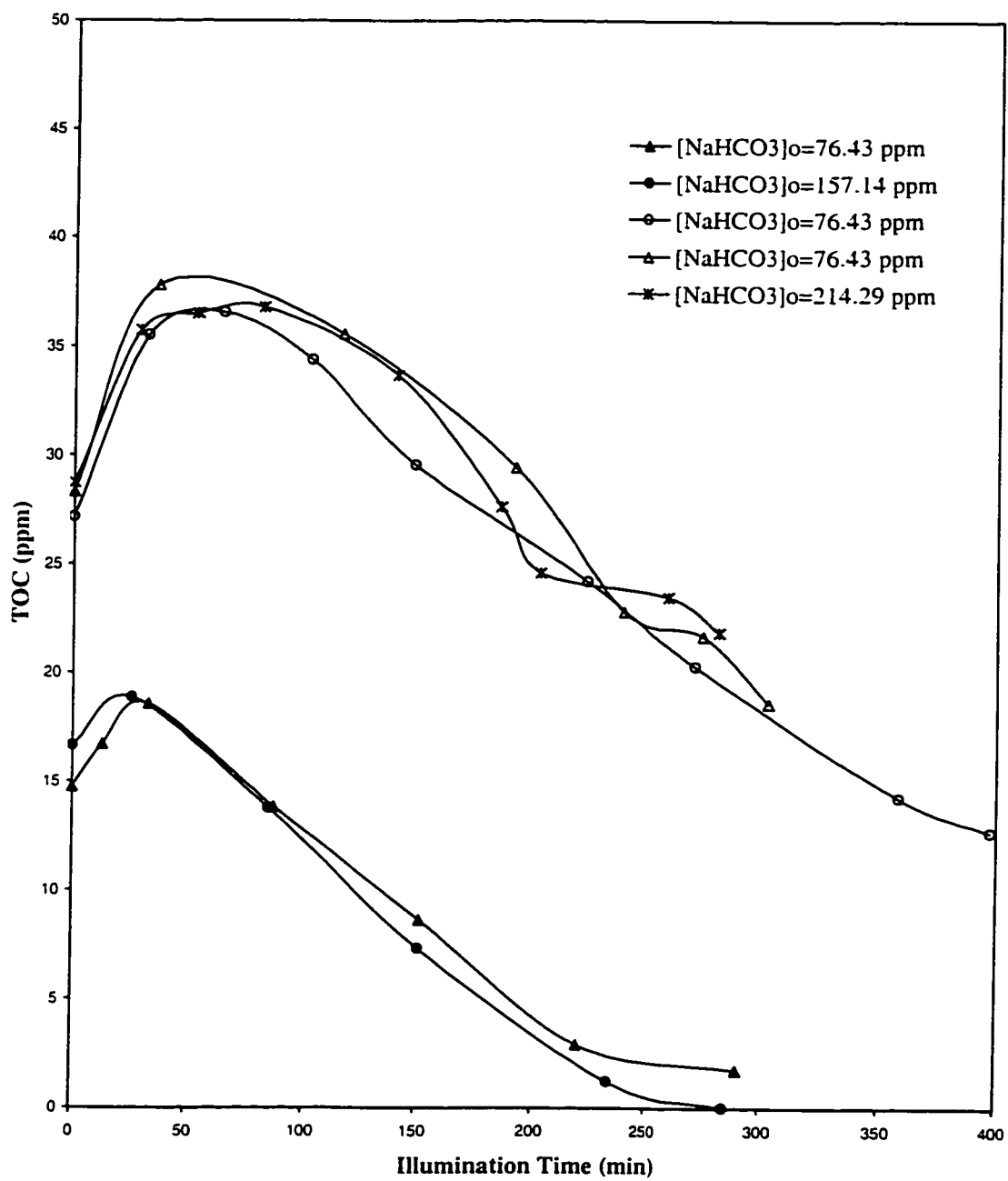


Figure 5.40: TOC profile for the photocatalytic degradation of the binary system (THF and 1,4-DIOX) in the presence of sodium bicarbonate.

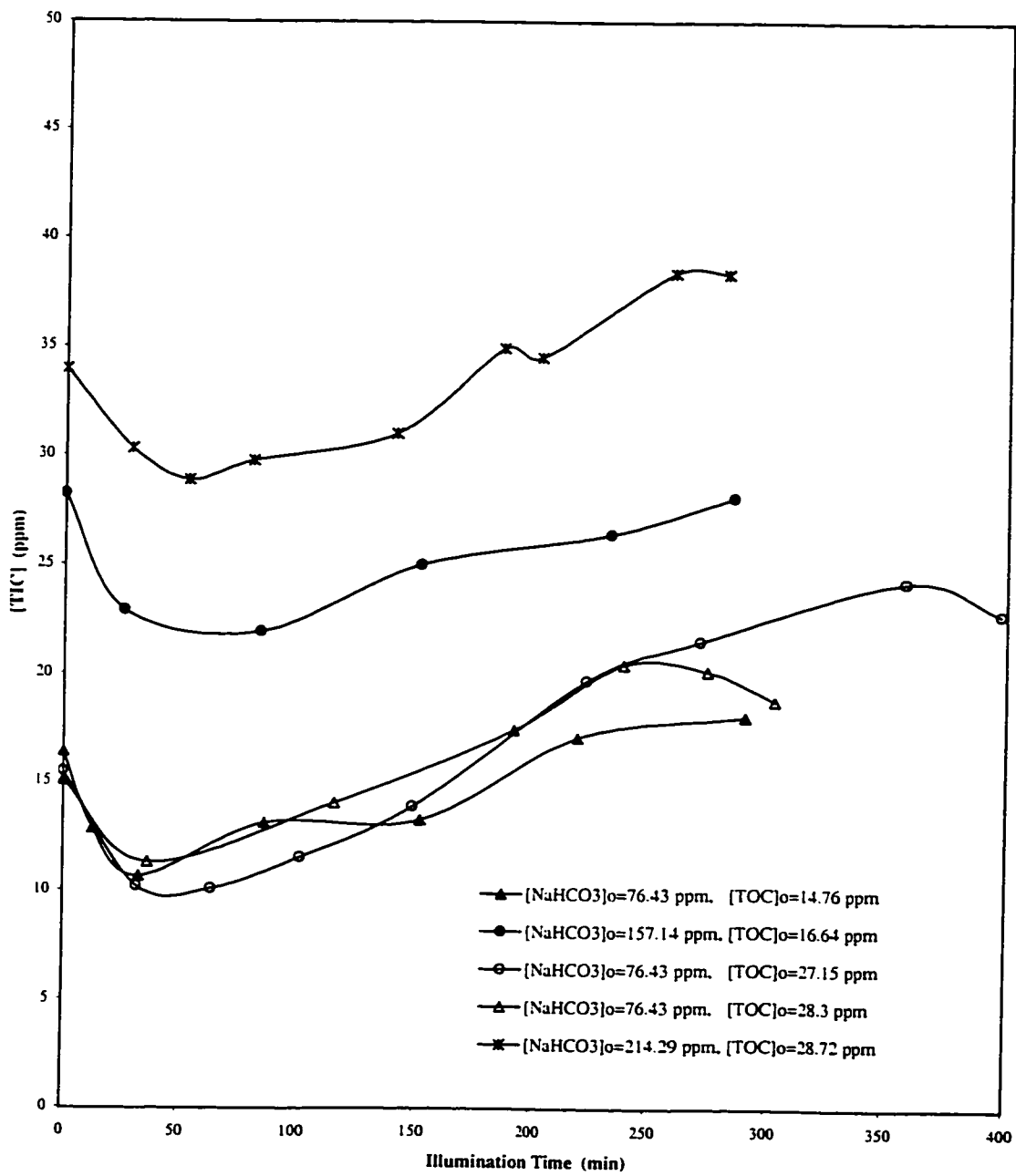


Figure 5.41: TIC profile for the photocatalytic degradation of the binary system (THF and 1,4-DIOX) in the presence of sodium bicarbonate.

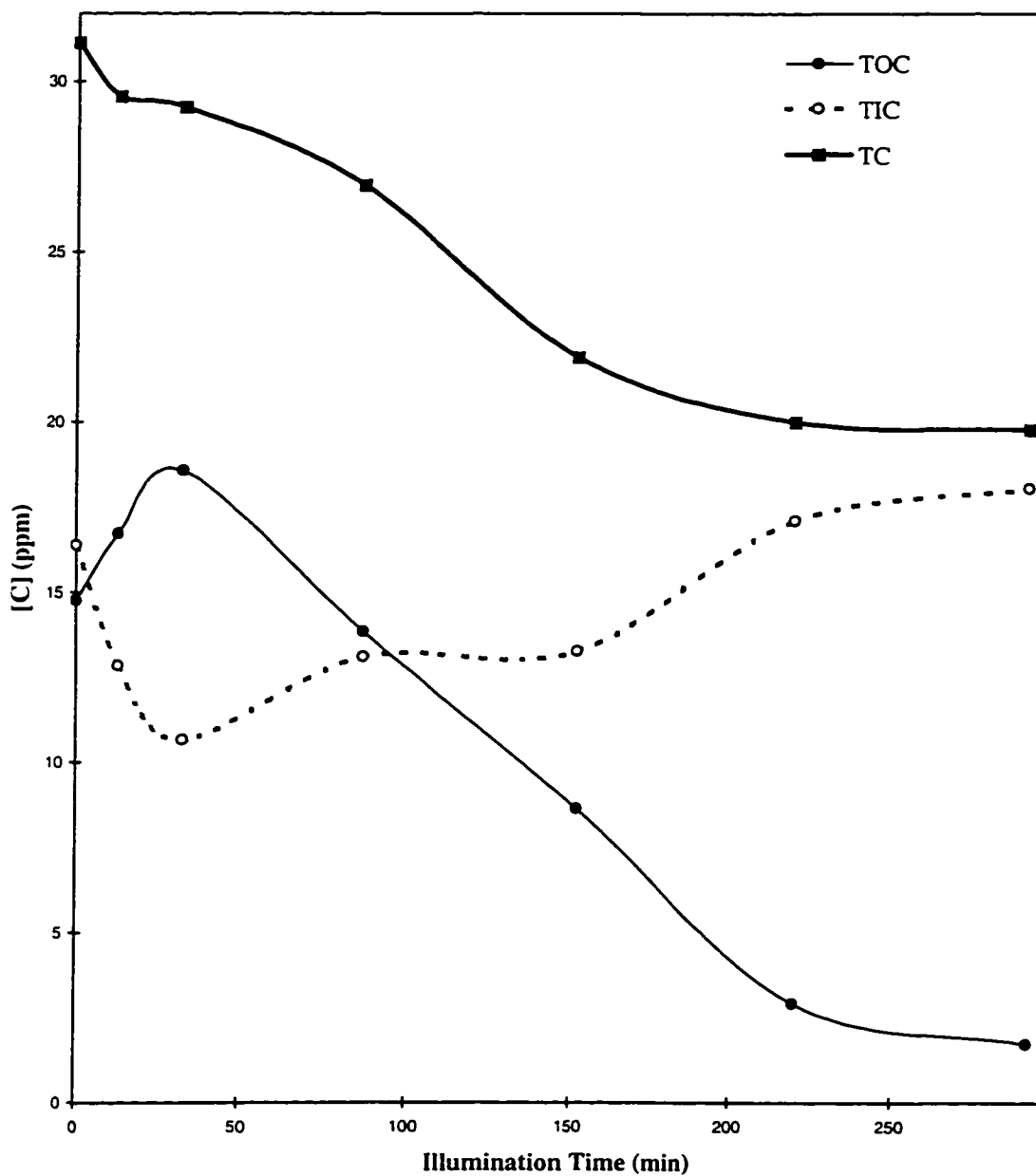


Figure 5.42: A typical carbon balance profile for the photocatalytic degradation of the binary system (THF and 1,4-DIOX) in the presence of sodium bicarbonate, $[\text{NaHCO}_3]=76.4 \text{ mg L}^{-1}$.

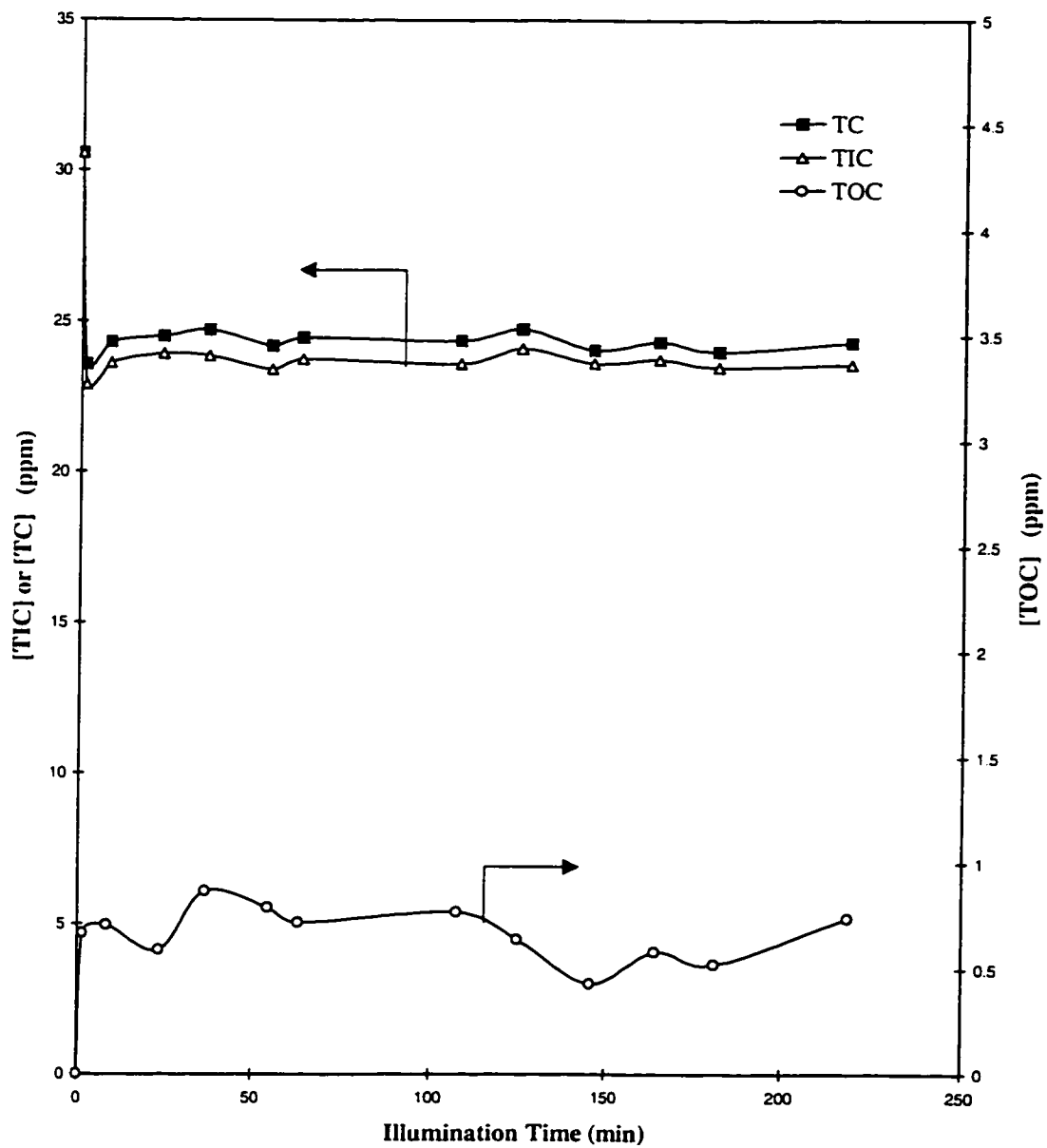


Figure 5.43: Effects of Photocatalysis on NaHCO_3 in the absence of organics; $[\text{NaHCO}_3]=214 \text{ mg L}^{-1}$.

Chapter 6

A NOVEL PACKED BED PHOTOREACTOR

In this chapter, a novel packed bed photoreactor with tellerette packings for the purpose of photocatalysis processes is presented. The experimental results for the photocatalytic degradation of 1,4-dioxane as a model organic pollutant in the tellerette packed bed photoreactor (TPBP) are discussed.

6.1 Introduction

Although the literature shows some insight in the area of photoreactors, a photoreactor which fulfills the criteria demanded by photocatalytic processes is still in the exploratory stages (see Chapters 2 and 3). It has been proven that slurry photoreactors offer superior mass transfer, high efficiency, and good mixing, but they are limited by the high cost of processing during

solid filtration or coagulation. To overcome this problem, it is necessary to immobilize the photocatalyst onto the packing surface. Immobilization is responsible for the mass transfer limitation of the organics diffusing to the surface of the catalyst. Although there are different photoreactor configurations studied previously (see Chapter 2), the design of an efficient photoreactor which eliminates mass transfer limitations while maintaining good light penetration has yet to be developed.

A good choice of a photoreactor configuration may be a packed bed photoreactor in which mass transfer restrictions are eliminated while still maintaining sufficient light penetration throughout the packing. As presented before [149], a novel fixed bed photoreactor employing tellerette packings was tested. The specifications and the method of immobilization have been explained in detail in Section 3.4.

6.2 Packed Bed Photoreactor Operation

The experimental procedures for the packed bed photoreactor were similar to those of the slurry photoreactor as explained in Chapter 3. In these experiments, 7.8 L of filtered deionized water (FDW) were fed into the photoreactor. Prior to each run, the system was aerated for half an hour. At the same time, the lights were on in order to destroy any background trace of organics possibly left in the system. Then, a certain amount of stock solution of the pollutant, in this case 1,4-dioxane, was injected into the system while the lights were off. The liquid was then allowed to recirculate for a couple of hours to reach equilibrium. The reaction was started by switching on the

lights. Periodically, samples were withdrawn from the mid-section of the photoreactor and analyzed by GC (see Section 3.5 for details). DO and pH meters monitored the dissolved oxygen and pH changes respectively during the course of the reaction.

No catalyst bleeding was observed during the runs. This was monitored visually as well as by measuring the absorbance at 350 nm at the end of each run. No significant changes for the absorbance in comparison to blank water runs were observed.

6.3 Results and Discussion

6.3.1 Light Distribution

Light is one of the essential components of any photoreactor. Therefore, designing a proper configuration in which light is properly distributed throughout the photoreactor is necessary. In the tellerette packed bed photoreactor (TPBP), the packings are designed such that sufficient light can penetrate throughout the system. Figure 6.1 depicts the UV light distribution in this photoreactor. The irradiances were measured from one side of the photoreactor while each point was illuminated from both sides. As depicted in this figure, a significant portion of the emitted light (approximately 20%) transmitted out of the photoreactor. This indicates that the photoreactor was irradiated with sufficient light throughout the system. Also, it is conclusive that the photoreactor diameter may be designed wider since the light is still able to penetrate through the packing.

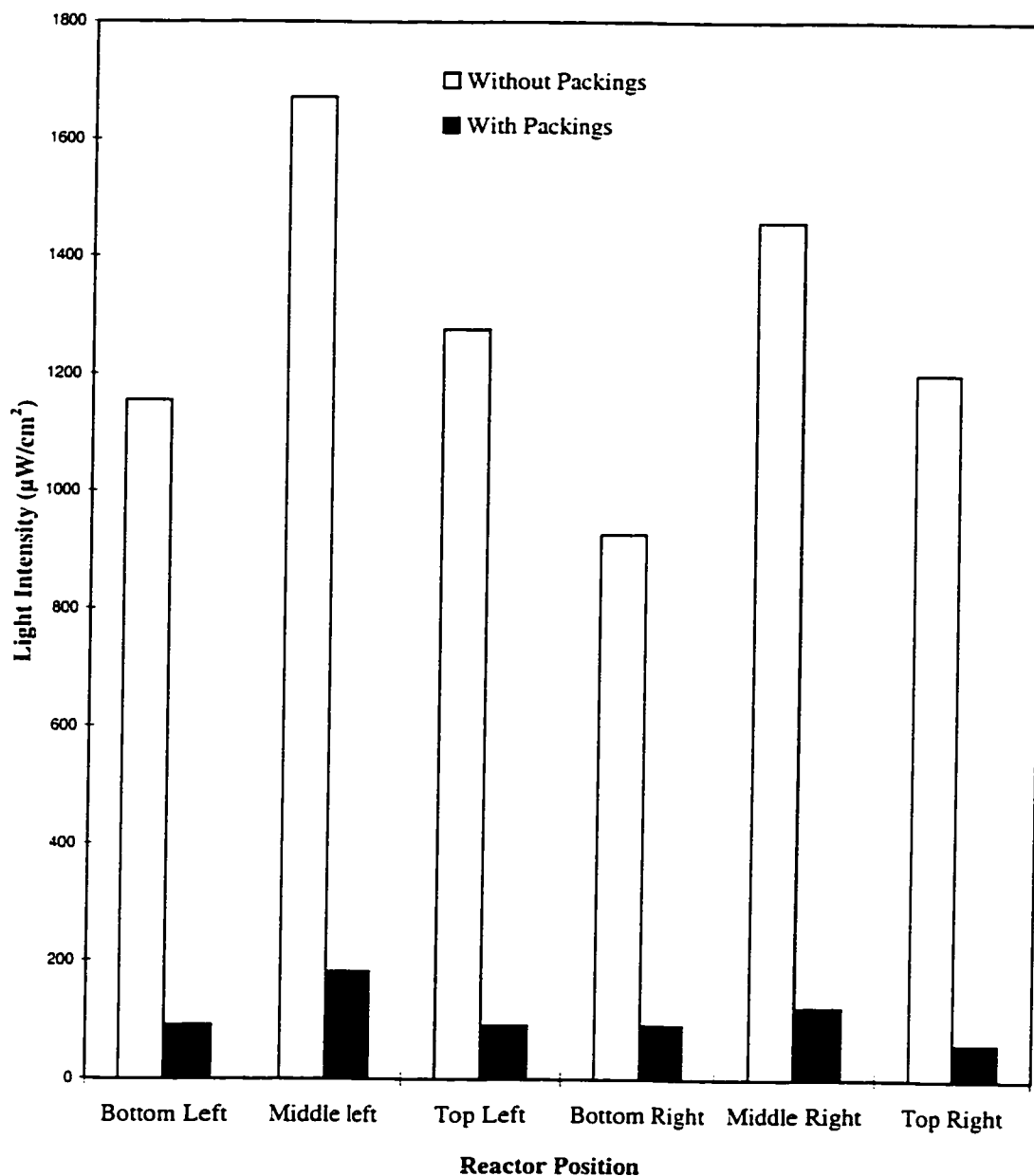


Figure 6.1: Light distribution in the packed bed photoreactor from one side. The light intensities were measured with a 320–380 nm electromagnetic wavelength sensor. The photoreactor was filled with water.

In Section 6.3.3, the details of radiation modelling will be discussed. Equation (6.7) is the Beer-Lambert law which predict the light distribution within the photoreactor. With the attenuation coefficient of $\mu=15 \text{ m}^{-1}$, the photoreactor diameter may be enlarged by three times so that 10% of emitted light is still reached to the center of the photoreactor.

6.3.2 Degradation of 1,4-Dioxane

To evaluate the performance of the packed bed photoreactor, the photocatalytic degradation of 1,4-dioxane was tested. The degradation rate in the immobilized system would be expected to be lower than that of the slurry photoreactor due to the lower catalyst surface area per unit volume in the photoreactor as well as the lower mass transfer rate of the compounds to the solid surface. Considering the slurry photoreactor used in the kinetic studies, the ratio of the photocatalyst surface area to the photoreactor volume was $75.750 \text{ m}^2 \text{ m}^{-3}$ while in the packed bed photoreactor it was $108.4 \text{ m}^2 \text{ m}^{-3}$. The ratio of the photocatalyst surface area to the photoreactor volume for the slurry photoreactor was about 700 times greater than that of the packed bed photoreactor. Hence, a higher degradation rate for 1,4-dioxane is expected in the slurry photoreactor. On the other hand, the cost and inconvenience of separation of the solid particles from the slurry favours the use of the immobilized photoreactors (see Chapter 2).

To analyze the packed bed photoreactor, the first order kinetics for 1,4-dioxane degradation was assumed.

$$-r_i = -\frac{V_r}{S} \frac{dC_i}{dt} = kC_i \quad (6.1)$$

where r_i = reaction rate of component i , [$\text{mol m}^{-2} \text{s}^{-1}$];

S = total surface area of the catalyst in the reactor, [m^2];

V_r = reactor volume, [m^3];

k = first order rate constant, [m s^{-1}].

or

$$-\frac{dC_i}{dt} = k_{app}C_i \quad (6.2)$$

where $k_{app} = k \frac{S}{V_r}$ ($[\text{s}^{-1}]$ or $[\text{min}^{-1}]$) is the apparent first order rate constant.

In Chapter 5 it was shown that 1,4-dioxane followed Langmuir - Hinshelwood type of kinetics. Since the initial concentration of 1,4-dioxane used in the packed bed photoreactor was low, first order kinetics satisfactorily fitted the experimental data.

Figure 6.3 shows the time course of the reaction occurring in the packed bed photoreactor. The first order kinetics (with $R^2 > 0.95$ for the rate constants) satisfied the experimental data (for example, see Figure 6.2). The degradation rate of 1,4-dioxane in the packed bed photoreactor was about 10 times lower in comparison to that in the slurry photoreactor. This expected decrease in the degradation rate was due to the significant difference in the photocatalyst surface areas to photoreactor volume ratio.

Although more investigation is necessary using this novel packed bed photoreactor, such as the examination of different organic pollutants and different packing sizes, some technical issues such as mass transfer enhance-

ment can be addressed. Figure 6.4 illustrates the first order rate constant change in terms of Reynolds number. The Reynolds number was estimated using the wire diameter as the characteristic length. The average velocity of the liquid (superficial velocity) in the column was used for the calculation of the Reynolds number. The average velocity was based on the empty column cross section. The range of the flow rates used in these experiments were 0-10.5 L min⁻¹. Figure 6.4 shows that first order rate constants did not change significantly with increasing flow rate, indicating that the system was not influenced by mass transfer limitations.

Although there is a lack of information regarding mass transfer correlations for tellerette packed bed reactors. Equations (6.3) and (6.4) are two different correlations estimated for small cylinders with perpendicular flow [68, 209]. These two models, plotted in Figure 6.5, have been used by analogy of heat and mass transfer.

$$Sh = (0.35 + 0.56Re^{0.52})Sc^{0.3} \quad (6.3)$$

$$Sh = (0.35 + 0.34Re^{0.5} + 0.15Re^{0.58})Sc^{0.3} \quad (6.4)$$

where Sh = Sherwood Number, [dimensionless];

$$Sc = \frac{\mu}{\rho D_{DIOX-H_2O}}, \text{ Schmidt Number, [dimensionless];}$$

$$Re = \text{Reynolds Number, [dimensionless].}$$

These two correlations are valid for the ranges of $Re=10^{-1} - 10^5$ and $Sc=0.7 - 1500$.

To determine the mass transfer coefficient in the present study, the lowest Sherwood number in this figure ($Sh=10$) is used. Mass transfer is poor at this Sherwood number and hence represents a worst-case condition. Therefore, mass transfer can be estimated by the following equation [209]:

$$k_L = \frac{Sh \cdot D_{DIOX-H_2O}}{d_{wire}} \quad (6.5)$$

where k_L = mass transfer coefficient, [$m s^{-1}$];

D_{DIOX-H_2O} = diffusion coefficient of 1,4-dioxane in water, [$m^2 s^{-1}$];

d_{wire} = diameter of wires (packings), [m].

As shown in Chapter 5, the Damköhler number, the ratio of the maximum possible reaction rate to the maximum possible mass transfer rate, is an indicator of mass transfer influence in the reactor. The Damköhler number for the packed bed photoreactor can be written as follows:

$$Da = \frac{k_{app}}{k_L a} \quad (6.6)$$

where Da = Damköhler number, [dimensionless];

k_L = mass transfer coefficient, [$m s^{-1}$];

a = specific surface area of the packings, [$m^2 m^{-3}$];

k_{app} = apparent reaction rate constant, [s^{-1}].

Using $Sh=10$, $D_{DIOX-H_2O} = 8.694 \times 10^{-10} m^2 s^{-1}$ (see Appendix D), $a_{packed} = 108.44 m^2 m^{-3}$, and $k_{app} = 0.002 min^{-1}$ (see Figure 6.4), and substituting them into Equations (6.5) and (6.6), the Damköhler number was estimated to be 5.7×10^{-2} . This number is still less than one which confirms

that mass transfer does not have a significant influence on the reaction rate.

6.3.3 Radiation Modelling and Mass Transfer in the Packed Bed Photoreactor

The focus in this section is on the mass transfer effects in different positions of the photoreactor. To do this, the radiation profile inside the photoreactor must be known or estimated by modelling. Although there is a scarcity of work on radiation modelling in photocatalysis, there are a few studies in the past, mostly in homogeneous media systems (for example see [9, 10, 54, 55, 56, 214, 224, 229]).

For radiation modelling of the packed bed reactor, the following assumptions were made:

1. The light provides parallel, uniform, and radial radiation (Radial Incidence Model (RI Model)). Therefore, neither the axial nor the angular dependence are considered in the radiation modelling [9].
2. The light scattering due to the packings is also neglected.
3. The effect of packings is embedded in the attenuation coefficient, which was estimated using the experimental data.
4. For each element of the photocatalyst surface, only the light from one side contributes to the intensity.

Although there are a few radiation models for homogeneous systems [9, 54, 55, 56] and heterogeneous systems [10], they are not applicable to this

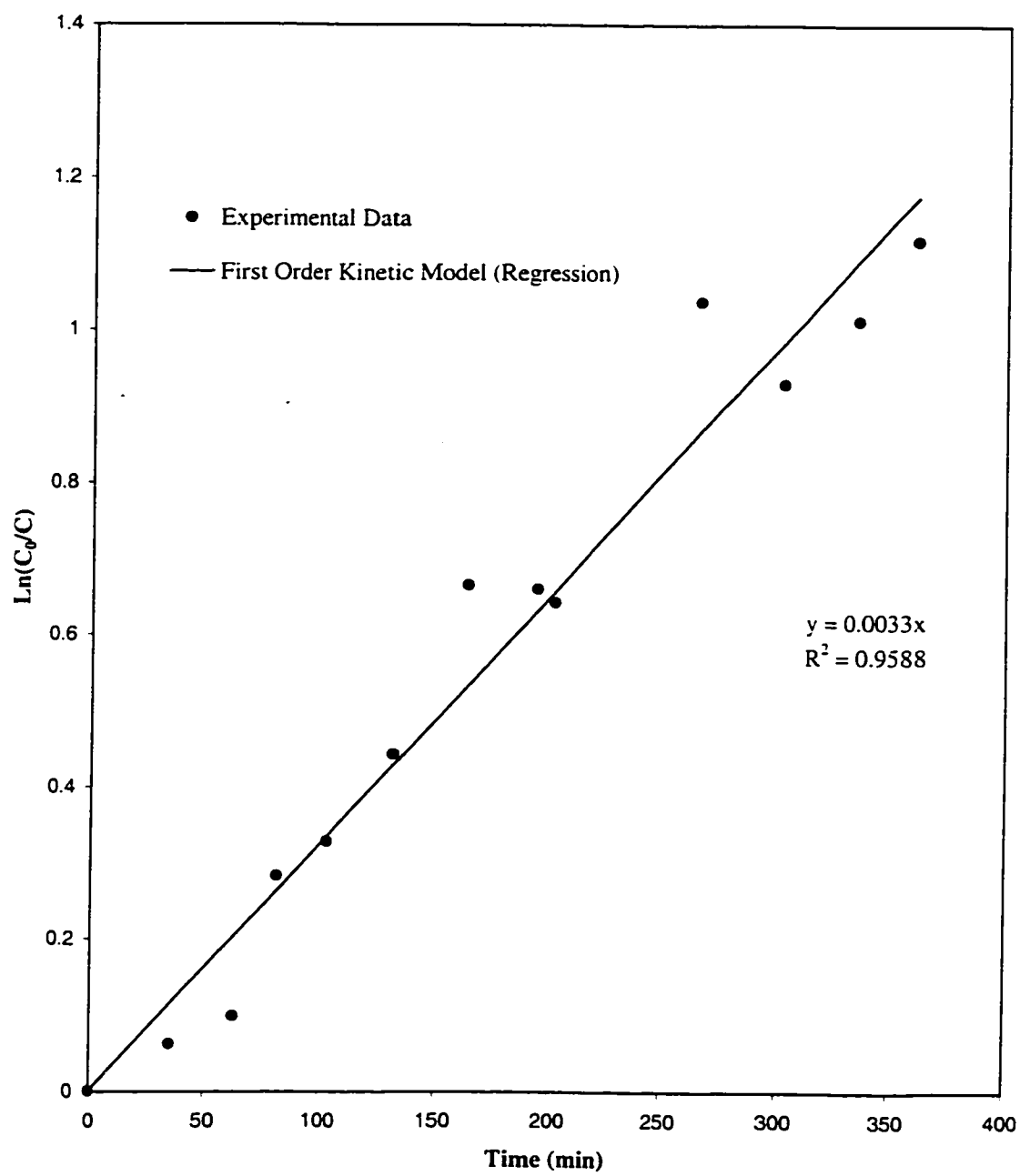


Figure 6.2: Test for first order kinetics of 1,4-dioxane in the packed bed photoreactor; $Q=2.08 \text{ L min}^{-1}$ (0.55 gpm).

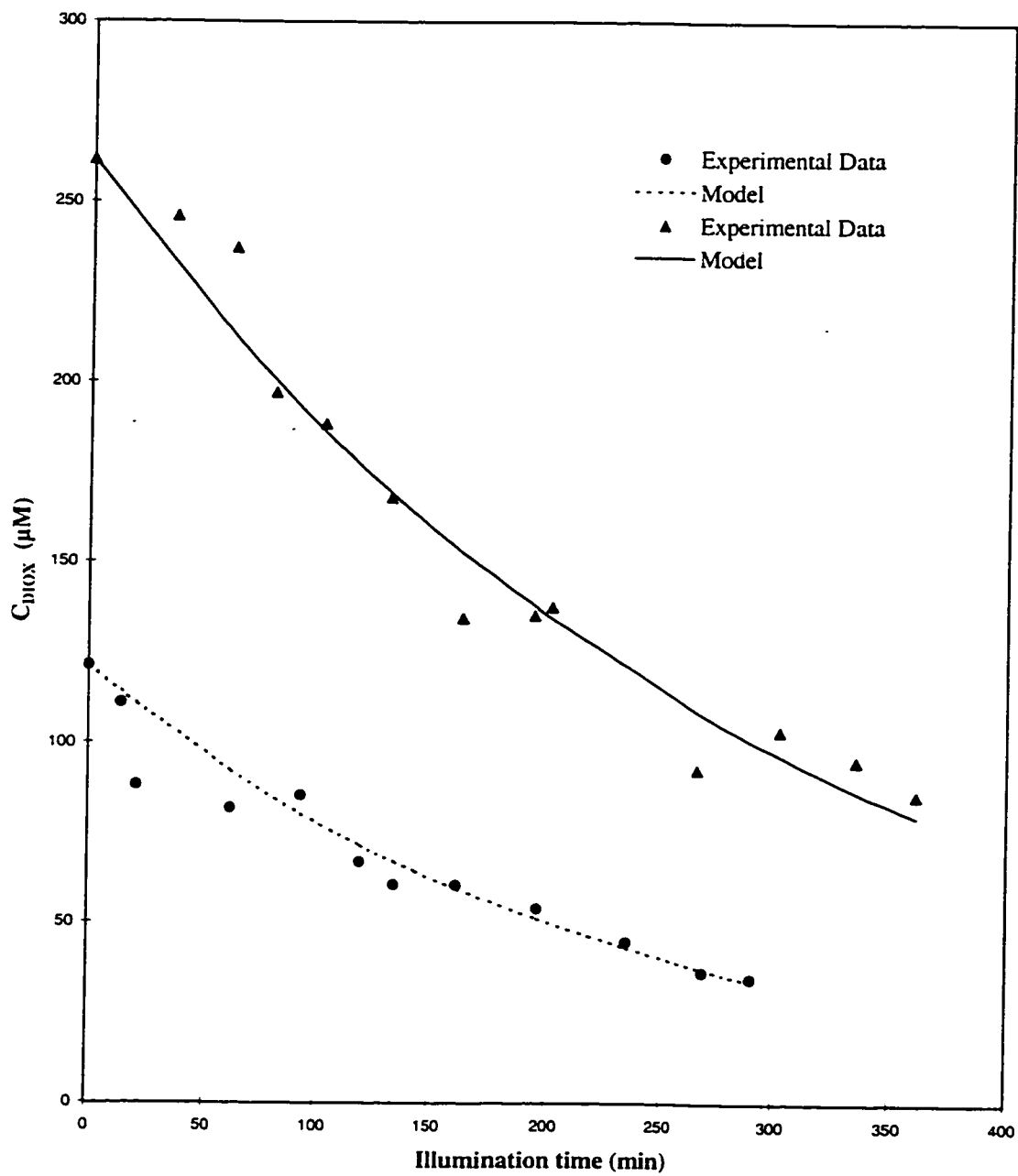


Figure 6.3: Photocatalytic degradation of 1,4-dioxane in the packed bed photoreactor (solid and dotted lines are first order kinetic models), $Q=2.08 \text{ L min}^{-1}$ (0.55 gpm); $\tau=3.75 \text{ min}$.

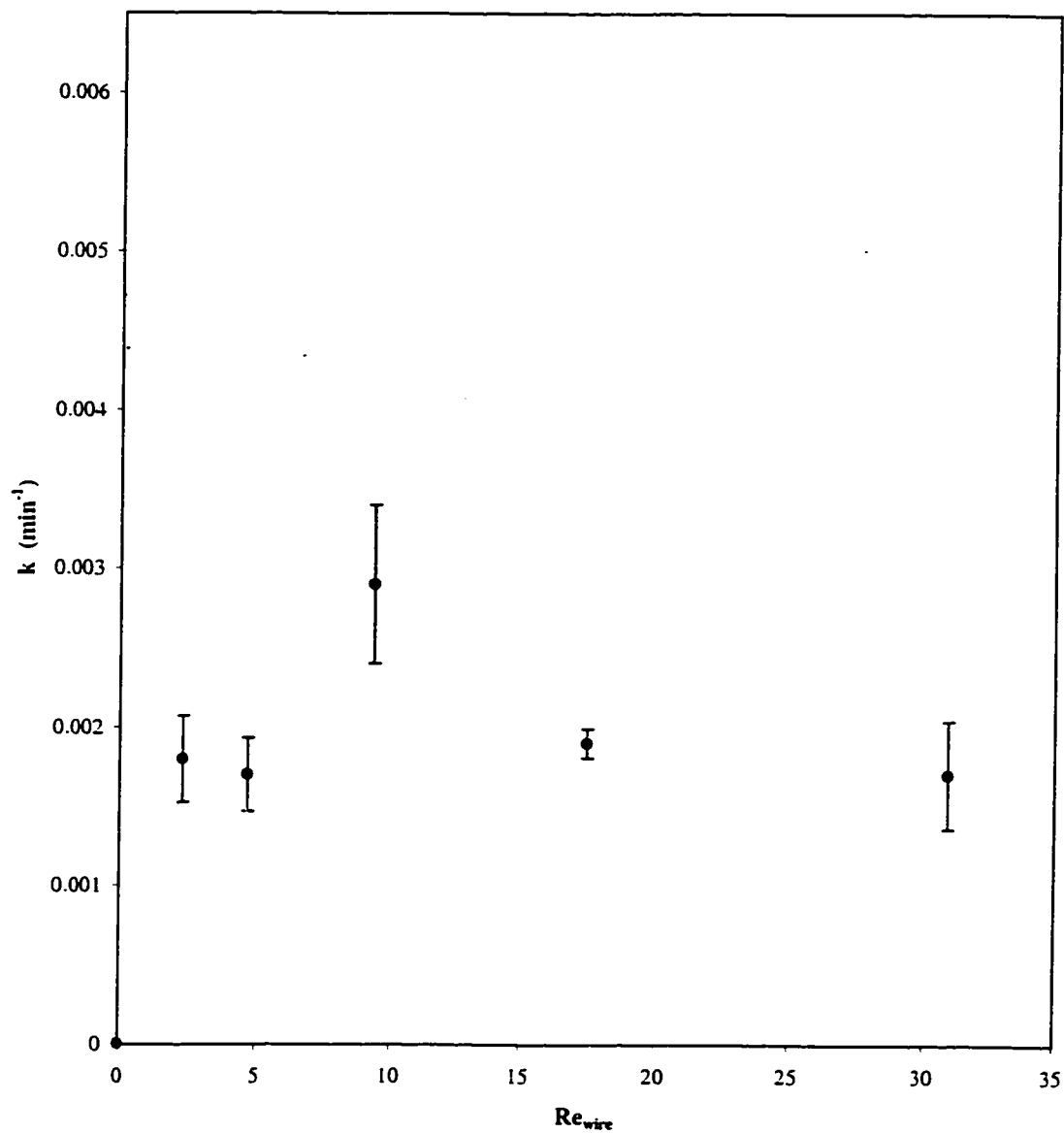


Figure 6.4: First order rate constant versus Reynolds number for the photocatalytic degradation of 1,4-dioxane in the packed bed photoreactor.

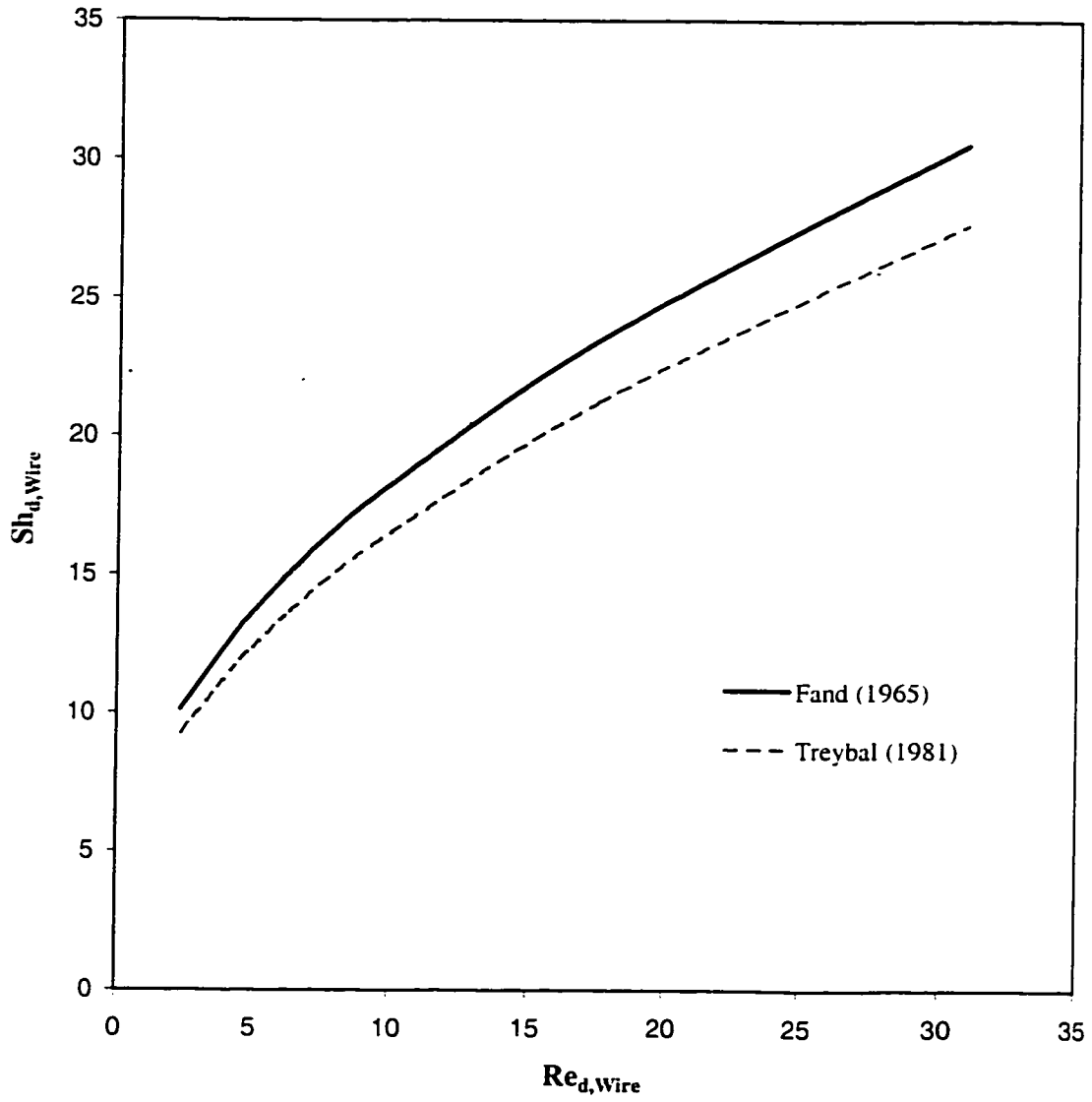


Figure 6.5: Mass transfer effect by correlations of the Sherwood number versus Reynolds number (Equations (6.3) and (6.4)) for a single cylinder with a perpendicular flow [68, 209].

packed bed photoreactor simply because each element of the photoreactor is only irradiated from one side and the light coming from the other side of the photoreactor cannot contribute significantly to the irradiance, due to the blocking effect of the packings. Also, they suffer from the drawback of the infinite irradiance prediction at the photoreactor center line [54]. Considering the aforementioned assumptions, a simple Beer-Lambert law may be applied to this system in order to show roughly the effects of mass transfer in different positions of the photoreactor. The Beer-Lambert law for this geometry (see Figure 6.6) may be written as follows:

$$\frac{I}{I_w} = e^{-\mu(R-r)} \quad (6.7)$$

where I = photon flux at any radius r . [Einstein $\text{m}^{-2} \text{s}^{-1}$];

I_w = photon flux at $r=R$. [Einstein $\text{m}^{-2} \text{s}^{-1}$];

R = radius of the photoreactor. [m];

μ = attenuation coefficient. [m^{-1}].

Based on the irradiance measurements, the attenuation coefficient for the packed bed photoreactor was estimated using the Beer-Lambert law as follows:

$$\frac{I_T}{I_o} = e^{-\mu D} \quad (6.8)$$

I_o is the emitted irradiance at one side of the photoreactor and I_T is the transmitted irradiance at the other side after passing through the length D , the photoreactor diameter (see Figure 6.1). Since I_T/I_o was different

throughout the photoreactor, the value of μ was estimated to be in the range of 3–30 m^{-1} .

Equation (6.7) is plotted in Figure 6.7 for different attenuation coefficients. As this figure shows, the transmitted light increases by decreasing attenuation coefficient.

The apparent kinetic rate constant, k_{app} , may be written as follows [213]:

$$k_{app} = kI^{0.5} \quad (6.9)$$

To estimate the local apparent rate constant, the following relationship for the small increments of $\Delta r = r_{i+1} - r_i$ in Figure 6.6 may be written:

$$(r_{i+1} - r_i) k_{app}|_{\frac{r_i+r_{i+1}}{2}} = \int_{r_i}^{r_{i+1}} k_{app}|_r dr \quad (6.10)$$

By substituting Equations (6.7) and (6.9) into Equation (6.10), we have:

$$k_{app}|_{\frac{r_i+r_{i+1}}{2}} = \frac{k'}{r_{i+1} - r_i} \int_{r_i}^{r_{i+1}} (\epsilon^{-\mu(R-r)})^{0.5} dr \quad (6.11)$$

The value of k' can be estimated using the overall k_{app} , which was found experimentally, as follows:

$$k' = kI_w^{0.5} = \frac{R \cdot k_{app}|_{overall}}{\int_0^R (\epsilon^{-\mu(R-r)})^{0.5} dr} \quad (6.12)$$

By substituting Equation (6.12) into Equation (6.11) and integrating, the following expression represents the local k_{app} in the photoreactor for the small increments of Δr :

$$k_{app}|_{\frac{r_i+r_{i+1}}{2}} = \frac{R.k_{app}|_{overall}}{\left(1 - e^{-\frac{\mu R}{2}}\right)(r_{i+1} - r_i)} \left(e^{-\frac{\mu}{2}(R-r_{i+1})} - e^{-\frac{\mu}{2}(R-r_i)}\right) \quad (6.13)$$

Figure 6.8 depicts the local apparent rate constants estimated using Equation (6.13). This figure indicates that the apparent rate constant is not significantly changing in different positions of the photoreactor for the low values of attenuation coefficients ($\mu < 10$). However, as attenuation increases, in other words, as the packings are tighter, and therefore the surface area increases, the apparent rate constant decreases in the region close to the center and increases in the vicinity of the photoreactor wall. This is due to the fact that when the packings are tighter, there is less light irradiation reaching the center region, while at the same time the surface area in the vicinity of the wall increases, therefore leading to a higher reaction rate. In general, it is conclusive that in the range of the attenuation coefficients of interest the apparent rate constant does not strongly affect the reaction rate in different positions of the photoreactor. The values of local Damköhler numbers were also estimated using Equation (6.6). The results are shown in Figure 6.9. The same trends were found for Damköhler numbers for different attenuation coefficients. As Figure 6.9 illustrates, the values of Damköhler numbers are still significantly less than one in different regions of the photoreactor, which indicates mass transfer limitations in this packed bed photoreactor are insignificant.

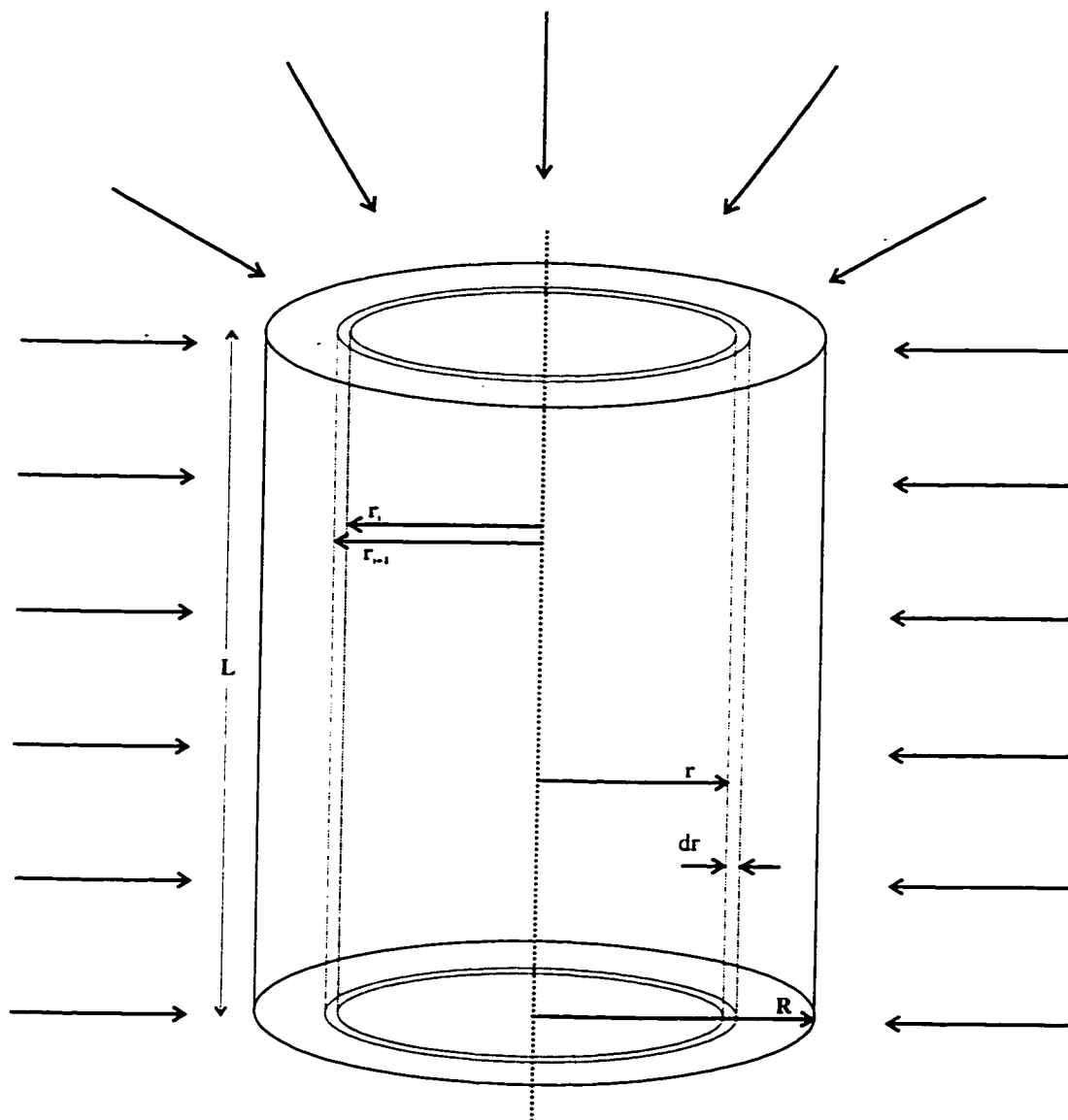


Figure 6.6: Cylindrical photoreactor geometry.

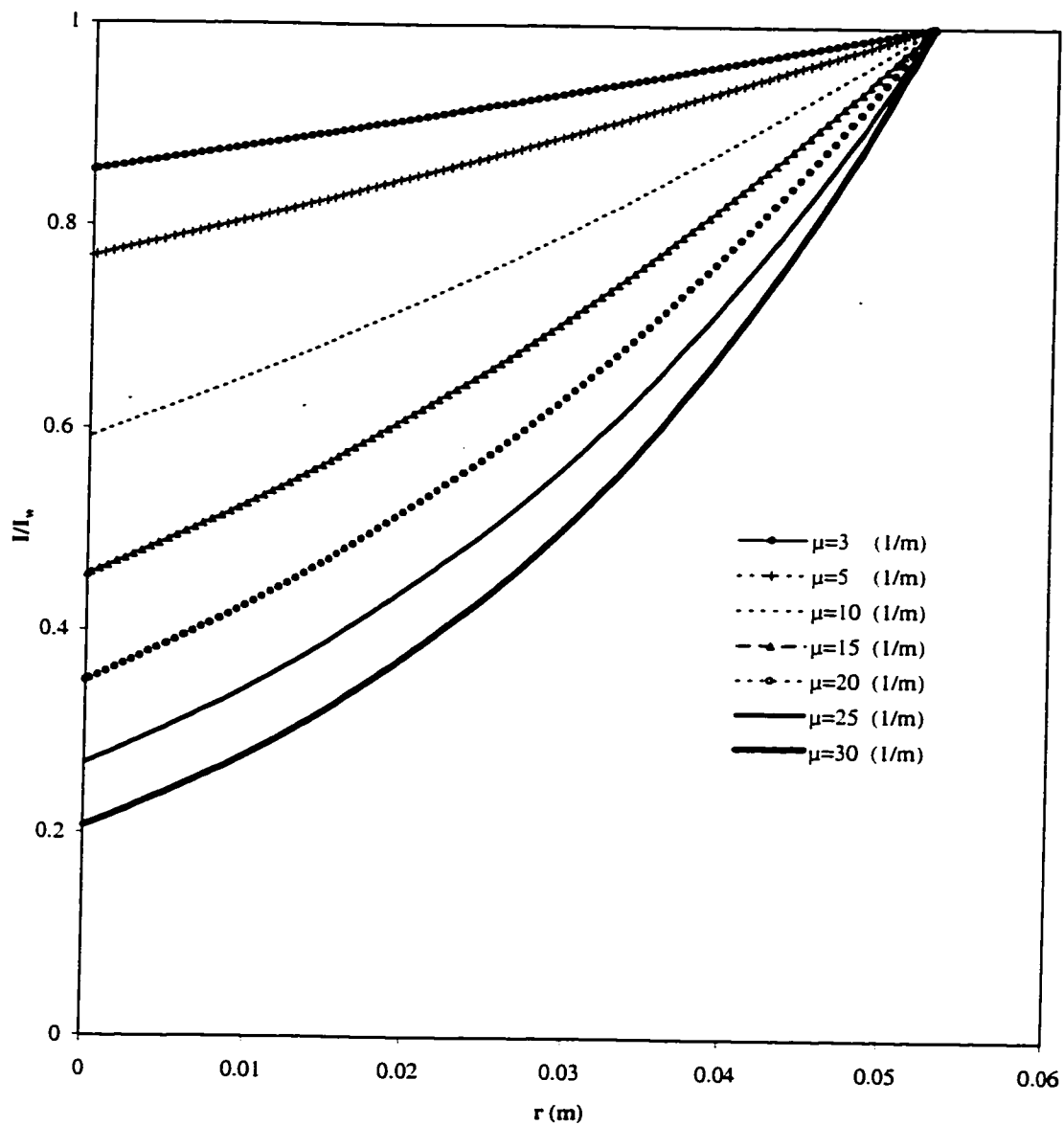


Figure 6.7: Irradiance distribution in the packed bed photoreactor with uniform, parallel, and radial radiation from outside using the Beer-Lambert law. The inner radius of the photoreactor is 0.0525 m.

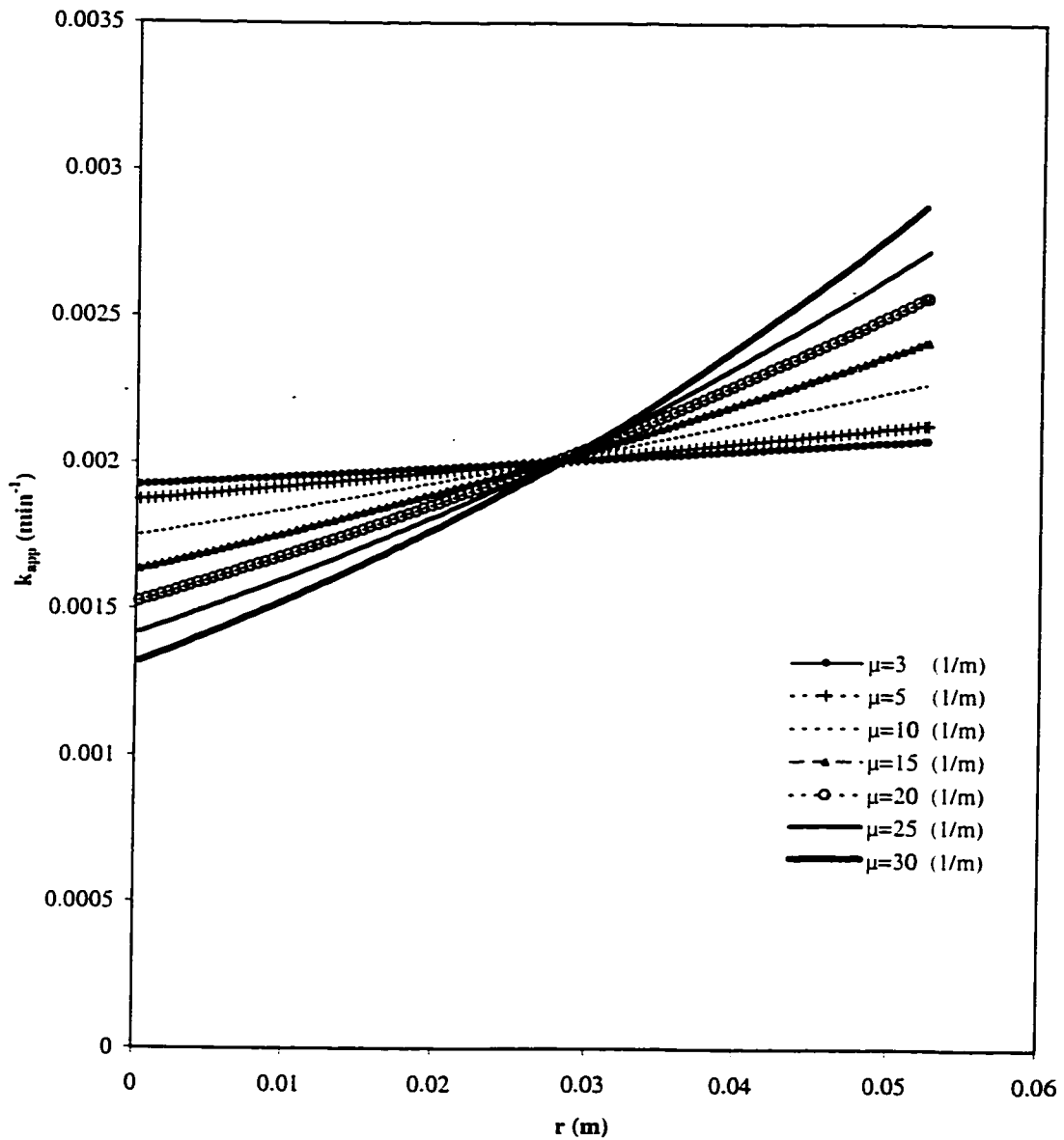


Figure 6.8: Local apparent rate constant profile for the degradation of 1,4-dioxane in the packed bed photoreactor for different attenuation coefficients. The radiation model is based on the Beer-Lambert law radiation model.

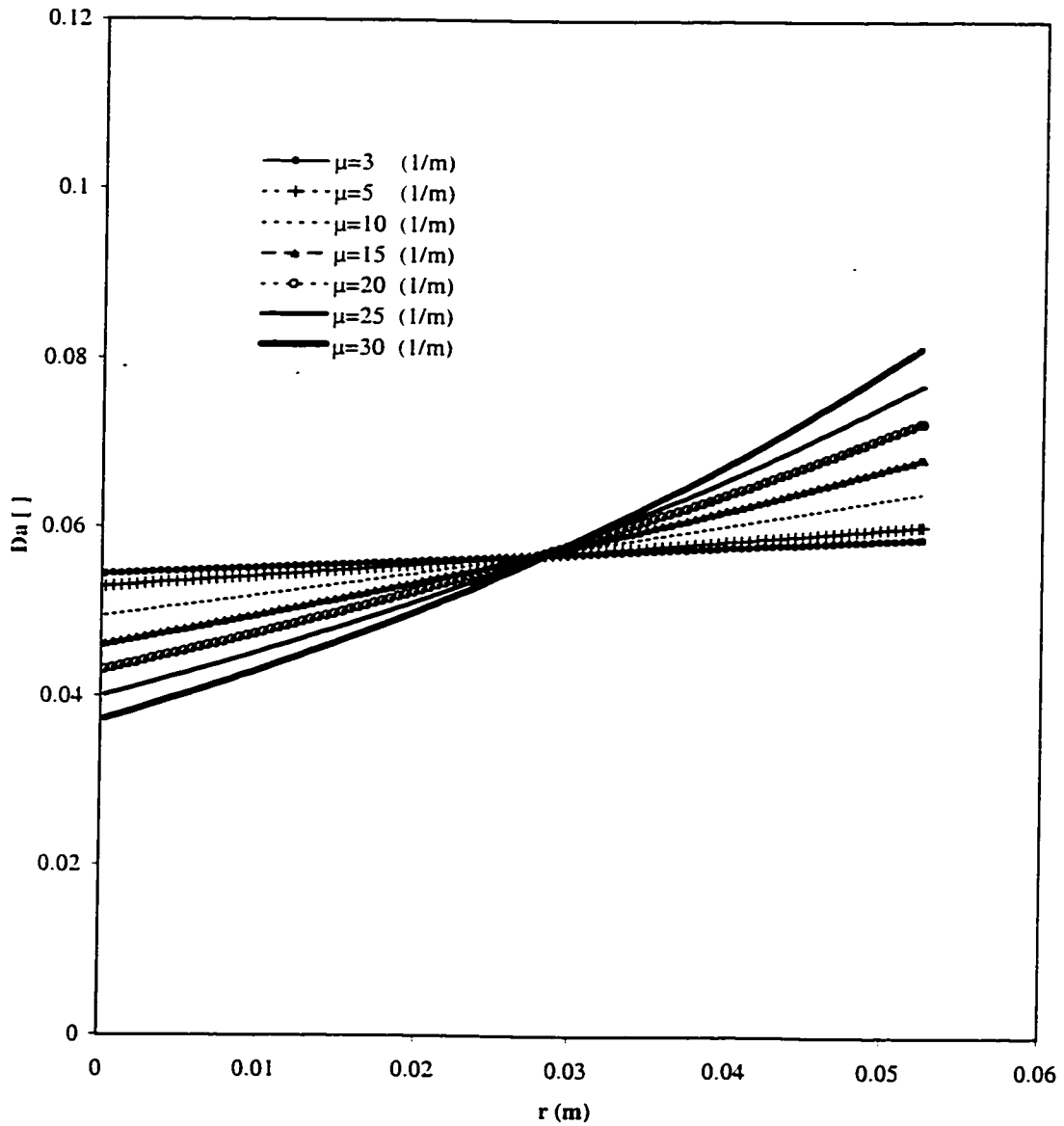


Figure 6.9: Local Damköhler number profile in the packed bed photoreactor for different attenuation coefficients. The radiation model is based on the Beer-Lambert law.

6.3.4 Energy Efficiency of the Packed Bed

Photoreactor

Bolton and Cater [31] defined the *Electrical Energy per Order* (EE/O) as a figure-of-merit to compare treatment efficiencies of different processes in which the light is one of the key parts of the process. As shown in Equation (6.14), the EE/O is expressed as the electrical energy in kilowatt hours (kWh) required to mineralize a pollutant by one order of magnitude in one cubic meter of contaminated water [30, 31, 190].

$$EE/O = \frac{P \times (\frac{t}{60}) \times 1000}{V_{tot} \times \log(C_o/C_f)} \quad (6.14)$$

where P = total lamp power, [kW];

t = irradiation time, [min];

V_{tot} = total volume of the liquid in the photoreactor, [L];

C_o = initial concentration, [μ M];

C_f = final concentration, [μ M].

The assumption of the first order kinetics is applied to this expression [31]. Therefore, Equation (6.14) may be simplified as follows [190]:

$$EE/O = \frac{38.4P}{V_{tot}k_{app}} \quad (6.15)$$

where k_{app} is the apparent first order rate constant of species i in terms of min^{-1} . The processes with higher efficiencies have lower EE/O values because they consume less electrical energy and also their conversion rates are higher.

Although there is a lack of information about EE/O values of different photocatalytic reactors for 1,4-dioxane degradation, the order of magnitude of the EE/O for this photoreactor may give useful information about its performance. For 1,4-dioxane with initial concentration of about $260 \mu\text{M}$, 6 UV lamps with 20 watts each, and $k_{app} = 0.002 \text{ min}^{-1}$, by using Equation (6.15) the EE/O was estimated to be $295.4 \text{ [kWh/(m}^3\text{ order)]}$. The value of the EE/O for the slurry photoreactor for the degradation of 1,4-dioxane with initial concentration of $316 \mu\text{M}$ was also found to be $15.4 \text{ [kWh/(m}^3\text{ order)]}$. Although the value of the EE/O for the slurry photoreactor is lower by one order of magnitude, the value of the EE/O for the packed bed photoreactor with the $260 \mu\text{M}$ initial concentration may still be considered reasonable in comparison to the EE/O values of other photocatalytic reactors which were used for other species with lower initial concentrations (see Table 6.1).

The EE/O value for this photoreactor is not comparable to the one used for degradation of 1,4-dioxane using UV photolysis (including hydrogen peroxide) [190], however this photoreactor is not optimized at all. Further improvements might be needed in order to optimize this photoreactor for its best performance. To optimize the performance of this tellerette packed bed photoreactor, the following improvements might be considered:

1. longer light path;
2. tighter packing for more surface area and light absorption (see Figure 6.1).

Improving this packed bed photoreactor can lead to a higher conversion rate, and therefore lower EE/O.

Table 6.1: Examples of the values of the EE/O for different photoreactors studied previously.

POLLUTANT	PHOTOREACTOR TYPE	C_0 [μM]	EE/O [kWh/(m ³ order)]	REFERENCE
1,4-Dioxane	TPBP	260	295.4	This study
1,4-Dioxane	Slurry	316	15.4	This study
1,4-Dioxane ¹	UV/H ₂ O ₂	1135	3.2	Safarzadeh-Amiri et al. [190]
1,4-Dioxane ²	UV – vis/Fe(II)/H ₂ O ₂	1135	2.3	Safarzadeh-Amiri et al. [190]
1,4-Dioxane ³	UV – vis/Ferrioxalate/H ₂ O ₂	1135	0.7	Safarzadeh-Amiri et al. [190]
Methylene Blue	Slurry	12	1291.4	Valladares [216]
Methylene Blue	Series Conical Basket	12	10.0	Valladares [216]
PCE	Slurry	282	47.4	Turchi [213]
Benzene	Slurry	279	47.5	Turchi [213]
Phenol	Slurry	100	145.8	Okamoto et al. [160]
Phenol	Immobilized glass coil	34.6	915.5	Al-Ekabi and Serpone [6]
Phenol	Slurry	1000	4557.7	Wei et al. [219]

¹ [H₂O₂]=250 mg L⁻¹

² [H₂O₂]=250 mg L⁻¹ and [Fe(II)]=40 mg L⁻¹

³ [H₂O₂]=200 mg L⁻¹ and [Fe(III)]=40 mg L⁻¹

6.4 Anodization of Pure Titanium to Titanium Dioxide

It is sometimes difficult to cover the entire surface area of the packings with titanium dioxide. One possibility for overcoming this problem may be the anodization of titanium wires, available commercially, to titanium dioxide; which are then used to produce tellerette packings. In this case, there is no need to immobilize the tellerette packings with titanium dioxide, making it cost effective. Depending on the method of anodization, a layer of titanium dioxide will be built up on the surface of the packings. This might enhance the efficiency of the photoreactor due to the increased surface area of titanium dioxide.

Preliminary experiments of anodizing pure titanium wires to titanium dioxide using 1 M sulfuric acid solution at constant voltage of 50 volts were performed. The anode was pure titanium wire and the cathode was a gold plated platinum. These experiments failed simply due to the unknown optimum conditions of the voltage and current density for this particular anodization process. To improve the method of anodization, the optimum condition of the growth mode should be found (see Section 7.2 for further recommendations).

6.5 Concluding Remarks

Designing an immobilized photoreactor with high mass transfer rate, high ratio of the photocatalyst surface area to the photoreactor volume, and suffi-

cient light penetration is in demand. It was shown that the photoreactor with stainless steel tellerette packing has no mass transfer limitations to transfer organic species onto the photocatalyst surface while maintaining sufficient UV light penetration throughout the system. In addition, this type of photoreactor has an advantage of low pressure drop across the column due to its high voidage (95.7%).

Additional experimental data involving different organic species are required using this photoreactor to compare its performance with other configurations. Longer light path and also tighter packing might be needed to improve the performance of this packed bed photoreactor.

Chapter 7

CONCLUSIONS AND RECOMMENDATIONS

In this chapter, the main conclusions obtained throughout this study are presented. In addition, recommendations for future work are suggested.

7.1 Conclusions

The following conclusions can be drawn from this thesis:

1. It is customary that data analysis in photocatalytic and many other chemical reactions is performed using the method of initial rates. This method has serious drawbacks, primarily related to the subjectivity in the estimation of initial rates from experimental data. In Chapter 4, it was shown that the plot of residuals in the linear (initial rate) analysis confirmed that there was a pattern amongst the data. This indicates

that there is a lack of constant variance within the data. Most importantly, the method of initial rates fails when applied to multicomponent systems, in which intermediate species or products are often present with no initial concentrations. The method of non-linear data analysis described in Chapter 4 does not suffer from these limitations. It employs all of the data from the entire experimental run to estimate the model parameters, resulting in a more objective set of estimates.

A superior approach based on the Box-Draper method of non-linear estimation using all the experimental data was described and compared to the method of initial rates. It was demonstrated that this technique resulted in better and more objective parameter estimates in these kinetic models.

2. Two different photocatalysts, Degussa P25 and Hombikat UV 100, were compared, their photoactivities estimated and their loads optimized.

Similar behavior was observed for both photocatalysts. However, the photoactivity of Degussa P25 was higher at low photocatalyst loadings ($[\text{TiO}_2] < 1 \text{ g L}^{-1}$). In contrast, the photoactivity of Hombikat UV 100 was almost twice that of Degussa P25 at higher photocatalyst loadings ($[\text{TiO}_2] > 1 \text{ g L}^{-1}$). The optimum photocatalyst loading for TiO_2 was 1.5 and 3.0–4.0 g L^{-1} for Degussa P25 and Hombikat UV 100, respectively.

By measuring UV extinction and transmittance at 350 nm at different TiO_2 loadings, it was shown that the system was highly transparent

at low Hombikat UV 100 titanium dioxide loading while it was opaque in the case of Degussa P25 TiO₂. At higher titanium dioxide loadings, the system was entirely opaque for both photocatalysts.

3. Photocatalytic degradation of two organic pollutants, tetrahydrofuran and 1,4-dioxane, was thoroughly studied in Chapter 5. It was demonstrated that these organic species are photocatalytically degradable.

Possible intermediates during the course of the photocatalytic degradation of tetrahydrofuran and 1,4-dioxane were experimentally identified using both GC/MS and IC methods. 2(3H)-Furanone, dihydro- (γ-butyrolactone), succinic acid, acetic acid, formic acid, 3-hydroxybutyric acid, and glycolic acid were identified as tetrahydrofuran intermediates during its photocatalytic reaction. 2-Hydroxytetrahydrofuran, dihydro-5-hydroxy-2(3H)-furanone, and 4-oxobutanoic acid were not detected but are believed to be tetrahydrofuran intermediates.

Similarly, 1,2-ethanediol, diformate, acetic acid, formic acid, 3-hydroxybutyric acid, and glycolic acid were identified as intermediates of the photocatalytic degradation of 1,4-dioxane. Although, 1,4-dioxane-2,3-diol (2,3-dihydroxy-1,4-dioxane) and [1,2-ethanediylbis(oxy)]bis[methanol] were not detected, it is speculated that they are also 1,4-dioxane intermediates.

4. Hypothetical reaction pathways were proposed for the photocatalysis of both tetrahydrofuran and 1,4-dioxane based on the proposed intermediates. Kinetic models were developed and the kinetic parameters

estimated using the method developed in Chapter 4. It was shown that the photocatalytic degradation of tetrahydrofuran and the binary system followed the modified Langmuir-Hinshelwood model. In addition, the photocatalytic degradations of tetrahydrofuran and 1,4-dioxane in a binary system were examined. It was found that their degradation rates were slower in the binary system compared to that of a single component system.

5. The effect of sodium bicarbonate on the photocatalytic degradation of the binary system was examined. It was shown that the presence of bicarbonate and carbonate ions as hydroxyl radical scavengers slows down the degradation rate of 1,4-dioxane but does not significantly alter the degradation rate of tetrahydrofuran. The slight enhancement in the tetrahydrofuran degradation rate in the presence of sodium bicarbonate may be due to an increase in pH. Also, there is a possibility that bicarbonate and carbonate ions reduce to other organic species during the photocatalytic reaction.

Therefore in photocatalysis processes, the presence of these anions should be taken into account. It is recommended that these anions be removed from the water or wastewater before the photocatalysis process is activated in order to eliminate their effects. Lowering the pH of the water or wastewater before photocatalysis treatment eliminates these anions in the form of CO_2 .

6. From a practical point of view, slurry photoreactors, which have high ratio of the photocatalyst surface area to the photoreactor volume, are highly efficient at mixing and promoting mass transfer but suffer from the drawback of solid particles separation subsequently required from the suspension. To overcome this disadvantage, immobilized photoreactors have been suggested as an alternative. Although significant contributions have been made on these types of photoreactors, they suffer from potential mass transfer limitations. In Chapter 6, a novel fixed bed photoreactor with stainless steel tellerette packings was introduced. The experiments in Chapter 6 revealed that mass transfer limitations in this packed bed photoreactor were insignificant. The reaction appeared to be kinetically controlled in this packed bed configuration. Although more investigation is needed on the tellerette packed bed photoreactor, it may have potential use in industrial applications due to the effective mass transfer, UV light penetration through the packings, and low pressure drop across the column.

7.2 Recommendations for Future Work

Although a number of insights into photocatalysis have been gained, important issues still remain unresolved. The following recommendations are proposed in order to direct future research in the field of photocatalysis.

1. It is recommended that a real wastewater sample which contains more organic and inorganic species than tested in the present work, be pho-

photocatalytically degraded. In this case, the effects of other parameters such as turbidity and interactions between different organic and inorganic species may be studied.

2. It is suggested that the carbon dioxide production be monitored during the course of the photocatalytic reactions in order to control the reactions in the system.
3. It is of interest to investigate the effect of hydrogen peroxide on the photocatalytic degradation of tetrahydrofuran and 1,4-dioxane since it has been shown that hydrogen peroxide is a better electron acceptor than oxygen and produces more hydroxyl radicals directly, therefore it enhances the photocatalyzed oxidation rates [167, 206].
4. The coupling of a biological process as a post-treatment, a pretreatment, or both offers another avenue of potential research for future investigations.
5. Further work is needed on the trickle bed photoreactor. Examination of the effects of different packing sizes, shapes, and immobilization methods is of interest in order to compare the present results with those of other immobilized photoreactor configurations. Studying the effects of different diameters of the photoreactor allow a better understanding of the light distribution for the scale up purposes.

Further study on the photocatalytic degradation of different organic pollutants would permit comparison of the efficiency of this configuration with that of others.

Finally, structural analysis of the coated stainless steel wires by means of a Scanning Electron Microscope (SEM) may provide interesting information about the quality of the titanium dioxide immobilization.

6. It is of interest to immobilize Hombikat UV 100 titanium dioxide on the above packing and compare its photoactivity with that of Degussa P25.

7. Photoreactor modelling and scale-up is still an area which demands further investigation.

8. It is recommended that different voltages and current densities be investigated to determine the optimum conditions for the anodization process. To do this, the potentiostatic anodization approach, in which a constant anode-to-cathode voltage drop is applied, should be tested and the maximum permissible current density found. The process of galvanostatic anodization, in which a constant current density is applied, should also be examined and the maximum permissible anode-to-cathode voltage be estimated. Furthermore, the combined growth mode offers a method to find the optimum process conditions. In order to do these experiments, a variable power supply should be provided.

In general, anodization of pure titanium wires to titanium dioxide in a similar form to the tellerette packing used in this study, is another interesting area of research.

Bibliography

- [1] G. E. Adams and J. W. Boag. Spectroscopic Studies of Reactions of the OH Radicals. *Proceedings of the Chemical Society, London*, page 112. 1964.
- [2] G. E. Adams, J. W. Boag, and B. D. Michael. Reaction of the Hydroxyl Radicals, Part 1. Transient Separation of Some Inorganic Radical-anions. *Trans. Faraday Soc.*, 61(2):1674–1680. 1965.
- [3] G. E. Adams, J. W. Boag, and B. D. Michael. Reaction of the Hydroxyl Radicals, Part 2. Determination of Absolute Rate Constants. *Trans. Faraday Soc.*, 61(2):1417–1424. 1965.
- [4] H. Al-Ekabi, G. Edwards, W. Holden, A. Safarzadeh-Amiri, and J. Story. Water treatment by heterogeneous photocatalysis. In W. Wesley Eckenfelder, Alan R. Bowers, and John A. Roth, editors, *Chemical Oxidation: Technologies for the Nineties, Proceeding of the First International Symposium*, volume 1, pages 254–261, Technomic Publishing Co., Inc., Lancaster, U.S.A, 1992.

- [5] H. Al-Ekabi, N. Serpone, E. Pelizzetti, C. Minero, M. A. Fox, and R. B. Draper. Kinetic Studies in Heterogeneous Photocatalysis 2. TiO₂-Mediated Degradation of 4-Chlorophenol Alone and in a Three Component Mixture of 4-Chlorophenol, 2,4-Dichlorophenol and 2,4,5-Trichlorophenol in Air Equilibrated Aqueous Media. *Langmuir*. 5(1):250–255. 1989.
- [6] Hussain Al-Ekabi and Nick Serpone. Kinetic Studies in Heterogeneous Photocatalysis. 1. Photocatalytic Degradation of Chlorinated Phenols in Aerated Aqueous Solutions over TiO₂ Supported on a Glass Matrix. *J. Phys. Chem.*, 92(20):5726–5731. 1988.
- [7] Ghassan Al-Sayyed, Jean-Christophe D'Oliveira, and Pierre Pichat. Semiconductor-sensitized photodegradation of 4-chlorophenol in water. *J. Photochem. Photobiol. A: Chem.*, 58(1):99–114, 1991.
- [8] M. Albert, Y. M. Gao, D. Toft, K. Dwight, and A. Wold. Photoassisted Gold Deposition on Titanium Dioxide. *Mater. Res. Bull.*, 27:961–966. 1992.
- [9] Orlando M. Alfano, Roberto L. Romero, and Alberto E. Cassano. Radiation Field Modelling in Photoreactors–I. Homogeneous Media. *Chem. Eng. Sci.*, 41(3):421–444, 1986.
- [10] Orlando M. Alfano, Roberto L. Romero, and Alberto E. Cassano. Radiation Field Modelling in Photoreactors–II. Heterogeneous Media. *Chem. Eng. Sci.*, 41(5):1137–1153, 1986.

- [11] Marc A. Anderson. US patent No. 5,308,454, 1994.
- [12] William A. Anderson. Industrial waste treatment. Internal Notes, Chem. Eng. Dept. , University of Waterloo. Waterloo, Ontario, Canada. 1996.
- [13] William A. Anderson. Personal Communication, University of Waterloo, Waterloo, Ontario, Canada, 1997.
- [14] Astro International Corporation. 100 Park Ave., League city, TX. *Astro International Manual*, 1990.
- [15] V. Augugliaro, V. Loddo, G. Marci, L. Palmisano, and M. Schiavello. Performance of a Continuous Flat Reactor for Phenol Degradation in Heterogeneous Photocatalytic System. *Chemical and Biochemical Engineering Quarterly*, 9(3):133–139, 1995.
- [16] V. Augugliaro, L. Palmisano, A. Sclafani, C. Minero E., and Pelizzetti. Photocatalytic degradation of phenol in aqueous titanium dioxide dispersions. *Toxicol. Environ. Chem.*, 16:89, 1988.
- [17] B. Aurian-Blajeni, M. Halmann, and J. Manassen. Photoreduction of carbon dioxide and water into formaldehyde and methanol on semiconductor materials. *Sol. Energy*, 25:165–170, 1980.
- [18] D. Bahnemann, D. Bockelmann, and R. Goslich. Mechanistic Studies of Water Detoxification in illuminated TiO₂ Suspensions. *Solar Energy Materials*, 24(1–4):564–583, 1991.

- [19] D. Bahnemann, J. Conningham, M. A. Fox, E. Pelizzetti, P. Pichat, and N. Serpone. Photocatalytic Treatment of Waters. In George R. Helz, Richard G. Zepp, and Donald G. Crosby, editors. *Aquatic and Surface Photochemistry*, pages 261–316, Lewis Publishers, Boca Raton, FL., U.S.A. 1994.
- [20] G. R. Bamwenda, S. Tsubota, T. Kobayashi, and M. Haruta. Photoinduced hydrogen production from an aqueous solution of ethylene glycol over gold supported on TiO₂. *J. Photochem. Photobiol. A: Chem.*, 77:59–67, 1994.
- [21] Y. Bard. *Nonlinear Parameter Estimation*. Academic Press, New York, 1974.
- [22] Reynaldo Barreto, Kimberly A. Gray, and Krista Anders. Photocatalytic Degradation of Methyl-*tert*-Butyl ether in TiO₂ Slurries: A Proposed Reaction Scheme. *Wat. Res.*, 29(5):1243–1248, 1995.
- [23] David Behar, Gideon Czapski, and Itzhak Duchovny. Carbonate radical in flash photolysis and pulse radiolysis of aqueous carbonate solutions. *J. Phys. Chem.*, 74(10):2206–2210, 1970.
- [24] I. R. Bellobono, M. Bonardi, L. Castellano, E. Selli, and L. Righetto. Photosynthetic membranes. 23. Degradation of some chloroaliphatic water contaminants by photocatalytic membranes immobilizing titanium dioxide. *J. Photochem. Photobiol., A: Chem.*, 67:109–115, 1992.

- [25] D. Bernhardt and H. Diekmann. Degradation of dioxane, tetrahydrofuran and other cyclic ethers by an environmental *Rhodococcus* strain. *Appl. Microbiol. Biotechnol.*, 36:120-123, 1991.
- [26] M. Bideau, B. Claudel, L. Faure, and H. Kazouan. The photo-oxidation of acetic acid by oxygen in the presence of titanium dioxide and dissolved copper ions. *J. Photochem. Photobiol. A: Chem.*, 61:269-280, 1991.
- [27] D. M. Blake. *Bibliography of Work on the Photocatalytic Removal of Hazardous Compounds from Water and Air*. National Renewal Energy Laboratory, 1994.
- [28] D. Bockelmann and D. Bahnemann. Photocatalytic Purification of Polluted Water: Characterization of a Novel Thin-Film-Fixed-Bed-Reactor (TFFB-Reactor). In *Proceeding of The First International Conference on AOT for Water and Air Remediation*, page 274, London Convention Center, London, Ontario, Canada, June 25-30, 1994.
- [29] Lysane Bolduc. The effect of a photocatalytic treatment on the biodegradability of wastewater. Master's thesis, University of Waterloo, Waterloo, Ontario, Canada, 1997.
- [30] James R. Bolton, Keith G. Bircher, William Tumas, and Chadwick A. Tolman. Figures-of-Merit for the Technical Development and Application of Advanced Oxidation Processes. *J. Adv. Oxid. Technol.*, 1(1):13-17, 1996.

- [31] James R. Bolton and Stephen R. Cater. Homogeneous Photodegradation of Pollutants in Contaminated Water: An Introduction. In George R. Helz, Richard G. Zepp, and Donald G. Crosby, editors. *Aquatic and Surface Photochemistry*, pages 467–490. Lewis Publishers, Boca Raton, FL., U.S.A. 1994.
- [32] James R. Bolton, Mihaela I. Stefan, and Kelly A. Hislop. Mechanisms and efficiency in the photodegradation of organic pollutants in aqueous solution. In *Proceedings of the second International Conference on Advanced Oxidation Technologies for Water and Air Remediation*, page 229. London, Ontario, Canada. 1995.
- [33] G.C. Bond. *Heterogeneous Catalysis-Principles and Applications*. Oxford Science Publications, Oxford, 1987.
- [34] E. Borgarello, R. Harries, and N. Serpone. Photochemical deposition and photorecovery of gold using semiconductor dispersions. a practical application of photocatalysis. *Nouv. J. Chim.*, 9(12):743. 1985.
- [35] E. Borgarello, N. Serpone, M. Grätzel, and E. Pelizzetti. Photodecomposition of H₂S in Aqueous Alkaline Media Catalyzed by RuO₂-loaded Alumina in the Presence of Cadmium Sulfide. Application of the Inter-Particle Electron Transfer Mechanism. *Inorg. Chim. Acta*, 112:197, 1986.
- [36] Enrico Borgarello, Nick Serpone, Gary Emo, Ron Harris, Ezio Pelizzetti, and Claudio Minero. Light-Induced Reduction of Rhodium

- (III) and Palladium (II) on Titanium Dioxide Dispersions and the Selective Photochemical Separation and Recovery of Gold (III), Platinum (IV), and Rhodium (III) in Chloride Media. *Inorganic Chemistry*, 25(25):4499–4503, 1986.
- [37] G. E. P. Box and N. R. Draper. The bayesian estimation of common parameters from several responses. *Biometrika*, 52:355–365, 1965.
- [38] G. E. P. Box and G. C. Tiao. *Bayesian Inference in Statistical Analysis*, Reading, Mass. Addison-Wesley, 1973.
- [39] G.E. Box, W.G. Hunter, and N.R. Draper. *Empirical Model-Building and Response Surfaces*. John Wiley & Sons, Inc., 1987.
- [40] George E.P. Box, William G. Hunter, and J. Stuart Hunter. *Statistics for Experimenters-An Introduction to Design, Data Analysis, and Model Building*. John Wiley and Sons, 1978.
- [41] Agustin Bravo, Josep Garcia, Xavier Domènech, and Jose Peral. Some aspect of photocatalytic oxidation of ammonium ion by titanium dioxide. *J. Chem. Res. (S)*, (9):376–377, 1993.
- [42] G. T. Brown and F. R. Darwent. Methyl orange as a probe for photooxidation reactions of colloidal TiO_2 . *J. of Phys. Chem.*, 88:4955, 1984.
- [43] Garrett N. Brown, John W. Birds, and Carl A. Koval. Development and characterization of a titanium dioxide-based semiconductor photoelectrochemical detector. *Anal. Chem.*, 64(4):427–434, 1992.

- [44] A. Brucato, D. Iatridis, L. Rizzuti, and P. L. Yue. Modelling of light transmittance and reflectance in flat fluidized photoreactors. *Can. J. Chem. Eng.*, 70:1063–1070, 1992.
- [45] S. Budvari, editor. *The Merck Index*. Merck and Co., Rahway, NJ, 11th edition, 1989.
- [46] Randy A. Bull and Jack D. Zeff. Hydrogen Peroxide in Advanced Oxidation Processes for Treatment of Industrial Process and Contaminated Groundwater. In W. Wesley Eckenfelder, Alan R. Bowers, and John A. Roth, editors, *Chemical Oxidation: Technologies for the Nineties, Proceeding of the First International Symposium*, volume 1, pages 26–36. Technomic Publishing Co., Inc., Lancaster, U.S.A. 1992.
- [47] Elizabeth C. Butler and Allen P. Davis. Photocatalytic oxidation in aqueous titanium dioxide suspensions: the influence of dissolved transition metals. *J. Photochem. Photobiol. A: Chem.*, 70:273–283, 1993.
- [48] Maria I. Cabrera, Orlando M. Alfano, and Alberto E. Cassano. Absorption and Scattering Coefficient of Titanium Dioxide Particulate Suspensions in Water. *J. Phys. Chem.*, 100(51):20043–20050, 1996.
- [49] Ruxiong Cai, Kazuhito Hashimoto, Kiminori Itoh, Yoshinobu Kubota, and Akira Fujishima. Photokilling of Malignant Cells with Ultrafine TiO₂ Powder. *Bull. Chem. Soc. Jpn.*, 64(4):1268–1273, 1991.
- [50] Ruxiong Cai, Kazuhito Hashimoto, Yoshinobu Kubota, and Akira Fujishima. Increment of Photocatalytic Killing of Cancer Cells Using

- TiO₂ with the Aid of Superoxide Dismutase. *Chemistry Letters*, 3:427-430, 1992.
- [51] Ruxiong Cai, Yoshinobu Kubota, Taro Shuin, Hideki Sakei, Kazuhito Hashimoto, and Akira Fujishima. Induction of Cytotoxicity by Photoexcited TiO₂ Particles. *Cancer Research*, 52:2346-2348, 1992.
- [52] B. Carnahan, H.A. Luther, and J. O. Wilkes. *Applied Numerical Methods*. John Wiley & Sons, Inc., 1969.
- [53] Elizabeth R. Carraway, Amy J. Hoffmann, and Michael R. Hoffmann. Photocatalytic oxidation of organic acids on quantum-sized semiconductor colloids. *Environ. Sci. Technol.*, 28(5):786-793, 1994.
- [54] A. E. Cassano, P. L. Silveston, and J. M. Smith. Photochemical Reaction Engineering. *Industrial and Engineering Chemistry*, 59(1):18-38, 1967.
- [55] A. E. Cassano and J. M. Smith. Photochlorination in a Tubular Reactor. *A.I.Ch.E. Journal*, 12(6):1124-1133, 1966.
- [56] Alberto E. Cassano, Carlos A. Martin, Rodolfo J. Brandi, and Orlando M. Alfano. Photoreactor Analysis and Design: Fundamentals and Applications. *Ind. Eng. Chem. Res.*, 34(7):2155-2201, 1995.
- [57] K. Chandrasekaran and J. K. Thomas. Photochemical reduction of carbonate to formaldehyde on TiO₂ powder. *Chem. Phys. Lett.*, 99:7-10, 1983.

- [58] Lorette Pruden Childs and David F. Ollis. Is photocatalysis catalytic? *J. Catal.*, 66:383-390, 1980.
- [59] Governmental American Conference. Threshold limit values for chemical substances and physical agents and biological exposure indices. ACGIH, Second Printing, 1993-94.
- [60] G.M. Cornwall. Federal policies for toxic contaminants control. In M. Moo-Young, C.W. Robinson, and G.J. Farquhar, editors. *Waste Treatment and Utilization*, page 3, Pergamon Press, Oxford, UK, 1980.
- [61] John C. Crittenden, Rominder P.S. Suri, David L. Perram, and David W. Hand. Decontamination of water using adsorption and photocatalysis. *Wat. Res.*, 31(3):411-418, 1997.
- [62] R. J. Davis, J. L. Gainer, G. O'Neal, and I-Wen Wu. Photocatalytic decolorization of wastewater dyes. *Water Environ. Res.*, 66(1):50, 1994.
- [63] D. W. DeBerry, A. Viehbeck, G. R. Peyton, and M. Karpinski. Investigation of photocatalytic oxidation for wastewater cleanup and reuse. No. RU-83/12, US Dept. of Interior, 1983.
- [64] Edward A. Dietz, Jr. and Kenneth F. Singley. Determination of chlorinated hydrocarbons in water by headspace gas chromatography. *Anal. Chem.*, 51(11):1809-1814, 1979.
- [65] R. Barton Draper and Marye Anne Fox. Titanium dioxide photooxidation of thiocyanate. $(SCN)_2^{\bullet-}$ studied by diffuse reflectance flash photolysis. *J. Phys. Chem.*, 94(11):4628-4634, 1990.

- [66] Harold F. Elkins, Edward F. Mohler, JR., and Lawrence R. Kumnick. Biological oxidation of oil refinery wastes in cooling tower systems. *Sewage and Industrial Wastes*. 28(12):1475-1483, 1956.
- [67] Octav Enea and Allen J. Bard. pH Effects on the Energetic of Irradiated TiO₂ Suspensions in Aqueous D-Glucose. *Nouveau Journal De Chimie*. 9(281):691-695, 1985.
- [68] R. M. Fand. Heat Transfer by Forced Convection from a Cylinder to Water in Crossflow. *Int. J. Heat Mass Transfer*, 8:995, 1965.
- [69] J. Fendler and J. Bolton. Panel Discussion on Sensitization and Immobilization of Catalysts on Various Supports. In Ezio Pelizzetti and Nick Serpone, editors, *Homogeneous and Heterogeneous Photocatalysis*. C. pages 699-701, D. Reidel Publishing Company, NATO ASI Series. 1986.
- [70] MISA (Municipal / Industrial Strategy for Abatement). The development document for the effluent monitoring regulation for the organic chemical manufacturing sector. Environment Canada, 1991.
- [71] MISA (Municipal / Industrial Strategy for Abatement). The development document for the pulp and paper sector. Environment Canada, 1991.
- [72] M.A. Fox. Mechanistic photocatalysis in organic synthesis. In N. Serpone and E. Pellizzetti, editors, *Photocatalysis, Fundamental and Applications*, page 421, John Wiley and Sons, New York, 1989.

- [73] Marye A. Fox and Thomas L. Pettit. Photoactivity of Zeolite-Supported Cadmium Sulfide: Hydrogen Evolution in the Presence of Sacrificial Donors. *Langmuir*, 5(4):1056, 1989.
- [74] Marye Anne Fox. Photocatalytic oxidation of organic substrates. In M. Schiavello, editor, *Photocatalysis and Environment: Trends and Applications*, pages 445–467. Kluwer Academic Publishers, Dordrecht, The Netherlands, 1988.
- [75] Marye Anne Fox and Maria T. Dulay. Heterogeneous photocatalysis. *Chem. Rev.*, 93:341–357, 1993.
- [76] M. Fujihira, Y. Satoh, and T. Osa. Heterogeneous Photocatalytic Reactions on Semiconductor Materials: Part III. Effect of pH and Cu^{2+} Ions on the Photo-Fenton Type Reaction. *Bull. Chem. Soc. Japan*, 55(3):666–671, 1982.
- [77] A. Fujishima. Photocatalytic reaction for environmental applications. In *Proceedings of the second International Conference on Advanced Oxidation Technologies for Water and Air Remediation*, page 226. London, Ontario, Canada, 1995.
- [78] A. Fujishima, R. Cai, K. Hashimoto, and Y. Kubota. Biochemical Application of TiO_2 Photocatalysis. In D. F. Ollis and H. Al-Ekabi, editors, *Photochemical Purification and Treatment of Water and Air: Proceedings of the first International Conference on TiO_2 Photocatalytic Purification and Treatment of Water and Air*, pages 193–205, Elsevier Science Publishers B.V., Amsterdam, The Netherlands, 1993.

- [79] A. Fujishima, R. X. Cai, J. Otsuki, K. Hashimoto, K. Itoh, T. Yamashita, and Y. Kubota. Biochemical Application of Photoelectrochemistry: Photokilling of Malignant Cells with TiO_2 Powder. *Electrochimica Acta*, 38(1):153–157, 1993.
- [80] A. Fujishima, T. Inoue, and K. Honda. Competitive Photoelectrochemical Oxidation of Reducing Agents at the TiO_2 Photoanode. *J. Amer. Chem. Soc.*, 101:5582, 1979.
- [81] Akira Fujishima. New Application of Photocatalysis Under Room Light Illumination. In *The First International Conference on Advanced Oxidation Technology for Water and Air Remediation*, pages 98–99, London Convention Center, London, Ontario, Canada, June 25–30, 1994.
- [82] Akira Fujishima and Kenichi Honda. Electrochemical photolysis of water at a semiconductor electrode. *Nature*, 238(5358):37–38, 1972.
- [83] Y. M. Gao, W. Lee, R. Trehan, R. Kershaw, K. Dwight, and A. Wold. Improvement of Photocatalytic Activity of Titanium (IV) Oxide by Dispersion of Au on TiO_2 . *Mater. Res. Bull.*, 26(12):1247–1254, 1991.
- [84] H. Gerischer. Solar photoelectrolysis with semiconductor electrodes. *Topics in Applied Physics*, 31:115–171, 1979.
- [85] N. Getoff. Electron beam remediation of water. a short review. In *The First International Conference on Advanced Oxidation Technology for Water and Air Remediation*, page 128, London Convention Center, London, Ontario, Canada, June 25–30, 1994.

- [86] S. Gill. A process for the step-by-step integration of differential equations in an automatic computing machine. *Proc. Cambridge. Soc.*, 47:96-108, 1951.
- [87] William H. Glaze and Joon-Wun Kang. Advanced oxidation processes. description of a kinetic model for the oxidation of hazardous materials in aqueous media with ozone and hydrogen peroxide in a semibatch reactor. *Ind. Eng. Chem. Res.*, 28:1573-1580, 1989.
- [88] William H. Glaze and Joon-Wun Kang. Advanced oxidation processes. test of a kinetic model for the oxidation of organic compounds with ozone and hydrogen peroxide in a semibatch reactor. *Ind. Eng. Chem. Res.*, 28:1580-1587, 1989.
- [89] Sheffield Gordon, Edwin J. Hart, Max S. Matheson, Joseph Rabani, and J. K. Thomas. Reaction constants of the hydrated electron. *J. Amer. Chem. Soc.*, 85(2):1375-1377, 1963.
- [90] M. Grätzel. Characterization and properties of semiconductor colloids. *Ann. Chim.*, 77:411, 1987.
- [91] M. Grätzel. *Heterogeneous Photochemical Electron Transfer*. CRC Press, Inc., 1989.
- [92] A. E. Greenberg, L. S. Clesceri, and D. E. Andrew. *Standard Methods for the Examination of Water and Wastewater*. American Public Health Association, Washington, DC, 18th edition, 1992.

- [93] Karl Heinz Gregor. Oxidative Decolorization of Textile Waste water with Advanced Oxidation Processes. In W. Wesley Eckenfelder, Alan R. Bowers, and John A. Roth, editors, *Chemical Oxidation: Technologies for the Nineties, Proceeding of the Third International Symposium*, volume 3, pages 161–193, Technomic Publishing Co., Inc., Lancaster, U.S.A. 1994.
- [94] Heung Yong Ha and Marc A. Anderson. Photocatalytic degradation of formic acid via metal-supported titania. *Journal of Environmental Engineering*, 122(3):217–221. 1996.
- [95] Andreas Haarstrick, Oemer M. Kut, and Elmar Heinzle. TiO₂-Assisted Degradation of Environmentally Relevant Organic Compounds in Wastewater Using a Novel Fluidized Bed Photoreactor. *Environ. Sci. Technol.*, 30(3):817–824. 1996.
- [96] H. Harada, T. Sakata, and T. Ueda. Effect of Semiconductor in Photocatalytic Decomposition of Lactic Acid. *J. Am. Chem. Soc.*, 107:1773, 1985.
- [97] H. Harada, T. Ueda, and T. Sakota. Semiconductor Effect on the Selective photocatalytic Reaction of α -Hydrocarboxylic Acids. *J. Phys. Chem.*, 93(4):1542–1548, 1989.
- [98] R. Hartung. *Health and Environmental Effects Assessment for 1,4-Dioxane*. Gelman Sciences, Ann Arbor, MI, 1989.

- [99] J.-M. Herrmann. Heterogeneous photocatalysis: an emerging discipline involving multiphase systems. *Catalysis Today*, 24:157–164, 1995.
- [100] J. M. Herrmann, J. Disdier, and P. Pichat. Photocatalytic Deposition of Silver on Powder Titania: Consequences for the Recovery of Silver. *J. Catal.*, 113:72, 1988.
- [101] J. M. Herrmann, C. Guillard, and P. Pichat. Heterogeneous photocatalysis: an emerging technology for water treatment. *Catalysis Today*, 17:7–20, 1993.
- [102] Jean-Marie Herrmann, Jean Disdier, Pierre Pichat, Asunción Fernández, Agustín González-Elipe, Guillermo Munera, and Christiane Leclercq. Titania-Supported Bimetallic Catalyst Synthesis by Photocatalytic Codeposition at Ambient Temperature: Preparation and Characterization of Pt-Rh, Ag-Rh, and Pt-Pd Couples. *J. Catal.*, 132:490–497, 1991.
- [103] C. G. Hill. *An Introduction to Chemical Engineering Kinetics and Reactor Design*. Wiley, New York, 1977.
- [104] Roger R. Hill, Graham E. Jeff, and David R. Roberts. Photocatalytic degradation of 1,4-dioxane in aqueous solution. *J. Photochem. Photobiol. A: Chem.*, 108:55–58, 1997.
- [105] Michael Hoffmann, Scot T. Martin, Wonyong Choi, and Detlef W. Bahnemann. Environmental applications of semiconductor photocatalysis. *Chemical Reviews*, 95(1):69–96, 1995.

- [106] K. Hofstadler, R. Bauer, S. Novalic, and Heisler G. New reactor design for photocatalytic wastewater treatment with TiO₂ immobilized on fused-silica glass fibers: Photomineralization of 4-chlorophenol. *Environ. Sci. Technol.*, 28(4):670-674, 1994.
- [107] O. A. Hougen and K. M. Watson. *Chemical Principles III Kinetics and Catalysis*. Wiley. New York, 1947.
- [108] P.H. Howard, editor. *Handbook of Environmental Fate and Exposure Data for Organic Chemicals*, volume II-Solvents. Lewis Publishers Inc., Chelsea, Michigan, 1990.
- [109] P.H. Howard, R.S. Boethling, W.F. Jarvis, W.M. Meylan, and E.M. Michalenko, editors. *Handbook of Environmental Degradation Rates*. Lewis Publishers Inc., Chelsea, Michigan, 1991.
- [110] Chen-Yung Hsiao, Chung-Li Lee, and David F. Ollis. Heterogeneous Photocatalysis: Degradation of Dilute Solutions of Dichloromethane (CH₂Cl₂), Chloroform (CHCl₃), and Carbon Tetrachloride (CCl₄) with Illuminated TiO₂ Photocatalyst. *J. Catal.*, 82:418-423, 1983.
- [111] D. Iatridis, P. L. Yue, L. Rizzuti, and A. Brucato. The absorption of light energy in flat fluidized photoreactors. *Chem. Eng. J.*, 45:1-8, 1990.
- [112] Yükeşi Inel and Durata Ertek (Hacıu). Photocatalytic Deposition of Bismuth III Ions Onto TiO₂ Powder. *J. Chem. Soc. , Faraday Trans.*, 89(1):129-133, 1993.

- [113] T. Inoue, A. Fujishima, S. Konishi, and K. Honda. Photoelectrocatalytic reduction of carbon dioxide in aqueous suspensions of semiconductor powders. *Nature (London)*, 277:637–638, 1979.
- [114] K Kalyanasundaram. In M. Grätzel, editor. *Energy Resources through Photochemistry and Catalysis*. Academic Press, New York, Chapter 7, 1983.
- [115] K. Kato. Photocatalytic property of TiO₂ anchored on porous alumina ceramic supported by the alkoxide method. *J. Ceramic Soc. Jpn.*, 1101:245–249, 1993.
- [116] Masahiro Kawasaki. Experiences with test scheme under chemical control law of Japan: An approach to structural-activity correlations. *Ecotox. Environ. Safety*, 4:444–454, 1980.
- [117] Laila B. Khalil, Nabil S. Youssef, Magdy W. Rophael, and Mona M. Moawad. Reduction of aqueous carbonate photocatalysed by treated semiconductors. *J. Chem. Tech. Biotechnol.*, 55:391–396, 1992.
- [118] H. Kisch. What is photocatalysis? In Nick Serpone and Ezio Pellizzetti, editors, *Photocatalysis: Fundamental and Applications*, page 1, John Wiley and Sons, New York, 1989.
- [119] Jan Kochany and Eva Lipczynska-Kochany. Application of the epr spin-trapping technique for the investigation of the reactions of carbonate, bicarbonate, and phosphate anions with hydroxyl radicals generated by the photolysis of H₂O₂. *Chemosphere*, 25(12):1769–1782, 1992.

- [120] P. A. Krieger. *High Purity Solvent Guide*. Burdick and Jackson. McGraw Park, IL.. 1984.
- [121] Celia C. H. Lee. Photocatalytic degradation of aqueous-phase organic contaminants in a fluidized bed reactor. Master's thesis. University of Waterloo, Waterloo, Ontario, Canada. 1995.
- [122] O. Levenspiel. *Chemical Reaction Engineering*. John Wiley and Sons, New York, 1972.
- [123] Nathan S. Lewis and Mary L. Rosenbluth. Theory of semiconductor materials. In Nick Serpone and Ezio Pellizzetti, editors, *Photocatalysis: Fundamental and Applications*, pages 45–98. John Wiley and Sons, New York. 1989.
- [124] X. Z. Li and M. Zhang. Decolorization and Biodegradability of Dyeing Wastewater Treated by a TiO₂-Sensitized Photo-Oxidation Process. *Wat. Sci. Tech.*, 34(9):49–55, 1996.
- [125] David R. Lide, editor. *CRC Handbook of Chemistry and Physics*. CRC Press, Inc., 76th edition, 1995–1996.
- [126] David R. Lide and G. W. A. Milne. *Handbook of Data on Organic Compounds*, volume III. CRC Press, Inc., 3rd edition, 1994.
- [127] M. Lindner, D. W. Bahnemann, B. Hirthe, and W.-D. Griebler. Solar Water Detoxification: Novel TiO₂ Powders as Highly Active Photocatalysts. *Journal of Solar Energy Engineering*, 119(2):120–125, 1997.

- [128] Amy L. Linsebigler, Guangquan Lu, and John T. Yates, Jr. Photocatalysis on TiO_2 Surfaces: Principles, Mechanisms, and Selected Results. *Chemical Review*, 95(3):735–758. 1995.
- [129] G. K. C. Low and R. W. Matthews. Flow-injection determination of organic contaminants in water using an ultraviolet mediated titanium dioxide film reactor. *Anal. Chim. Acta*, 231(1):13–20, 1990.
- [130] A. Lozano, J. Gracia, X. Domènech, and J. Casado. Heterogeneous photocatalytic oxidation of manganese(II) over TiO_2 . *J. Photochem. Photobiol. A: Chem.*, 69:237–240. 1992.
- [131] F. J. Ludzack and M. B. Ettinger. Industrial wastes: Chemical structures resistant to aerobic biochemical stabilization. *Journal of the Water Pollution Control Federation (JWPCF)*, 32(11):1173–1200, 1960.
- [132] D. Mackay, W.Y. Shiu, and K.C. Ma. *Illustrated Handbook of Physical - Chemical Properties and Environmental Fate for Organic Chemicals*, volume IV—Oxygen, nitrogen, and sulfur containing compounds. Lewis Publishers, Boca Raton, 1992.
- [133] D. Mackay, W.Y. Shiu, and K.C. Ma. *Illustrated Handbook of Physical - Chemical Properties and Environmental Fate for Organic Chemicals*, volume III—Volatile Organic Chemicals. Lewis Publishers, Boca Raton, 1993.

- [134] G. W. Malaney and R. M. Gerhold. Structural determinants in the oxidation of aliphatic compounds by activated sludge. *JWPCF*, 41(2):R18-R33, 1969.
- [135] S. E. Manahan. *Environmental Chemistry*. Lewis publishers Inc., fifth edition, 1991.
- [136] Héctor D. Mansilla, Jorge Villasenor, Gabriel Maturana, Jaime Baeza, Juanita Freer, and Nelson Durán. ZnO-catalysed photodegradation of kraft black liquor. *J. Photochem. Photobiol. A: Chem.*, 78(3):267-273, 1994.
- [137] Yun Mao, Christian Schöneich, and Klaus-Dieter Asmus. Identification of Organic Acids and Other Intermediates in Oxidative Degradation of Chlorinated Ethanes on TiO₂ Surfaces en Route to Mineralization. A Combined Photocatalytic and Radiation Chemical Study. *J. Phys. Chem.*, 95(24):10080-10089, 1991.
- [138] R. W. Matthews. Hydroxylation reactions induced by near-ultraviolet photolysis of aqueous titanium dioxide suspensions. *J. Chem. Soc. Faraday Trans. I*, 80(2):457-471, 1984.
- [139] R. W. Matthews. Solar-Electric Water Purification Using Photocatalytic Oxidation with TiO₂ as a Stationary Phase. *Solar Energy*, 38(6):405-413, 1987.
- [140] R. W. Matthews. An adsorption water purifier with in situ photocatalytic regeneration. *J. Catal.*, 113:549-555, 1988.

- [141] R. W. Matthews. Environmental photochemical and photocatalytic processes. degradation of organic compounds. In E. Pelizzetti and M. Schiavello, editors, *Photochemical Conversion and Storage of Solar Energy, Proceedings of the Eighth International Conference on Photochemical Conversion and Storage of Solar Energy*, pages 427–449, Kluwer Academic Publishers, Dordrecht, The Netherlands, 1991.
- [142] R. W. Matthews. Photooxidative Degradation of Colored Organics in Water Using Supported Catalysts TiO_2 on sand. *Wat. Res.*, 25(10):1169–1176, 1991.
- [143] R. W. Matthews, M. Abdullah, and G. K.-C. Low. Photocatalytic oxidation for total organic carbon analysis. *Analytical Chimica Acta*, 233:171–179, 1990.
- [144] Ralph W. Matthews. Photooxidation of organic impurities in water using thin films of titanium dioxide. *J. Phys. Chem.*, 91:3328–3333, 1987.
- [145] Ralph W. Matthews. Solar-Electric Water Purification Using Photocatalytic Oxidation with TiO_2 As a Stationary Phase. *Solar Energy*, 38(6):405, 1987.
- [146] Ralph W. Matthews. Kinetics of photocatalytic oxidation of organic solutes over titanium dioxide. *J. Catal.*, 111:264–272, 1988.

- [147] V. Maurino, P. Calza, C. Minero, E. Pelizzetti, and M. Vincenti. Light-Assisted 1,4-Dioxane Degradation. *Chemosphere*, 35(11):2675–2688, 1997.
- [148] Mehrab Mehrvar, William A. Anderson, and Murray Moo-Young. Non-linear Parameter Estimation for a Dynamic Model in Photocatalysis. *Submitted to Chem. Eng. Sci.*, 1997.
- [149] Mehrab Mehrvar, William A. Anderson, and Murray Moo-Young. A novel packed bed photoreactor design for the use of the photocatalysis process in degradation of water pollutants. In *47th Canadian Chemical Engineering Conference*. Edmonton, Alberta, Canada, October 1997.
- [150] Mehrab Mehrvar, William A. Anderson, and Murray Moo-Young. Reaction mechanisms and kinetic models for the photocatalytic degradation of tetrahydrofuran and 1,4-dioxane in water. In *47th Canadian Chemical Engineering Conference*, Edmonton, Alberta, Canada, October 1997.
- [151] Mehrab Mehrvar, Murray Moo-Young, and William A. Anderson. Kinetics of the photocatalytic degradation of tetrahydrofuran and 1,4-dioxane in water. In *46th Canadian Chemical Engineering Conference*, page 234, Kingston, Ontario, Canada, October 1996.
- [152] Bogidar V. Mihaylov, James L. Hendrix, and John H. Nelson. Comparative catalytic activity of selected metal oxides and sulfides for the photo-oxidation of cyanide. *J. Photochem. Photobiol. A: Chem.*, 72:173–177, 1993.

- [153] Andrew Mills, Richard H. Davies, and David Worsley. Water purification by semiconductor photocatalysis. *Chem. Soc. Rev.*, 22(6):417–425. 1993.
- [154] D. Monheit, S. Grayer, N. Godinger, V. Katzir, and M. Halmann. Simultaneous photoreduction of carbonate and nitrogen on titanium dioxide in alkaline aqueous carbonate. In *Abstract of 5th International Conference on Photochemical Conversion and Storage of Solar Energy*, pages 75–76, Osaka, 1984.
- [155] Murray Moo-Young, William A. Anderson, Jenő M. Scharer, Inge Van Kemenade, and Mehrab Mehrvar. Physicochemical pretreatment in bioremediation enhancement. In D. L. Wise, editor. *Global Environmental Biotechnology*, pages 405–410. Elsevier Science B. V., 1997.
- [156] C. Moralejo. Panel discussion. In *The First International Conference on Advanced Oxidation Technology for Water and Air Remediation*. London Convention Center, London, Ontario, Canada, June 25–30. 1994.
- [157] Masayuki Murabayashi, Kiminori Itoh, Koichi Kawashima, Ryuji Masuda, and Seiichi Suzuki. Photocatalytic Degradation of Chloroform with TiO₂ Coated Glass Fiber Cloth. In D. F. Ollis and H. Al-Ekabi, editors, *Photochemical Purification and Treatment of Water and Air: Proceedings of the first International Conference on TiO₂ Photocatalytic Purification and Treatment of Water and Air*, pages 783–788, Elsevier Science Publishers B.V., Amsterdam, The Netherlands, 1993.

- [158] M. K. Nazeeruddin, A. Kay, I. Rodicio, R. Humphry-Baker, E. Müller, P. Liska, N. Vlachopoulos, and M. Grätzel. Conversion of Light to Electricity by *cis*-X₂Bis(2,2'-bipyridyl-4,4'-dicarboxylate)ruthenium(II) Charge-Transfer Sensitizers (X = Cl⁻, Br⁻, I⁻, CN⁻, and SCN⁻) on Nanocrystalline TiO₂ Electrodes. *J. Am. Chem. Soc.*, 115(14):6382–6390, 1993.
- [159] S. Notthakun, J. C. Crittenden, D. W. Hand, D. L. Perram, and M. E. Mullins. Regeneration of adsorbents using heterogeneous advanced oxidation. *J. Environ. Eng.*, 119:695–714, 1993.
- [160] Ken-ichi Okamoto, Yasunori Yamamoto, Hiroki Tanaka, and Akira Itaya. Kinetics of Heterogeneous Photocatalysis Decomposition of Phenol over Anatase TiO₂ Powder. *Bull. Chem. Soc. Jpn.*, 58(7):2023–2028, 1985.
- [161] Ken-ichi Okamoto, Yasunori Yamamoto, Hiroki Tanaka, Masashi Tanaka, and Akira Itaya. Heterogeneous Photocatalysis Decomposition of Phenol over TiO₂ Powder. *Bull. Chem. Soc. Jpn.*, 58(7):2015–2022, 1985.
- [162] D. F. Ollis. Heterogeneous photocatalysis for water purification: Prospects and problems. In Ezio Pelizzetti and Nick Serpone, editors, *Homogeneous and Heterogeneous Photocatalysis*, C, pages 651–656, D. Reidel Publishing Company, NATO ASI, 1986.

- [163] D. F. Ollis, C. Hsiao, L. Budiman, and C. Lee. Heterogeneous photoassisted catalysis: Conversions of perchloroethylene, dichloroethane, chloroacetic acids and chlorobenzene. *J. Catal.*, 88(1):89–96, 1984.
- [164] D. F. Ollis, E. Pelizzetti, and N. Serpone. Heterogeneous photocatalysis in the environment: Application to water purification. In N. Serpone and E. Pellizzetti, editors. *Photocatalysis, Fundamental and Applications*. page 603, John Wiley and Sons, New York, 1989.
- [165] David F. Ollis. Contaminant degradation in water. *Environ. Sci. Technol.*, 19(6):480–484, 1985.
- [166] David F. Ollis. Solar-Assisted Photocatalysis for Water Purification: Issues, Data, Questions. In E. Pelizzetti and M. Schiavello, editors. *Photochemical Conversion and Storage of Solar Energy, Proceedings of the Eighth International Conference on Photochemical Conversion and Storage of Solar Energy*, pages 593–622. Kluwer Academic Publishers, Dordrecht, The Netherlands, 1991.
- [167] David F. Ollis, Ezio Pelizzetti, and Nick Serpone. Photocatalyzed destruction of water contaminants. *Environ. Sci. Technol.*, 25(9):1522–1529, 1991.
- [168] David F. Ollis and Craig Turchi. Heterogeneous photocatalytic for water purification: Contaminant mineralization kinetics and elementary reactor analysis. *Environ. Prog.*, 9(4):229–234, 1990.

- [169] Thomas T. Ortyl and Garnet E. Peck. Surface charge of titanium dioxide and its effect on dye adsorption and aqueous suspension stability. *Drug Development and Industrial Pharmacy*, 17(17):2245–2268, 1991.
- [170] H. A. Painter and E. F. King. Ring test program 1981-84. assessment of biodegradability of chemicals in water by manometric respirometry. Comm Eur Communities (Rep.) EUR 9962 (CA 103, 183-290). 1985.
- [171] Simo O. Pehkonen, Ron Siefert, Erel Yigal, Sam Webb, and Michael R. Hoffmann. Photoreduction of iron oxyhydroxides in the presence of important atmospheric organic compounds. *Environ. Sci. Technol.*, 27(10):2056–2062, 1993.
- [172] Sigrid Peldszus, Peter M. Huck, and Susan A. Andrews. Determination of short-chain aliphatic, oxo- and hydroxy-acids in drinking water at low microgram per liter concentrations. *Journal of Chromatography A*, 723:27–34, 1996.
- [173] José Peral, Juan Casado, and Javier Doménech. Light-Induced Oxidation of Phenol over ZnO Powder. *J. Photochem., Photobiol. A: Chem.*, 44:209–217, 1988.
- [174] José Peral and Xavier Domenech. Photocatalytic Cyanide Oxidation From Aqueous Copper Cyanide Solutions Over TiO₂ and ZnO. *J. Chem. Technol. Biotechnol.*, 53(1):93–96, 1992.
- [175] J-D. Phyper and B. Ibbotson. *The Handbook of Environmental Compliance Ontario*. McGraw-Hill Ryerson, Toronto, 1991.

- [176] Pierre Pichat and Jean-Marie Herrmann. Adsorption-desorption, related mobility and reactivity in photocatalysis. In N. Serpone and E. Pellizzetti, editors, *Photocatalysis, Fundamental and Applications*, pages 217–250. John Wiley and Sons, New York, 1989.
- [177] Yu. V. Pleskov and Gurevich Yu. Ya. *Semiconductor photoelectrochemistry*. Consultants Bureau, New York, 1986.
- [178] Ann Lorette Pruden and David F. Ollis. Photoassisted heterogeneous catalysis: The degradation of trichloroethylene in water. *J. Catal.*, 82:404–417, 1983.
- [179] G. Li Puma and P. L. Yue. Effects of radiation wavelength on the rate of mineralization of organics by heterogeneous photocatalysis. In *The First International Conference on Advanced Oxidation Technology for Water and Air Remediation*, page 308. London Convention Center, London, Ontario, Canada, June 25–30, 1994.
- [180] Gregory B. Raupp, Jill A. Nico, Suneetha Annangi, Rajnish Changrani, and Rao Annapragada. Two-flux radiation-field model for an annular packed-bed photocatalytic oxidation reactor. *AIChE*, 43(3):792–801, 1997.
- [181] Park M. Reilly. Internal Notes in Statistics, Chem. Eng. Dept. , University of Waterloo, Waterloo, Ontario, Canada, 1990.
- [182] Park M. Reilly and Hugo Patino-Leal. A bayesian study of the error-in-variables model. *Technometrics*, 23(3):221–231, 1981.

- [183] Georg Riegel and James R. Bolton. Photocatalytic Efficiency Variability in TiO₂ Particles. *J. Phys. Chem.*, 99(12):4215-4224, 1995.
- [184] M. Robertson and R. B. Henderson. US patent No. 4,892,712 : Washington, D. C., 1989.
- [185] P. A. Romachandran and R. V. Chaudhari. *Topics in Chemical Engineering, Three Phase Catalytic Reactors*, volume 2. Gordon and Breach Science Publishers, 1983.
- [186] T. L. Rose and C. Nanjundiah. Rate Enhancement of Photooxidation of CN⁻ with TiO₂ Particles. *J. Phys. Chem.*, 89(17):3766-3771, 1985.
- [187] J. Sabate, M. Anderson, H. Kikkawa, M. Edwards, and C. G. Hill, Jr. A Kinetic Study of the Photocatalytic Degradation of 3-Chlorosalicylic Acid over TiO₂ Membranes Supported on Glass. *J. Catal.*, 127:167-177, 1991.
- [188] J. Sabate, M. A. Anderson, M. A. Aguado, J. Giménez, S. Cervera-March, and C.G. Hill, Jr. Comparison of TiO₂ powder Suspensions and TiO₂ Ceramic Membranes Supported on Glass as Photocatalytic Systems in the Reduction of Chromium VI. *J. Mol. Catal.*, 71:57-68, 1992.
- [189] Frank Sabin, Thomas Türk, and Arnd Vogler. Photo-oxidation of organic compounds in the presence of titanium dioxide: determination of the efficiency. *J. Photochem. Photobiol. A.: Chem.*, 63:99-106, 1992.

- [190] Ali Safarzadeh-Amiri, James R. Bolton, and Stephen R. Cater. Ferroxalate-Mediated Photodegradation of Organic Pollutants in Contaminated Water. *Wat. Res.*, 31(4):787-798, 1997.
- [191] S. Sasaki. The Scientific Aspects of the Chemical Substance Control Law in Japan. In O. et al. Hutzinger, editor, *Aquatic Pollutants: Transformation and Biological Effects*, pages 283-298, Pergamon Press, Oxford, U.K., 1978.
- [192] S. Sato and T. Kadowaki. Photocatalytic activities of metal oxide semiconductors for oxygen isotope exchange and oxidation reactions. *J. Catal.*, 106:295, 1987.
- [193] Mario Schiavello, editor. *Photoelectrochemistry, Photocatalysis, and Photoreactors : Fundamental and Developments*. series NATO. Dordrecht, 1985.
- [194] Scientific Division, Yellow Springs Instrument Co., P.O.Box 279, Yellow Springs, Ohio 45387, U.S.A. *Instruction Manual, YSI Model 57, Dissolved Oxygen Meter*, 1975.
- [195] Jon P. Scott and David F. Ollis. Integration of chemical and biological oxidation processes for water treatment: Review and recommendations. *Environ. Prog.*, 14(2):88-103, 1995.
- [196] N. Serpone. *Heterogeneous Photocatalysis at Work. I. Selective Separations and Recovery of Metals from Industrial Waste Streams*. A.I.Ch.E. Meeting, New York, November 1987.

- [197] N. Serpone, E. Borgarello, M. Barbani, E. Pelizzetti, P. Pichat, J.-M. Hermann, and M. A. Fox. Photochemical Reduction of Gold(III) on Semiconductor Dispersions of TiO_2 in the Presence of Cyanide Ions: Dispersal of CN^- by Treatment with Hydrogen Peroxide. *J. Photochem.*, 36:373, 1987.
- [198] Nick Serpone, Enrico Borgarello, Ron Harris, Paul Cahill, Marco Borgarello, and Ezio Pelizzetti. Photocatalysis Over TiO_2 Supported on a Glass Substrate. *Solar Energy Materials*.
- [199] Nick Serpone, Enrico Borgarello, and Ezio Pelizzetti. Photoreduction and photodegradation of inorganic pollutants: II. Selective reduction and recovery of Au, Pt, Pd, Rh, Hg, and Pb. In M. Schiavello, editor, *Photocatalysis and Environment: Trends and Applications*, pages 527–565. Kluwer Academic Publishers, Dordrecht, The Netherlands, 1988.
- [200] Nick Serpone, Enrico Borgarello, and Ezio Pelizzetti. Photoreduction and photodegradation of inorganic pollutants: I. Cyanides. In M. Schiavello, editor, *Photocatalysis and Environment: Trends and Applications*, pages 499–526, Kluwer Academic Publishers, Dordrecht, The Netherlands, 1988.
- [201] D. Sliney and M. Wolbarsht. *Safety with Lasers and other Optical Sources*. Plenum, New York, 3rd edition, 1980.
- [202] J. M. Smith. *Chemical Engineering Kinetics*. McGraw-Hill, New York, 1973.

- [203] J. M. Smith. *Grant and Hackh's Chemical Dictionary*. McGraw-Hill. New York. 1987.
- [204] F. D. Snell and L. S. Ettre, editors. *Encyclopedia of Industrial Chemical Analysis*. Wiley. New York. N.Y., USA. 1971.
- [205] Jie Sun. Heterogeneous photocatalytic oxidation of acetone in a flow reactor. Master's thesis. University of Waterloo. Waterloo. Ontario. Canada, 1995.
- [206] Lizhong Sun and James R. Bolton. Determination of the Quantum Yield for the Photochemical Generation of Hydroxyl Radicals in TiO₂ Suspensions. *J. Phys. Chem.*, 100(10):4127-4134. 1996.
- [207] Cecilia Sundby. Bicarbonate effects on photo-inhibition: Including an explanation for the sensitivity to photo-inhibition under anaerobic conditions. *FEBS Letters*, 274(1/2):77-81, 1990.
- [208] K. Suzuki. Photocatalytic Air Purification on TiO₂ Coated Honeycomb Support. In D. F. Ollis and H. Al-Ekabi, editors. *Photochemical Purification and Treatment of Water and Air: Proceedings of the first International Conference on TiO₂ Photocatalytic Purification and Treatment of Water and Air*, page 421, Elsevier Science Publishers B.V., Amsterdam, The Netherlands, 1993.
- [209] Robert E. Treybal. *Mass-Transfer Operations*. McGraw-Hill, Inc., Tokyo, Japan, third edition, 1981.

- [210] C. S. Turchi and D. F. Ollis. Photocatalytic reactor design: An example of mass-transfer limitations with an immobilized catalyst. *J. Phys. Chem.*, 92:6852–6853, 1988.
- [211] Craig S. Turchi and David F. Ollis. Heterogeneous photocatalysis: Intermediates and mutual rate inhibition. *J. Catal.*, 119:483–496, 1989.
- [212] Craig S. Turchi and David F. Ollis. Photocatalytic degradation of organic water contaminants: Mechanisms involving hydroxyl radical attack. *J. Catal.*, 122:178–192, 1990.
- [213] Craig Steven Turchi. *Heterogeneous Photocatalytic Degradation of Organic Water Contaminants: Kinetics and Hydroxyl Radical Mechanisms*. PhD thesis, North Carolina State University, Raleigh, North Carolina, USA, 1990.
- [214] Ana R. Tymoschuk, Orlando M. Alfano, and Alberto E. Cassano. The Multitubular Photoreactor. 1. Radiation Field for Constant Absorption Reactors. *Ind. Eng. Chem. Res.*, 32(7):1328–1341, 1993.
- [215] J. Valladares, J. R. Bolton, and H. de Lasa. Photocatalytic Reactor for the Mineralization of Organic Wastewater Pollutants. Kinetics and Mass Transport Phenomena. In *The First International Conference on Advanced Oxidation Technology for Water and Air Remediation*, page 346, London Convention Center, London, Ontario, Canada, June 25–30, 1994.

- [216] Julio E. Valladares. *A New Photocatalytic Reactor for the Photodegradation of Organic Contaminants in Water*. PhD thesis, University of Western Ontario, London, Ontario, Canada, 1995.
- [217] Karel Verschueren. *Handbook of Environmental Data on Organic Chemicals*. Van Nostrand Reinhold Company Inc., New York, N.Y., USA, second edition, 1983.
- [218] James L. Weeks and Joseph Rabani. The pulse radiolysis of deaerated aqueous carbonate solutions. I. transient optical spectrum and mechanism. II. pK for OH radicals. *J. Phys. Chem.*, 70(7):2100–2106, 1966.
- [219] Tsong-Yang Wei, Yung-Yun Wang, and Chi-Chao Wan. Photocatalytic oxidation of phenol in the presence of hydrogen peroxide and titanium dioxide powders. *J. Photochem. Photobiol. A: Chem.*, 55:115–126, 1990.
- [220] Stacey Lee Wilkinson. Heterogeneous photocatalysis in a flat plate reactor. Master's thesis, University of Waterloo, Waterloo, Ontario, Canada, 1994.
- [221] Aron Wold. Photocatalytic Properties of TiO₂. *Chem. Mater.*, 5(3):280–283, 1993.
- [222] World Health Organization—WHO. *Polychlorinated Biphenyls and Terphenyls*, 1976.
- [223] Xiaogen Yang and Terry T. Peppard. Solid-Phase Microextraction for Flavor Analysis. *J. Agric. Food. Chem.*, 42(9):1925–1930, 1994.

- [224] Toshiyuki Yokota and Shinji Suzuki. Estimation of Light Absorption Rate in a Tank Type Photoreactor With Multiple Lamps Inside. *J. Chem. Eng. Jap.*, 28(3):300-305, 1995.
- [225] Hiroshi Yoneyama, Hiroyuki Uchida, Susumu Kuwabata, and Itoh Shigeyoshi. Enhancement of Photodegradation Rate of Dilute Organic Pollutants on TiO₂ Photocatalyst with use of Inert Adsorbent as the Support. In *The First International Conference on Advanced Oxidation Technology for Water and Air Remediation*, pages 112-113. London Convention Center, London, Ontario, Canada, June 25-30, 1994.
- [226] P. L. Yue. Introduction to the modelling and design of photoreactors. In Mario Schiavello, editor, *Photoelectrochemistry, Photocatalysis, and Photoreactors: Fundamental and Developments*, NATO, pages 527-547, Dordrecht, 1985.
- [227] P. L. Yue. Modelling of kinetics and reactor for water purification by photo-oxidation. *Chem. Eng. Sci.*, 48(1):1-11, 1993.
- [228] P. L. Yue. Modelling, scale-up and design of multiphasic photoreactors. In D. F. Ollis and H. Al-Ekabi, editors, *Photochemical Purification and Treatment of Water and Air: Proceedings of the first International Conference on TiO₂ Photocatalytic Purification and Treatment of Water and Air*, pages 495-510, Elsevier Science Publishers B.V., Amsterdam, The Netherlands, 1993.
- [229] Richard G. Zepp and David M. Cline. Rates of Direct Photolysis in Aquatic Environment. *Environ. Sci. Technol.*, 11(4):359-366, 1977.

- [230] Zhouyao Zhang and Janusz Pawliszyn. Headspace solid-phase microextraction. *Anal. Chem.*, 65(14):1843–1852, 1993.

APPENDICES

Appendix A

Method of Statistical Analysis of Dynamic Model

In this appendix, the details of the statistical analysis for the dynamic model discussed in Chapters 4 and 5 are explained. Sensitivity equations along with the dynamic models are discussed.

To compute the gradient vector q_i in Equation (4.17), the Jacobian matrix, J_i , as defined in Equation (4.18) should be first estimated. If the dynamic model consists of n differential equations with p parameters, a set of $n \times p$ sensitivity equations should be solved numerically. Hence, the elements of the Jacobian matrix in the sensitivity equations, which are called sensitivity coefficients, will be computed.

In the following, an example of a dynamic model with its sensitivity equations is demonstrated.

A.1 Dynamic Model

As an example, consider the dynamic model of Equations (5.70) which was developed for the kinetics of the mixture of THF and DIOX in Chapter 5. In this dynamic model, there are three differential equations with seven parameters which have $3 \times 7 = 21$ sensitivity equations. Let:

$$\begin{aligned} k_{THF} &= \theta_1, & K_{THF} &= \theta_2, & k_{DIOX} &= \theta_3, & K_{DIOX} &= \theta_4, \\ k_{GBL} &= \theta_5, & K_{GBL} &= \theta_6, & k_{app} &= \theta_7 \end{aligned}$$

and

$$[THF] = C_1, \quad [DIOX] = C_2, \quad [GBL] = C_3$$

Hence, the dynamic model may be written as follows:

$$\begin{aligned} \frac{dC_1}{dt} &= -\theta_7 C_1 - \frac{\theta_1 \theta_2 C_1}{1 + \theta_2 C_1 + \theta_4 C_2 + \theta_6 C_3} \\ \frac{dC_2}{dt} &= \frac{-\theta_3 \theta_4 C_2}{1 + \theta_2 C_1 + \theta_4 C_2 + \theta_6 C_3} \\ \frac{dC_3}{dt} &= \theta_7 C_1 - \frac{\theta_5 \theta_6 C_3}{1 + \theta_2 C_1 + \theta_4 C_2 + \theta_6 C_3} \end{aligned} \tag{A.1}$$

A.2 Sensitivity Equations

In total, 21 sensitivity equations of the dynamic model in Equations (A.1) were derived. These sensitivity equations, shown in Equations (A.3), along

with the dynamic model were numerically solved using the Runge-Kutta method to find the Jacobian matrix in each iteration (see Figure 4.3).

It was assumed that the concentrations of all species are known at $t = 0$. Hence, the initial conditions for the sensitivity equations are as follows:

$$\left(\frac{\partial C_i}{\partial \theta_j}\right)\bigg|_{t=0} = 0 \quad (i = 1, 2, 3 \text{ and } j = 1, 2, \dots, 7) \quad (\text{A.2})$$

The sensitivity equations of the dynamic model in Equations (A.1) are as follows (Equations (A.3)):

Appendix B

Preparing Solutions for both Calibrations and Runs

Stock solutions for both calibrations and runs were prepared in 40-mL vials. After weighing a specific amount of filtered deionized water (FDW) in a 40-mL vial, the organic(s) of the choice were injected into the vial through its Silicon-Teflon septum. For the standards, the stock solution was diluted into other 40-mL vials. Depending on the initial concentration needed for the runs, a specific amount of the stock solution separately prepared was injected directly into the photoreactor.

To prepare both stock and standard solutions, the concentrations of tetrahydrofuran and 1,4-dioxane were calculated using the following equations:

$$C_{THF} = \frac{\rho_{THF} V_{THF}}{V_{FDW} + 10^{-6} V_{THF}} \quad (B.1)$$

$$C_{DIOX} = \frac{\rho_{DIOX} V_{DIOX}}{V_{FDW} + 10^{-6} V_{DIOX}} \quad (B.2)$$

where C_{THF} = THF concentration, [mg L⁻¹];

C_{DIOX} = DIOX concentration, [mg L⁻¹];

ρ_{THF} = 0.8892 mg μ L⁻¹, THF density;

ρ_{DIOX} = 1.034 mg μ L⁻¹, DIOX density;

V_{FDW} = The volume of filtered deionized water, [L];

V_{THF} = Pure THF volume injected into V_{FDW} L of FDW, [μ L];

V_{DIOX} = Pure DIOX volume injected into V_{FDW} L of FDW, [μ L].

Toluene was used as the internal standard (I.S.) in GC analysis. The internal standard concentration used in both standards and samples was 40 mg L⁻¹. The stock solution of toluene was prepared using the following equation:

$$C_{TOL} = \frac{\rho_{TOL} V_{TOL}}{V_{FDW} + 10^{-6} V_{TOL}} \quad (B.3)$$

where C_{TOL} = Toluene concentration, [mg L⁻¹];

ρ_{TOL} = 0.866 mg μ L⁻¹, Toluene density;

V_{TOL} = Pure toluene volume injected into V_{FDW} L of FDW [μ L].

For definition of other parameters see Equations (B.1) and (B.2).

After preparing the stock and standard solutions, $V_{I.S.}$ mL of the internal standard stock solution was injected into either standard or sample vials according to the following equations:

for standards:

$$V_{I.S.} = \frac{40V_{std}}{C_{I.S.,stock}} \quad (B.4)$$

where V_{std} = Standard solution volume. [mL];

$V_{I.S.}$ = mL of internal standard stock solution to be added to V_{std} mL of standard solution:

$C_{I.S.,stock}$ = Concentration of internal standard stock solution. [mg L^{-1}].

for samples:

$$V_{I.S.} = \frac{40V_s}{C_{I.S.,stock}} \quad (B.5)$$

where V_s = Sample solution volume. [mL];

$V_{I.S.}$ = mL of internal standard stock solution to be added to V_s mL of sample to be analyzed.

Since toluene is relatively volatile, the internal standard stock solutions were prepared daily before GC analysis as needed.

Appendix C

Error Analysis

Any experimental work involves different sources of errors such as equipment, measurement, preparation of solutions, and human errors. However, using statistical methods, the errors can be controlled and therefore minimized. In the following, two statistical methods are illustrated as examples of controlling the errors. The errors in GC analysis was very common and needed to be controlled carefully.

The 95% confidence limits in the estimation of the parameters in this study were computed using a proper statistical method and were reported along with the estimated parameters.

C.1 Quality Control Analysis

The calibration of the GC system in the range of interest was controlled with a single point check after each batch of samples. To be confident about the data analyses, a quality control chart was made using a single point check.

The measurement was acceptable, unless it was not within the controlling limit regions then another calibration curve was made. Figure C.1 depicts a quality control sample chart in which the sample analyses for the initial concentration of 1,4-dioxane in the slurry photoreactor are shown.

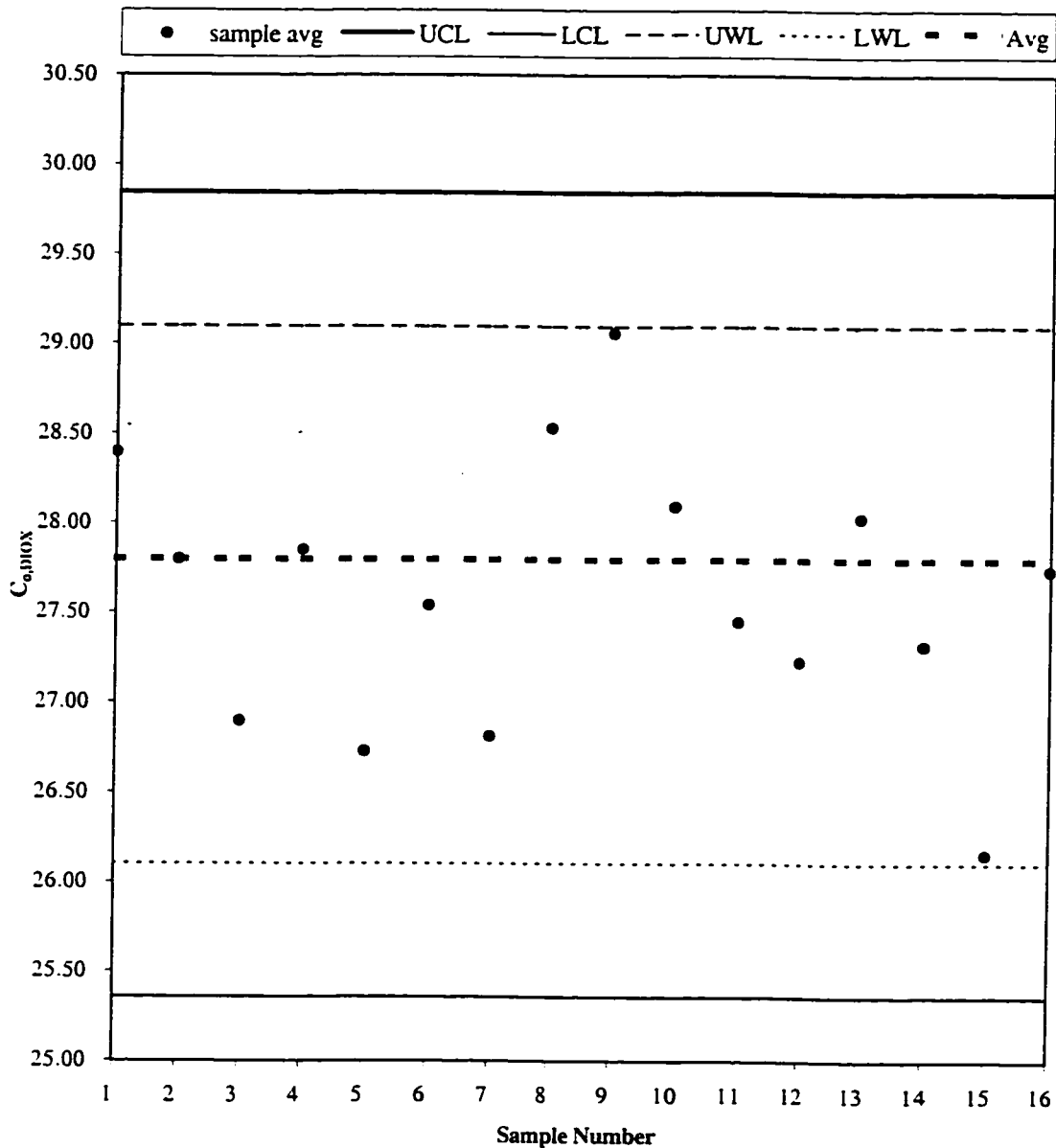


Figure C.1: A sample of quality control chart for controlling GC analysis. Samples were analyzed to find the initial concentration of 1,4-dioxane in the slurry photoreactor. Definitions: σ = standard deviation, sample avg = sample average, UCL = Upper Control Limit ($+3\sigma$), LCL = Lower Control Limit (-3σ), UWL = Upper Warning Limit ($+2\sigma$), LWL = Lower Warning Limit (-2σ), Avg = Average.

C.2 Analysis of Variance Using the Method of Hierarchical Design Experiments

As an example, the experimental data during the photocatalyst optimization trials were analyzed (see Section 5.5). The solutions were prepared in such a way that the initial concentration of 1,4-dioxane in the photoreactor in each run for both photocatalysts be the same, i.e., 27.8 mg L⁻¹. Due to the experimental error, GC analysis showed a slightly different result.

Analysis of variance using hierarchical design experiments explained by Box et al. [40] was performed for these trials. These analyses resulted in significant errors involved in the initial concentrations for those experiments. Figure C.2 depicts the 2 × 8 × 2 hierarchical design experiments for these trials. Table C.2 shows the analysis of variance for the photocatalyst optimization experiments.

The sample data are summarized in Table C.1. Using Table C.1, the following terms are computed:

$$\begin{aligned}
 P: & \quad (441.08^2 + 442.14^2) \frac{1}{16} & = 24,377.459 \\
 R: & \quad (56.79^2 + 55.59^2 + \dots + 55.48^2) \frac{1}{2} & = 24,394.227 \\
 D: & \quad (28.36^2 + 28.43^2 + \dots + 27.63^2) & = 24,405.373 \\
 \text{Correction for the Mean} & = \frac{(SUM)^2}{n} = \frac{883.22^2}{32} & = 24,377.424
 \end{aligned}$$

And the results are summarized in Table C.2. As Table C.2 shows, the error in the experiments was insignificant. The variances and standard deviations

can be computed as follows:

$$\begin{aligned}\sigma_D^2 + 2\sigma_R^2 + 16\sigma_P^2 &= 0.035 \\ \sigma_D^2 + 2\sigma_R^2 &= 1.198 \\ \sigma_D^2 &= 0.697\end{aligned}$$

Therefore,

$$\begin{aligned}\sigma_D^2 &= 0.697 \quad \text{and} \quad \sigma_D = 0.835 \\ \sigma_R^2 &= 0.251 \quad \text{and} \quad \sigma_R = 0.500\end{aligned}$$

where σ_D^2 = Variance of data;

σ_R^2 = Variance of runs;

σ_D = Standard deviation for data;

σ_R = Standard deviation for runs.

It is conclusive that the GC measurements error is the principle component of the measurement error as the other errors are found to be not significant. Thus, they do not contribute significantly to the measurement error.

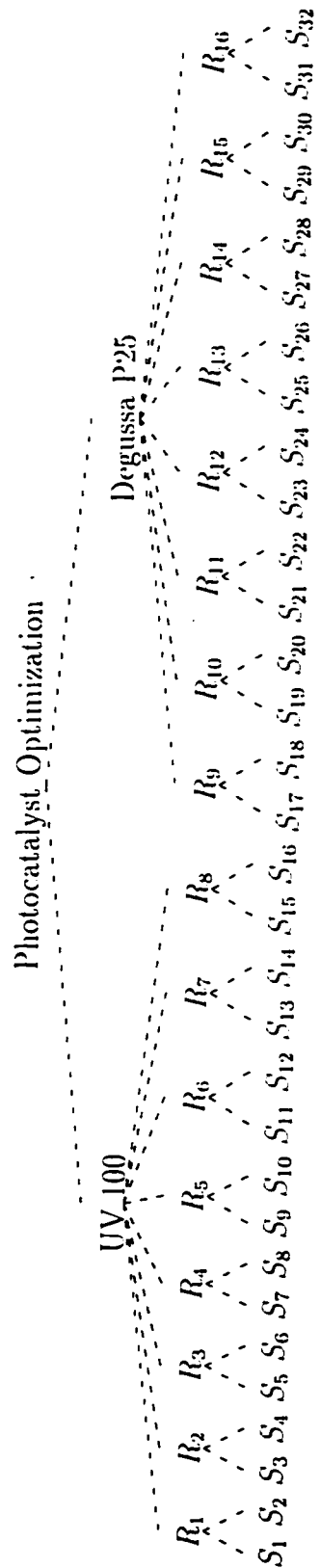


Figure C.2: The $2 \times 8 \times 2$ hierarchical design experiments for the initial concentrations of 1,4-dioxane in the photoreactor for photocatalyst optimization trials, S_i 's are the initial concentrations of 1,4-dioxane in the slurry photoreactor for the i^{th} run and R_i is the i^{th} run.

Table C.1: Sample data in the hierarchical design experiments shown in Figure C.2.

PHOTO-CATALYST	TRIAL	NO. (<i>i</i>)	DATA ($S_i = C_{0i}$)	$S(R) = \sum_{i=1}^{i+1} S_i$	$S(P) = \sum_{i=1}^{i+7} S(R)_i$	$S_{tot} = \sum_{i=1}^{32} S_i$
UV 100 <i>TiO</i> ₂	<i>R</i> ₁	1	28.36	56.79	441.08	883.22
		2	28.43			
	<i>R</i> ₂	3	27.74	55.59		
		4	27.85			
	<i>R</i> ₃	5	26.09	53.79		
		6	27.70			
	<i>R</i> ₄	7	27.20	55.70		
		8	28.50			
	<i>R</i> ₅	9	26.55	53.45		
		10	26.90			
	<i>R</i> ₆	11	27.18	55.08		
		12	27.90			
	<i>R</i> ₇	13	26.81	53.62		
		14	26.81			
	<i>R</i> ₈	15	28.84	57.06		
		16	28.22			
Degussa P25 <i>TiO</i> ₂	<i>R</i> ₉	17	29.98	58.12		
		18	28.14			
	<i>R</i> ₁₀	19	27.31	56.19		
		20	28.88			
	<i>R</i> ₁₁	21	28.75	54.90		
		22	26.15			
	<i>R</i> ₁₂	23	27.02	54.45		
		24	27.43			
	<i>R</i> ₁₃	25	27.40	56.06		
		26	28.66			
	<i>R</i> ₁₄	27	26.54	54.63		
		28	28.09			
	<i>R</i> ₁₅	29	26.35	52.31		
		30	25.96			
	<i>R</i> ₁₆	31	27.85	55.48		
		32	27.63			

Table C.2: Analysis of variance (ANOVA) using hierarchical design experiments for the photocatalyst optimization experiments.

Source of Observation	Sum of Squares (SofS)	DF ¹	Mean Square ($MS = \frac{SofS}{DF}$)	E(MS)	$F_{cal.}$ ²	$F_{95\%, \nu_1, \nu_2}$ ³	Significant?
Photocatalyst (P)	24,377.459-24,377.424 =0.035	1	0.035	$\sigma_D^2 + 2\sigma_R^2 + 16\sigma_I^2$	$\frac{\sigma_D^2 + 2\sigma_R^2 + 16\sigma_I^2}{\sigma_D^2 + 2\sigma_R^2}$ =0.029	$F_{95\%, 1, 14}$ =4.6	No
Runs (R)	24,394.227-24,377.459 =16.768	2×7 =14	1.198	$\sigma_D^2 + 2\sigma_R^2$	$\frac{\sigma_D^2 + 2\sigma_R^2}{\sigma_D^2}$ =1.719	$F_{95\%, 14, 16}$ ~ 2.3	No
Data (D)	24,405.373-24,394.227 =11.146	16×1 =16	0.697	σ_D^2			
Total	24,405.373-24,377.424 =27.949	31					

¹ Degrees of Freedom

² Calculated F-distribution

³ 95% Confidence level for F-distribution with ν_1 and ν_2 degrees of freedom, extracted from literature [40]

Appendix D

Diffusion Coefficient of 1,4-Dioxane in Water

The diffusion coefficient of 1,4-dioxane in water was calculated by using the following equation [209]:

$$D_{AB}^{\circ} = \frac{(117.3 \times 10^{-18})(\phi M_B)^{0.5} T}{\mu \nu_A^{0.6}} \quad (\text{D.1})$$

where D_{AB}° = diffusivity of A in very dilute solution in solvent B, [$\text{m}^2 \text{s}^{-1}$];

M_B = molecular weight of solvent, [kg kmol^{-1}];

T = temperature, [K];

ν_A = solute molal volume at normal boiling point, [$\text{m}^3 \text{kmol}^{-1}$] (0.0756 for water as solute);

ϕ = association factor for solvent (2.26 for water as solvent);

μ = solution viscosity, [$\text{kg m}^{-1} \text{s}^{-1}$].

For 1,4-dioxane, ν_A is estimated as follows [209]:

$$\nu_A = 0.0148(4) + 0.0037(8) + 0.0074(2) = 0.1036 \text{ m}^3 \text{ kmol}^{-1}$$

Hence, at $T=25^\circ\text{C}$:

$$\begin{aligned} D_{DIOX-H_2O} &= \frac{(117.3 \times 10^{-18})(2.26 \times 18.02)^{0.5} \times 298}{(0.01 \times 10^{-1})(0.1036)^{0.6}} \\ &= 8.694 \times 10^{-10} \text{ m}^2 \text{ s}^{-1} \end{aligned} \quad (\text{D.2})$$

Appendix E

Cost Estimation for a Photocatalysis Process

In this section, an economic evaluation of a photocatalysis application for water and wastewater treatment systems is presented. The cost estimated is based on the most severe conditions in which the reactions take place for 24 h. All costs are estimated in Canadian Dollars.

The following lists different costs involved in a general process of photocatalysis.

Capital Cost:

Considering the effective life of a photoreactor for 15 years, the capital cost of the photoreactor including auxiliary equipment, installation, etc. would be approximately \$0.001/(h L).

Operation Cost:

The operating cost including labor would normally be about \$0.0002/(h L).

Input Energy Cost:

The most expensive cost in the photocatalysis process is the energy cost. The cost of the energy input would be about \$0.020/(h L).

Consumable Materials Cost:

The cost of consumable materials such as TiO_2 , probes, etc. would be \$0.002/(h L) on average.

Therefore, the total cost is calculated as follows:

$$\begin{aligned} \text{Total Cost/Reactor Volume} &= \text{Capital Cost} + \text{Operating Cost} \\ &+ \text{Energy Cost} \\ &+ \text{Consumable Material Cost} \end{aligned}$$

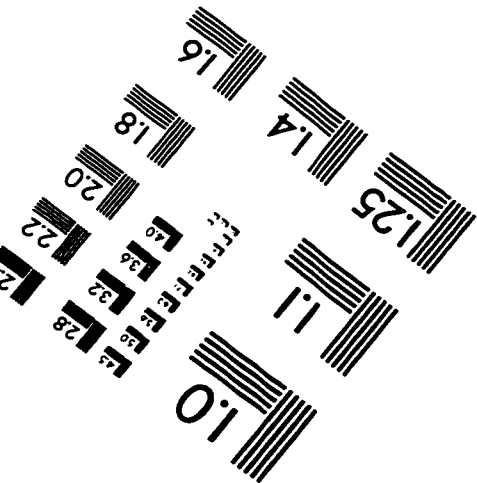
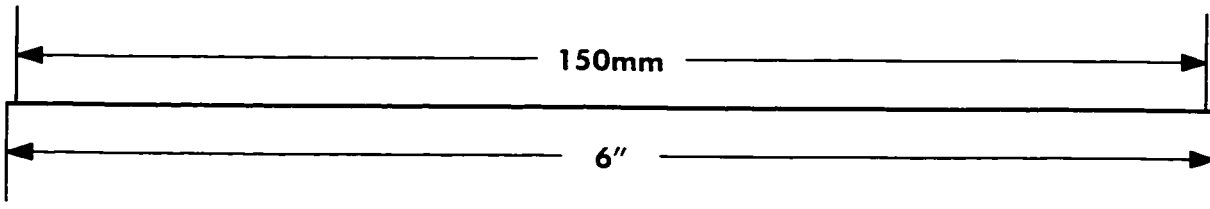
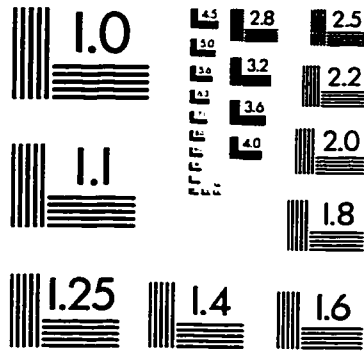
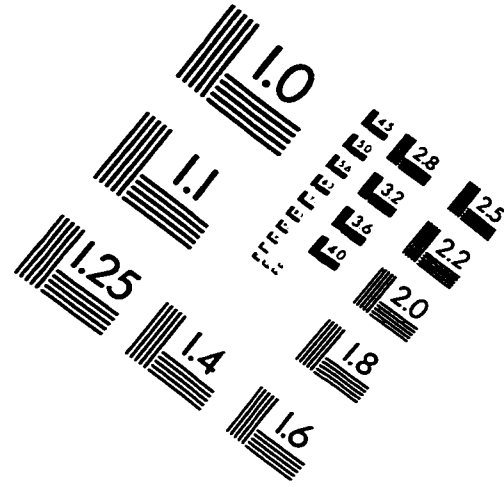
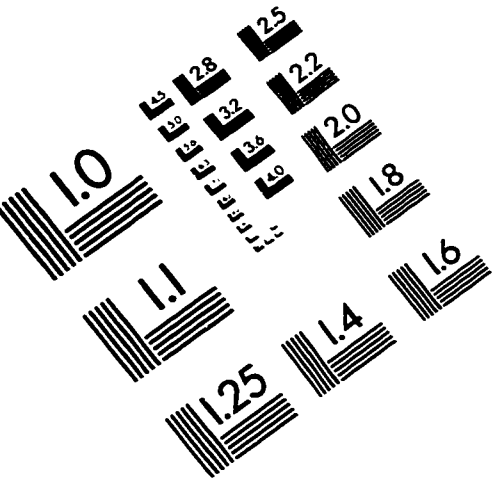
Therefore, we have:

$$\begin{aligned} \text{Total Cost/Reactor Volume} &= \$0.001/(h L) \times 24 h + \$0.0002/(h L) \times 24 h \\ &+ \$0.020/(h L) \times 24 h + \$0.002/(h L) \times 24 h \\ &= \$0.56/L \end{aligned}$$

or

$$\text{Total Cost} = \$ 2.1/\text{gal}$$

IMAGE EVALUATION TEST TARGET (QA-3)



APPLIED IMAGE, Inc
1653 East Main Street
Rochester, NY 14609 USA
Phone: 716/482-0300
Fax: 716/288-5989

© 1993, Applied Image, Inc., All Rights Reserved

